ANL-76-88
Part I

ANL-76-88
Part I

RADIOLOGICAL AND ENVIRONMENTAL RESEARCH DIVISION ANNUAL REPORT

Fundamental Molecular Physics and Chemistry

July 1975—September 1976

U of C-AUA-USERDA

ARGONNE NATIONAL LABORATORY, ARGONNE, ILLINOIS

Prepared for the U. S. ENERGY RESEARCH AND DEVELOPMENT ADMINISTRATION under Contract W-31-109-Eng-38

DISCLAIMER

The facilities of Argonne National Laboratory are owned by the United States Government. Under the terms of a contract (W-31-109-Eng-38) between the U. S. Energy Research and Development Administration, Argonne Universities Association and The University of Chicago, the University employs the staff and operates the Laboratory in accordance with policies and programs formulated, approved and reviewed by the Association.

MEMBERS OF ARGONNE UNIVERSITIES ASSOCIATION

The University of Arizona
Carnegie-Mellon University
Case Western Reserve University
The University of Chicago
University of Cincinnati
Illinois Institute of Technology
University of Illinois
Indiana University
Iowa State University
The University of Iowa
Kansas State University
The University of Kansas
Loyola University
Marquette University
Michigan State University
The University of Michigan
University of Minnesota
University of Missouri
Northwestern University
University of Notre Dame
The Ohio State University
Ohio University
The Pennsylvania State University
Purdue University
Saint Louis University
Southern Illinois University
The University of Texas at Austin
Washington University
Wayne State University
The University of Wisconsin

Printed in the United States of America
Available from
National Technical Information Service
U. S. Department of Commerce
5285 Port Royal Road
Springfield, Virginia 22161
Price: Printed Copy $8.00; Microfiche $3.00

Distribution Category:
Biology and Medicine (UC-48)

ANL-76-88
Part I

ARGONNE NATIONAL LABORATORY
9700 South Cass Avenue
Argonne, Illinois 60439

RADIOLOGICAL AND ENVIRONMENTAL RESEARCH DIVISION ANNUAL REPORT

Fundamental Molecular Physics and Chemistry

July 1975 through September 1976

R. E. Rowland, Division Director
Mitio Inokuti, Section Head

Preceding Report: 75-60, Part I, July 1974–June 1975

FOREWORD

This is the sixth Annual Report since the Section (formerly Radiation Physics Section) began to issue its own volume. The Section's activities in the past year were true to the tradition of basic studies aimed at detailed elucidation of radiation actions on matter in three areas — electron collisions with molecules, photoabsorption and photoionization, and pertinent theories. In response to current national needs, the Section also has expanded its goals to include chemical physics of atmospheric-pollutant interactions resulting from non-nuclear energy technologies. Much of the Section's expertise is useful for the basic understanding of the characterization and behavior of pollutant molecules as well as naturally occuring ones in the atmosphere. Furthermore, the Section has added to its staff a new member, P. M. Dehmer, who is now developing a major program dedicated to atmospheric chemistry.

The papers in the present volume are ordered in accordance with the subjects treated. Papers 1–6 concern electron energy-loss spectroscopy; papers 7–24 photoabsorption, photoionization, and photoelectron analysis; papers 25–34 electron collisions and related topics; papers 35–36 the delivery of radiation energy to matter; and papers 37–40 energetic collisions of atoms and molecules.

Examples of our major achievements include the full operation of the electron energy-loss spectrometer (as described in papers 3 and 4), a versatile theory of molecular photoionization and electron-molecule collisions (papers 9–14 and 25), high-resolution photoelectron analysis (papers 16–18), the initiation of photoion analysis (paper 19). In addition, notable achievements concern theoretical studies on properties of highly stripped ions (papers 29 and 32) — a subject of crucial importance to fusion-energy research. Work by Y.-K. Kim in this area has now received well-deserved recognition and support by ERDA-DMFE, and will see fruition in the near future.

Finally, we are proud to have played major roles in various conferences and organizations outside the laboratory. Examples of our recent activities in this respect include the Ninth International Conference on the Physics of

Electronic and Atomic Collisions, Seattle, 1975, the Second International Conference on Inner-Shell Ionization Phenomena, Freiburg, 1976, and NATO Institutes on Photoionization (1975) and on Molecular Spectroscopy (1976). Also, the Section Head works on report committees of the International Commission on Radiation Units and Measurements, as well as on the Editorial Board of Radiation Research.

TABLE OF CONTENTS

Fundamental Molecular Physics and Chemistry

ELECTRON ENERGY-LOSS ANALYSIS OF CARBON TETRAFLUORIDE AND CARBON TETRACHLORIDE*

R. H. Huebner, R. J. Celotta,† and S. R. Mielczarek†

Apparent oscillator-strength distributions for CF_4 and CCl_4 were derived from the electron energy-loss spectra (shown in Figures 1 and 2) obtained with 100-eV incident electrons scattered at 0°. Our results for CF_4 agree closely with the previous electron-impact results[1] obtained with 500-eV incident electrons. Photoabsorption results[2,3] for CF_4 show a similar spectral shape, although the absolute magnitudes of the optical values are higher by as much as a factor of two. The distributions obtained for CF_4 by optical and electron-impact techniques are compared in Figure 3.

The energy-loss spectrum of CCl_4 is in qualitative agreement with that reported[4] for 25-keV incident electrons below 14 eV, but does not show many of the sharp structures observed in that work at higher energies. Oscillator strengths we derive for CCl_4 between 11 and 21 eV agree to within ± 10% of the photoabsorption values measured by Person et al.,[5] when normalized at 12.2 eV. The comparison is shown in Figure 4. Our results also agree closely with the photoabsorption values reported by Rowland and Molina[6] for the solar window region (5–7 eV) shown in Figure 5. Depletion of the stratospheric ozone layer should result after photodissociation of CCl_4 by the same sequence of events as described[6] for chlorofluoromethanes. However, since CCl_4 has been in industrial use for many years, its effects on the photochemistry of the stratosphere should already be reasonably near equilibrium.

---

*Extended abstract of a paper presented at the Annual Meeting of the Division of Electron and Atomic Physics of the American Physical Society, 6-8 Dec. 1976, Lincoln, Nebraska.

†National Bureau of Standards, Washington, D.C.

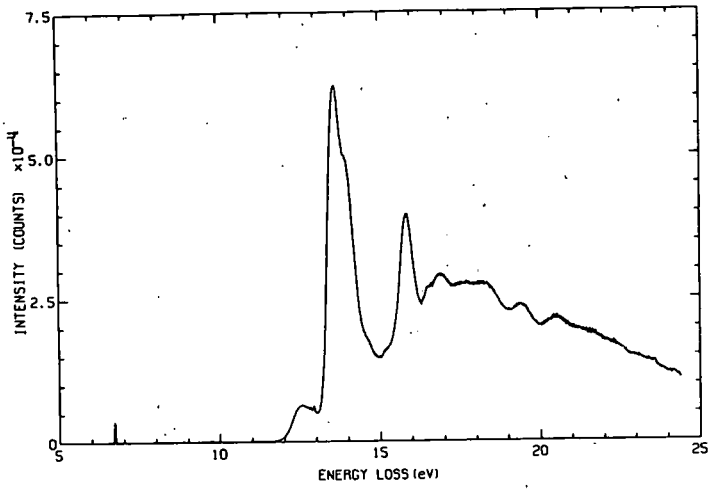

FIG. 1.--The electron energy-loss spectrum of carbon tetrafluoride (CF_4) obtained for 100-eV electrons scattered within 20 mrad of the incident direction. The sharp peak at 6.7 eV and structures near 13 eV and above 20 eV are due to slight amounts of mercury and nitrogen impurities in the system.
(ANL Neg. 149-76-164)

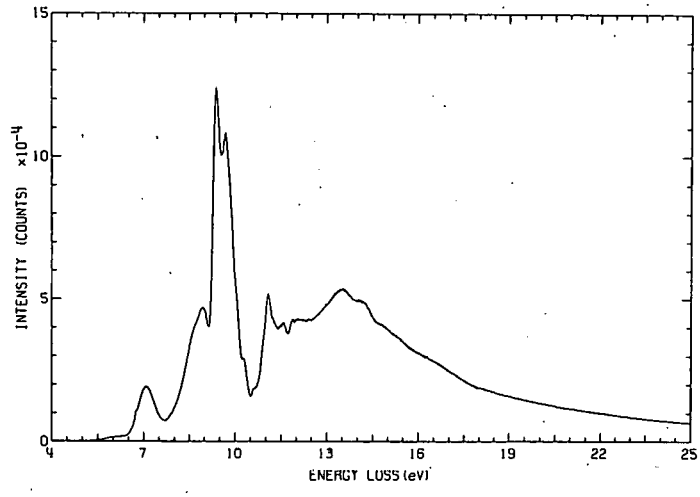

FIG. 2.--The electron energy-loss spectrum of carbon tetrachloride (CCl_4) obtained for 100-eV electrons scattered within 20 mrad of the incident direction.
(ANL Neg. 149-76-169)

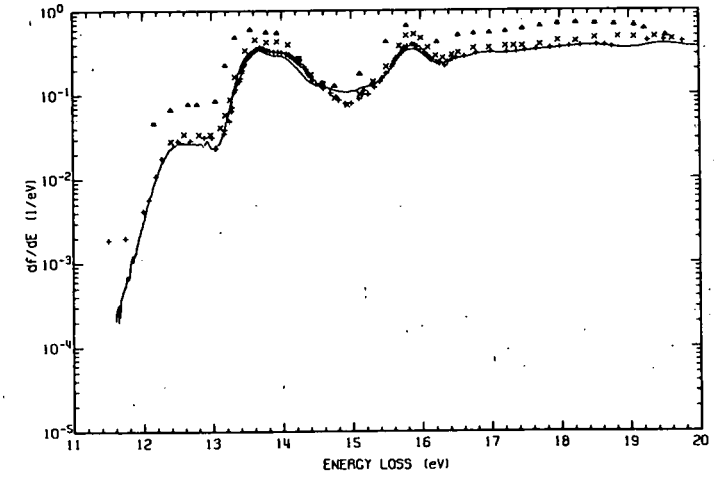

FIG. 3.--Comparison of the oscillator-strength distributions for CF_4: +, electron-impact values, Ref. 1; solid line, present work, and optical values; x, Ref. 2; Δ, Ref. 3. The present results were normalized so that integrated f values for the bands at 12.5 and 13.5 eV would agree with values reported by Ref. 1.
(ANL Neg. 149-76-168)

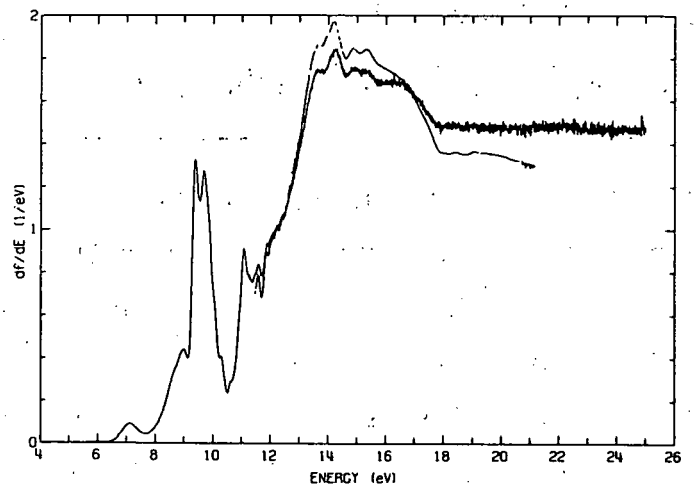

FIG. 4.--Comparison of the apparent oscillator-strength distribution obtained for CCl_4 with optical results. The upper curve in the 14 eV region shows the photoabsorption values of Person et al.;[5] it falls below the electron-impact results below about 12.5 eV and above 17 eV. (ANL Neg. 149-76-166)

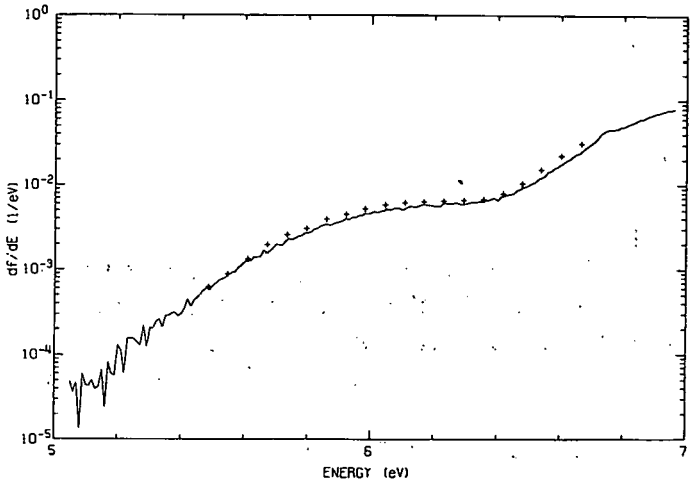

FIG. 5.--Comparison of the apparent oscillator strengths (solid line) obtained for CCl_4 with the optical values (+, Ref. 6) in the solar window region. (ANL Neg. 149-76-162)

References

1. W. R. Harshbarger and E. N. Lassettre, J. Chem. Phys. 58, 1505 (1973).
2. G. R. Cook and B. K. Ching, J. Chem. Phys. 43, 1794 (1965).
3. P. Sauvageau, R. Gilbert, P. P. Berlow, and C. Sandorfy, J. Chem. Phys. 59, 762 (1973).
4. J. S. Lee, T. C. Wong, and R. A. Bonham, J. Chem. Phys. 63, 1609 (1975).
5. J. C. Person, D. E. Fowler, and P. P. Nicole, Radiological and Environmental Research Division Annual Report, July 1974–June 1975, ANL-75-60, Part I, p. 26.
6. F. S. Rowland and M. J. Molina, Rev. Geophys. Space Phys. 13, 1 (1975).

APPARENT OSCILLATOR STRENGTHS FOR WATER VAPOR*

R. H. Huebner, M. E. O'Connor,† R.J. Celotta,‡ and S.R. Mielczarek‡

Electron energy-loss spectra for H_2O were measured for 100-, 300-, and 400-eV electrons scattered close to the incident direction (Figure 1). Apparent oscillator-strength distributions were obtained by the small-angle method,[1-3] and were all normalized at 14.58 eV to df/dE = 0.198 eV^{-1}, which gave the best overall fit to available optical data. This value is a factor of 1.3 larger than the optical value of 0.1526 eV^{-1} reported in Ref. 4 for the same energy. Apparent oscillator-stength distributions derived from these spectra

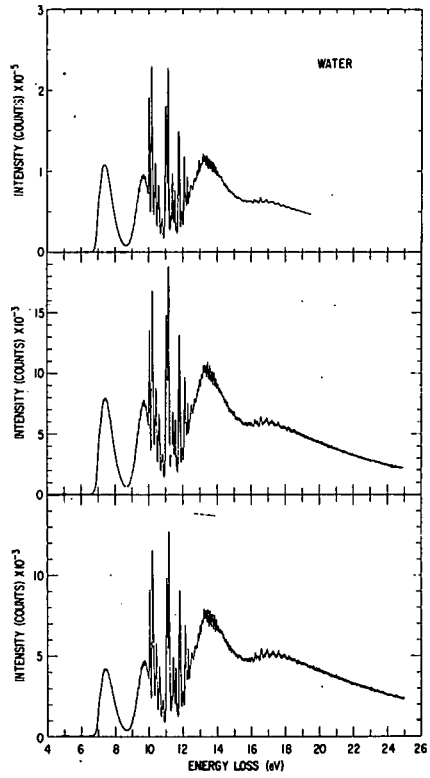

FIG. 1.--Energy-loss spectra of water vapor for electrons scattered within 20 mrad of the incident direction: top, T = 100 eV; center, T = 300 eV; bottom, T = 400 eV.
(ANL Neg. 149-76-132).

*Extended abstract of a paper submitted to the 1977 Joint American Physical Society/American Association of Physics Teachers Meeting of the American Physical Society, Chicago, Ill., 7–10 February 1977.

†Argonne Center for Educational Affairs Undergraduate Research Participant from Clarke College, Dubuque, Iowa.

‡National Bureau of Standards, Washington, D.C.

are nearly identical for energy losses less than 15 eV. These results show excellent agreement with the composite of available photoabsorption data and provide an independent source of f values for the many discrete transitions in this region.

The absorption spectrum of H_2O in the region from 6.60 to 8.60 eV consists mainly of a continuum having a maximum at about 7.4 eV. This absorption continuum has been measured by Watanabe et al.,[5] Harrison et al.,[6] Tsubomura et al.,[7] and Laufer and McNesby.[8] Our values from the T = 300 eV spectrum are compared with the data of these workers in Figure 2. Our values are in excellent agreement with those of Watanabe et al.[5] The values of Laufer and McNesby[8] are about 15% higher. The data of Harrison et al.[6] are nearly 30% higher than ours, while measurements of Tsubomura et al.[7] are about 30% lower. Thus, our values are consistent with optical values for this band, although the broad range of reported optical values does not permit a good test of our accuracy.

The region from 8.60 to 9.90 eV consists of a continuum underlying a series of diffuse bands. Our results (Figures 2 and 3) agree with observations of these bands by Watanabe et al.[5] The f values they derived are also in good agreement with our values (± 3%). The structure was not observed by Laufer and McNesby,[8] however, the shape of their curve and the f values they obtained agree to within ± 4% of our values. This agreement between our values and the optical data is excellent for this band.

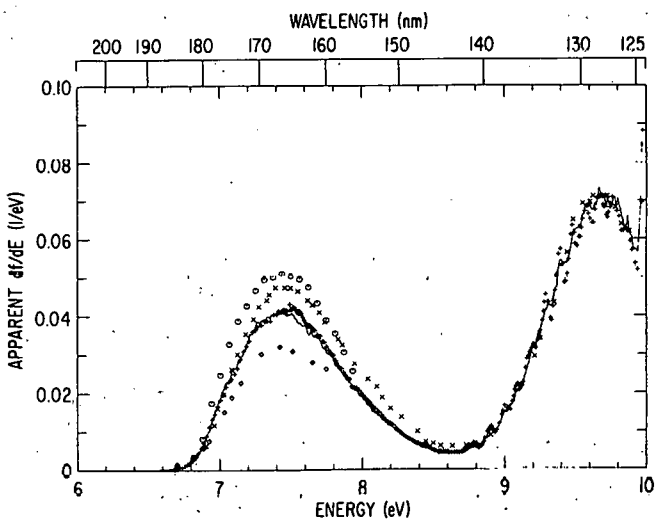

FIG. 2.--Comparison of the apparent oscillator-strength distribution for water vapor (solid line) with optical values (+, Ref. 9; ⊙, Ref. 6; x, Ref. 8; and ◇, Ref. 7) in the 6 to 10 eV energy-absorption region. (ANL. Neg. 149-76-130)

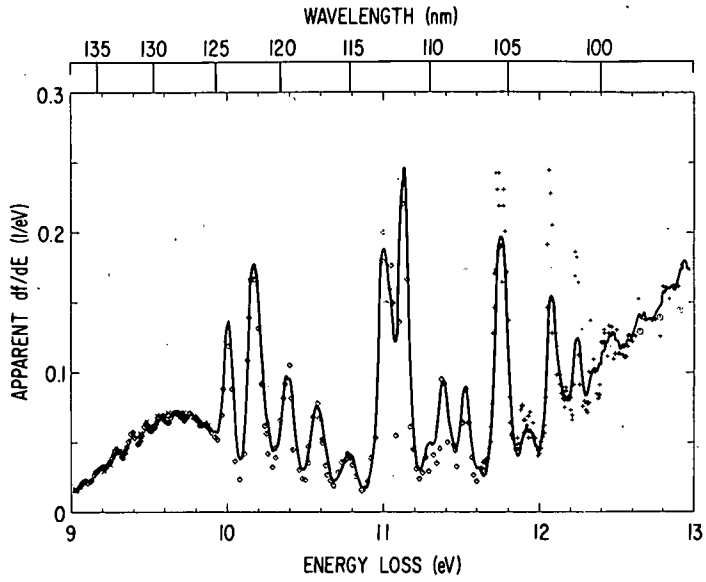

FIG. 3.--Comparison of the apparent oscillator-strength distribution for water vapor (solid line) with optical values (+, Ref. 10; ⊙, Ref. 12, x, Ref. 8; and ◇ , Ref. 9) in the 9 to 13 eV energy-absorption region. (ANL Neg. 149-76-127, Rev. 1)

There are many discrete absorption bands between 10.00 and 12.50 eV (Figure 3). Watanabe et al.[9] measured the photoabsorption cross sections up to 11.7 eV. Watanabe and Jursa[4] reported values in the region from 11.7 to 15.6 eV. Although their data are not shown in Figure 3, we see qualitatively the same structure up to 12.50 eV, although their values are slightly lower than ours. An extensive set of optical values from 11.7 to 18.0 eV are available from the work of Katayama et al.[10] The direct comparison of these photoabsorption data with the present data in the region from 10.00 to 12.50 eV is complicated by the difference in energy resolution achievable by the two different methods. The higher resolution optical measurements show deeper valleys, higher peaks, and narrower peak widths than the lower resolution energy-loss data. This can be seen in Figure 3, where these data are compared. However, the structure and average intensities are in qualitatively good agreement.

The diffuse bands observed in the region from 13.00 to 15.00 eV by our electron energy-loss measurements, overlap those observed by Person and co-workers[11] and Katayama et al.[10] (Figure 4). The measurements of Person and co-workers are estimated to be accurate to ± 3%. The energy positions of our peaks closely match theirs throughout this region, but our intensities gradually become larger than theirs as the energy loss increases above about 14.00 eV. This is true for all data sets obtained for different incident energies.

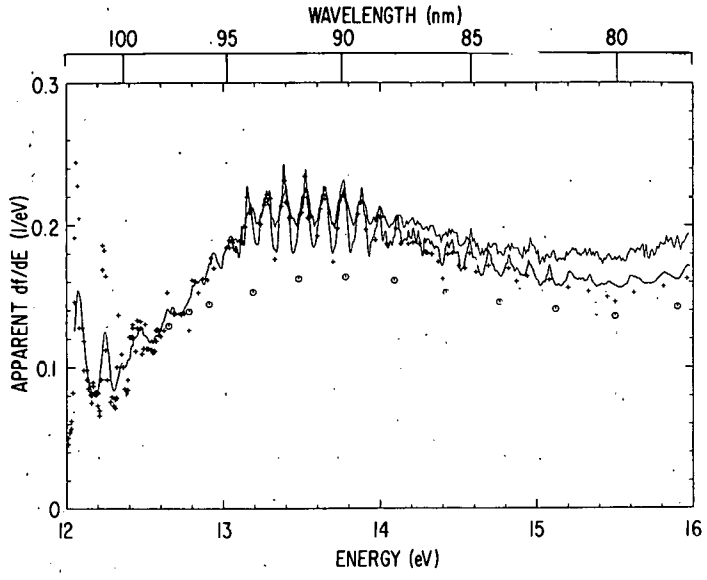

FIG. 4.--Comparison of the apparent oscillator-strength distribution for water vapor (solid line upper) with optical values (+, Ref. 10; ⊙, Ref. 12; and solid line lower, Ref. 11) in the 12 to 16 eV energy absorption region.
(ANL Neg. 149-76-126)

In contrast to the good agreement obtained for the low-energy regions, the deviation of our data from the optical measurements appears to increase markedly above 15.00 (Figure 5). However, between our values and those of Person and co-workers[11] and Katayama et al.[10] there is no more than a 24% difference. Data of Metzger and Cook,[12] on the other hand, differ from our data by 28 to 64% over the same energy-loss region. We cannot fully explain this behavior, but we suspect some instrumental distortion may be occurring at large energy losses.

Total f values for a given band between two energies, E_1 and E_2, may be obtained from the oscillator distributions we obtain by integration:

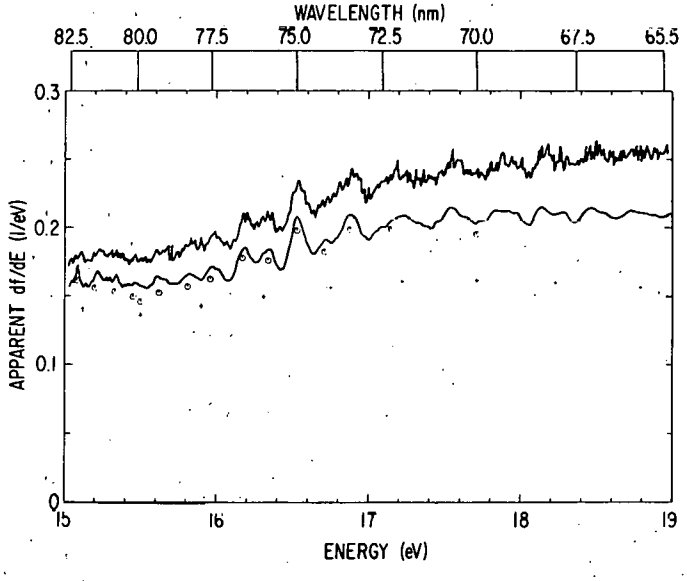

FIG. 5.--Comparison of the apparent oscillator-strength distribution for water vapor (solid line upper) with optical values (+, Ref. 12; ⊙, Ref. 10; and solid line lower, Ref. 11) in the 15 to 19 eV energy absorption region.
(ANL Neg. 149-76-131)

$$f = \int_{E_1}^{E_2} (df/dE)\, dE \ .$$

Table 1 lists the values obtained for bands in the range 0 to 15 eV. Here a difference of no more than ± 13% from the average is observed. The total integrated f values over the regions 0 to 15 eV agree for the three runs to within ± 2.5% of the average. These results indicate that for energy-loss values less than about 15.00 eV, the f values for H_2O do not depend strongly on the incident energy. For energy losses between 15 and 25 eV the three distributions differ by no more than ± 30%, although they gradually rise above the vacuum ultraviolet photoabsorption measurements. Previously reported electron-impact values in this spectral region are considerably smaller than both the optical data and our present results.

TABLE 1. Comparison of Integrated Oscillator-Strength Values for Water for Different Incident Energies (T).

Energy Band		Integrated F Value Between E_1 and E_2			
E_1, eV	E_2, eV	T = 100 eV	T = 300 eV	T = 400 eV	Average
6.60	8.65	0.0344	0.0400	0.0320	0.0355
8.65	9.93	0.0465	0.0498	0.0432	0.0465
9.93	10.08	0.0128	0.0129	0.0118	0.0125
10.08	10.30	0.0213	0.0219	0.0203	0.0212
10.30	10.49	0.0114	0.0119	0.0107	0.0113
10.49	10.69	0.00967	0.00986	0.00898	0.00950
10.69	10.88	0.00562	0.00564	0.00519	0.00548
10.88	11.08	0.0199	0.0223	0.0194	0.0205
11.08	11.23	0.0182	0.0200	0.0182	0.0188
11.23	11.32	0.00377	0.00388	0.00348	0.00371
11.32	11.47	0.0103	0.0100	0.00940	0.00991
11.47	11.59	0.00737	0.00761	0.00702	0.00733
11.59	11.66	0.00228	0.00203	0.00200	0.00210
11.66	11.86	0.0216	0.0228	0.0212	0.0218
11.86	12.00	0.00796	0.00727	0.00706	0.00743
12.00	12.19	0.0193	0.0195	0.0184	0.0190
12.19	12.31	0.0122	0.0121	0.0116	0.0120
12.31	12.38	0.0071	0.0069	0.0066	0.0068
12.38	12.50	0.0142	0.0143	0.0136	0.0140
12.50	12.56	0.0072	0.0072	0.0069	0.0071
0.00	15.00	0.763	0.774	0.740	0.759

References

1. R. H. Huebner and R. J. Celotta, Argonne National Laboratory Radiological and Environmental Research Division Annual Report, July 1971–June 1972, ANL-7960, Part I, p. 49.
2. R. H. Huebner, R. J. Celotta, S. R. Mielczarek, and C. E. Kuyatt, J. Chem. Phys. 59, 5434 (1973); J. Chem. Phys. 63, 2411 (1975); J. Chem. Phys. 63, 4490 (1975).
3. M. Inokuti, Rev. Mod. Phys. 43, 297 (1971).
4. K. Watanabe and A. S. Jursa, J. Chem. Phys. 41, 1650 (1964).
5. K. Watanabe and M. Zelikoff, J. Opt. Soc. Am. 43, 753 (1953).
6. A. J. Harrison, B. J. Cederholm, and M. A. Terwilliger, J. Chem. Phys. 30, 355 (1959).
7. H. Tsubomura, R. Kimura, K. Kaya, J. Tanaka, and S. Nagakura, Bull. Chem. Soc. Japan 37, 417 (1964).
8. A. H. Laufer and J. R. McNesby, Can. J. Chem. 43, 3487 (1965).
9. K. Watanabe, M. Zelikoff, and E. C. Y. Inn, Air Force Cambridge Research Center, Technical Report No. 53-23, p. 75 (1953).
10. D. H. Katayama, R. E. Huffman, and C. L. O'Bryan, J. Chem. Phys. 59, 4309 (1973).
11. J. C. Person, Argonne National Laboratory, personal communication.
12. P. H. Metzger and G. R. Cook, J. Chem. Phys. 41, 642 (1964).

IMPROVEMENTS IN THE ELECTRON ENERGY-LOSS SPECTROMETER

H. Tanaka,* R. H. Huebner, O. J. Steingraber, and D. Spence

Several design modifications and improvements in the EELS system are summarized.

The design, construction, and preliminary testing of the electron energy-loss spectrometer (EELS) have been previously reported.[1-3] During the past year several design modifications and improvements have been made, such as upgrading of the magnetic shielding of the instrument, improving the collision region design and shielding, and redesigning the electron monochromator and associated electronic controls. The newly-designed high-resolution electron monochromator for the EELS system is described separately elsewhere in this report.[4]

A double-layer magnetic shield was designed and fabricated to fit inside the vacuum chamber, and it surrounds the monochromator-analyzer assembly. High-permeability magnetic-shielding material with an inner thickness of 0.0625 in and outer thickness of 0.03125 in was used to construct the shields. After fabrication the entire shielding assembly was vacuum annealed at 2050 F ± 25 F for one hour and cooled at a rate of 450 F/hr to 1600 F and then at a rate of 600 F/hr to ambient temperature.

In situ measurement of the residual magnetic field with a Hall effect probe indicated a residual 4-mG field in the vertical direction and a horizontal component of about 3 mG along the axis of the chamber. This is an improvement of better than a factor of 10 from the previous magnetic shielding used. Some inhomogenieties in the magnetic field were observed, particularly near the access ports and pumping orifice. In these regions the residual magnetic field increased because of the concentration and penetration of the magnetic flux at the edges of the orifice. The variations in the magnetic field were

*Postdoctoral appointee from Sophia University, Tokyo, Japan.

mapped out inside the chamber and did not exceed ± 5 mG within 6 in of the center of the chamber except close to the pumping port, where the measured field reaches 20 mG at a few points. However, in the regions where the electron beam passes at low energies, the residual magnetic fields are low enough that no detectable effects are expected.

Figure 1 shows a cutaway diagram of the newly designed collision region. It consists of gas jet, a 120° sector beam collector, and an inner and outer electrostatic shield. The gas jet was fabricated from molybdenum with the length-to-diameter ratio of 10. Three jets with diameters of 0.015, 0.020, and 0.025 in can be interchanged and are sealed to the support gas tube by gold gasket of 0.005-in thickness. An inner electrostatic shield constructed of molybdenim is a 0.25-in diameter tube that fits snugly around the gas jet. This defines the uniform potential region in the scattering volume above the gas jet orifice. The electron beam enters through a slot, and electrons scattered into the analyzer pass through a large diameter hole. The unscattered beam passes through the slot on the opposite side of the tube and is intercepted by the sector beam collector. In Figure 1 the beam would pass from left to right for a scattering angle 90° into the analyzer.

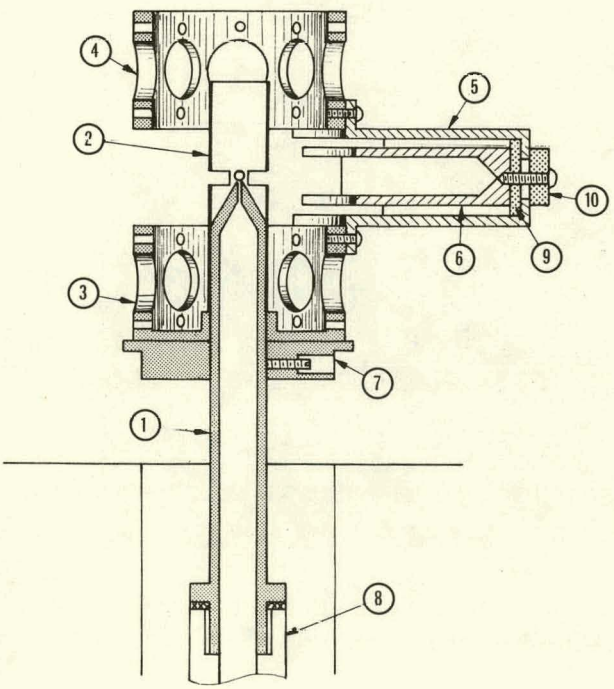

FIG. 1.--A cut-away diagram of the collision region assembly: (1) gas jet, (2) inner shield, (3) outer shield (bottom), (4) outer shield (top), (5) outer shield for beam collector, (6) 120° sector beam collector, (7) support collar, (8) support gas tube, (9) and (10) insulators.

The outer electrostatic shield support and beam collector are fabricated from titanium. However, all inner surfaces surrounding the collision region are screened with 100 × 100 mesh molybdenum wire (0.002-in diameter) cloth to provide as uniform a surface potential in this region as possible. The monochromator-exit and analyzer-entrance cones protrude inside the outer shield, so that the effect of stray electric fields on the electron trajectories in the collision region should be negligible.

The design of a hemispherical deflector monochromator for high-resolution operation is described elsewhere.[4] The electron optical lenses and hemispherical deflectors were fabricated from a vacuum arc-cast, high-purity molybdenum. A photograph of the completed monochromator assembly and the collision regions are shown in Figure 2. Since the operating voltage requirements are different for the new monochromator, a new voltage control unit and other electronic modifications were needed. These have also been completed. The new control units utilize coaxial shielded cables for all voltage leads to

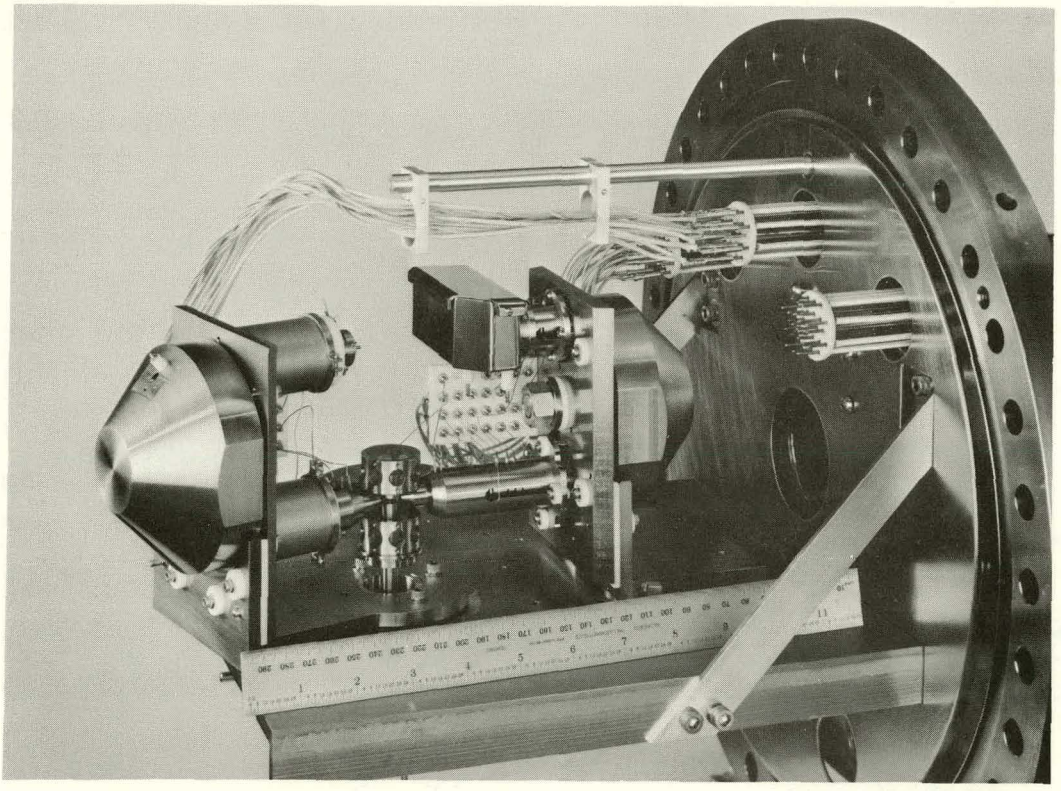

FIG. 2.--Photograph of the completed monochromator-analyzer assembly and collision region assembly. (ANL Neg. 149-76-320)

reduce transient voltage pickup, and all battery voltage sources have been replaced by compact ac-dc constant-voltage output, low current power supplies. Tests of the operation of the EELS system with all the incorporated improvements will be initiated in the next fiscal year.

References

1. D. Spence and R. H. Huebner, Radiological and Environmental Research Division Annual Report, July 1971–June 1972, ANL-7960, Part I, p. 45.
2. R. H. Huebner, D. Spence, and O. J. Steingraber, Radiological and Environmental Research Division Annual Report, July 1972–June 1973, ANL-8060, Part I, p. 74.
3. R. H. Huebner, D. Spence, and O. J. Steingraber, Radiological and Environmental Research Division Annual Report, July 1973–June 1974, ANL-75-3, Part I, p. 37.
4. H. Tanaka and R. H. Huebner, Electron-Optical Design Parameters for a High-Resolution Electron Monochromator, this report.

ELECTRON-OPTICAL DESIGN PARAMETERS FOR A HIGH-RESOLUTION ELECTRON MONOCHROMATOR

H. Tanaka* and R. H. Huebner

Detailed design parameters of a new, high-resolution electron monochromator are presented. The design utilizes a hemispherical filter as the energy-dispersing element and combines both cylindrical and aperture electrostatic lenses to accelerate, decelerate, transport, and focus the electron beam from the cathode to the interaction region.

Introduction

Methods for producing and focusing electron beams with an adjustable mean energy and narrow-energy spread are well known. For applications at intermediate and low incident energies (i.e., at less than a few keV) electrostatic energy filters and electron-optical lenses have been widely used. However, design details of any electron-monochromator system can differ in various ways, depending on the specific operating characteristics desired. In this report we present a new design for an electron monochromator to be used with the electron energy-loss spectrometer system.

The new electrostatic energy selector was designed to give the highest possible currents for an electron beam having a low-to-intermediate mean energy (≤ 1 keV) and a full width at half-maximum (FWHM, the energy resolution width) that is ≤ 0.050 eV. The design was also constrained to be compatible with the geometrical configuration of the electron energy-loss spectrometer (EELS) system.

Our design mainly follows the development set out by Simpson and Kuyatt for the use of electrostatic energy filters of a hemispherical shape. However, in the overall electron optical design of the monochromator, we have relied on the principles discussed in Refs. 1–4. Figure 1 is a schematic diagram of our monochromator.

*Postdoctoral Appointee from Sophia University, Tokyo.

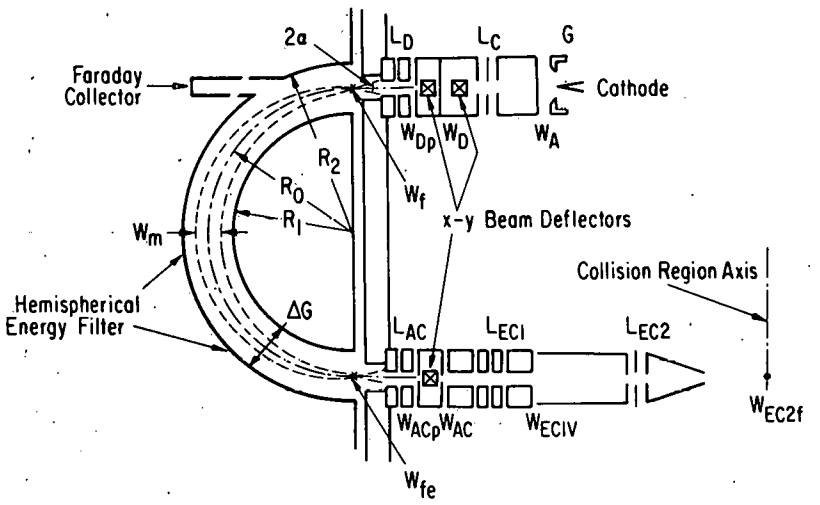

FIG. 1.--Diagram of the high-resolution electron monochromator.

Design of Hemispherical Electrostatic Deflectors

The energy-dispersing element used in the monochromator is an electrostatic hemispherical deflector with a mean radius of 1.5 in and virtual input and exit apertures.

Energy Resolution

With entrance and exit virtual slits of equal width W_f, and with mean radius R_0 as well, the resolving power $\Delta E_{\frac{1}{2}}/E_0$ at a given mean energy E_0 can be estimated[2] by

$$\Delta E_{\frac{1}{2}}/E_0 = W_f/2R_0 \ , \tag{1}$$

where $\Delta E_{\frac{1}{2}}$ is the FWHM of the monochromatized energy distribution. The base width ΔE_b of the energy distribution is given[2] by

$$\Delta E_b/E_0 = W_f/R_0 + \alpha^2 = 2.5\ \Delta E_{\frac{1}{2}}/E_0 \ , \tag{2}$$

where α is the divergence half-angle of the electron beam at the entrance of the hemispheres given by

$$\alpha^2 = W_f/4R_0 \ . \tag{3}$$

Thus, for the selected value $R_0 = 1.5$ in and $W_f = 0.02$ in, Eqs. 1–3 determine the parameters given in Table 1. However, the value we actually chose is a somewhat more desirable compromise between intensity and energy resolution.

TABLE 1. Parameters of the Hemispherical Deflector.

Parameters		Calculated values	
$\Delta E_{\frac{1}{2}}/E_0$		0.006	
$\Delta E_b/E_0$		0.017	
α, rad		0.058	
W_m/R_0		0.1	
$W_m/\Delta G$		0.29	
E_0, eV	2.5	5	7
$\Delta E_{\frac{1}{2}}$, eV	0.017	0.033	0.047
ΔE_b, eV	0.043	0.083	0.118
ΔV, V	1.714	3.429	4.800
I_i, μA	0.52	1.40	2.30
$I_{\Delta E_{\frac{1}{2}}}$, μA	0.09	0.47	1.10

Filling Factor

The maximum deviation W_m of an electron from the central path is given[2] by

$$W_m/R_0 = \Delta E_{\frac{1}{2}}/E_0 + \alpha + (W_f/2R_0 + \Delta E_{\frac{1}{2}}/E_0)^2 (2\alpha)^{-1} , \qquad (4)$$

where $W_f/2R_0 \ll 1$ and $\Delta E_{\frac{1}{2}}/E_0 \ll 1$.

In order to transmit the whole divergent beam, a separation $\Delta G = 0.5$ in between the hemispherical electrodes has been chosen. The ratio $W_m/\Delta G$ is called the filling factor. For our design, W_m/R_0 and $W_m/\Delta G$ can be simply calculated and are given in Table 1. The separation ΔG also determines the potential difference ΔV that needs to be applied between electrodes in order for the electron beam to be properly focused at a given mean energy, E_0. Then, E_0 is given by

$$\Delta V = E_0(R_2/R_1 - R_1/R_2) , \qquad R_2 > R_1 , \qquad (5)$$

where R_1 and R_2, respectively, are the inner and outer radii of hemispheres. The calculated values of ΔV at three values of E_0 are given in Table 1.

Space Charge in Spherical Deflectors

Once the value of $\Delta E_{\frac{1}{2}}$ and the size of the deflector are chosen, only

the mean energy, E_0, at the spherical deflectors remains to be selected. The optimum value of E_0 can be found by use of the space-charge model discussed by Simpson and Kuyatt.[2] The total space-charge-limited current, I_i, entering the spherical deflector is given by[1]

$$I_i = 19.3\, E_0^{\frac{1}{2}}\, \Delta E_{\frac{1}{2}} \,. \tag{6}$$

The maximum monochromator current for a hemispherical monochromator with virtual apertures is given[1] by

$$I_{\Delta E_{\frac{1}{2}}} = 19.3\, E_0^{\frac{1}{2}}\, (\Delta E_{\frac{1}{2}})^2 / \Delta E_k \,, \tag{7}$$

where $\Delta E_k \cong 0.25$ eV for a thermionic source. The use of virtual apertures avoids the space-charge limitation on current passed through a real aperture at a fixed voltage, allowing a greater flexibility in choosing E_0 and the monochromatized current. Table 1 gives typical values of these parameters for arbitrary choices of E_0. The charging-up effect due to the contamination on the surface of a real aperture can be avoided by using the virtual apertures.

Herzog Correction

The fringing fields at the input and output planes of the hemispherical deflector are compensated for by applying the Herzog correction.[5,6] This can be done by adjusting either of the two parameters, $2d_m/\Delta G$ and $b/\Delta G$, where b, d_m, and ΔG are defined in Figure 2. We choose $d_m = 0.1$ in and $\Delta G = 0.5$ in, and thus $2d_m/\Delta G = 0.4$. With this choice, $b/\Delta G = 0.56$ is determined from the graph in Figure 2 of the paper by Herzog.[5] Thus, the diameter of the lens elements adjacent to the entrance and exit planes of the hemispherical deflector should be d = 0.28 in.

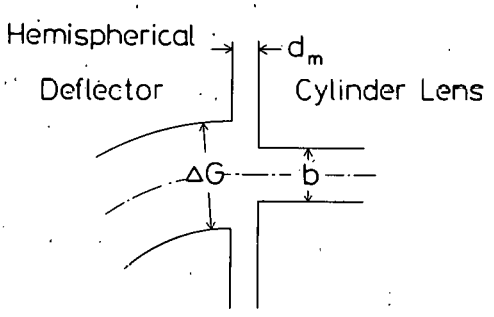

FIG. 2.--Diagram of the parameters used in the Herzog electric-field correction.

Design of One-Stage Decelerator

The electrostatic lenses (Figure 1) must be designed to produce an electron beam that has the optimum values of E_0, α, and W_f and to focus it at the virtual slit of the spherical deflector. The input lens L_D and output lens L_{AC} image the entrance aperture W_D and output aperture W_{AC} onto the corresponding virtual apertures at the entrance and exit planes of the deflector, in each case with a magnification of 1.5. Both L_D and L_{AC} are double-cylinder lenses; the former, acting as a single-stage decelerator, reduces the input energy of the electron beam by a factor of 10, while the latter acting as a single-stage accelerator reaccelerates it by the same factor. With these lenses the defining apertures (W_D, W_{AC}, W_{Dp}, and W_{ACp}) intercept the electrons in a region of relatively high kinetic energy, and the effects of surface potentials and space charge are minimized. The pupil diameter, W_{Dp}, limits the beam half-angle at the entrance of the hemispherical deflector. It is located at the second focal point of L_D so that its image is focused at infinity. This provides for a zero beam angle at the monochromator entrance. The design of these lenses follows the principles outlined by Kuyatt.[1] The focusing properties of these lenses are calculated from the lens equations of Spangenberg[7] and from the matrix method of Kuyatt.[1] The double-cylinder lens parameters are taken from the more accurate calculations in Ref. 8.

Initial Design Conditions

The initial design considerations for the L_D lens suggest a decelerating lens with a 10:1 voltage ratio. We opted for a two-element cylinder lens to do this job with an overall length of about one inch and with a filling factor of about 0.5. The parameters of the hemispherical deflector (Table 1) also required a magnification $M_D = 1.5$ and an initial object diameter $W_{AC} = W_f/M_D = 0.013$-in diameter. To achieve the desired $\theta_{pf} = 0.071$ rad and $\theta_{bf} = 0$, we must position a pupil (see Appendix A) of appropriate size such that the initial pencil half-angle be restricted by

$$\theta_{pi} = M_D \theta_{pf} (V_{Di}/V_{Do})^{\frac{1}{2}} = 0.0336 \text{ rad.}$$

Parameters of L_D (and L_{AC} Lens

Using the matrix method of Ref. 8, the properties of a double-cylinder lens with a spacing $g = 0.1\ D$ can be calculated. Parameters of lens L_D are indicated in Figure B-1 of Appendix B, along with the appropriate lens equations. The elements of the matrix B (see Eq. B-1) for a decelerating double-cylinder lens with a deceleration ratio 10:1 can be obtained from Table II in Ref. 8, and are $b_{11} = 2.0200$, $b_{21}D = -1.2511$, $b_{12}/D = 0.14412$, and $b_{22} = 1.4762$. Substituting these values into Eq. B-2, we find

$$f_o = 2.5270\,D \qquad f_i = 0.7992\,D$$
$$F_o = 1.1799\,D \qquad F_i = 1.6140\,D\ . \tag{8}$$

The Newtonian lens equation retains its usual form,

$$pq = f_o f_i\ , \tag{9}$$

and the magnification M is given by the usual formula,

$$M_D = f_o/p = q/f_i\ . \tag{10}$$

For our design we choose M = 1.5 and so

$$p = f_o/M_D = 2.5270\,D/1.5 = 1.685\,D\ , \tag{11}$$

and

$$q = f_i/M_D = 0.7992\,D \times 1.5 = 0.533\,D\ .$$

The total length is then

$$\ell = p + F_o + f_i + q = 5.677\,D\ . \tag{12}$$

Filling Factor

We can calculate the beam size, d_D, at the reference plane of L_D by projecting the size of the virtual aperture, W_f, back to the center of the lens; thus

$$d_D \simeq W_f + 2\,(q + F_i)\,\alpha = 0.02\ \text{in} + 0.305\,D\ .$$

The filling factor is then given by

$$d_D/D = 0.305 + 0.02\ \text{in}/D\ . \tag{13}$$

Pupil

The diameter of pupil d_p required at second focal point of the lens L_D is

$$d_p = 2p \times 0.0336 \text{ rad} = 0.017\text{-in diameter} . \quad (14)$$

The location of the pupil should be at $F_o = 1.1799\,D$ to make the beam angle at the entrance of the hemispherical deflector zero. The values of C_{SD} for decelerating lenses (see Appendix C) can be deduced from the values of C_{SA} that Read et al.[9] calculated for accelerating lenses. The relation is

$$C_{SD} = M_A^4 C_{SA} (f_i/f_o)^3 . \quad (15)$$

Angular Characteristic of a Beam

The beam half-angle for the output lens L_{AC} is given

$$\theta_{ABC} = (W_{AC}/2)(P - F_i)^{-1} , \quad (16)$$

where $P - F_i$ is the distance between the focal point and the image of L_{AC} (see Appendix A for definitions). For a lens with a diameter D = 0.15 in, the calculated parameters are shown in Table 2. The construction of output lens L_D.

TABLE 2. Parameters of Lenses L_D and L_C

Parameters	Calculated values[a]	Parameters	Calculated values[a]
g	0.015	ℓ	0.852
f_o	0.379	d_D/D	0.44
F_o	0.177	d_p	0.017
f_i	0.120	θ_{ACp}	0.034
F_i	0.242	θ_{ACb}	0.026
p	0.253	Δr_D	0.004[b]
q	0.180	Δr_{AC}	0.001

[a]All linear and angular dimensions given in inches and radians, respectively.

[b]The spherical-aberration constant $C_{SD} = 4$ must be used for the lens L_D with a magnification $M_A = 1/M_D$.

Design of Gun with Diode

The electron source is a diode gun of the Pierce type. Its design accommodates either a hairpin throiated-iridium filament or an indirectly heated dispenser cathode. Both the diameter W_A of the anode and its distance from the cathode are chosen to deliver the maximum space-charge limited current (I_i in Table 1) to the entrance virtual slit W_f of the spherical electrostatic deflectors.

Space-Charge-Limited Current

In order to form a beam of known current density, energy, and geometrical parameters, we start with the space-charge-limited diode as our initial electron source, as in the schematic diagram (Figure 3). The space-charge-limited current density J_A is easily calculated from the voltage and the spacing of the diode:[1]

$$J_A \equiv I_A/S_A = 2.33\ V_A^{\frac{3}{2}}/d^2\ , \qquad (17)$$

where S_A is the area of the anode aperture.

Location of Focal Point

Let V_A be the accelerating voltage between the cathode and anode, and ϵ (z) be the electric field at distance z from the anode. The expression Spangenberg[7] obtained (his Eq. 15.66 on p. 458) from the aperture lens formula assumes that beyond the anode aperture the gradient of the potential is zero. A similar expression for a space-charge-limited diode, is given[1] by

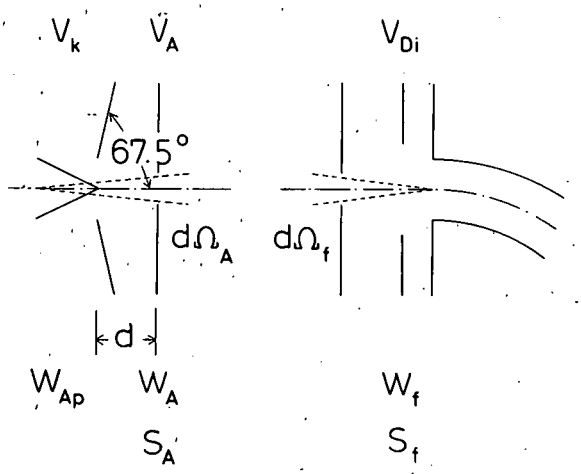

FIG. 3.--Schematic diagram of the electron-optical and geometrical parameters relating the beam produced at the electron gun with beam focused at the hemispherical deflector.

$$\epsilon(z) = (4V_A/3d^{4/3})\, z^{1/3} \quad . \tag{18}$$

The focal length of the anode is then

$$f_{AD} = 4V_A\,(\epsilon(0) - \epsilon(d))^{-1} = -3d \quad . \tag{19}$$

Angular Characteristics in a Beam

The beam half-angle is

$$\theta_{Ab} = r_A/3d \quad , \qquad r_A = W_A/2 \quad , \tag{20}$$

which depends on the radius r_A of the anode orifice. The path of an electron emitted parallel to the cathode surface has a slope[1] of

$$\gamma \equiv 2\,\theta_{Ap} = (E_k/E_A)^{\frac{1}{2}} = (V_k/V_A)^{\frac{1}{2}} \tag{21}$$

when it reaches the anode orifice. In this expression $E_k = eV_k = kT = 0.1$ eV. Take the anode orifice to be the window for the system. This window, before the anode lens, is formed by pencils with half-angle θ_{Ap} and within the central ray parallel to the axis. Hence, the pupil is at a distance -3d from the anode lens. The size of the pupil can be shown to be

$$W_{Ap} = 3d\gamma \quad . \tag{22}$$

Voltage of Anode

Assume that the final beam at the hemisphere entrance is space-charge limited at voltage V_{Di} with convergence half-angle α and non-space-charge radius $W_f/2 = r_f$. In practice, r_f can be made close to the minimum radius of the space-charge beam. Richtstrahlwert (brightness) is defined[1] by

$$R = I(S \cdot d\Omega)^{-1} \quad , \tag{23}$$

where I is the current through a differential area S and $d\Omega$ is the solid angle subtended by the electrons. Conservation of current, together with the law of Helmholtz and Lagrange,[1] namely $V_A\, d\Omega_A\, S_A = V_{Di}\, d\Omega_f\, S_f$, leads to

$$dI/V_A\, d\Omega_A\, S_A = dI/V_{Di}\, d\Omega_f S_f \quad . \tag{24}$$

Hence, we see that the ratio of Richtstrahlwert to electron energy is a conserved quantity. Thus,

$$R_A/V_A = 0.74\, V_A^{\frac{3}{2}} V_k^{-1} d^{-2}, \qquad R_f/V_{Df} = 3.9\, V_D^{\frac{1}{2}} (W_f/2)^{-2} \tag{25}$$

where $R_A = J_A/d\Omega_A$, $R_f = I_i/S_f d\Omega_f$, and $I_i = 38.5\, V_{D2}^{\frac{3}{2}} \alpha^2$. Then V_A is given by

$$V_A = [21.1\, V_{Di}^{\frac{1}{2}} V_k (d/W_k)^2]^{2/3} . \tag{26}$$

Total Current

The total current[1] from the diode is

$$I_A = J_A \pi (W_A/2)^2 = 7.32\, V_A^{3/2} (W_A/2)^2/d^2 . \tag{27}$$

Anode Diameter

To keep the alignment from being critical, make the anode orifice about twice as large as necessary, say 0.026 inches in diameter. In this way, edge effects of the anode orifice will also be avoided. The selected values of the parameters of the gun and of its constituent are shown in Table 3.

Design of Condenser Lens

To get a well-collimated beam at the entrance to the hemispherical deflector, we designed a fixed decelerator (as discussed earlier) with all apertures placed on the high-voltage side of this lens. Since the diode voltage and the input voltage to the decelerator are fixed by these considerations, we need an intermediate energy-matching lens. This lens should be capable of operation over the range of V_A shown in Table 3 and of V_{Di} ($\equiv E_0/e$) shown in Table 1, so that current can be varied with diode voltage, and final energy can be adjustable. Owing to its flexibility, we have chosen the three-element aperture lens as our condenser lens. The electron-optical properties of such lenses have been calculated in Refs. 10 and 11, and some specific quantities are identified in Appendix B. With such a lens we want to image the anode orifice of the diode onto the 0.013-in diameter entrance aperture of the decelerator with constant magnification. It is possible to use these asymmetric

TABLE 3. Parameters of the Gun

Parameters	Calculated values		
V_k, V	0.1		
d, in	0.215		
W_A (= $2r_A$) (diameter in inches)	0.026		
θ_{AB}, rad	0		
θ_{Ap}, rad	0.021	0.019	0.018
W_{Ap} (diameter in inches)	0.029	0.025	0.024
V_{Di}, V	2.5	5	7
V_A, V	52.9	66.7	74.6
I_A, μA	10	15	17

lenses in such a way that with an object at a fixed position and energy, the energy and magnification of its image may be varied at a fixed image position. Such a lens is frequently referred to as a three-element zoom lens. Figure B-2 in Appendix B defines the parameters of the three-element aperture lens.

Three-Element Aperture Lens

In order to operate the condenser lens as a zoom lens, we need to know the relations between V_{C2}/V_{C1} and V_{C3}/V_{C1} for fixed values of the mid-object distance P and mid-image distance Q. Read et al.[10] have calculated this relation for six different pairs of values of A/D. P and Q are measured to the left and right, respectively, of the central aperture in units of the aperture diameter D. Because of the limited space available, we chose A/D = 1, P = Q = 5D, and D = 0.1-in diameter, respectively. The voltage ratio V_{C2}/V_{C1} for such a lens can be read from the graph of Figure 4.

Magnification

As the energy of the image is varied, its size and pencil angle also vary. The three quantities are connected by the Helmholtz-Lagrange relation

$$M_{C\,max} V_{C3} \theta_{pi} = V_{C1} \gamma \quad , \tag{28}$$

where $M_{C\,max}$ is the maximum magnification, and γ and θ_{pi} are the pencil angles at the entrances to the anode and decelerator lens, respectively. The

minimum magnification is given by

$$M_{C\,min} = W_D W_A \,. \tag{29}$$

The variation of the magnification of our zoom lens, as calculated in Refs. 10 and 11, is shown in Figure 5. The upper branch (AFED in Figure 5) of the curve is for $V_{C2} < V_{C1}$ and the lower branch (ABCD in Figure 5) for $V_{C2} > V_{C1}$. Clearly for the case $V_{C2} > V_{C1}$ the magnification is nearly unity over the entire anticipated range of V_{C3}/V_{C1}.

Other Parameters

The filling factor, d_c/D, the beam half-angle, θ_{Cb} at W_D, and the spherical aberration Δr_C, calculated in the same way as previously, are as shown in Table 4.

Design of Energy-Change Lens

The monochromator focuses the image at W_f onto its exit plane at W_{fe} with unit magnification. The electrons at W_{fe} are accelerated by L_A (symmetrical to L_D) and focused at W_{AC}. In traversing lenses, L_{EC1} and L_{EC2}, the electrons from W_{AC} are further accelerated to the desired final kinetic energy of 10 eV to 1000 eV, and are focused onto the beam of atoms and molecules.

Lens L_{EC1} can be used in two ways" (a) in the case of low incident energy, it works as a three-element einzel lens, and (b) in the case of high incident energy it works as a double-cylinder accelerator lens (see Appendix B).

Lens L_{EC2} must ensure that the final image size and position at the target beam are independent of the final electron energy. For this we again choose a three-element aperture zoom lens (see Design of Condenser Lens and Appendix B).

Lens L_{EC1}

The L_{EC1} lens is composed of our lens elements which can be combined to form either a double-cylinder accelerator lens or a three-element einzel lens. In either case, the object at W_{AC} is focused onto the virtual slit at the right edge of L_{EC1}.

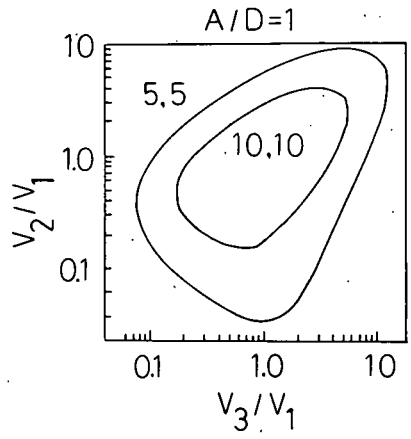

FIG. 4.--Plot of the voltage ratios V_2/V_1 and V_3/V_1 for a three-element aperture lens such that it operates as a zoom lens, with fixed pairs of object and image positions, P/D, Q/D, respectively (taken from Ref. 9). [Note: This diagram applies to both the condenser lens V_C and the second energy-change lens V_{EC2}, and so the preceding subscripts are suppressed here.]

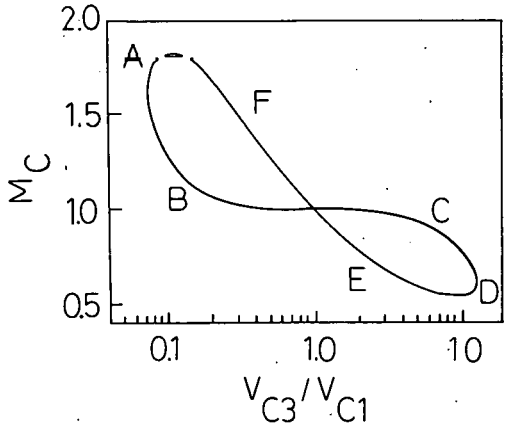

FIG. 5.--The magnification M of a three-element aperture lens for fixed values of P/D = Q/D = 5 with voltage ratio V_{C3}/V_{C1} (taken from Ref. 9).

TABLE 4. Parameters of Lens L_C

Parameters	Calculated values		
V_{C1} (= V_A), V	52.9	66.7	74.6
V_{C3} (= V_{D1}), V	25	50	70
V_{C3}/V_{C1}	0.47	0.75	0.94
V_{C2}/V_{C1}	3.5	4.6	5.3
V_{C2}, V	185	230	371
$M_{C\,max}$	1.9	1.3	1.1
$M_{C\,min}$		0.5	
d_C/D [a]	0.68	0.65	0.64
θ_{Cb}, rad [b]		0.026	
Δr_C, in [c]	0.007	0.006	0.006

[a] For $d_C = W_A + 2P_i(\theta_{Ab} + \theta_{Ap})$.

[b] For $\theta_{Cb} = (W_D/2)/Q - F_2$, $F_2 = 0.25$.

[c] For $C_{SD} = 10^2$ for $M_A = 1$ from Refs. 10 and 11, $\alpha_D = \theta_{Ab} + \theta_{Ap}$.

Einzel Lens

When the inner two cylinders of the four-element lens, L_{EC1}, are tied to the same potential, V_{EC12}, and the outer two to the same potential, $V_{EC11} = V_{EC13}$, L_{EC1} works as an einzel lens. The lens parameters are identified in Figure 6a. In our case, the values of D, P, Q, S, and g/D are constrained to fit the geometric parameters of our system; the values actually selected are D = 0.15 in diameter, P = Q = 3.1 D, S = 2.0 D, and g/D = 0.1. In the equations for the general pair of lenses (Appendix B, Eqs. B-3 and B-4), we make the replacements $f_1' \rightarrow f_2$, $f_2' \rightarrow f_1$, $F_1' \rightarrow F_2$, and $F_2' \rightarrow F_1$. The result is

$$f_1^* = f_2^* = f_1 f_2/(2F_2 - S), \quad F_1^* = F_2^* = F_1 - F_1^* + S/2 , \tag{30}$$

$$p = f_2^*/M, \quad q = f_1^* M , \tag{31}$$

$$P = p + F_1^*, \quad Q = q + F_2^* . \tag{32}$$

From the values calculated in Ref. 9 for double-cylinder lenses having

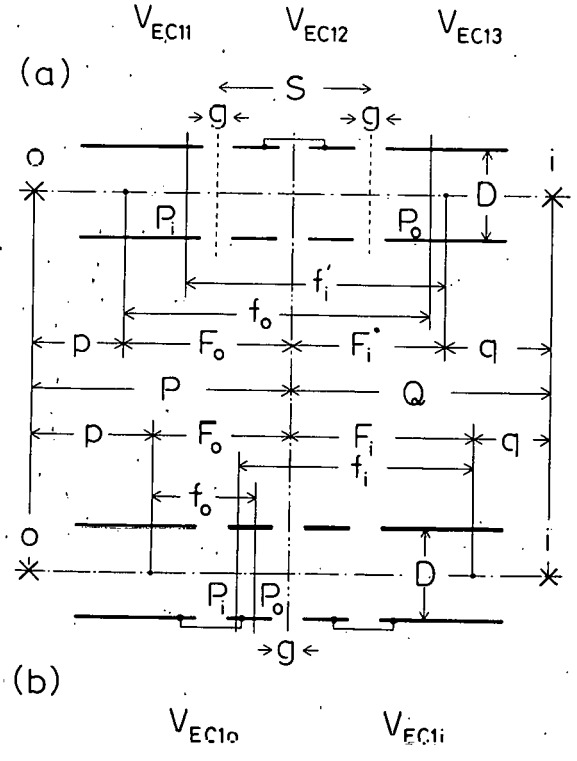

FIG. 6.--Diagram depicting the electron-optical parameters of lens L_{EC1} used as (a) an einzel lens, or (b) a double-cylinder accelerating lens.

g/D = 0.1, it follows that $V_{EC12}/V_{EC11} = 7$, $f_1 = 1.2$ D, $F_1 = 2.0$ D, $f_2 = 3.1$ D, and $F_2 = 1.7$ D. Thus, we have $f_1^* = f_2^* = 2.7$ D, $F_1^* = F_2^* = 0.3$ D, and P = Q = 3.0 D, since M = 1. The specific value of V_{EC12}/V_{EC11} giving the best focus can be found empirically. Flexibility in this mode of operation is an advantage. The results are shown in Table 5.

Double-Cylinder Lens

To get a high incident energy, the output electrons from the monochromator need to be accelerated in two stages because the energy ratio of the lens should be less than 10 (because of lens characteristics). When the first and second lenses are tied to one potential and the third and fourth ones to a second potential, lens L_{EC1} works as double-cylinder lens for preaccelerating. The lens parameters are defined in Figure 6b. As in the preceding case in which L_{EC1} was operated as an einzel lens, the values of D, P, Q, and g/D are also chosen to fit the geometric constraints of the system; the value of each of these parameters can be determined from the graph given in Refs. 10 and 11. From the values so determined, we find that $V_{EC1i}/V_{EC1o} = 9$ and $M_{EC1D} = 0.75$. The parameters are shown in Table 6.

Lens L_{EC2}

The virtual object at W_{EC1V} is focused onto the gas jet at the collision center by the final accelerator lens L_{EC2} with required incident energies. The

TABLE 5. Parameters of the Einzel Lens L_{EC1E}[a]

Parameters	Calculated values		
M_{EC1E}		1	
W_{EC1V} (diameter in inches		0.013	
θ_{EC1p}, rad		0.034	
θ_{EC1b}, rad		0.015	
V_{EC12}/V_{EC11}		7	
V_{EC12}, V	175	350	490
d_{EC1E}/D		0.34	
Δr_{EC1E}, in		0.0003	

[a] $V_{EC11} = V_{Do}$; $d_{EC1E} = W_{AC} + 2P(\theta_{ACp} + \theta_{ACb})$; $C_{SD} = 1.5$ (from Refs. 10 and 11); $\alpha_D = \theta_{ACp} + \theta_{ACb}$.

zoom-lens design of the asymmetric three-aperture electrostatic lenses is the same as that already described and also as in Appendix B. For D = 0.1-in diameter, P = Q = 10 D and spacing = 0.1 D. We use Figure 4, taken from Refs. 10 and 11, to choose the voltage ratios V_{EC22}/V_{EC21} appropriate to the required values of V_{EC23}/V_{EC21}. The selected values of the parameters are listed in Table 7.

TABLE 6. Parameters of the Double-Cylinder Lens L_{EC1D}[a]

Parameters	Calculated values		
M_{EC1D}	0.75		
W_{EC1V} (diameter in inches)	0.010		
θ_{EC1p}, rad	0.015		
θ_{EC1b}, rad	0.018		
V_{EC12}/V_{EC10}	9		
V_{EC1i}, V	225	450	630
d_{EC1D}/D	0.34		
Δr_{EC1D}, in	0.0006		

[a] $V_{EC10} = V_{Do}$; $\theta'_{EC1b} = (W_{EC1V}/2)/(Q - F_2)$, $F_2 = 1.3$ D; $C_S = 4$; $\alpha_D = \theta_{ACp} + \theta_{ACb}$.

TABLE 7. Parameters of Lens L_{EC2}[a]

Parameters	Calculated values	
M_{EC2}	1	
W_{EC2V} (diameter in inches)	0.010 ~ 0.013	
θ_{EC2p}, rad	(a) 0.067 ~ 0.024	(b) 0.030 ~ 0.011
θ_{EC2b}, rad	(a) 0.013	(b) 0.010
V_{EC23}/V_{EC21}	0.25 ~ 2	
V_{EC22}/V_{EC21}	1 ~ 4	
V_{EC23}, V	(a) 6.25 ~ 140	(b) 56.25 ~ 1260
V_{EC22}, V	(a) 25 ~ 280	(b) 225 ~ 2520
d_{EC2}/D	(a) 1	(b) 0.76
Δr_{EC2}, in	0.042 ~ 0.005	

[a] $V_{EC21} = V_{EC13}$; $d_{EC2}(a) = W_{EC1V} + 2P(\theta_{EC1p} + \theta_{EC1b})$ and $d_{EC2}(b) = W_{EC1V} + 2P(\theta_{EC1p} + \theta_{EC1b})$; $C_{SD} = 3.6 \times 10^2 \sim 1.4 \times 10^2$ for $M_A = 1$ from Ref. 10.

We wish to thank our colleagues, particular Dr. D. Spence and Dr. J. L. Dehmer, for many helpful discussions during this work.

References

1. C. E. Kuyatt, National Bureau of Standards, Washington, D.C. 20234, unpublished lecture notes (1967).
2. J. A. Simpson and C. E. Kuyatt, Rev. Sci. Instrum. 38, 103 (1967).
3. F. H. Read, J. Comer, R. E. Imhof, J. N. H. Brunt, and E. Harting, J. Electron. Spectrosc. Related Phenom. 4, 293 (1974).
4. D. Roy, A. Delage, and J.-D. Carette, J. Phys. E. 8, 109 (1975).
5. R. Herzog, Z. Physik 47, 596 (1935).
6. H. Wallnik and H. Ewald, Nucl. Instrum. Methods 36, 9 (1965).
7. K. R. Spangenberg, Vacuum Tubes, McGraw-Hill, New York (1948).
8. D. DiChio, S. Natali, C. E. Kuyatt, and A. Galejs, Rev. Sci. Instrum. 45, 566 (1974).
9. F. H. Read, A. Adams, and J. R. Soto-Montiel, J. Phys. E 4, 625 (1970).
10. F. H. Read, J. Phys. E 3, 127 (1970).
11. E. Harting and F. H. Read, Electrostatic Lenses, Elsevier Scientific Publishing Co., Amsterdam (1976).

APPENDIX A. Definition of Some Electron-Beam Characteristics

At least two defining apertures are needed to collimate an electron beam. These define the beam and pencil half-angles θ_b and θ_p, respectively. It is the pencil half-angle θ_p that appears in the Helmholtz-Lagrange relation linking the angular characteristics of the electron beam at different points in a focusing system. One aperture called a "window" serves to define the radial extent of an object or image. A second aperture called a "pupil" defines θ_p of the rays coming from each point in the object. In the absence of real apertures, one still can posit the existence of "virtual windows" and "pupils" at any object or image position that is determined by a pair of real apertures and the electron-optical focal properties of the system. These are shown diagramatically in Figure A-1. The pupil is located at the cross-over point for rays extending from points at the window, and the combination of the two also defines the beam half-angle, θ_b, as shown in Figure A-1. At the cross-over, θ_p and θ_b become the beam and pencil angles of the image formed there.

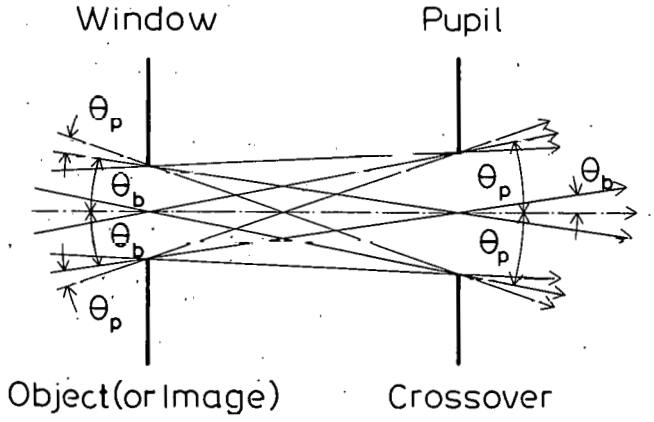

FIG. A-1.--Angular parameters for a beam passing through limiting apertures.

APPENDIX B. Lens Equations for Two- and Three-Element Cylindrical Lenses

Parameters of a two-element cylinder lens are shown in Figure B1 with the reference plane of the lens indicated by a vertical dashed line. According to Kuyatt, a matrix B can be defined

$$B = \begin{pmatrix} b_{11} & b_{12} \\ b_{21} & b_{22} \end{pmatrix} = \begin{bmatrix} F_i/f_i & (F_0F_i - f_0f_i)/f_i \\ -1/f_i & -F_0/f_i \end{bmatrix} \qquad \text{(B-1)}$$

for a decelerating lens of this type. This matrix transforms the position and angular coordinates for any ray entering from the left to the corresponding coordinates of the exiting ray on the right. It can also be used to relate any object distance P to its corresponding image distance, Q. The focal points f_0 and f_i, and the mid-plane focal points, F_0 and F_i, are related to the elements of B by

$$f_0 = b_{12}^{-1} - b_{21}/(b_{11}b_{22}), \qquad F_0 = -b_{21}/b_{22}$$

$$f_0 = b_{21} \qquad F_i = b_{21}/b_{11}. \qquad \text{(B-2)}$$

The properties of a three-element cylinder lens as shown in Figure B-2 can also be calculated. Equations for a pair of cylinder lenses separated by a distance S are given as

$$f_2^* = f_2 f_2'/(F_1' + F_2 - S) \qquad f_1^* = f_1 f_1'/(F_1' + F_2 - S) \qquad \text{(B-3)}$$

$$F_1^* = f_1 f_2/(F_1' + F_2 - S) + S/2, \quad F_2^* = F_2' - f_1'f_2'/(F_1'F_2 - S) + S/2, \qquad \text{(B-4)}$$

where all quantities are defined as in Figure B-2.

The diagram of the equivalent three-element aperture lens is shown in Figure B-3. The focal properties of such lenses have been discussed extensively by Harting and Read.[10,11]

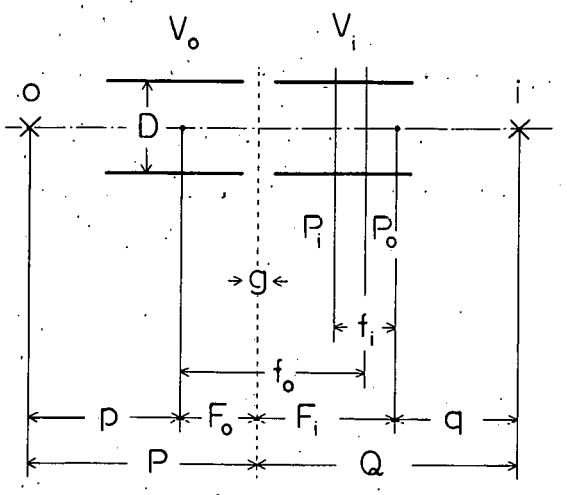

FIG. B-1.--Electron optical parameters of a two-element cylinder lens.

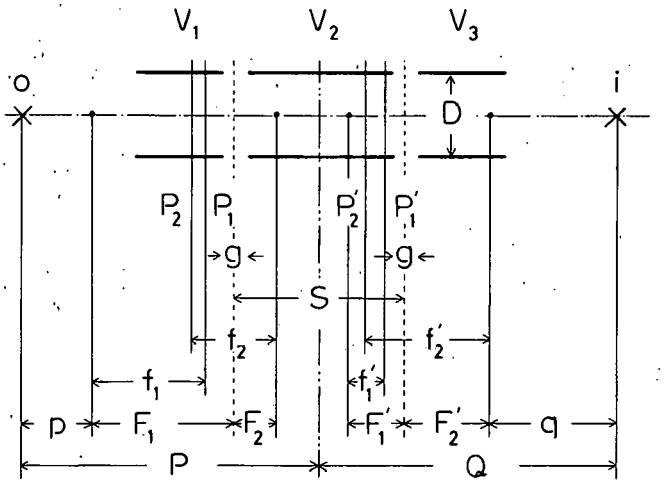

FIG. B-2.--Electron optical parameters of a three-element cylinder lens.

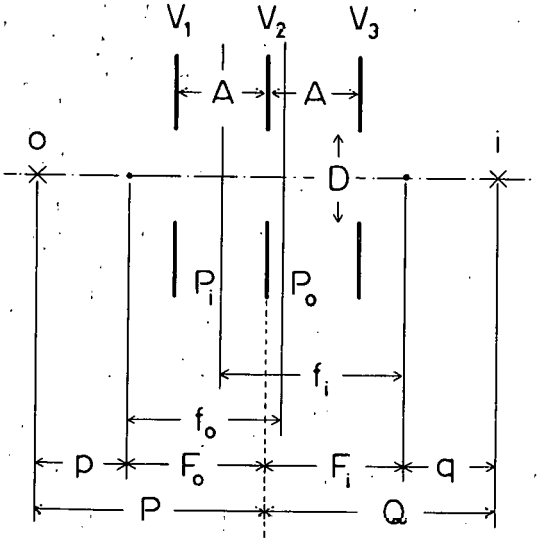

FIG. B-3.--Electron optical parameters of a three-element aperture lens.

APPENDIX C. Spherical Aberration

If a point object emits rays which have a maximum inclination α_C to the lens axis, and if the corresponding spread of image due to the spherical aberration has a radius Δr_C in Figure C-1, the spherical-aberration coefficient C_{SC} is defined by[9]

$$\Delta r_C = M_A C_{SC} \alpha_C^3 , \qquad (C\text{-}1)$$

where M_A is the magnification for the accelerating lens.

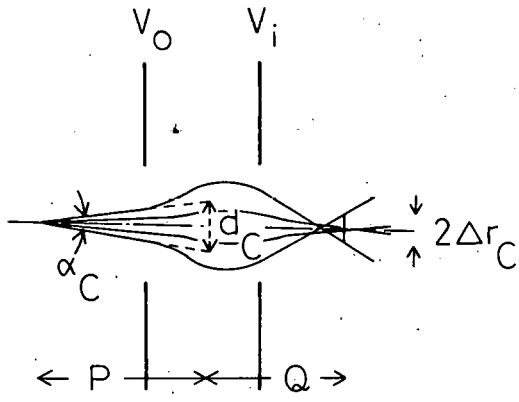

FIG. C-1.--Diagram depicting the spherical aberration parameters of an electrostatic lens.

APPARENT OSCILLATOR-STRENGTH DENSITIES FROM ELECTRON ENERGY-LOSS MEASUREMENTS*

R. H. Huebner

Electron energy-loss intensities depend on both physical and instrumental parameters of the measurement. Although the energies of the spectral features are readily compared among data of different workers or with optical data, direct comparison of intensities is usually meaningless. Even if the physical parameters are the same, spectrometers of different designs do not necessarily produce identical energy-loss spectra. The spectral differences arise mainly from different instrumental characteristics, such as energy resolution and angular acceptance.

However, it is possible to relate the measured energy-loss intensities to the oscillator strength of a transition, provided the momentum transfer ($\hbar K$) is kept sufficiently small. Two complementary methods have been developed for the determination of oscillator strengths from electron energy-loss measurements: The extrapolation method and the small-angle method. It is important to note that both methods necessarily involve extrapolation to $(Ka_0)^2 = 0$. This is so because in order to conserve both energy and momentum in any actual collision, a nonvanishing minimum amount of momentum must be transferred. However, in any real scattering experiment, the acceptance angle of the analyzer is nonvanishing, thus permitting inelastic scattering corresponing to a range of momentum transfer values that changes with the amount of energy lost. Correction for this factor is of particular importance in the derivation of oscillator-strength densities by the small-angle method.

---

*Summary of a symposium lecture presented at the 1976 Canadian Association of Physicists-American Physical Society-Sociedad Mexicana de Fisica Joint Congress, 14–17 June 1976, Quebec, Canada. Also, two lectures concerning this topic were delivered at the NATO Advanced Study Institute on High Energy Chemical Spectroscopy and Photochemistry, Nijenrode Castle, Breukelen, The Netherlands, 9–20 August 1976.

A variety of atomic and molecular gases has been analyzed recently by the small-angle method. Comparisons with optically determined oscillator strengths show good agreement (± 15%) with optical values generally considered reliable. However, discrepancies as large as factors of two to four have been found in some comparisons, clearly indicating certain optical values to be in error. Also, for sharp, discrete bands the integrated f values obtained by electron impact are free from line-saturation errors that beset optical measurements when the instrumental resolution exceeds the natural absorption line width of the transition. Such values are needed for comparison with ab initio theoretical calculations that are now beginning to achieve spectroscopically significant accuracies for transitions to Rydberg as well as valence states.

For many complex molecules reliable oscillator-strength densities are still not available over significant spectral regions. Many such molecules are becoming of increasing environmental concern, particularly where energy absorption or energy transfer plays a role in their decomposition and photochemical reactivity. Electron energy-loss measurements provide an increasingly important way of studying the energy-absorbing properties of those molecules.

ELECTRON-IMPACT SPECTROSCOPY: AN OVERVIEW OF THE LOW-ENERGY ASPECTS

R. J. Celotta[†] and R. H. Huebner

Electron-scattering experiments have become a major tool in elucidating the energy-absorbing properties of atoms and molecules. In this chapter we confine our attention to low-energy aspects, i.e., for incident energies below one kilovolt. This review emphasizes the results of electron scattering experiments rather than techniques. Our focus is further restricted to collisions of electrons with electrically neutral targets in their ground state. Recent developments are highlighted within a unifying framework dictated by the controlable physical parameters of the electron-scattering process.

The chapter is organized into four major sections: (1) a guide to theoretical aspects, (2) single-parameter experiments, (3) multi-parameter experiments, and (4) practical applications and future research directions. Special attention is focused on the analysis of electron energy-loss measurements to yield transition oscillator strengths.

A preliminary draft of the chapter has been completed and is being reviewed and edited. Publications is expected within the coming year.

---

*Abstract of a chapter to be published in Electron Spectroscopy, Vol. II., C. R. Brundle and A. D. Baker, Eds., Academic Press, New York.

[†]National Bureau of Standards, Washington, D.C. 20234.

ABSORPTION CROSS SECTIONS AT HIGH ENERGIES. SCATTERED LIGHT CORRECTIONS AND RESULTS FOR ETHANE FROM 22 TO 58 eV

J. C. Person and P. P. Nicole

A new lamp has been utilized to make measurements of the absorption cross section for ethane in the energy range from 22 to 58 eV, and a new procedure is applied to correct the data for the effects of scattered light.

Introduction

The oscillator-strength distribution is a valuable input to theoretical radiation physics, and the differential oscillator strength is directly proportional to the absorption cross section σ. Furthermore, reliable σ values are valuable in many fields, such as photochemistry and the chemistry of planetary atmospheres. We have previously reported[1,2] accurate σ values that were measured using lamps emitting either the hydrogen many-line spectrum or the helium Hopfield continuum. At photon energies E above 21.2 eV, we have reported only a few values[2b] measured using resonance radiation in helium or neon. The present report describes a major increase in the energy range of our apparatus as the result of our new lamp, which provides a multitude of closely-spaced lines giving good light intensities up to 44 eV — with useful light up to 57.6 eV. In the high-energy region there is an increase in the relative importance of the contribution from light that is scattered into the absorption cell. Therefore, we have developed an improved correction for the effects of scattered light, and we have applied the correction to data for ethane.

Apparatus

The monochromator, together with the double ion chamber[3] that is used to determine σ by measuring the ratio of the ion currents in two chambers, have been described previously.[1,2] The new lamp,[4] a VUV Associates model LS101, was used with a low pressure (< 1 torr) of argon. A 0.25 μF capacitor was charged to 3.4 to 4.7 kV and discharged through the lamp at 60 Hz by a rotating spark gap.

Correction for Scattered Light

One of the experimental difficulties encountered when using a monochromator is the presence of light scattered through the exit slit. This light does not have the same energy as the true light that has been diffracted at the grating, and the scattered light can produce errors in σ — the scattered light may have a different value of σ and some of the scattered light may be off the optical axis and enter the front chamber preferentially. (The off-axis light makes the apparent σ too large.) The contribution of the off-axis light has been reduced somewhat by the introduction of a collimator hole in front of the front chamber (an 0.53- × 0.25-cm hole located 0.64 cm behind the exit slit).

In the past,[1,2] we have corrected for scattered light by measuring the ion currents when the monochromator is set a few eV above the high-energy emission limit of the lamp, and then subtracting these currents from the values measured at lower energies. The error in assuming a constant contribution from scattered light was reduced by using only data where the estimated scattered-light current was less than 4% of the measured current. This procedure is increasingly difficult to apply as E increases and the grating efficiency decreases. Also, we can make better use of the data if we recognize that the rapid change in the true light intensity that occurs at an emission line produces a wide variation in the relative contribution of scattered light, for the scattered-light intensity will change more slowly than the true light intensity. Thus, we can test for errors in the scattered-light correction because an error in the correction will result in a systematic correlation between the calculated σ value and the light intensity.

The new scattered-light correction is determined by first correcting the measured ion currents, i_F and i_B (the subscripts F and B refer to the front and back ion chambers, respectively), by subtracting the ion currents, i_{HF} and I_{HB}, that result from scattered light as measured with the monochromator set at high energy ($\approx$ 69 eV). At lower energies, the ion currents from scattered light, i_{SF} and i_{SB}, are given by $i_{HF} + i_{CF}$ and $i_{HB} + i_{CB}$, where i_{CF} and i_{CB} are the corrections required by the variation of the scattered-light intensity with energy. If we express the Beer-Lambert law as

$$u = \exp(-\sigma n L_F) \quad , \tag{1}$$

where n is the number of molecules per unit volume and L_F is the length of the front chamber, and we assume the Beer-Lambert law holds in the absorption cell, then

$$(i_F - i_{HF} - i_{CF})/(i_B - i_{HB} - i_{CB}) = R = (1 - u)/(u - u^m) \quad , \tag{2}$$

where $m = (L_F + L_B)/L_F$ and L_B is the length of the rear chamber. We find that our fitting procedure works better if we combine the effects of i_{CF} and i_{CB} and fit

$$c = i_{CF} - i_{CB} R \quad . \tag{3}$$

We approximate u over a narrow energy range (i.e., a range of approximately a full line width) by

$$u = a_1 + a_2 E \quad , \tag{4}$$

and we use a nonlinear, least-squares fitting procedure[5] to evaluate c, a_1, and a_2. If the i_F values have not changed by more than a factor of three in the energy range, the c values are poorly determined, and we disregard them when we construct a moving average of c. The averaged c values are then used to compute σ from Eqs. 1 and 5, where

$$(i_F - i_{HF} - c)/(i_B - i_{HB}) = (1 - u)/(u - u^m) \quad . \tag{5}$$

Results for Ethane

We have tested the lamp and scattered-light correction using data for ethane. The ethane was Phillips Research Grade with a stated purity of 99.96 mol percent. We took data in four energy regions: Region 1, 22.3 to 28.2 eV; Region 2, 27.6 to 31.4 eV; Region 3, 28.3 to 36.9 eV; and Region 4, 34.3 to 57.6 eV. In Region 1 the entrance and exit slits were each 10μ wide (giving a resolution $\approx$ 0.006 eV fwhm), in Region 2 the exit slit width was increased to 50μ, and in Regions 3 and 4, the entrance slit width was also increased to 50μ (giving a resolution in Regions 2 to 4 of 0.03 to 0.12 eV). The ethane pressure and the lamp operating voltage were the same in Region 2 as they were in Region 4. Figure 1a shows the photon flux entering the absorption cell in

arbitrary units (one unit $\approx 3 \times 10^4$ photons/sec); the flux was estimated from the ion currents by assuming that ethane has an ionization yield of unity in this energy range. It is evident from the figure that the lamp produces a profusion of lines, and many of the lines are from argon ions (e.g., the Ar VI lines at 44 eV, the Ar VII lines at 42 eV, and the Ar V lines at 36.5 eV). We were pleased by the good intensities for energies below 50 eV. At higher energies the grating efficiency decreases rapidly, with 57.6 eV representing the highest usable energy.

c Values

We determined i_{HF} and i_{HB} for each of the four energy regions so that the averaged c values plotted in Figure 1b are not directly comparable among the four regions. Also, we analyzed the high energy (Region 4) data in two different ways, and the c values agree within 10% in the region of overlap. The arbitrary units for c are the same as for the photon flux in Figure 1a, so the c values are small enough that they are important only when the flux is low (e.g., $E \approx 46$ eV and $E > 50$ eV).

One form of scattered light is light of a nearby energy that comes into the cell by a reflection at the exit slit or at a baffle. Such light should have a structure, depending on the emission spectrum, and the structure in Region 1 may be evidence for this type of scattered light. The lower resolution used in the other regions may tend to remove any structure during the averaging procedure; the difference in the shape of c in Regions 2 and 3 may result from different averaging. The flat regions on the ends of the curves result from an artificial extension of the moving average to the ends of the region. This extension may need improvement for $E > 50$ eV, and further experience with the method is necessary.

Preliminary Absorption Cross Sections

The σ values calculated by using the u values from Eq. 5 have been smoothed somewhat, and a crude estimate has been made of the uncertainty (the estimate neglects uncertainties in the electrometer calibrations and in the

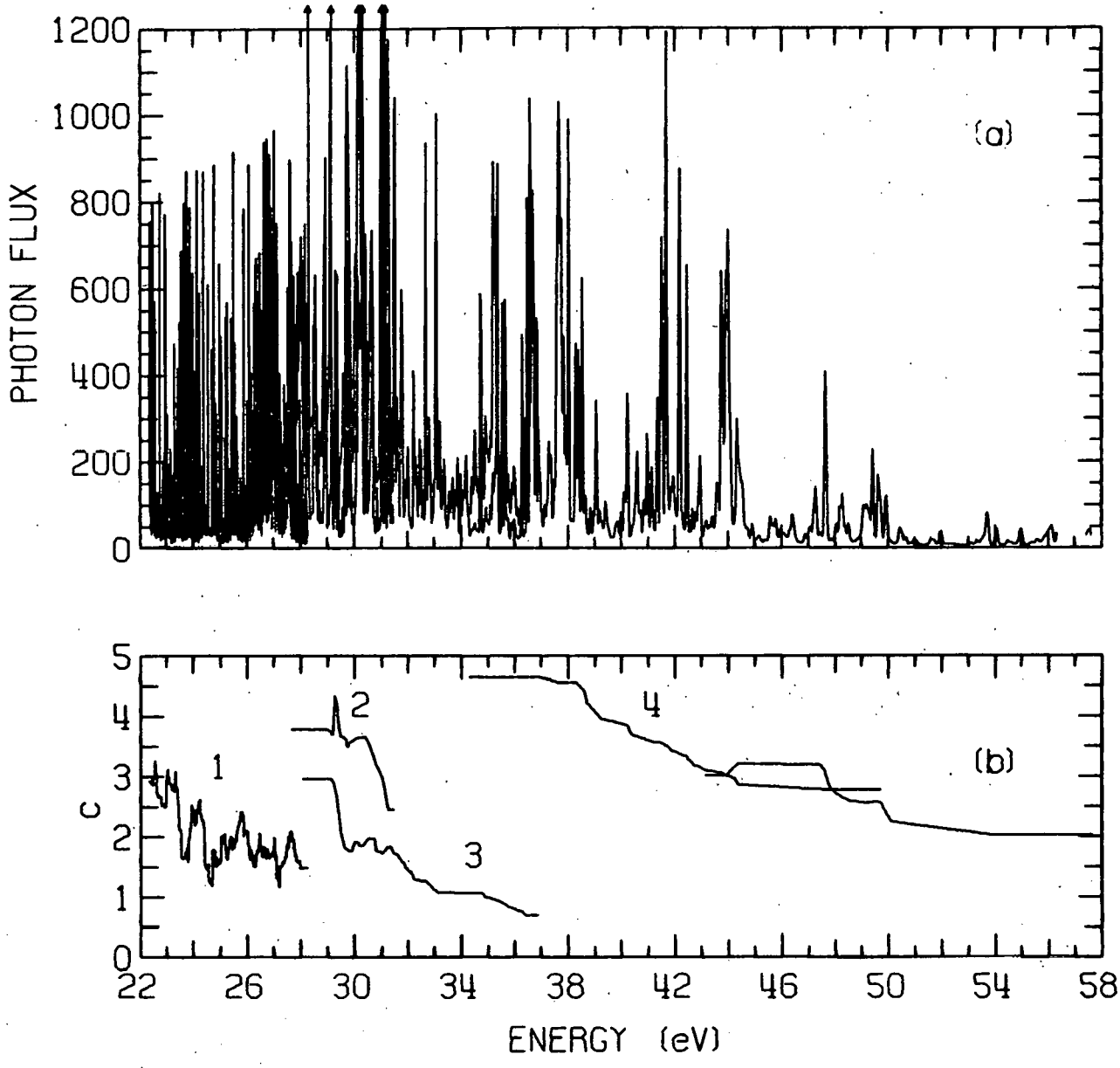

FIG. 1.--Photon flux (a) and scattered-light correction (b) vs. photon energy. One unit on the ordinate $\approx 3 \times 10^4$ photons/sec.

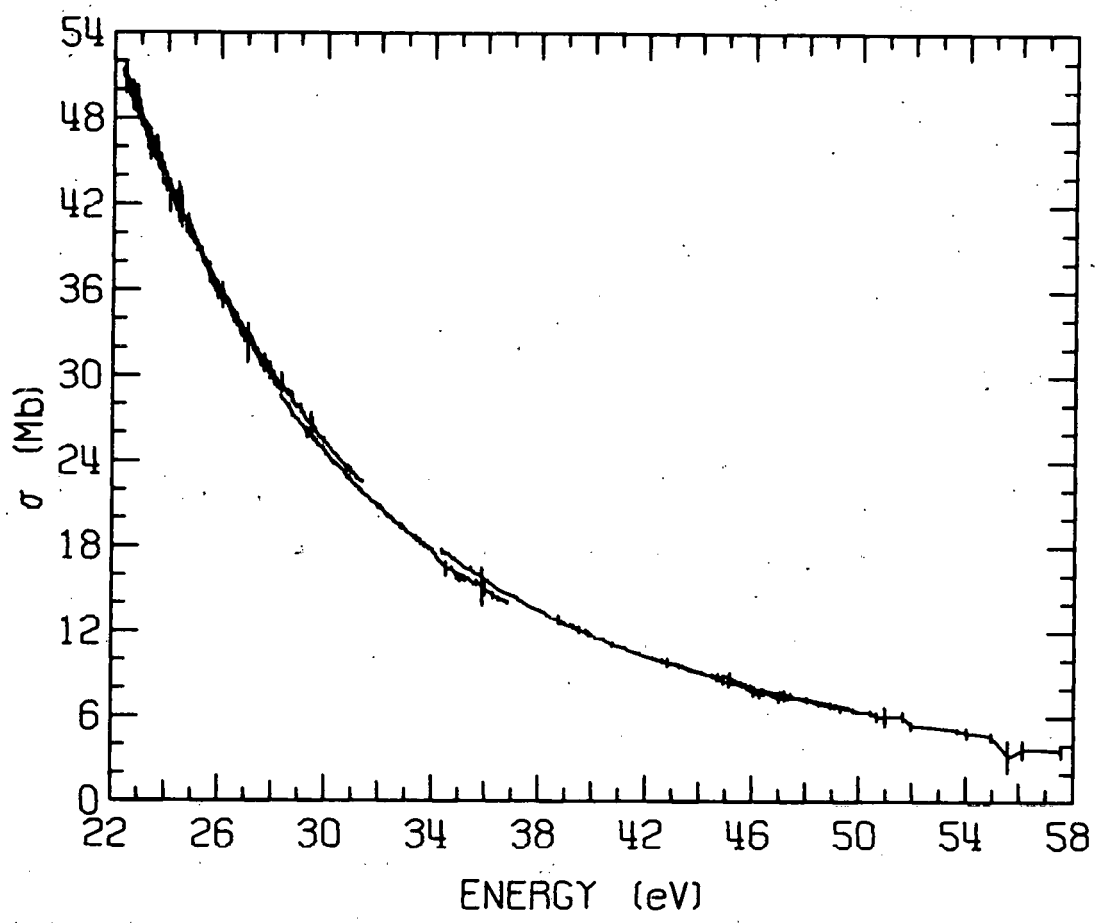

FIG. 2.--Absorption cross sections for ethane (1 MB = 10^{-18} cm^2).

pressure measurement, and it probably underestimates the uncertainty in the correction for scattered light). Figure 2 shows the σ values as line segments connecting the points shown with error bars (the error bars are nearly within the width of the line for much of the 30 to 40 eV region), and Figure 3 shows the data for Region 1 on an expanded scale in order to illustrate the density of points in this region. The units of σ are Mb; 1 Mb = 10^{-18} cm^2. The 4 to 5% offset for the data of Region 3 is a matter of some concern (the data of Regions 1 and 2 agree within 1% in the narrow region of overlap). We do not expect the scattered-light correction to be the cause of this offset because of the large photon flux in this energy range, but the offset may indicate an error in

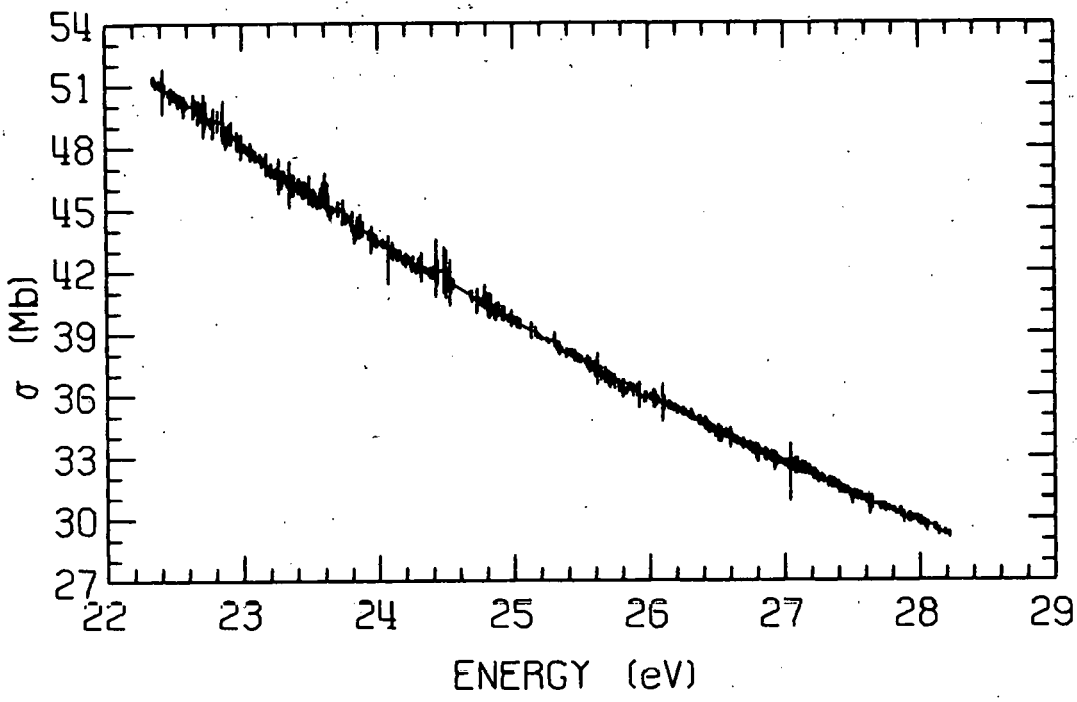

FIG. 3.--Absorption cross sections for ethane in Region 1.

the electrometer calibration. A calibration error would produce an error approximately twice as large in Region 3 as it would in the other regions, since the data in Region 3 were taken using a low optical density (u = 0.59 to 0.77). Thus, a calibration error of $\approx$ 3% could explain the offset.

The data in Region 1 shown in Figure 3 could have been influenced by second-order light, which would have a much lower σ value. However, the smoothness of the decline in σ shows the contribution of second-order light to be small (also, in Figure 3 the average only includes σ values determined at energies where the photon flux in Figure 1a is at least 50, so that the intensity of first-order light is always large).

Thus, Figures 2 and 3 show that the σ values for ethane decrease rather smoothly for $22 < E < 58$ eV, and the values should be accurate to $\approx$ 5% when the photon flux is large. At higher energies we expect uncertainties of 10 to 50%, and more work is needed on the error estimates. Thus, the data are preliminary, but the results are encouraging for our goal of providing accurate σ values over a wide energy range.

References

1. J. C. Person, D. E. Fowler, and P. P. Nicole, Radiological and Environmental Research Division Annual Report, July 1974–June 1975, ANL-75-60, Part I, p. 26.
2. J. C. Person and P. P. Nicole, Radiological and Environmental Research Division Annual Report, July 1973–June 1974, ANL-75-3, Part I, pp. 53 and 63.
3. J. A. R. Samson, Techniques of Vacuum Ultraviolet Spectroscopy, John Wiley, New York, p. 267 (1967).
4. Ibid., p. 164.
5. P. H. Froehle, Argonne National Laboratory Reactor Analysis and Safety Division, personal communication (1976).

COLLISIONAL IONIZATION OF HIGHLY EXCITED RYDBERG STATES OF POLYATOMIC MOLECULES*

J. C. Person, R. L. Watkins,† and Dana Lee Howard‡

The ionization produced by collisions of highly excited Rydberg states of the rare gas atoms has been studied by several workers, and very large ionization rates have been reported when the collisions are with polyatomic molecules.[1,2] Since highly excited Rydberg states have long radiative lifetimes, molecular Rydberg states will have long lifetimes when their nonradiative decay processes, such as predissociation, are slow. Thus, it has been possible to observe collisional ionization for Rydberg states of molecules (see Ref. 3 and references therein). However, little is known about the rate of constants for the collisional ionization or unimolecular decay of Rydberg states of polyatomic molecules. These rates are of practical interest, as Rydberg states may be useful intermediate states in isotope separation schemes.[4–6]

In the laboratory we have observed[7–10] collisional ionization in acetone-$\underline{h}_6$ and $\underline{d}_6$, acetaldehyde-$\underline{h}_4$ and $\underline{d}_4$, ethyl bromide-$\underline{h}_5$ and $\underline{d}_5$, methyl bromide-$\underline{h}_3$ and d_3, methyl acetate-$\underline{h}_6$ and $\underline{d}_6$, methanol-$\underline{h}_4$ and $\underline{d}_4$, propyne-$\underline{h}_4$ and $\underline{d}_4$, acetylene-$\underline{h}_2$ and $\underline{d}_2$, and ethylene-$\underline{d}_4$. Figure 1 illustrates the increase in the apparent ionization yield (the fraction of photon absorption events that lead to ionization events) as the pressure increases. From the high-pressure limit on such plots, we find $\eta_c y^*$ where η_c is the fraction of collisions that produces ionization and y^* is the quantum yield for producing the Rydberg states. We also evaluate $k_2 y^*/k_1$, where k_1 and k_2 are the specific rate constants for

---

*Summary of a paper published in J. Phys. B: Atom. Mol. Phys. 9, 1811 (1976).

†Undergraduate Research Participant, Fort Hays Kansas State College, Hays, Kansas 67602.

‡Undergraduate Research Participant, Wisconsin State University—Superior, Superior, Wisconsin 54881.

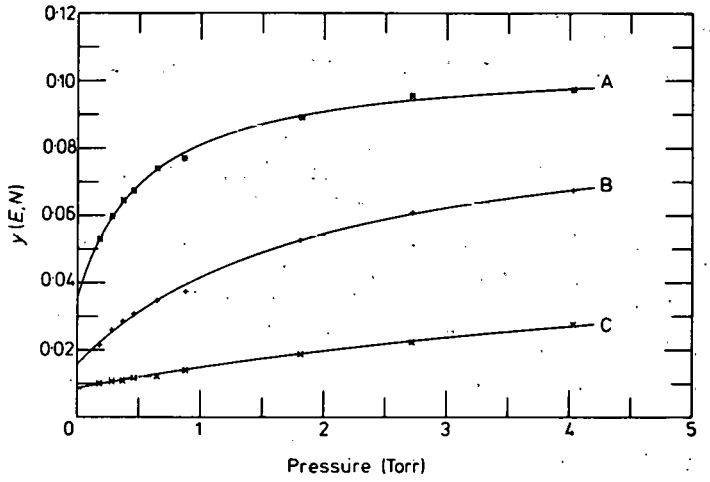

FIG. 1.--Apparent ionization yield plotted against pressure (pressure adjusted to 0 C) for acetone E = 9.69, 9.68, and 9.66 eV, curves A, B, and C, respectively.

$$M^* \xrightarrow{k_1} \text{Neutral products}$$

and

$$M^* + M \xrightarrow{k_2} \text{Ionic products},$$

and Table 1 gives the results at excitation energies E in the range of 0.01 to 0.08 eV below the ionization potential I. In gas mixtures, there can also be ionization by collisions with the added gas molecules

$$M^* + A \xrightarrow{k_2'} \text{Ionic products},$$

and the k_2/k_2' values given in Table 1 show that the polyatomic molecules are much more effective at producing collisional ionization than are the atomic gases. We may use ionization yield data[7,9] for E values slightly above I to estimate y^* values of 0.15, 0.20, 0.20, 0.40, and 0.20 for acetone, acetyldehyde-$\underline{h}_4$ and $\underline{d}_4$, methyl bromide, and ethylene-$\underline{d}_4$, respectively. Figures 2 and 3 show η_c and k_2/k_1 as functions of ΔE (= I − E). The rapid decrease of k_2/k_1 as ΔE increases is primarily the result of (a) the increase in k_1 (due to the increased electron density in the core ion of the Rydberg orbital) and (b) the smaller fraction of collisions that are able to supply the large ΔE values.

Our results for four polar molecules are most consistent with large values of the collisional ionization rate constant k_2 and with k_1 being determined by the predissociation rate (e.g., at $\Delta E = 0.02$ eV, $k_2/k_1 \cong 10^{-17}$ cm^3, $10^{-9} \leq k_2 \leq 10^{-7}$ cm^3 s^{-1} and $10^8 \leq k_1 \leq 10^{10}$ s^{-1}). For ethylene-$\underline{d}_4$

TABLE 1. Collisional ionization results.[a]

Gas	E, eV	(1) $\eta_c y^*$	(2) $k_2 y^*/k_1$ 10^{-18} cm^3	(3) k_2/k_2' He	Ne	Ar	N_2
CH_3COCH	9.69	0.070 ± 0.003	3.7 ± 0.3	2000	800	2000	1200
I = 9.705 eV	9.68	0.078 ± 0.006	1.10 ± 0.06	1000	500	1400	900
	9.66	0.05 ± 0.02	0.20 ± 0.03	500	—	800	800
	9.65	0.022 ± 0.007	0.11 ± 0.03	700	200	300	300
	9.64	0.007 ± 0.002	0.06 ± 0.04	200	80	—	300
CH_3CHO	10.20	0.167 ± 0.005	1.74 ± 0.06	700			
I = 10.23 eV	10.18	0.18 ± 0.05	0.30 ± 0.02	1400			
	10.17	— [b]	0.09 ± 0.01	—			
	10.15	0.01 ± 0.01	0.04 ± 0.01	—			
CD_3CDO	10.20	0.20 ± 0.06	0.73 ± 0.06	1600			
I = 10.235 eV	10.18	— [b]	0.16 ± 0.02	≥ 2000			
	10.17	— [b]	0.06 ± 0.01	3000			
	10.15	— [b]	0.028 ± 0.005	—			
CH_3Br	10.52	0.264 ± 0.005	8.1 ± 0.3	1700		≥ 3000	
I = 10.54 eV	10.50	0.40 ± 0.09	0.73 ± 0.04	1000		1200	
	10.48	— [b]	0.09 ± 0.02	≥ 3000		500	
C_2D_4	10.56	0.019 ± 0.005	0.13 ± 0.02			—	
I = 10.53 eV	10.54	0.014 ± 0.003	0.24 ± 0.06			300	
	10.52	0.024 ± 0.003	0.15 ± 0.01			20	
	10.50	— [b]	0.021 ± 0.004			40	
	10.48	— [b]	0.008 ± 0.003			50	

[a] This table supercedes the preliminary one in Ref. 10.

[b] Pressure range insufficient to provide estimate.

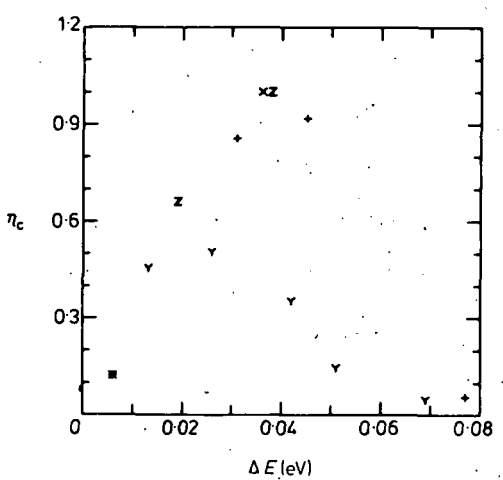

FIG. 2.--The collisional ionization yield calculated from $\eta_c y^*$ after estimating y^*. The symbols Y, +, X, Z, and * represent the data for CH_3COCH_3, CH_3CHO, CD_3CDO, CH_3Br and C_2D_2, respectively.

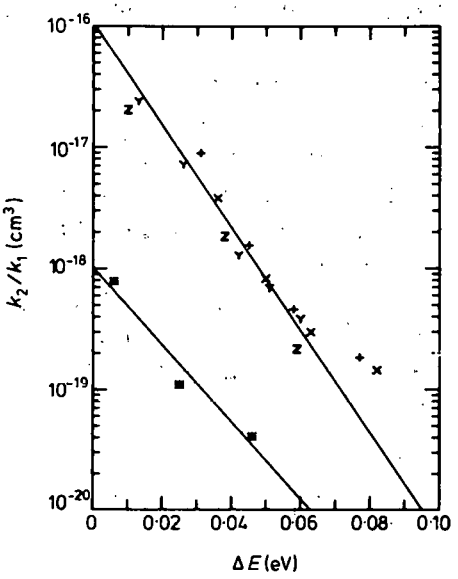

FIG. 3.--The ratio k_2/k_1 calculated from k_2y^*/k_1 after estimating y^*. The symbols have the same meaning as those in Figure 2. The two lines are fitted to the data with $\Delta E \leq 0.06$ eV.

we find smaller k_2/k_1 values, which we interpret as indicating a decrease in k_2 (e.g., at $\Delta E = 0.02$ eV, $k_2/k_1 \cong 2 \times 10^{-19}$ cm^3 and $10^{-11} \leq k_2 \leq 10^{-9}$ cm^3 s^{-1}). For the polar molecules, the large k_2 values imply that the electron transfer occurs while the collision partners are far apart; these rates can be understood in terms of the collisions of slow electrons, although the detailed mechanism remains unclear. For C_2D_4, the smaller k_2 values also can be explained by electron collisions, or by processes such as excitation transfer to vibrationally excited molecules or associative ionization. Thus, the Rydberg states of polyatomic molecules behave like the Rydberg states of atoms, except that k_1 is likely to be much faster as a result of predissociative processes.

References

1. H. Hotop and A. Niehaus, J. Chem. Phys. 47, 2506 (1967).
2. T. Sugiura and K. Arakawa, Recent Developments in Mass Spectrometry, K. Ogata and T. Hayakawa, Eds., University of Tokyo, Tokyo, p. 848 (1970).
3. C. E. Klots, J. Chem. Phys. 62, 741 (1975).
4. R. V. Ambartsumyan, G. I. Bekov, V. S. Letokhov, and V. I. Mishin, Zh. Eksp. Teor. Fiz. Pis. Red. 21, 595 (1975) [Sov. Phys.—JETP Lett. 21, 279 (1975)].
5. L. N. Ivanov and V. S. Letokhov, Kvant. Elektron. 2, 585 (1975) [Sov. J. Quant. Electron. 5, 329 (1975)].

6. T. F. Gallagher, S. A. Edelstein, and R. M. Hill, Stanford Research Institute, unpublished (1974).
7. J. C. Person and P. P. Nicole, Radiological Physics Division Annual Report, July 1967–June 1968, ANL-7489, p. 105.
8. J. C. Person, Proc. 6th Int. Conf. on Physics of Electronic and Atomic Collisions, MIT, Cambridge, Mass., Abstracts, p. 990 (1969).
9. J. C. Person and P. P. Nicole, Radiological Physics Division Annual Report, July 1969–June 1970, ANL-7760, Part I, p. 97.
10. J. C. Person, R. L. Watkins, and D. L. Howard, Proc. 9th Int. Conf. on Physics of Electronic and Atomic Collisions, J. S. Risley and R. Geballe, Eds., University of Washington, Seattle, Abstracts, p. 723 (1975).

MOLECULAR EFFECTS ON INNER-SHELL PHOTOABSORPTION. K-SHELL SPECTRUM OF N_2. †

J. L. Dehmer and Dan Dill*

K-shell photoabsorption spectra of the first-row diatomic molecules N_2, CO, and NO are known to depart drastically from the behavior characteristic of K-shell excitation in atoms. Below the K-shell thresholds these spectra are dominated by a single, very intense peak rather than by normal Rydberg structure, and the first 10 to 20 eV of the continuum exhibit a broad band of enhanced absorption, rather than a monotonic decrease. The experimental data from Ref. 1 are shown in Figure 1. We use the multiple-scattering model to compute the discrete part and the first 100 Ry of the photoionization continuum for K-shell photoionization of N_2. The discrete spectrum and the low-energy continuum are shown in Figure 2, and the entire continuum in Figure 3. This calculation accounts for both novel features described above and shows that they arise from centrifugal-barrier effects manifested as shape resonances in high-ℓ components of the final-state wavefunctions. These effects are molecular in origin, and result from the interaction between the photoelectron and the anisotropic molecular field. The full paper also discusses the energy

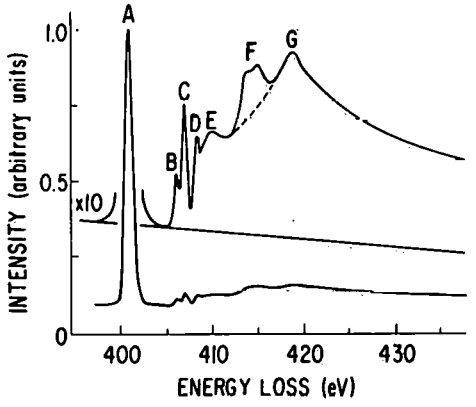

FIG. 1.--"Pseudo-photon" absorption spectrum of N_2 in the vicinity of the K-shell edge (409.9 eV) by Wight et al.[1]

† Summary of a paper, J. Chem. Phys., in press.

* Alfred P. Sloan Foundation Fellow and consultant, Radiological and Environmental Research Division. Permanent address: Department of Chemistry, Boston University, Boston, Massachusetts 02215.

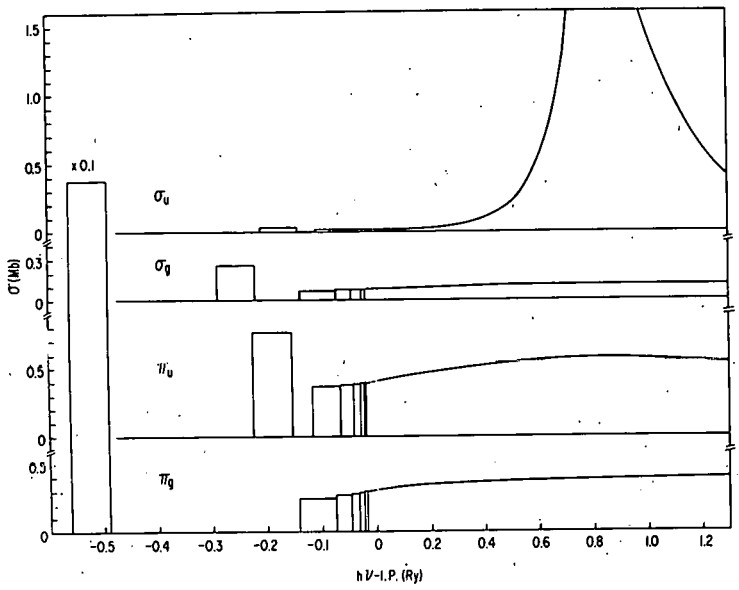

FIG. 2.--Partial photoionization cross sections for the four dipole-allowed channels for K-shell photoionization of N_2.
(ANL Neg. 149-76-33)

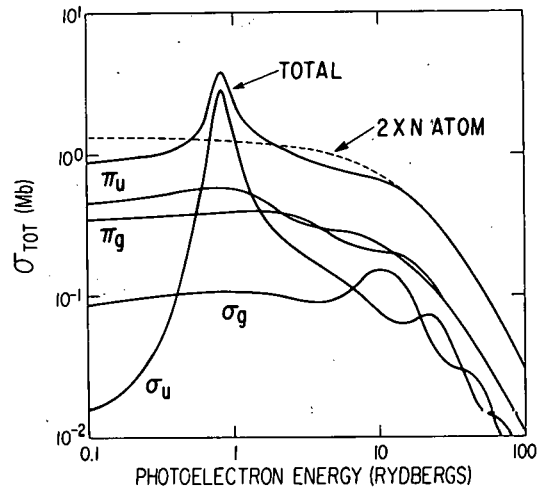

FIG. 3.--Partial photoionization cross sections for the K shell of N_2. Dashed line represents twice the K-shell cross section for photoionization of atomic nitrogen, as computed from a Hartree-Slater potential.

dependence of the photoelectron angular distributions, Kronig structure in the high-energy continuum, the bearing of the present results on valence-shell spectra, and the likelihood of widespread observation of shape resonances in ionization processes in other molecules.

Reference

1. G. R. Wight, C. E. Brion, and M. J. van der Wiel, J. Electron Spectrosc. Relat. Phenomena 1, 457 (1973).

HALOGEN K-SHELL PHOTOIONIZATION IN HF, F_2, HCl, AND Cl_2[†]

J. Siegel,[*] Dan Dill,[*‡] and J. L. Dehmer

We have calculated K-shell photoionization from the hydrogen halide and diatomic halide forms of fluorine and chlorine using the multiple-scattering method, and we have compared the results to the corresponding atomic cross sections calculated with the Hartree-Slater model, to elucidate specifically molecular effects in photoionization.

Multiple-Scattering Method

The multiple-scattering method[1-3] represents the electron-molecule interaction in terms of a multicenter potential (Figure 1) composed of spherical regions centered on the constituent atoms and an outer sphere surrounding the molecule as a whole: regions I_i are the atomic spheres, region III is exterior to the outer sphere, and region II is the interstitial volume between the atomic and outer spheres. Only the monopole component of the molecular potential in regions I_i and III is used, and the potential in region II is set to a constant value. Electron exchange is incorporated by the Slater[4,5] statistical approximation. A key advantage of the method is the accurate representation of the nuclear singularities. The success of the method in accounting for the $f(\ell = 3)$ resonance at 0.8 Ry in the K-shell photoionization of N_2 attests to the importance of such an accurate representation.[6,7] (For an overview and references to resonance effects in other molecules see, e.g., Ref. 8.)

Molecular K-Shell Photoionization

Molecular K-shell photoionization can be thought of as a two-stage process consisting of (1) the photon absorption proper, within the K shell,

---

[†]Summary of a talk given at the Annual Meeting of the Division of Electron and Atomic Physics, Am. Phys. Soc., 6–9 Dec. 1976, Lincoln, Nebraska.

[*]Dept. of Chemistry, Boston University, Boston, Mass. 02215.

[‡]Alfred P. Sloan Research Fellow and Consultant, Radiological and Environmental Research Division.

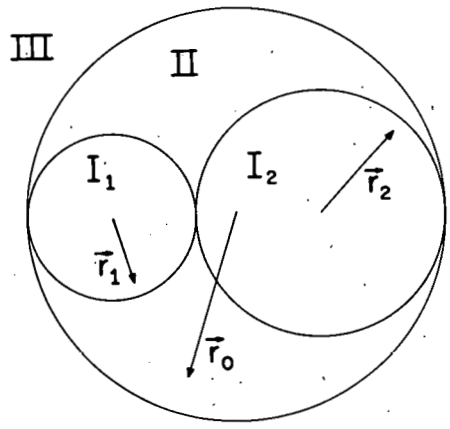

FIG. 1.--Multiple-scattering regions. (ANL Neg. 149-5951)

resulting in an electric-dipole $s \rightarrow p$ transition, and (2) the escape of the p electron from the core region to the exterior of the molecule. The electron experiences a torque during this escape owing to the anisotropic molecular potential, and this results in dispersion of photoelectric current into a range of orbital momentum channels. Owing to the cylindrical symmetry of the molecular potential we can analyze this dispersion separately for $\Lambda = 0 (\Sigma \rightarrow \Sigma)$ and $\Lambda = 1 (\Sigma \rightarrow \Pi)$ ionization. The Π photocurrent corresponds to electronic motion about the internuclear axis, whereas the Σ photocurrent corresponds to motion in the plane of the internuclear axis. Thus, Π photocurrent probes the most symmetric regions of the molecular potential, while Σ photocurrent probes the singularities at both nuclei. Accordingly, the Σ photocurrent is frequently the more sensitive probe of molecular effects. (The f resonance in N_2 is of Σ symmetry.)

Integrated Cross Sections

Specifically, we have computed the squared moduli $|A_{\ell p}(\Lambda)|^2$ of the continuum p-electron amplitude within the K shell, with $\Lambda = \Sigma (\Pi)$ (Figures 2 and 3), for each contributing orbital momentum ℓ in the exterior of the molecule. Adding the contribution from each ℓ, we obtain the integrated cross section for each Λ in units $(4/3)\pi^2 \alpha h\nu R_{ps}^2$, where R_{ps} is the K shell $s \rightarrow p$ energy-normalized, electric-dipole transition amplitude. This amplitude only varies by several percent over the spectral range studied, 0 to 5 Ry.

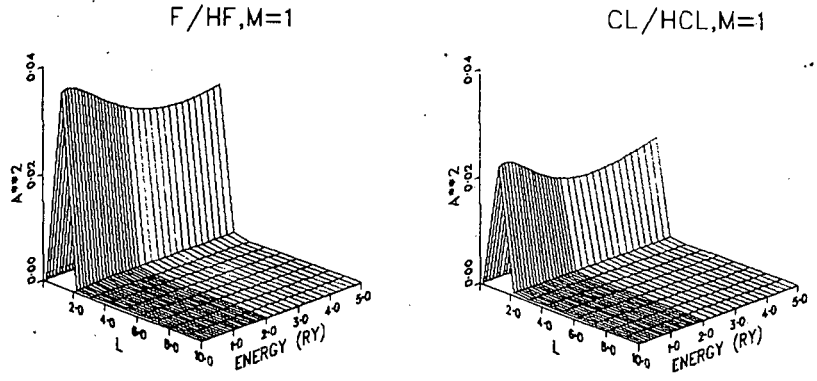

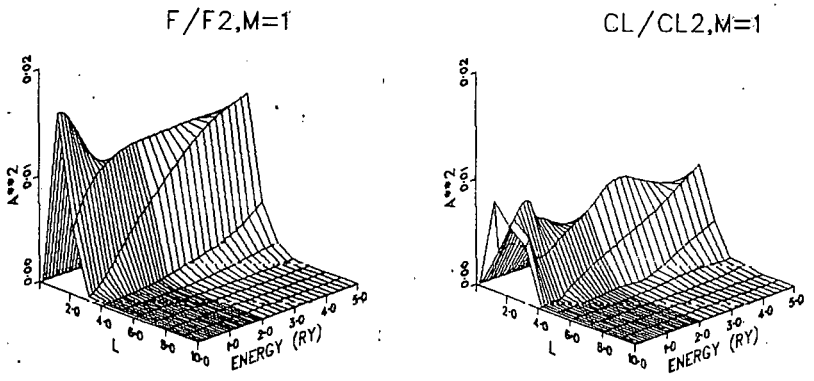

FIG. 2.-- Squared-moduli $|A_{\ell p}(\Pi)|^2$ as functions of energy.

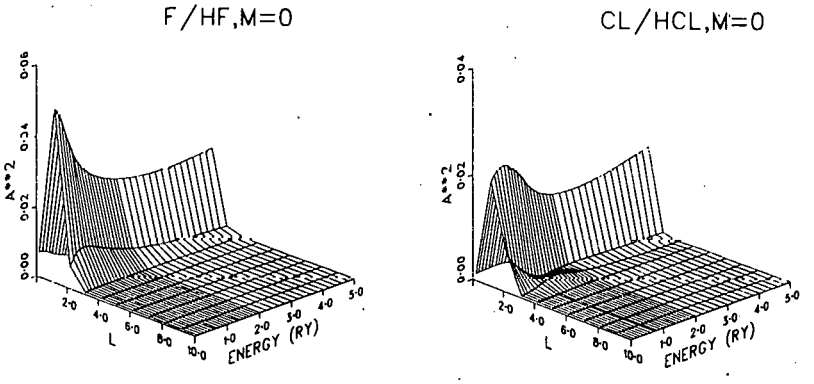

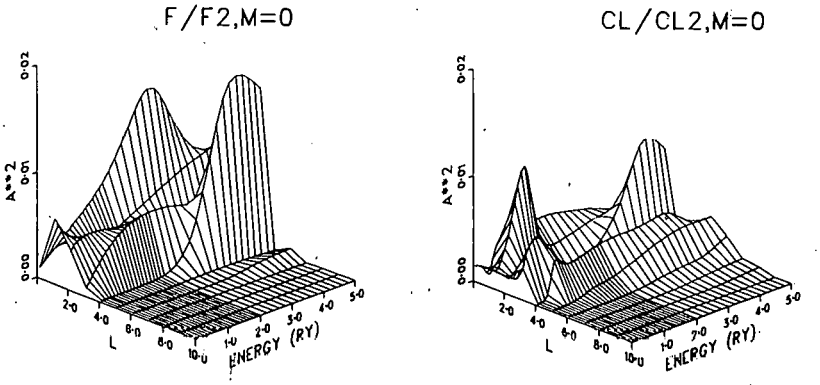

FIG. 3.--Squared-moduli $|A_{\ell p}(\Sigma)|^2$ as functions of energy.

Consider first Π-symmetry ionization (Figure 2). For HF and HCl the photocurrent is confined almost entirely to the p channel. For F_2 and Cl_2, however, the photocurrent is dispersed throughout channels from $\ell = 1$ to $\ell = 4$ or 5 ($\ell = 0$ cannot contribute to the Π photocurrent). The F_2 photocurrent remains in lower channels, while the Cl_2 photocurrent is more evenly dispersed over the range of ℓ channels. For all four molecules no single feature stands out at any particular energy, and thus the overall cross sections for Π symmetry show a nonresonant variation with energy, as seen in Figure 4.

Consider next the Σ results (Figure 3). Again, for HF and HCl the p channel dominates, but now there is some contribution from the s and d channels owing to the increased anisotropy in the Σ channel. This increased anisotropy is most pronounced, however, for F_2 and Cl_2, for which there is considerable current with ℓ as high as 6, with dramatic shifts in the channel of dominance. But, as with Π symmetry, no single channel sufficiently overwhelms the others at any particular energy to yield resonant variation in the overall cross section.

Finally, consider the Σ- and Π-symmetry cross sections (Figure 4). As expected, there is no dominant feature, but the detailed structure clearly correlates with the ℓ-channel variations. The effect of the hydrogen atom is to enhance the cross section at threshold relative to the atomic halogen result, with a subsequent drop below the atomic value. On the other hand, the effect of one halogen atom on the other is to depress the cross section at threshold, with subsequent enhancement. This may be a general pattern in (near) homonuclear diatomic molecules. The effect is so pronounced in N_2, for example, that a resonant enhancement results.[6-8] The overall similarity of the HF and HCl spectra reflects the similar spectral variation in their orbital momentum distributions.

Angular Distributions

The angular distribution of the photocurrent depends on whether the molecules are randomly oriented (for a general discussion see, e.g., Ref. 9),

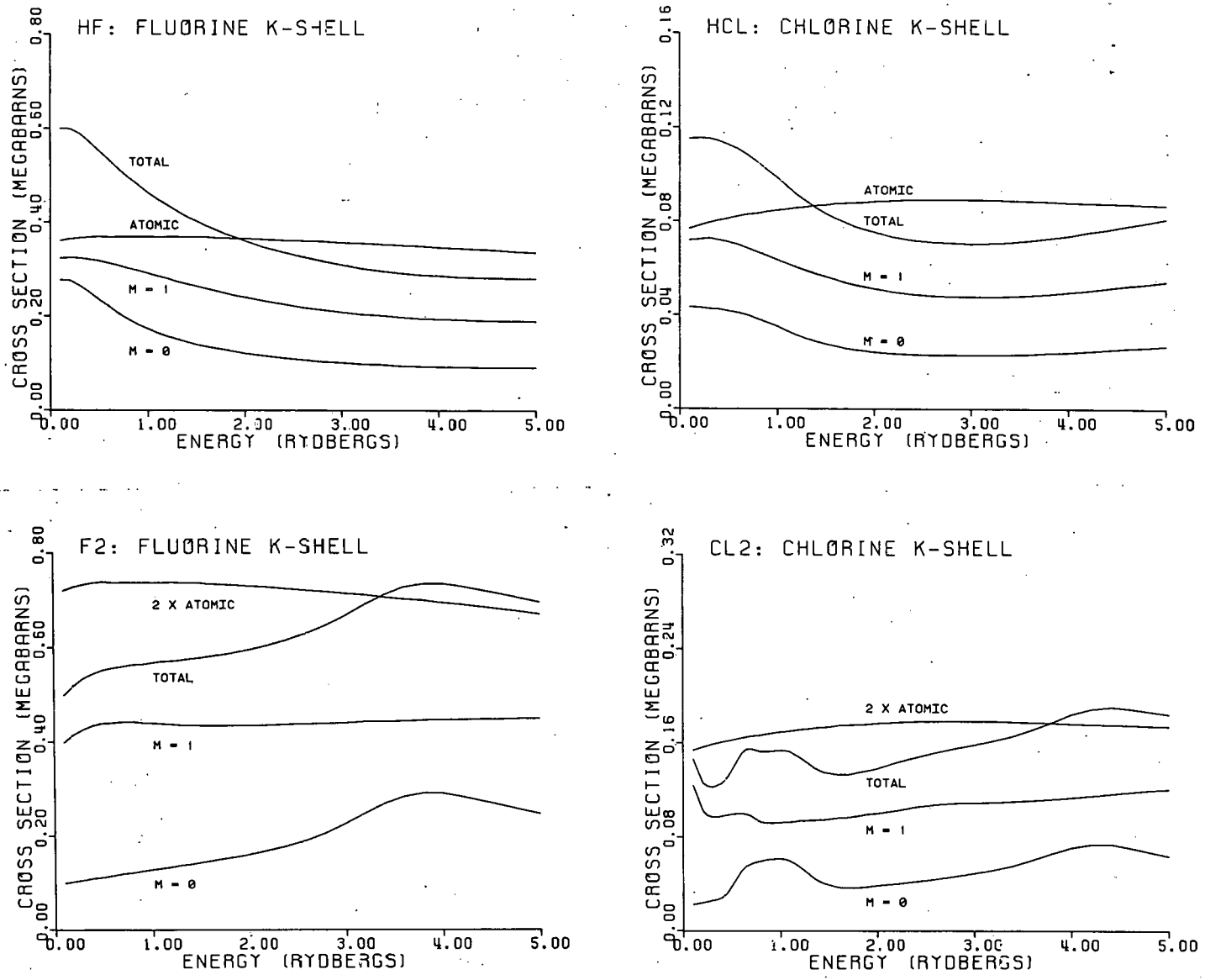

FIG. 4.--Integrated cross sections as $\Sigma(M=0)$ component, $\Pi(M=1)$ component, their sum, and the corresponding atomic cross section. (ANL Neg. 149-76-301)

as in the gas phase, or have a definite orientation,[10-12] as by adsorption onto a surface. In particular, the random-orientation distributions are restricted by conservation of parity and angular momentum to the form $a + b\cos^2\theta$,[13] while the fixed-molecule distributions are restricted in complexity only by the orbital momentum composition of the photoelectric amplitude.

The random-molecule results are expressed in terms of the asymmetry parameter β which ranges from $\beta = +2$ for a $\cos^2\theta$ distribution, peaked along the electric vector of the light, through $\beta = 0$ for an isotropic distribution, to $\beta = -1$ for a $\sin^2\theta$ distribution, peaked perpendicular to the electric vector. For all four molecules, β is close to 2 (Figure 5), the more so as the energy increases. That β does not equal exactly 2, as it does for atomic K-shell ionization, reflects mainly the inequivalence of the Σ and Π ionization channels (see e.g., Ref. 14), which vanishes at high energy. The structure for Cl_2 reflects the rich ℓ-channel distribution at low energy, where the Σ-Π inequivalence is greatest.

We have computed fixed-molecule angular distributions for the molecules aligned along or perpendicular to the electric vector of the light, which accesses separately Σ- and Π-symmetry ionization, respectively. The photoelectron ejection angle is measured from the internuclear axis; hydrogen is set at $\theta = 180°$. The results mirror closely the ℓ-channel composition of the photocurrent, albeit with further richness due to the interference between ionization amplitudes with different ℓ. (Such interference vanishes in the integrated cross section.)

Thus for Π symmetry (Figure 6) the distributions for HF and HCl are essentially p-like, peaked along the electric vector of the light. For F_2 the components in higher ℓ channels yield a small dimple, while for Cl_2 the more pronounced and structured dispersion into higher ℓ-channels superimposes a ripple effect on the overall p-like structure.

The greater ℓ-channel dispersion for Σ symmetry results in correspondingly richer distributions (Figure 7). The photocurrent is again peaked along the electric vector, which is now along the internuclear axis. Further, we see clearly the enhancement at threshold for HX, and the depression for X_2. The

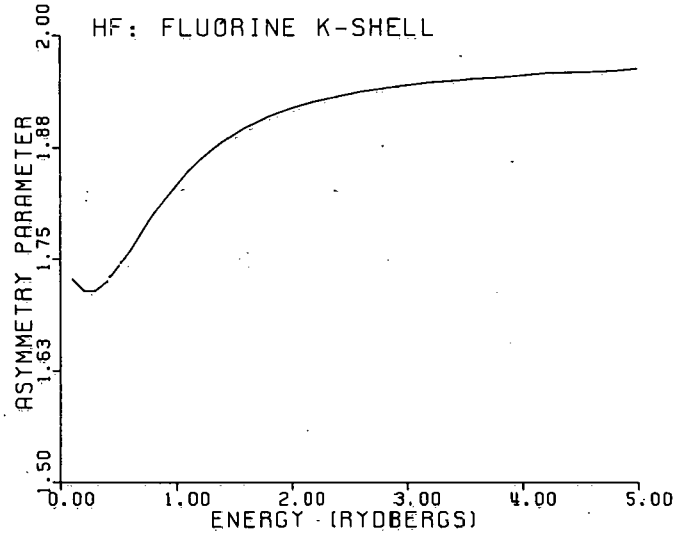

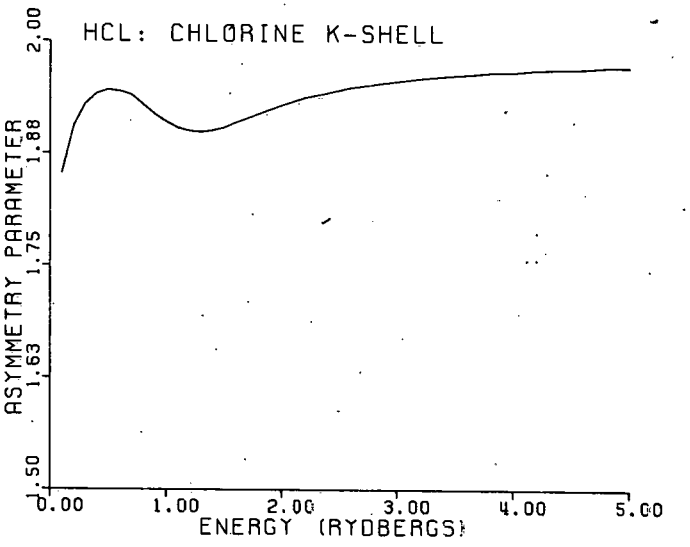

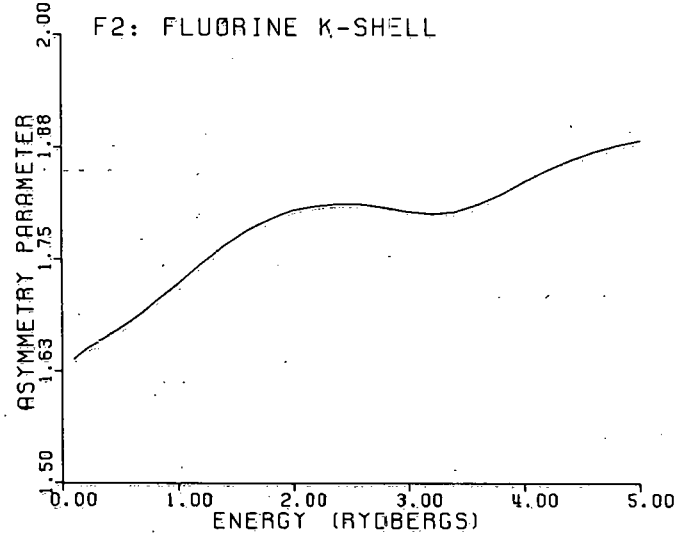

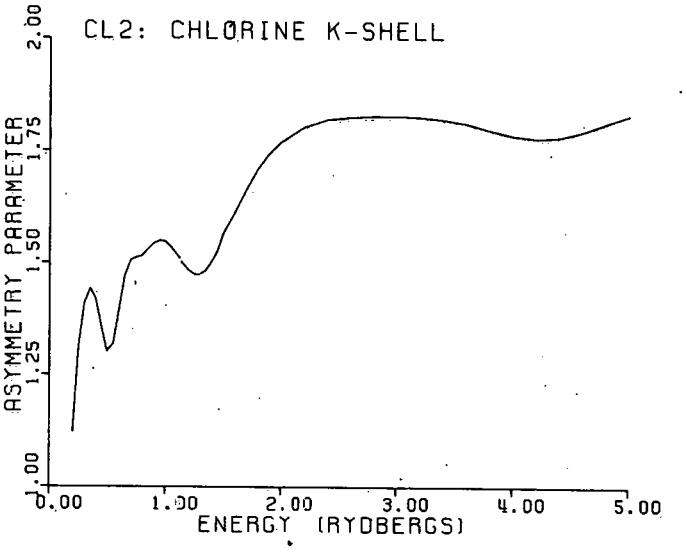

FIG. 5.--Asymmetry parameters β of the random-molecule angular distributions. (ANL Neg. 149-76-302).

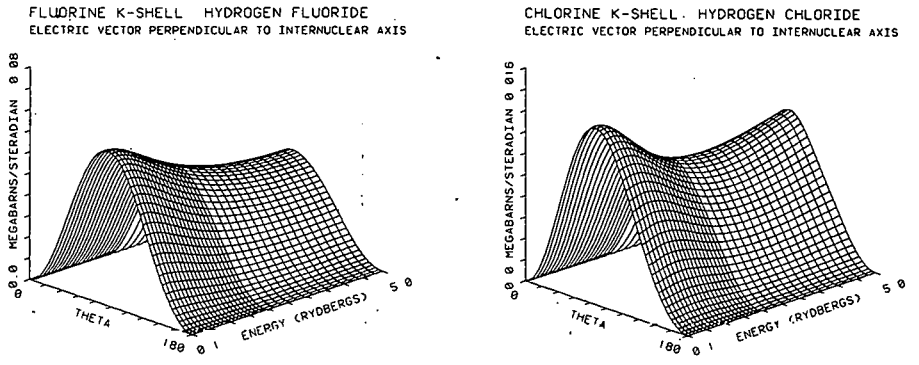

FIG. 6.--Fixed-molecule angular distributions for Π-symmetry ionization. (ANL Neg. 149-76-304)

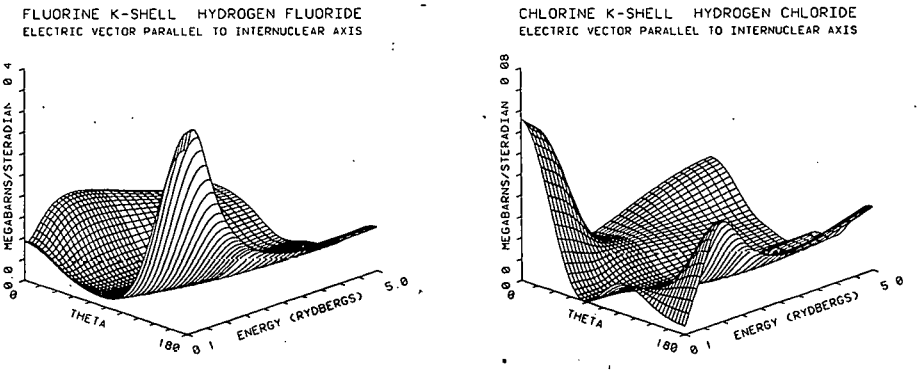

FIG. 7.--Fixed-molecule angular distributions for Σ-symmetry ionization. (ANL Neg. 149-76-303)

swinging of photocurrent between $\theta = 0°$ and 180° in the HX spectra is due to interference of ℓ-channel amplitudes of differing parity. The F_2 and Cl_2 distributions are similar in spite of differing orbital momentum composition: the photocurrent is concentrated in an extremely small solid angle about each atom.

Conclusion

The anisotropic molecular potential disperses inner-shell photoelectric current among a range of orbital momentum channels. This dispersion is largely hidden in random-molecule experiments unless there are extreme (resonant) variations with energy in ℓ-channel composition. In contrast, fixed-molecule experiments probe directly the orbital momentum dispersion.

References

1. D. Dill and J. L. Dehmer, J. Chem. Phys. 61, 692 (1974).
2. J. Siegel, D. Dill, and J. L. Dehmer, J. Chem. Phys. 64, 3204 (1976).
3. K. H. Johnson, Advances in Quantum Chemistry, P. O. Löwdin, Ed., Academic Press, New York, Vol. 7, p. 143 (1973).
4. F. Herman and S. Skillman, Atomic Structure Calculations, Prentice-Hall, Englewood Cliffs, N.J. (1963).
5. J. C. Slater, Phys. Rev. 81, 385 (1951).
6. J. L. Dehmer and D. Dill, Phys. Rev. Letters 35, 213 (1975).
7. J. L. Dehmer and D. Dill, J. Chem. Phys. 65, 5327 (1976).
8. J. L. Dehmer and D. Dill, Proc. 2nd Int. Conf. on Inner-Shell Ionization Phenomena, 29 March–2 April 1976, Freiburg, West Germany, Plenum Publr., New York, pp. 387–394 (1976).
9. D. Dill, Photoionization and other Probes of Many-Electron Interactions, NATO-ASI Ser. B, F. J. Wuilleumier, Ed., Plenum Publr., New York, pp. 387–394 (1976).
10. D. Dill, J. Chem. Phys. 65, 1130 (1976).
11. D. Dill, J. Siegel, and J. L. Dehmer, J. Chem. Phys. 65, 3158 (1976).
12. S. Wallace, D. Dill, and J. L. Dehmer, to be published.
13. C. N. Yang, Phys. Rev. 74, 764 (1948).
14. D. Dill, Phys. Rev. A 6, 160 (1972).

SPECTRAL VARIATION OF FIXED-MOLECULE PHOTOELECTRON ANGULAR DISTRIBUTIONS*

Dan Dill,[†‡] Jon Siegel,[‡] and J. L. Dehmer

We have computed the angular distribution of electrons ejected by electric-dipole interactions from the K shells of CO and N_2 molecules held fixed in space, e.g., by adsorption onto a surface. The predicted distributions are very rich in structure, manifesting directly the spectral variation of the orbital momentum composition of the photocurrent. Experimental determination of such distributions will provide a sensitive and detailed probe of

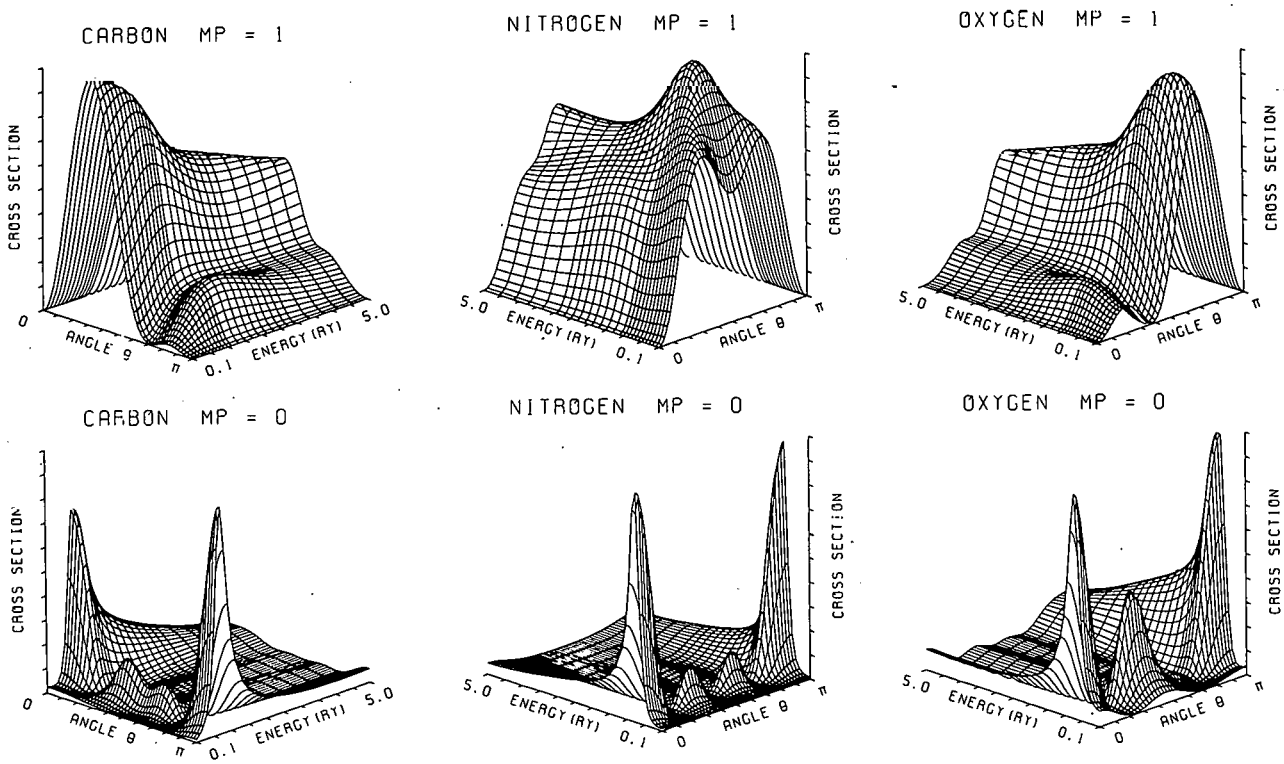

FIG. 1.--Calculated fixed-molecule K-shell photoelectron angular distributions for CO and N_2. The vertical scale has been adjusted in each plot to obtain a maximum size of the surface. See Figure 2 for the same surfaces on an absolute scale. The plane of the two horizontal axes represents zero cross section. For CO, carbon is at $\theta = 0$, oxygen is at $\theta = \pi$. (ANL Neg. 149-76-220)

*Summary of an article published in J. Chem. Phys. 65, 3158 (1976).

[†]Alfred P. Sloan Foundation Fellow and consultant, Radiological and Environmental Research Division.

[‡]Department of Chemistry, Boston University, Boston, Massachusetts 02215.

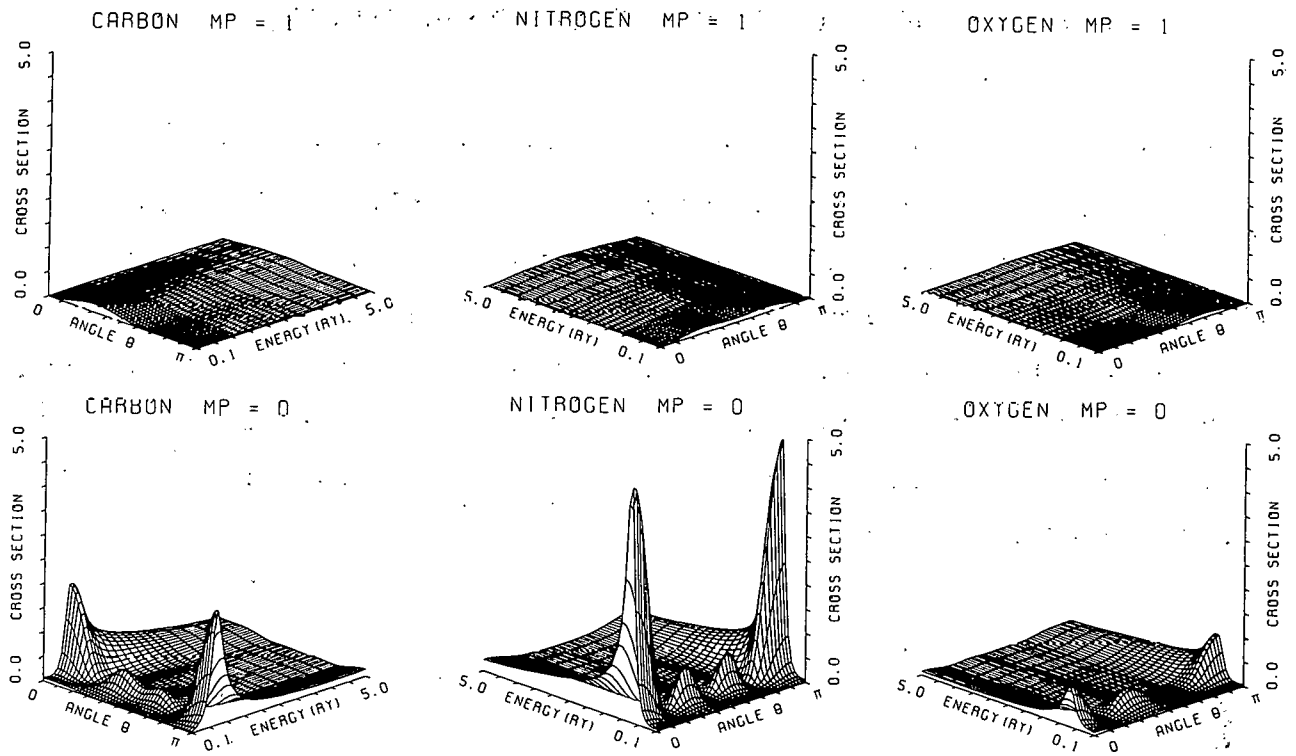

FIG. 2.--Data of Figure 1 plotted in units of megabarns per steradian. (ANL Neg. 149-76-219)

molecular photoionization dynamics. The main results are seen in Figures 1 and 2, which show the oriented-molecule angular distributions for the K shells of N_2 and CO on a relative scale (Figure 1) to bring out the structure of the surfaces and on an absolute scale (Figure 2). The large four-lobed peak (as a function of energy) for light polarization oriented along the molecular axis (MP = 0) is a clear manifestation of the f-wave shape resonance discussed earlier[1] for N_2.

Reference

1. J. L. Dehmer and Dan Dill, Phys. Rev. Lett. 35, 213 (1975).

FIXED-MOLECULE PHOTOELECTRON ANGULAR DISTRIBUTIONS*

Dan Dill†

Expressions are obtained for the angular distribution of electrons ejected by electric dipole interaction from molecular targets fixed in the laboratory coordinate frame. The analysis is geometrical and independent of any particular dynamical description of the photoionization process. Thus, the results will serve as the framework for study of the dynamics of particular processes, such as photoionization of molecules oriented on surfaces or by molecular-beam techniques.

*Abstract of an article published in J. Chem. Phys. 65, 1130 (1976).

†Alfred P. Sloan Foundation Fellow; consultant, Radiological and Environmental Research Division. Permanent address: Department of Chemistry, Boston University, Boston, Massachusetts 02215.

FIXED-MOLECULE PHOTOELECTRON ANGULAR DISTRIBUTIONS OF CO FOR FIXED SOURCE-DETECTOR ORIENTATION

S. Wallace,* D. Dill,*† and J. L. Dehmer

Dill, Siegel, and Dehmer[1,2] have computed fixed-molecule photoelectron angular distributions (FMADs) for fixed source-molecule orientation. Here we treat the alternative case of fixed source-detector orientation for all possible target orientations, an arrangement which corresponds to that of typical photoelectron spectrometers. We have computed carbon K-shell ionization of CO at the $\Sigma(f)$ resonance[2-4] (0.8 Ry kinetic energy) for several detection directions using dipole transition amplitudes computed by the multiple-scattering formulation of inner-shell photoionization.[5,6]

Geometrical Conventions

A diagram of the coordinate system is given in Figure 1. The orientation of the molecule is given by the set of Euler angles‡ $\hat{R} = \{\alpha,\beta,0\}$ which carries the laboratory frame (primed) coordinates into the molecule frame (unprimed) coordinates. The first two rotations, through α and β, align the directions $\hat{z}'$ (defined as either the axis of linear polarization or the propagation direction for natural and circular polarizations) and $\hat{z}$ (defined as the internuclear axis, with oxygen at the positive end). The third rotation, through γ about the transformed axis $\hat{z}'$ is moot since this is the molecular symmetry axis, and γ is arbitrarily set at zero.

The orientation of the detector is defined as $\hat{k}_e^{\gamma} = (\theta,\phi)$, the usual polar angles specifying the detection direction with respect to the laboratory frame axis $\hat{z}'$. The angle ϕ is arbitrarily measured from the source-detector plane.

*Department of Chemistry, Boston University, Boston, Massachusetts 02215.

†Alfred P. Sloan Research Fellow and Consultant to Radiological and Environmental Research Division.

‡Conventions on Euler angles, spherical harmonics, rotation matrices, and angular momentum phase factors are those given in Ref. 7.

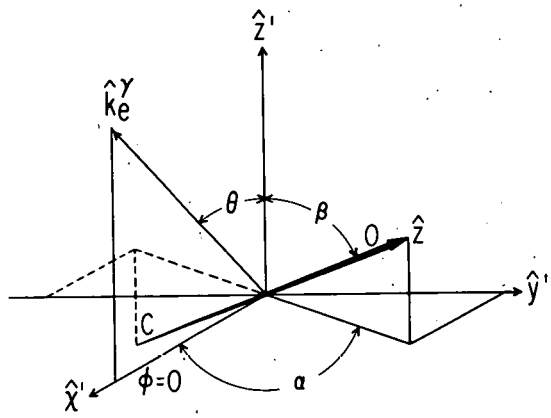

FIG. 1.--Coordinate system for fixed-detector FMAD. Euler angles $\{\alpha,\beta,0\}$ specify the molecule orientation, polar angles $\hat{k}_e^{\gamma} = (\theta,\phi)$ specify the detection direction; $\hat{z}'$ is either the axis of linear polarization, or the axis of propagation for natural and circularly polarized light; $\hat{z}$ is the internuclear axis, with oxygen at the positive end. (ANL Neg. 149-77-5)

Working Expression for Cylindrically Symmetric Target

The general formula for the FMAD as measured from a position fixed with respect to the light source is Eq. 23 of Ref. 2,

$$\left.\frac{d\sigma(\vec{k}_e^{\gamma})}{d\hat{R}_\gamma}\right|_{m_p} = 4\pi^2\alpha h\nu \sum_{\substack{\ell m m_\gamma \\ \ell' m' m'_\gamma}} (-1)^{m+m_\gamma-m_p}[(2\ell'+1)(2\ell+1)/4\pi]^{\frac{1}{2}}$$

$$\times i^{(\ell'-\ell)} e^{i(\sigma_\ell-\sigma_{\ell'})} D^{(-)\Gamma_0 *}_{\ell' m' m_\gamma}(k_e^\gamma)\, D^{(-)\Gamma_0}_{\ell m m_\gamma}(k_e^\gamma)$$

$$\times \sum_{K_e M_e \gamma} (-1)^{-M_e^\gamma} (\ell m, \ell'-m' | K_e M_e)(\ell 0, \ell' 0 | K_e 0)(2K_e+1)^{-\frac{1}{2}} Y_{K_e M_e^\gamma}(\hat{k}_e^\gamma)$$

$$\times \sum_{K_\gamma} (1 m_\gamma, 1-m'_\gamma | K_\gamma m_\gamma)(1 m_p, 1-m_p | K_\gamma 0)$$

$$\times \sum_{K} (K_e - M_e, K_\gamma M_\gamma | KM)(K_e - M_e^\gamma, K_\gamma 0 | K - M_e^\gamma) D^{K}_{M,-M_e^\gamma}(\hat{R}_\gamma) . \qquad (1)$$

Here α is the fine structure constant, σ_ℓ is the Coulomb phase shift $\arg\Gamma(\ell+1-i/k_e)$, $D^{(-)\Gamma_0}_{\ell m m_\gamma}$ is the dipole transition amplitude, $D^{K}_{M_e - M_e \gamma}(\hat{R}_\gamma)$ is the rotation matrix element, and $\hat{R}_\gamma = \{0, \beta_\gamma, \gamma_\gamma\} = \hat{R}^{-1}$ is the set of Euler angles which carries the molecule frame into the laboratory frame. The polarization quantum number is $m_p = 0$ for linear polarization, $m_p = \pm 1$ for left- and right-circular polarizations (positive and negative helicities), respectively. After simplification of Eq. 1 by imposing cylindrical symmetry, we obtain the working expression[8]

$$\left.\frac{d\sigma(\vec{k}_e \gamma)}{d\Omega(\alpha,\beta)}\right|_{m_p} = \sum_{KM} A_{KM}^{m_p}(\vec{k}_e \gamma)\, Y_{KM}(\beta,\alpha)\,, \tag{2}$$

where

$$A_{KM}^{m_p}(\vec{k}_e \gamma) = 4\pi^2 \alpha h\nu \sum_{\substack{\ell m \\ \ell' m'}} i^{(\ell' - \ell)} e^{i(\sigma_\ell - \sigma_{\ell'})} D_{\ell' m'}^{(-)\Gamma_0 *}(k_e \gamma) D_{\ell m}^{(-)\Gamma_0}(k_e \gamma)$$

$$\times C^{KMm_p}_{\ell m, \ell' m'}(\hat{k}_e \gamma) \tag{3}$$

with

$$C^{KMm_p}_{\ell m, \ell' m'}(\hat{k}_e \gamma) = (-1)^{m + m' - m_p} (2K+1)^{-\frac{1}{2}} [(2\ell'+1)(2\ell+1)]^{\frac{1}{2}}$$

$$\times \sum_{K_e} (2K_e+1)^{-\frac{1}{2}} (\ell m, \ell' - m' | K_e m - m')(\ell 0, \ell' 0 | K_e 0) Y^*_{K_e M}(\hat{k}_e \gamma)$$

$$\times \sum_{K_\gamma} (1 m_p, 1 - m_p | K_\gamma 0)(1 m, 1 - m' | K_\gamma m - m')(K_e m' - m, K_\gamma m - m' | K 0)$$

$$\times (K_e M, K_\gamma 0 | K M)\,. \tag{4}$$

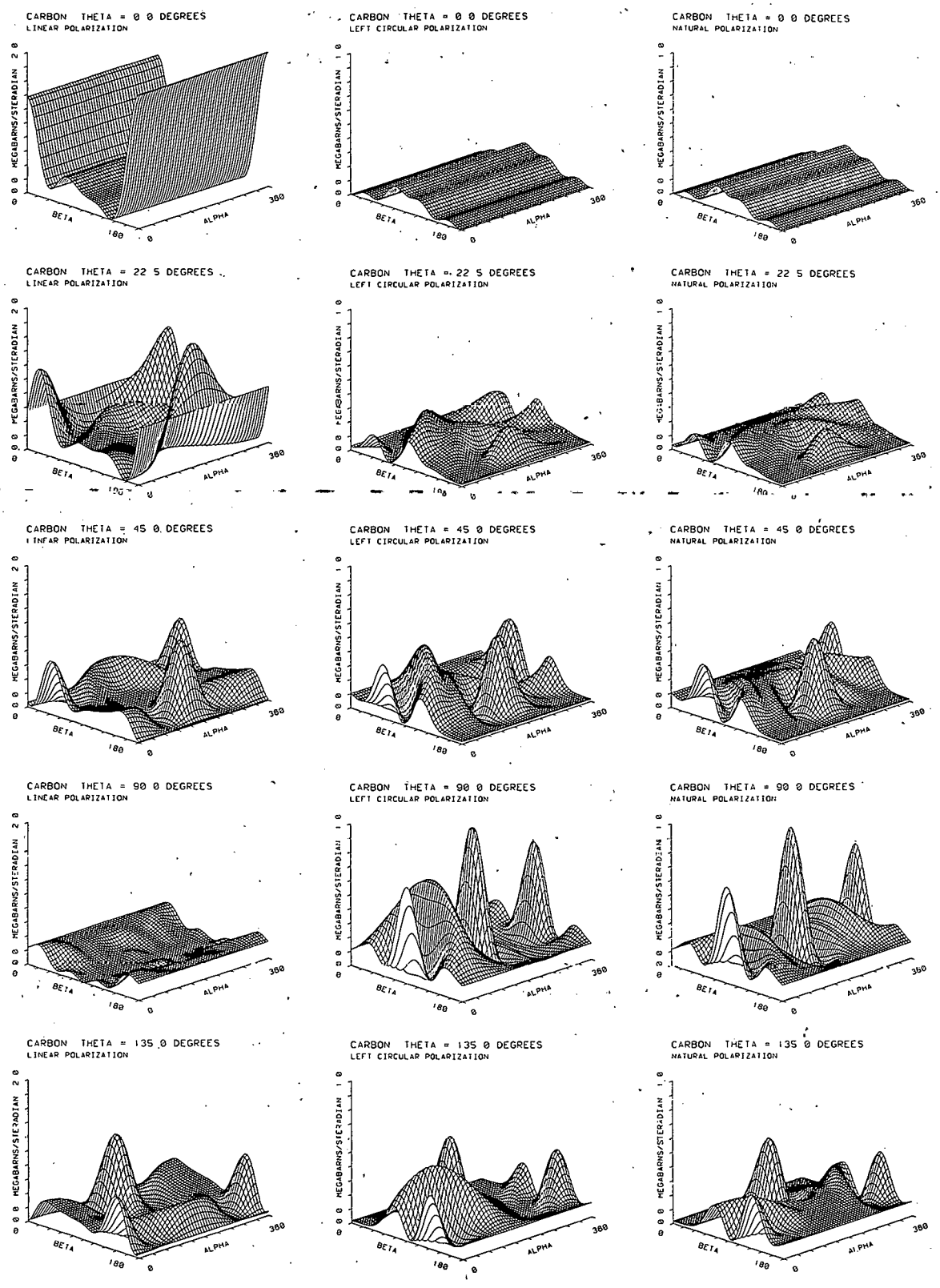

FIG. 2.--Differential cross sections for K-shell photoionization from carbon in CO, at 0.8 Rydberg kinetic energy, as a function of molecule orientation and detection direction. (ANL Neg. 149-76-308)

All dynamics are contained in the transition amplitudes $D_{\ell m}^{(-)\Gamma_0}(k_e^{\gamma})$. Details of the derivation are given elsewhere.[8]

Dependence of the Cross Section on Helicity

In the usual gas phase photoionization experiment the angular distribution is independent of helicity because of the random orientation of the target. Fixed-molecule distributions, however, exhibit a definite handedness. This follows in the present example from the relation

$$A_{KM}^{-m_p}(\theta,\phi,k_e^{\gamma}) = A_{KM}^{m_p *}(\theta,-\phi,k_e^{\gamma}) , \tag{5}$$

which yields a mirror symmetry between the cross sections for ionization with alternative helicities ($m_p = \pm 1$). At our choice of $\phi = 0$ at the source-detector plane this mirror symmetry simplifies to

$$\left.\frac{d\sigma(\theta,0)}{d\Omega(\alpha,\beta)}\right|_{m_p} = \left.\frac{d\sigma(\theta,0)}{d\Omega(-\alpha,\beta)}\right|_{-m_p} . \tag{6}$$

That is, the cross section for negative helicity is given by the mirror image in the angle α of the cross section for positive helicity.

Angular Distributions

The calculated differential photoionization cross sections for the K shell of carbon in CO for several detector angles are plotted in Figure 2. Since the kinetic energy of the electron is given by the difference between the energy of the ionizing radiation and the K-shell ionization potential of the corresponding atom, the distribution from each atom may be probed selectively by kinetic energy analysis at the detector.

Geometrical features in the distributions may be understood by reference to Figure 1. (1) All distributions are invariant with respect to α at $\beta = 0°$, $180°$, since here the molecule and laboratory frame z axes are aligned and, therefore, rotations through α are about the molecular symmetry axis. (A special case occurs for $\theta = 0°$, at which source and detector are aligned:

distributions are independent of α for all values of β.) (2) For linear polarization there is a mirror symmetry about $\alpha = 0°$, or equivalently, about $\alpha = 180°$. This may be seen immediately from Eq. 6 with $m_p = 0$, and is due to the fact that, at a given value of β, the interaction for equal displacements α on either side of the source-detector plane must be equivalent. (3) The distributions for right- and left-circularly polarized light are mirror images in α of each other, as may again be seen from Eq. 6. (4) Because natural polarization is expressed as the incoherent sum of right- and left-circular polarizations, as a consequence of (3) the distributions for natural polarization are symmetric about $\alpha = 0°$, or $\alpha = 180°$. (5) The distribution for a given detector angle θ, and with β varying from 0° to 180°, is the same as the distribution for a detector angle $\pi - \theta$, with β varying from 180° to 0°, i.e.,

$$\left.\frac{d\sigma(\pi - \theta, \phi)}{d\Omega(\alpha, \beta)}\right|_{m_p} = \left.\frac{d\sigma(\theta, \phi)}{d\Omega(\alpha, \pi - \beta)}\right|_{m_p}, \tag{7}$$

as follows from Eqs. 2–4. (6) A special case of (5) is the mirror symmetry in β for all polarizations at $\theta = 90°$, as follows immediately from Eq. 7.

Dynamical features of the distributions arise from three effects: (1) the degree of alignment of the electric vector of the light and the molecule, (2) the degree of alignment of the molecule and the detector, and (3) the orientation of the carbon end of the molecule with respect to the detector. In general, the cross section should be large when the molecular axis is most nearly aligned with the electric vector of the light, since this probes the Σ resonance, and when it is most nearly aligned with the detection direction, since at the resonance electrons are ejected preferentially along the molecular axis.[6] Conversely, when the molecular axis is perpendicular to either the electric vector or the detection direction, the cross section is, in general, quite small.[6] Degree of alignment with the ionizing electric field seems to be the dominant criterion when the two conflict. The orientation of the carbon end of the molecule affects the differential cross section because of scattering from the oxygen: when the carbon is directed away from the detector the cross section will be smaller than when it is directed toward the detector.

Dill, Siegel, and Dehmer[2] explored the dependence of the distribution upon detection direction alone for a particular target orientation. Here the distributions are more complicated owing to the interplay of geometry and dynamics. For linear polarization at $\theta = 0°$, the distribution is symmetric about $\alpha = 0°$ at all β since the source and detector are aligned, and is greater at $\beta = 180°$ since here the carbon end is toward the detector. At $\theta = 90°$, the source and detector are perpendicular. When the molecule is also perpendicular to the source (at $\beta = 90°$), the cross section nearly vanishes, yet as β varies slightly from 90°, the molecule begins to respond again to the light. At intermediate values of θ, however, the distributions are not so easily explained in terms of limiting cases. The dominant feature in the distributions for $\theta = 22.5°$ and $\theta = 45°$ (linear polarization) falls close to those values of α and β which align the carbon end of the molecule with the detection direction ($\alpha = 180°$, $\beta \cong 180° - \theta$). In the distributions for circular and natural polarizations at the same values of θ, however, the corresponding feature is shifted toward lower values of β, i.e., toward values that would place the molecule nearer the plane of the rotating electric vector. (Direct comparisons of distributions for linear and circular polarizations must be made with allowance for the different definitions of z' in the two cases.) Such complex interplay between geometry and dynamics is seen throughout the distributions.

The differential cross sections for oxygen are very similar to those for carbon in gross features, but structural (ℓ-component) differences do arise. Provided that the oxygen is rotated into the position occupied by the carbon ($\beta \rightarrow \pi - \beta$, $\alpha \rightarrow \alpha + \pi$), the distributions may be compared directly to reveal the differences in dynamics between the two atoms, all of which are contained in the dipole amplitudes $D^{(-)\Gamma_0}_{\ell m}(k_e \gamma)$. Cross sections for oxygen at selected angles θ will be found elsewhere.[8]

Conclusion

Fixed-molecule angular distributions provide a means for determining the orientation of molecules aligned in space — and we have in mind particularly species adsorbed on surfaces. The treatment here of arbitrary detection

angle is particularly appropriate to the arrangement of typical photoelectron spectrometers. If interactions with the surface are small, theory and experiment may be compared directly to determine orientation; even if the molecules are not perfectly aligned, the theoretical expressions may be integrated over appropriate tolerances in the orientation angles to fit the observations. If surface effects are non-negligible, they will need to be included in the computation of the dipole amplitudes, and such cases as those in which molecular symmetries had been assumed will need to be generalized once again to include the geometry of the perturbations. But even without this effort, some of the adsorption-site geometry may be inferred simply from the magnitude and periodicity of the perturbations. Consider a carbon monoxide molecule standing on end in an interstitial space formed by four metal atoms of a surface. As the molecule (surface) is rotated about the molecular axis, perturbations from cylindrical symmetry, four in number and of equal or unequal (depending on the site) magnitude, should be observed. Further, which end protrudes — carbon or oxygen — may be inferred from the argument that the more perturbed atom will give the more perturbed distribution, provided that the difference in effect at embedded and protruding ends is discernible. Further simplifications of these proposals, based on integration over all detection directions rather than molecular orientation ("integrated FMAD"), will be provided.[8]

Finally, the handedness of the interaction for circularly polarized light expressed in Eq. 6 deserves further study. This result, as mentioned, was heretofore unseen because of failure to resolve molecular orientation in the usual random-molecule gas phase of calculations.

References

1. D. Dill, J. Chem. Phys. 65, 1130 (1976).
2. D. Dill, J. Siegel, and J. L. Dehmer, J. Chem. Phys. 65, 3158 (1976).
3. J. L. Dehmer and D. Dill, Phys. Rev. Lett. 35, 213 (1975).
4. J. L. Dehmer and D. Dill, J. Chem. Phys. 65, 5327 (1976).
5. D. Dill and J. L. Dehmer, J. Chem. Phys. 61, 692 (1974).
6. J. Siegel, D. Dill, and J. L. Dehmer, J. Chem. Phys. 64, 3204 (1976).
7. M. E. Rose, Elementary Theory of Angular Momentum, Wiley, New York, (1957).
8. S. Wallace, D. Dill, and J. L. Dehmer, to be published.

MOLECULAR EFFECTS IN INNER-SHELL PHOTOABSORPTION. SHAPE RESONANCES AND EXTENDED X-RAY ABSORPTION FINE STRUCTURE (EXAFS).*

J. L. Dehmer and Dan Dill†

With few exceptions, inner-shell photoabsorption spectra of molecules exhibit strong shape resonances near threshold, weak fine structure extending far into the continuum, or both. We establish the main characteristics of these one-electron effects by reviewing selected experimental data. Then we describe recent calculations based on the multiple-scattering model which show in detail how these effects are caused by the anisotropic molecular field, which mixes high-ℓ partial-wave components into the final-state wavefunction. Finally, we predict how these molecular effects will manifest themselves in future experiments on photoelectron angular distributions from randomly-oriented and fixed molecules.

*Abstract of paper published in Invited Papers, 2nd Int. Conf. on Inner-Shell Ionization Phenomena, March 29—April 2, 1976, Freiburg, West Germany, W. Mehlhorn and R. Brenn, Eds., University of Freiburg, p. 221 (1976).

†Alfred P. Sloan Research Fellow; Consultant, Radiological and Environmental Research Division. Permanent address: Department of Chemistry, Boston University, Boston, Massachusetts 02215.

RYDBERG STATES OF BUTADIENE*

K. B. Wiberg,† K. S. Peters,† G. B. Ellison,† and J. L. Dehmer

The ultraviolet spectrum of butadiene is a key element in interpreting the spectra of the conjugated polyenes (see, e.g., Ref. 1). In this work, a spectroscopic problem in this prototype system is resolved by use of high-resolution photoelectron spectroscopy. The question of interpretation concerns a Rydberg state of 1,3-butadiene appearing between 56,000 and 63,000 cm^{-1} in the uv absorption spectrum, shown as the lower curve in Figure 1. McDiarmid[2] suggested that, in addition to the Rydberg series with origin at A in Figure 1, there were two additional series with origins at 59,121 cm^{-1} and 60,312 cm^{-1} (marked B and C in Figure 1).

Comparison of the uv absorption spectrum and the high-resolution photoelectron spectrum shows that peaks B and C occur in both spectra. If we make the reasonable assumption that the vibrational structure of a Rydberg state is similar to that of the molecular ion, we are led to the conclusion that peaks B and C are, in fact, vibrational structures associated with a single

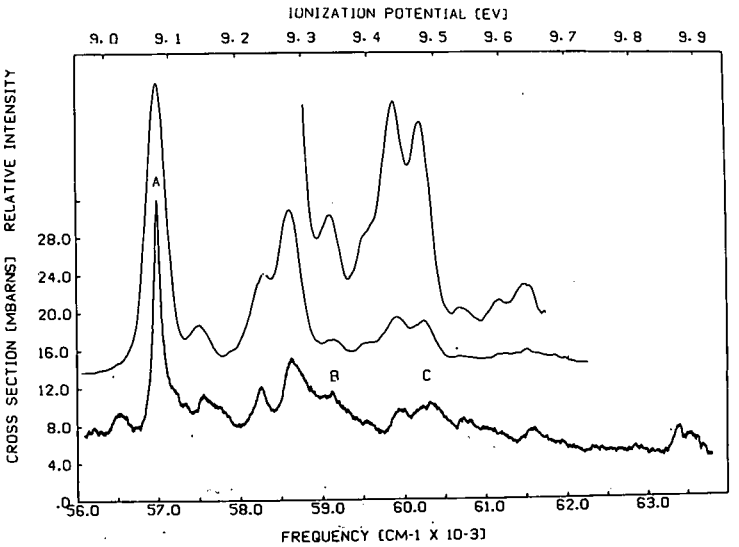

FIG. 1.--Comparison of the ultraviolet spectrum (lowest curve) and the photoelectron spectrum (upper curves) for 1,3-butadiene.

*Summary of a paper submitted for publication.

†Department of Chemistry, Yale University, New Haven, Connecticut 06520.

Rydberg series whose origin is peak A. In fact, these two features correspond very well to sums of fundamental vibration frequencies, i.e., B and C represent $\nu_4 + \nu_9$ and $2\nu_4$, respectively.

References

1. B. H. Hudson and B. E. Kohler, Chem. Phys. Lett. 14, 299 (1972); J. Chem. Phys. 59, 4984 (1973).
2. R. A. McDiarmid, J. Chem. Phys. 64, 514 (1976).

WAVELENGTH DEPENDENCE OF THE PHOTOELECTRON ANGULAR DISTRIBUTIONS FOR ATOMIC OXYGEN*

J. L. Dehmer and P. M. Dehmer

The importance of photoionization of atomic oxygen in the ionosphere has recently stimulated several calculations of the photoelectron angular distributions.[1-3] We report measurements of these angular distributions for the OII $^4S^o$, $^2D^o$, and $^2P^o$ final states with HeI, II radiation. The atomic oxygen is produced in a microwave discharge and the ejected photoelectrons are observed with a rotatable hemispherical electrostatic analyzer. In addition, photoionization branching ratios are determined for HeI, II. Comparisons will be made with theory and with a previous measurement of 584 Å branching ratio.[4]

References

1. A. F. Starace, S. T. Manson, and D. J. Kennedy, Phys. Rev. A 9, 2453 (1974).
2. S. T. Manson, D. J. Kennedy, A. F. Starace, and D. Dill, Planet. Space Sci. 22, 1335 (1974).
3. E. R. Smith, Phys. Rev. A 13, 1058 (1976).
4. J. A. R. Samson and V. E. Petrosky, Phys. Rev. A 9, 2449 (1974).

---

*Abstract of a talk presented at the 1976 Annual Meeting of the DEAP, American Physical Society, December 6-8, Lincoln, Nebraska.

ANGULAR DISTRIBUTION OF Xe 5s → εp PHOTOELECTRONS. DIRECT EVIDENCE FOR ANISOTROPIC FINAL-STATE INTERACTIONS*

J. L. Dehmer and Dan Dill†

Photoionization of the Xe 5s subshell by electric dipole interaction can be written schematically as

$$Xe(5s^2 5p^6\ {}^1S_0, \pi_0 = +1) + \gamma(j_\gamma = 1, \pi_\gamma = -1) \rightarrow Xe^+(5s5p^6\ {}^2S_{\frac{1}{2}}, \pi_c = +1) + e^-[\ell s, \pi_e = (-1)^\ell] \ . \quad (1)$$

The orbital momentum ℓ of the photoelectron is restricted by the angular-momentum balance

$$\vec{J} = \vec{J}_0 + \vec{j}_\gamma = \vec{J}_c + \vec{s} + \vec{\ell} \quad (2)$$

to the range $\ell \leq 2$. Further, the parity of the photoelectron is $\pi_e = -1$ (odd) owing to the parity balance

$$\pi = \pi_\gamma \pi_0 = -\pi_0 = \pi_e \pi_c = (-1)^\ell \pi_c \ . \quad (3)$$

Hence, the orbital momentum is fixed at the single value $\ell = 1$.

A simple analysis of the differential cross section for reaction 1 predicts a pure $\cos^2\theta$ angular distribution, relative to the electric vector of the light. The distribution is just that of the continuum p wave with $\ell_z = 0$, i.e.,

$$\frac{d\sigma}{d\Omega} = \frac{\sigma}{4\pi}[1 + \beta P_2(\cos\theta)] \propto Y_{10}{}^2 \propto \cos^2\theta \ , \quad (4)$$

corresponding to an asymmetry parameter $\beta = 2$.

In sharp contrast, our measurement of the angular distribution gives the asymmetry parameter $\beta = 1.4 \pm 0.1$ at 304 Å. The discrepancy is due to

---

*Summary of a paper published in Phys. Rev. Letters 37, 1049 (1976).

†Alfred P. Sloan Research Fellow and consultant, Radiological and Environmental Research Division. Permanent address: Department of Chemistry, Boston University, Boston, Massachusetts 02215.

the assumption implicit in the simple analysis that the photoelectron experiences no anisotropic interactions during its escape from the rest of the atom. Such interactions result in angular-momentum exchanges which can change the orientation of the photoelectron orbital momentum and thereby its angular distribution.[1] In this spectral range of process 1 the interaction likely represents the combined effect of coupling with the $Xe^{+}(5s^{2}5p^{5}\ ^{2}P^{0})$ + εd (and εs) electron continuum (by Coulomb and spin-orbit interactions) and of coupling of the continuum p electron with its own spin. We summarize the results of our analysis by noting that spin-orbit coupling is essential in this case, but that spin-independent interactions, such as interchannel coupling, are expected to play a major role. We leave the question of the relative importance of these or other effects (such as initial-state correlations) to be resolved by detailed calculations now possible in other laboratories.

Reference

1. Dan Dill, Phys. Rev. A 7, 1976 (1973).

WAVELENGTH DEPENDENCE OF THE BRANCHING RATIO FOR THE 5p SUBSHELL OF Xe

J. L. Dehmer

Viewed separately, recent measurements by Samson et al. and by Wuilleumier et al. lead to different wavelength dependences of the $^2P_{\frac{3}{2}}:^2P_{\frac{1}{2}}$ branching ratio of the 5p subshell of Xe. The interpretation may be clarified somewhat by combining a new measurement with both earlier sets of data.

Recently, Samson et al.[1] combined some new data with reanalyzed earlier data in order to describe the wavelength dependence of the branching ratio (BR) for the 5p subshell of Xe (BR-Xe 5p) from the $^2P_{\frac{1}{2}}$ threshold to a photon energy of 40.8 eV (304 Å). This work strongly suggests the BR-Xe 5p has a constant value of 1.54. Data in the soft x-ray energy range, 60 eV to 110 eV, have now been obtained by Wuilleumier et al.,[2] using the ACO storage ring in Orsay, together with a grazing incidence monochromator. Their data imply the BR-Xe 5p has a constant value of 2.0 in this energy range.

Clearly, some data in the photon energy, (40 eV − 60 eV) between these two sets of measurements are desirable to resolve this apparent inconsistency. Using undispersed radiation from a hollow-cathode lamp, I was able to obtain a value of BR-Xe 5p = 1.75 ± 0.1 at 48.4 eV (256 Å). A hemispherical spectrometer set at the magic angle 54°44' was used for the measurement. The entrance lens was tuned to optimize the intensity and resolution of the $^2P_{\frac{3}{2}}$ and $^2P_{\frac{1}{2}}$ peaks produced by 256 Å (HeII) radiation, and it was assumed the transmission of the spectrometer was equal for the corresponding 36.3 eV and 35.0 eV electrons.

Uniting the three independent measurements, together with the flexibility afforded by the respective stated errors, the following picture emerges for the wavelength dependence of the BR-Xe 5p: Near the $^2P_{\frac{1}{2}}$ threshold, the BR-Xe 5p has a nearly constant value of 1.54. Preferentially using Samson's most recent measurements, taken with a cylindrical mirror analyzer, it is easy to argue that the BR-Xe 5p begins a slow rise at $\hbar\omega \sim 25$ eV. The rise

takes the curve smoothly through Samson's 304 Å value (~ 1.63) and the present 256 Å point (1.75 ± 0.1) to mesh with the high-energy points which lie very near the statistical value of 2.0. Certainly more extensive study of the energy dependence of this quantity is necessary to confirm the tentative interpretation presented here on the basis of the new intermediate energy measurement.

References

1. J. A. R. Samson, J. L. Gardner, and A. F. Starace, Phys. Rev. A 12, 1459 (1975).
2. F. Wuilleumier, M. Y. Adam, V. Schmidt, N. Sandner, and W. Mehlhorn, Book of Extended Abstracts, International Conf. on the Physics of X-Ray Spectra, August 30—September 2, 1976, National Bureau of Standards, Gaithersburg, Maryland, p. 329; full paper to be published.

PHOTOION ANGULAR DISTRIBUTION FROM DISSOCIATIVE PHOTOIONIZATION OF H_2.[†]

J. L. Dehmer

Photoionization of H_2 by 304 Å radiation can produce the $2p\sigma_u$, $2p\pi_u$, and $2s\sigma_g$ repulsive states of H_2^+. The angular distributions of energetic (>2 eV) protons from these states have been measured relative to the incident unpolarized light beam with a rotating hemispherical electrostatic analyzer. Axial recoil conditions apply in this situation, so that the photofragment angular distribution[1] should exhibit asymmetry parameters $\beta = 2$ for Σ-Σ electronic transitions and $\beta = 1$ for Σ-Π transitions. Unlike photodissociation processes forming neutral products, the present process leads to the ejection of photoelectrons with alternative symmetries. Consequently, measurement of the photoion angular distribution in dissociative photoionization yields the branching ratio between the alternative channels available to the photoelectron, which cannot be deduced by observation of the photoelectron itself.

Reference

1. R. N. Zare, Mol. Photochem. 4, 1 (1972).

[†]Abstract of a paper contributed to the Annual Meeting of the Division of Electron and Atomic Physics, American Physical Society, December 6–8, 1976, Lincoln, Nebraska.

HIGH-RESOLUTION PHOTOIONIZATION STUDY OF ION-PAIR FORMATION IN H_2, HD, AND D_2. *†

W. A. Chupka,‡** P. M. Dehmer, and W. T. Jivery‡††

A new photoionization mass spectrometer which is significantly superior to previous instruments in both wavelength resolution and ion intensity has been used in the study of photon-induced ion-pair formation at 78°K in para-H_2, ordinary H_2 and D_2 (the ortho-para equilibrium mixtures), and HD in the wavelength region from 718 Å to 700 Å at a wavelength resolution (FWHM) of 0.035 Å for para-H_2, 0.07 Å for ordinary H_2 and D_2, and 0.15 Å for HD. The threshold for formation of ion pairs from para-H_2 occurs at $715.753 \pm {}^{0.046}_{0.008}$ Å ($17.3223 \pm {}^{+0.0002}_{-0.0011}$ eV), and this value together with the accurately known values of the dissociation energy of H_2 and the ionization potential of atomic hydrogen yields a value of the electron affinity of the hydrogen atom of $0.7542 \pm {}^{0.0013}_{0.0004}$ eV, in excellent agreement with the theoretical value of 0.75421 eV calculated by Pekeris.[1] The observed thresholds for ion-pair formation in D_2 and HD are also in excellent agreement with the calculated positions. For para-H_2 the region within 0.5 Å of the threshold has a continuum-like appearance and contains window resonances which are interpreted as predissociating members of a Rydberg series converging to $H_2^+(v=9, N=2)$. The continuum results from closely-spaced predissociating Rydberg states converging to $H_2^+(v=9, N=0)$, which were not resolved in the present experiment. A number of other tentative Rydberg state assignments were made for para-H_2, based on the results of an analysis using multichannel quantum defect theory. No Rydberg state identifications were attempted for the other

---

* A full report is given in J. Chem. Phys. 63, 3929 (1975).

† The major part of the work was done in the Physics Division.

‡ Physics Divisision, Argonne National Laboratory.

** Present address: Department of Chemistry, Yale University, New Haven, Connecticut 06520.

†† Present address: 402 Lake Avenue, Ironwood, Michigan 49938.

systems because of the greatly increased complexity of their spectra. For HD, which can dissociate to either $H^+ + D^-$ or $H^- + D^+$, the H^-/D^- ratio is ~ 2 just above threshold and appears to decrease with decreasing wavelength; however, this is due, at least in part, to discrimination by the detection system against the more energetic H^- ions.

Reference

1. C. L. Pekeris, Phys. Rev. 126, 1470 (1962).

HIGH-RESOLUTION PHOTOIONIZATION STUDY OF RYDBERG SERIES IN H_2— SERIES CONVERGING TO $H_2^+(^2\Sigma_g^+, v=1-6)$*

P. M. Dehmer and W. A. Chupka†

Introduction

The photoabsorption spectrum from the ground rotational state of molecular hydrogen consists of two interacting Rydberg series converging to each vibrational level of the ion core. The lower members of the series correspond to $np\sigma\ ^1\Sigma_u^+$ and $np\pi\ ^1\Pi_u$ series of states, but as n increases there is a transition from Hund's case (b) to Hund's case (d) as a result of the effects of ℓ uncoupling, and the series converge, respectively to the $N=0$ and $N=2$ rotational levels of the ion core. During the course of the ℓ uncoupling the two series perturb each other strongly, resulting in large energy-level shifts and intensity variations. In addition to these interactions between the series converging to the same vibrational level of the ion ($\Delta v=0$ interactions), there may be further intense perturbations from low n Rydberg states converging to higher excited vibrational states of the ion ($\Delta v\neq 0$ interactions). During the last several years, the multichannel quantum defect theory (QDT) method for the analysis of spectral data has been applied to the problem of interpreting these interacting Rydberg series.[1]

In the present work, the two-channel quantum defect theory methods employed by Herzberg and Jungen[2] are used to identify members of autoionizing Rydberg series in para-H_2 ($^2\Sigma_g^+$, $v=4-6$), thus extending the analysis of Herzberg and Jungen. In addition, observed autoionization intensities are compared with intensities calculated from two-channel quantum defect theory, and observed linewidths are compared with those calculated using a perturbation approach.

---

*A full report is given in J. Chem. Phys. 65, 2243 (1976).

†Physics Division, Argonne National Laboratory. Present address: Department of Chemistry, Yale University, New Haven, Connecticut 06520.

Results and Discussion

Relative photoionization cross sections were measured for para-H_2 at 78 K and at a wavelength resolution of 0.016 Å in the wavelength region from 805 to 715 Å. The data are shown in Figure 1. The regions near the vibrational convergence limits are shown in more detail in Figure 2.

The QDT method of analysis uses the concept of a single channel to describe the discrete levels and the adjoining continuum of an unperturbed Rydberg series. The level positions are described by a quantum defect δ, and an ionization potential I, and the level intensities are described by an oscillator strength density df/dE. Configuration interaction is replaced by the concept of channel mixing. Two-channel mixing may then be used to describe the two interacting R(0) Rydberg series in para-H_2 or the interacting R(1) series in ortho-H_2. Higher order interactions may be included via a perturbation approach following Herzberg and Jungen or, alternatively, the two-channel QDT may be extended to include a larger number of vibration and rotation channels. In our work, the level positions, intensities, and widths were calculated in the manner described by Herzberg and Jungen, and the results are compared to the quantities we measured. Representative results for the series converging to the v=1 and v=4 vibrational levels of $H_2^+ \, ^2\Sigma_g^+$ are given in Table 1. The complete results are given in detail elsewhere.[3]

In general, we find that the agreement between calculated and observed quantities is excellent in regions of the spectrum where $\Delta v \neq 0$ interactions are weak or absent. However, as one goes to higher energy, the spacing between successive vibrational levels decreases owing to the anharmonicity of the H_2^+ potential curve. This results in increasingly significant overlap of Rydberg series converging to the higher vibrational levels, and as a consequence, the number of $\Delta v \neq 0$ interaction is greatly increased. Thus, the simple two-channel quantum defect theory becomes increasingly unable to reproduce the observed spectrum.

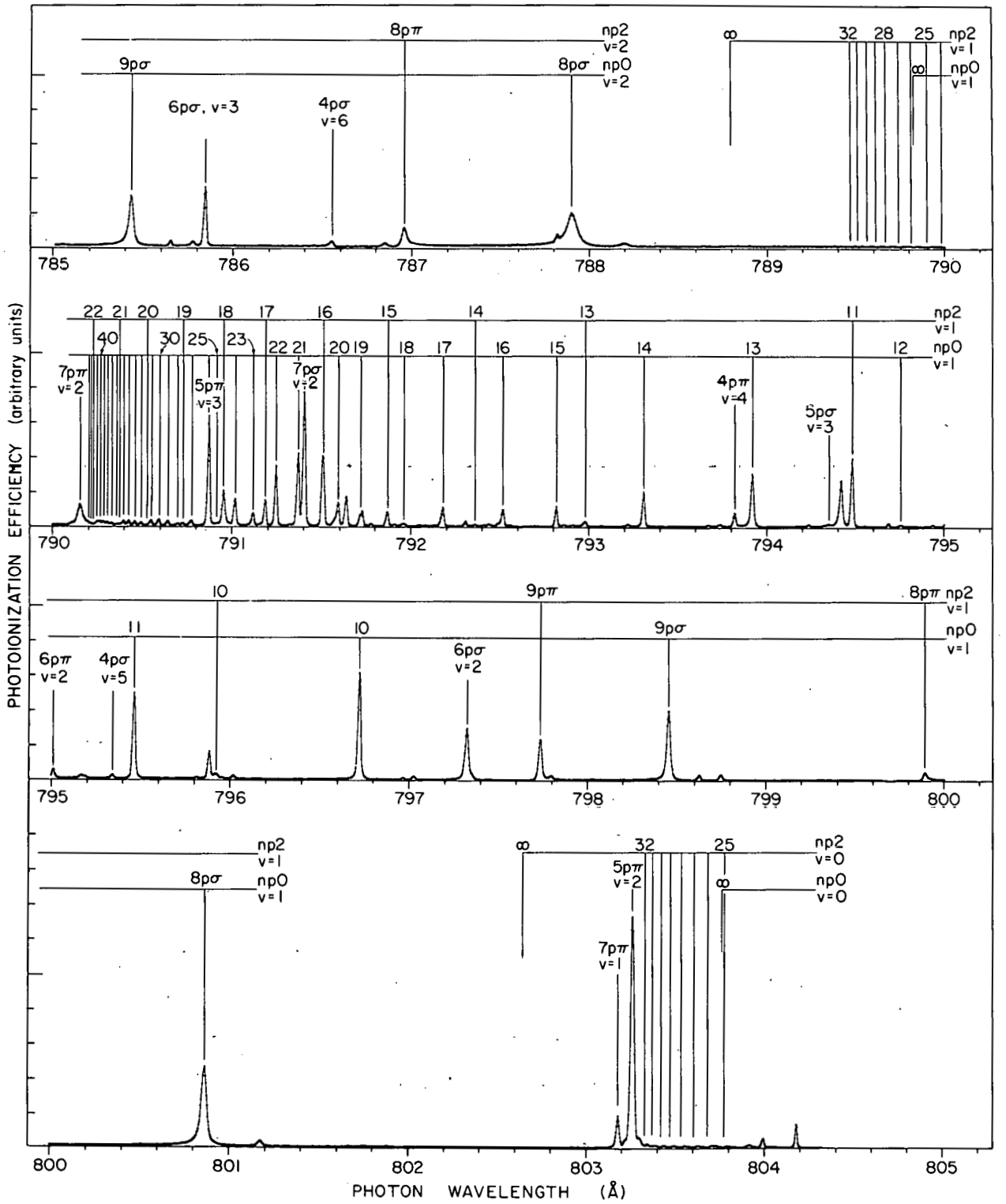

FIG. 1.--Relative photoionization cross section of para-H_2 at 78 K taken at a wavelength resolution of 0.016 Å, showing the R(0) npσ and npπ Rydberg series.

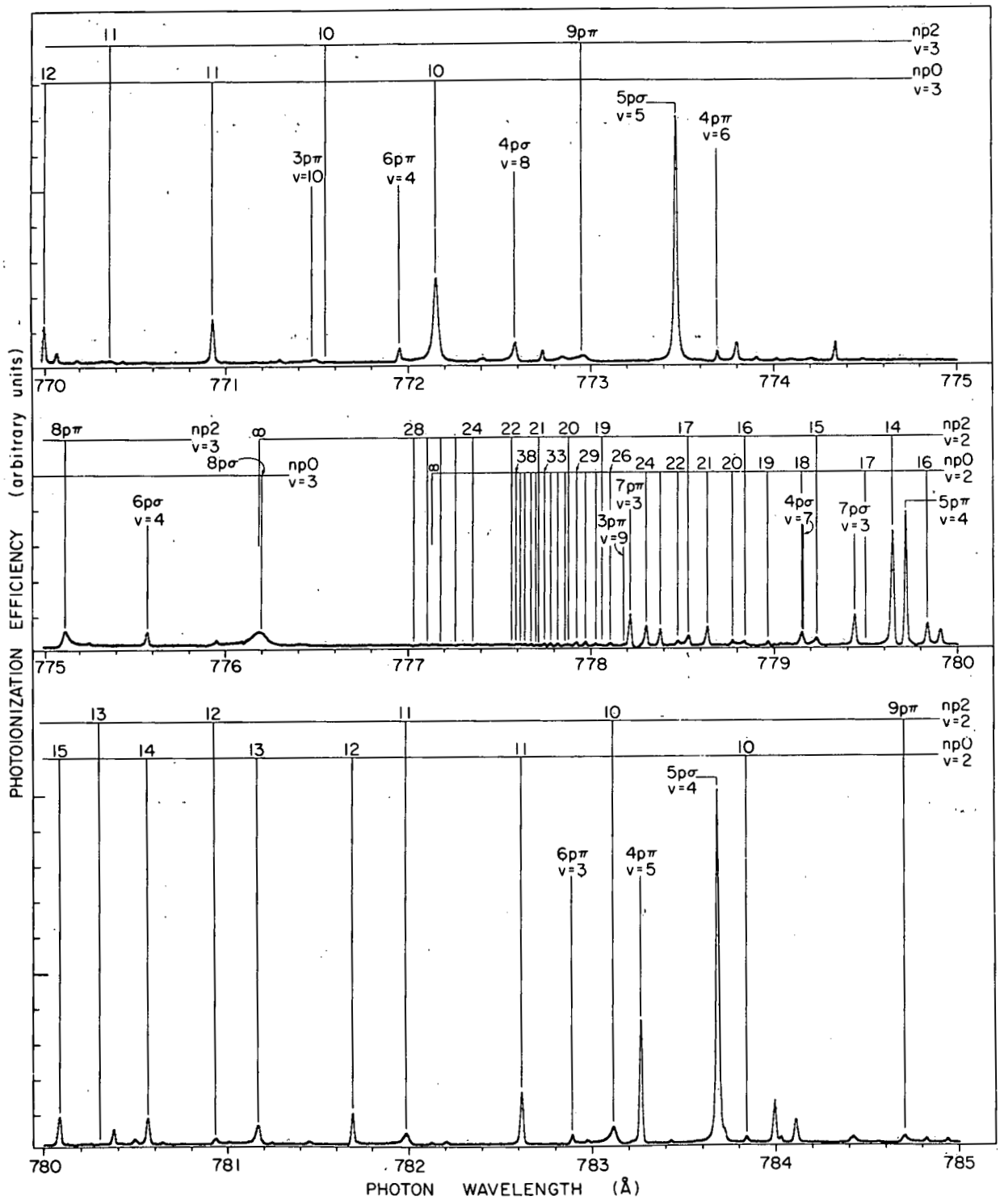
PHOTOIONIZATION EFFICIENCY (arbitrary units)
PHOTON WAVELENGTH (Å)
np2 v=3
npO v=3
9pπ
5pσ v=5
4pπ v=6
3pπ v=10
6pπ v=4
4pσ v=8
8pπ
8pσ
6pσ v=4
7pπ v=3
3pπ v=9
4pσ v=7
7pσ v=3
5pπ v=4
np2 v=2
npO v=2
5pσ v=4
6pπ v=3
4pπ v=5

FIG. 1 (contd.)

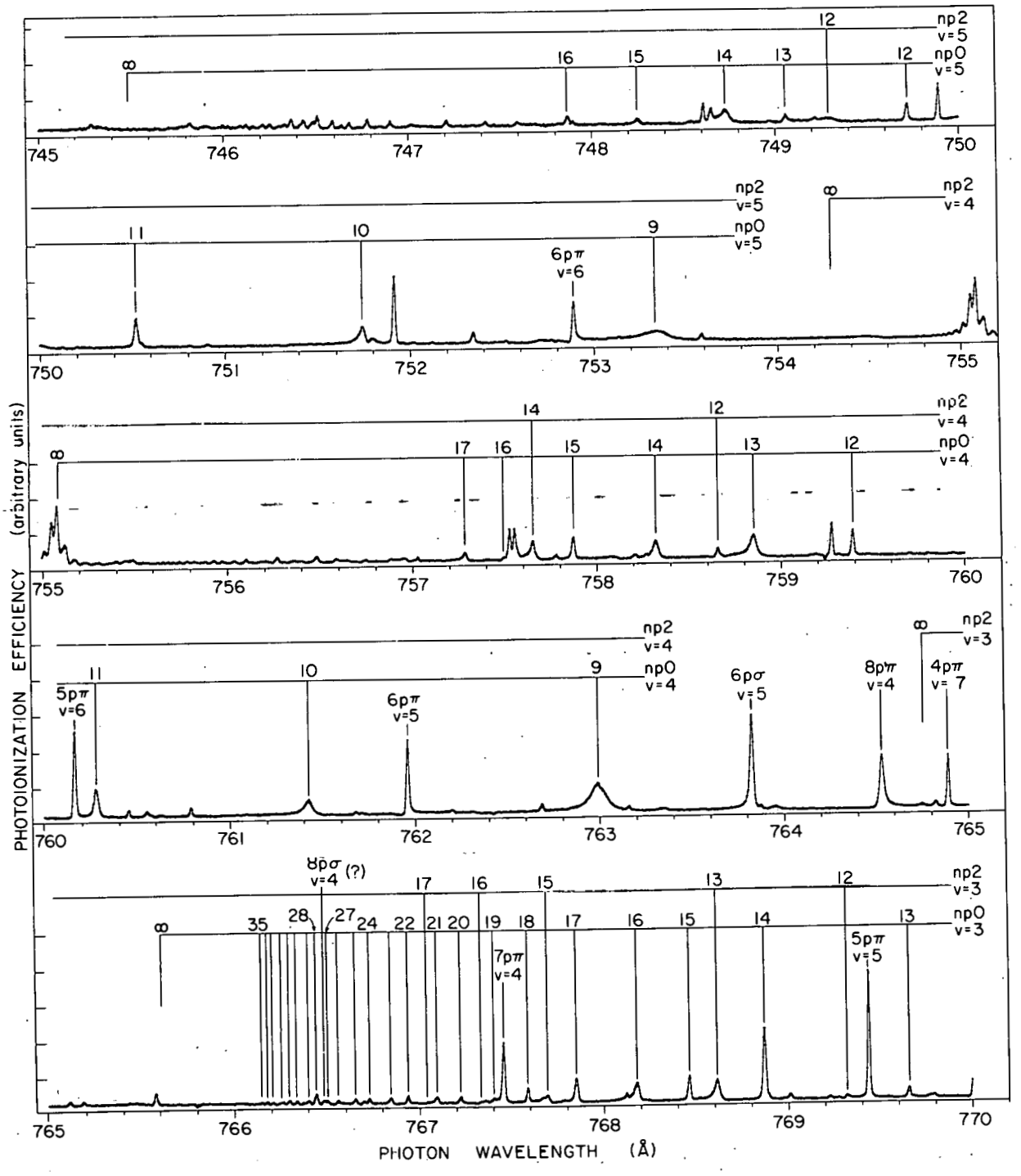
PHOTOIONIZATION EFFICIENCY (arbitrary units)
PHOTON WAVELENGTH (Å)
np2 v=5
npO v=5
np2 v=4
npO v=4
np2 v=3
npO v=3
6pπ v=6
6pπ v=5
5pπ v=6
6pσ v=5
8pπ v=4
4pπ v=7
8pσ v=4 (?)
7pπ v=4
5pπ v=5

FIG. 1. (contd.)

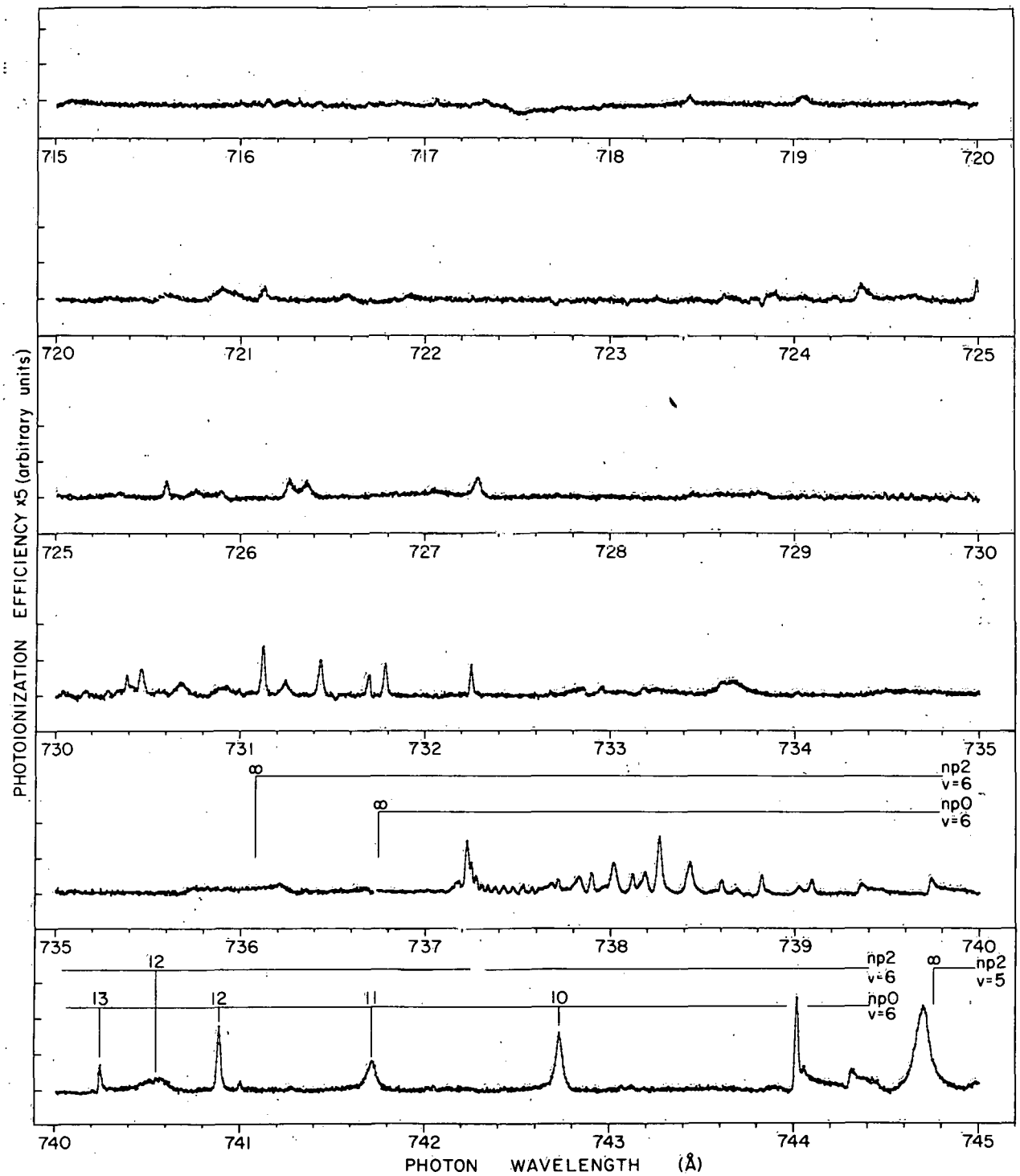
PHOTOIONIZATION EFFICIENCY x5 (arbitrary units)
715
716
717
718
719
720
721
722
723
724
725
726
727
728
729
730
731
732
733
734
735
736
737
738
739
740
741
742
743
744
745
∞
np2
v=6
npO
v=6
12
13
11
10
np2
v=5
PHOTON WAVELENGTH (Å)

FIG. 1. (contd.)

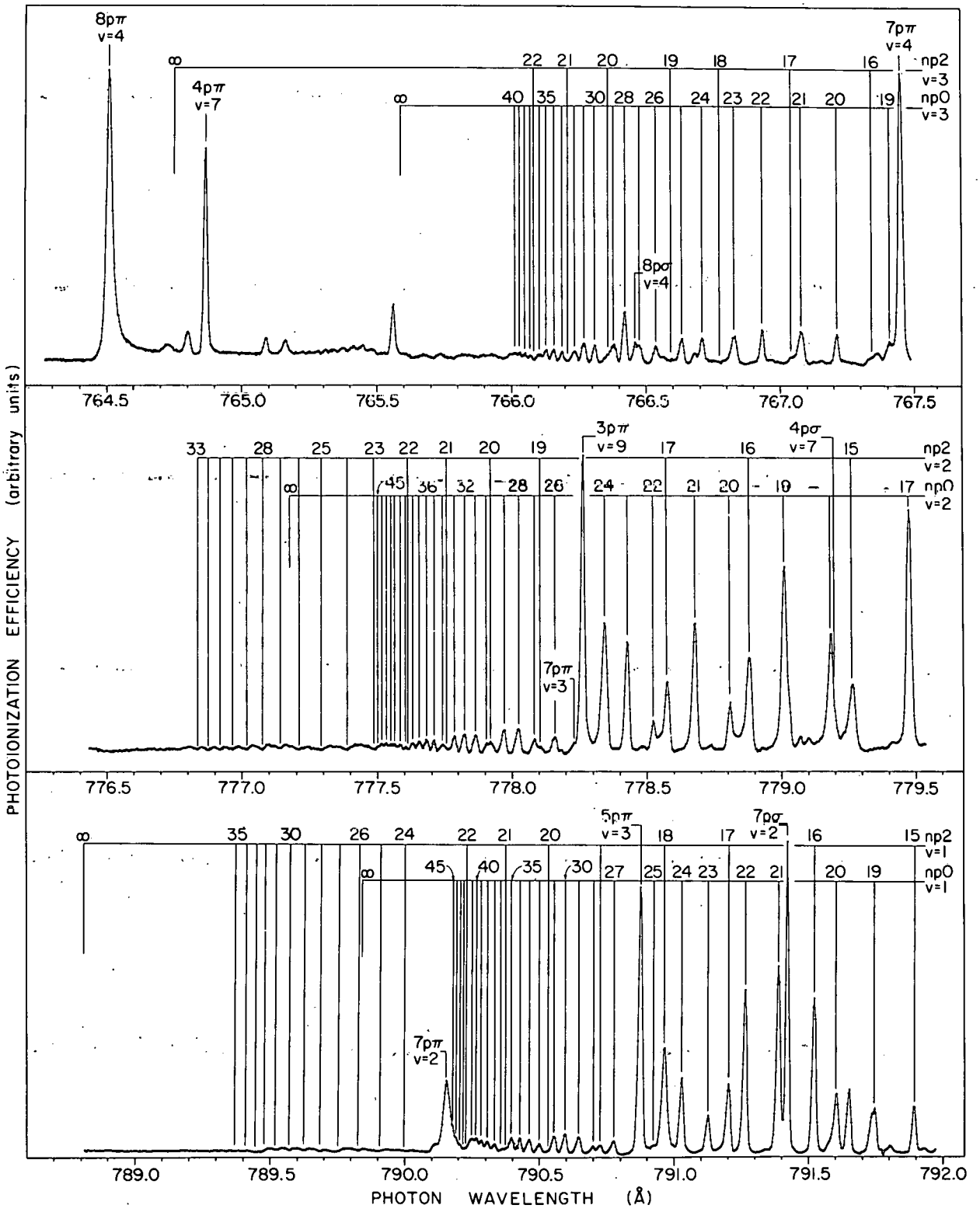

FIG. 2.--Relative photoionization cross section of para-H_2 in the regions of the $H_2^+(^2\Sigma_g^+, v=1-6)$ convergence limits at 78 K taken at a wavelength resolution of 0.016 Å.

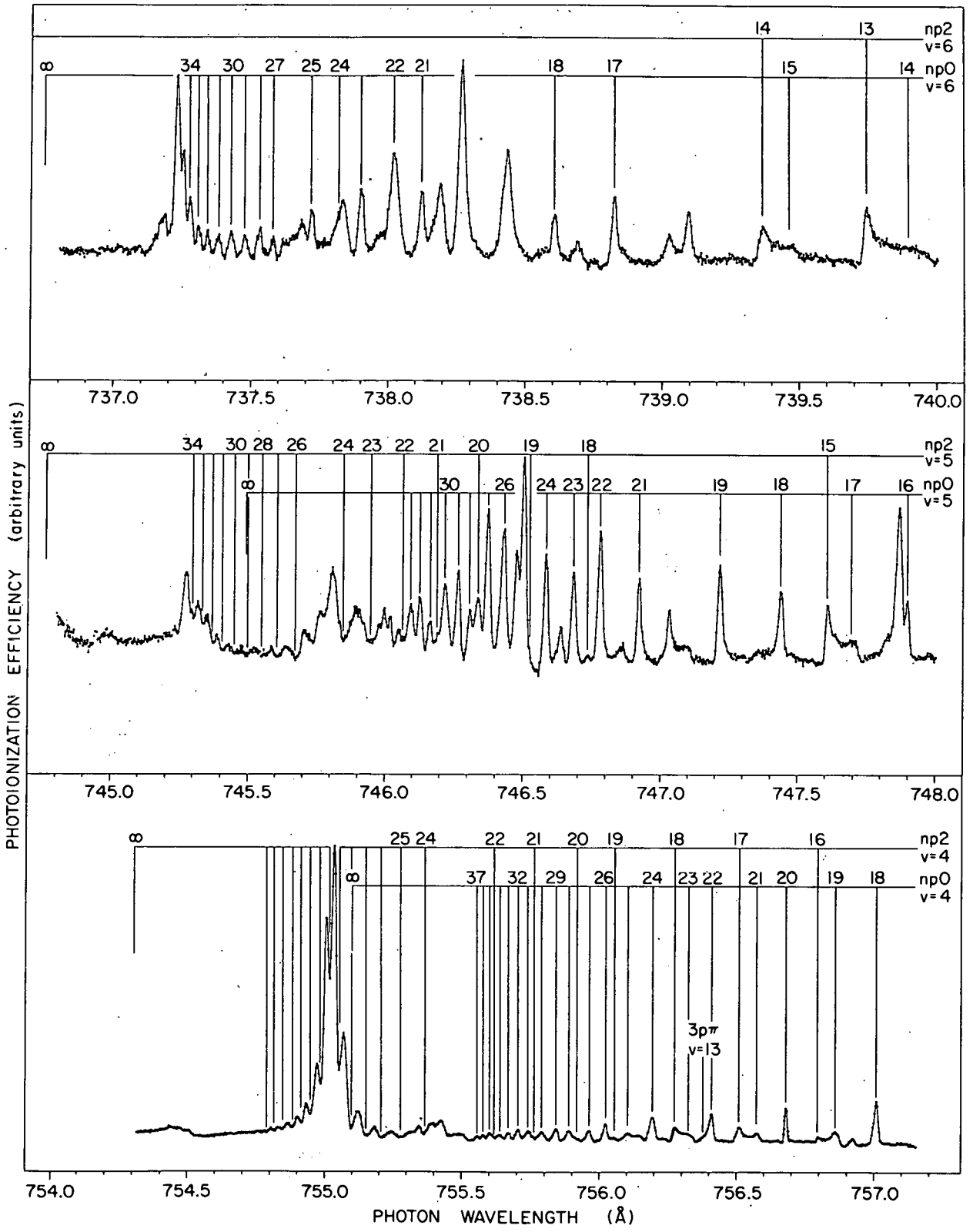
PHOTOIONIZATION EFFICIENCY (arbitrary units)
∞ 34 30 27 25 24 22 21 18 17 14 13 np2 v=6
15 14 npO v=6
737.0 737.5 738.0 738.5 739.0 739.5 740.0
∞ 34 30 28 26 24 23 22 21 20 19 18 15 np2 v=5
∞ 30 26 24 23 22 21 19 18 17 16 npO v=5
745.0 745.5 746.0 746.5 747.0 747.5 748.0
∞ 25 24 22 21 20 19 18 17 16 np2 v=4
∞ 37 32 29 26 24 23 22 21 20 19 18 npO v=4
3pπ v=13
754.0 754.5 755.0 755.5 756.0 756.5 757.0
PHOTON WAVELENGTH (Å)

FIG. 2. (contd.)

TABLE 1. Calculated and Observed Line Positions, Intensities, and Widths for R(0) Rydberg States in Para-H_2

Series converging to $H_2^+(^2\Sigma_g^+, v=1)$

	CALCULATED				OBSERVED		
State	n_0^*	λ (Å)	Intensity[a]	Γ (cm^{-1})	λ (Å)	Intensity[b,c]	Γ (cm^{-1})[c]
7P2	7.214	803.213			803.166		
8P0	7.936	800.856	89.3	3.7	800.855	100.0	5.1
8P2	8.306	799.882	4.2	2.7	799.895	5.7	2.8
9P0	8.972	798.432	66.8	1.7	798.448	55.8	2.4
9P2	9.443	797.587	0.0	2.9	797.722	27.5	2.3
10P0	10.008	796.730	47.4	0.6	796.724	60.9	0.9
10P2	10.625	795.947	4.4	2.7	795.934	3.8	
11P0	11.055	795.478	30.0	0.1	795.479	47.6	1.3
12P0	11.817	794.768	15.6	1.7	794.766	1.1	
11P2	12.152	794.499	10.9	0.2	794.498	32.7	
13P0	12.943	793.944	22.0	0.8	793.942	32.3	
12P2	13.388	793.674	0.1	1.0			
14P0	14.013	793.338	17.6	0.2	793.338	16.7	
13P2	14.730	793.004	4.7	1.3	793.008	3.2	
15P0	15.113	792.845	8.4	0.0	792.845	8.5	
16P0	15.945	792.538	12.2	0.4	792.539	8.8	
14P2	16.450	792.374	0.0	0.8	792.384	1.3	
17P0	17.038	792.202	9.3	0.0	792.202	10.0	
18P0	17.876	791.985	7.1	0.5	791.991	2.1	
15P2	18.286	791.889	0.8	0.4	791.897	9.9	
19P0	19.015	791.734	7.2	0.1	791.737	14.4	
20P0	19.843	791.579	4.6	0.3	791.605	17.0	
16P2	20.256	791.509	0.9	0.2	791.523	33.1	
21P0	21.018	791.389	5.4	0.0	791.385	39.8	
22P0	21.883	791.269	4.2	0.2	791.259	34.2	
17P2	22.360	791.208	0.1	0.3	791.196	17.1	
23P0	23.048	791.127	3.8	0.0	791.127	8.3	
24P0	23.951	791.032	3.9	0.1	791.030	16.7	
18P2	24.653	790.965	0.8	0.5	790.960	31.5	
25P0	25.147	790.921	1.7	0.0	790.920	0.6	

Series converging to $H_2^+(^2\Sigma_g^+, v=4)$

	CALCULATED				OBSERVED		
State	n_0^*	λ (Å)	Intensity	Γ (cm^{-1})	λ (Å)	Intensity	Γ (cm^{-1})
4P0	3.719	803.177			804.151		
4P2	4.115	793.924			793.838		
5P0	4.741	783.978			783.703		
5P2	5.129	779.630			779.728		
6P0	5.774	774.328			775.593		
6P2	6.153	771.976			771.941		
7P0	6.816	768.793			768.570		
7P2	7.190	767.383			767.451		
8P0	7.867	765.328	76.2	20.8	766.480		
8P2	8.246	764.397	12.2	7.7	764.510	1.7	
9P0	8.921	763.026	61.5	10.7	762.990	98.1	16.1
9P2	9.332	762.335	1.4	9.6			
10P0	9.975	761.424	46.7	4.5	761.424	23.3	8.4
10P2	10.456	760.849	0.6	10.3			
11P0	11.029	760.262	32.2	1.1	760.275	25.4	4.1
11P2	11.618	759.747	6.0	9.7			
12P0	12.096	759.384	18.4	0.0	759.389	13.8	0.0
13P0	12.793	758.926	14.2	5.6	758.853	35.0	6.2
12P2	13.205	758.689	5.5	1.3	758.656	5.5	1.6
14P0	13.934	758.320	17.5	2.5	758.319	20.7	4.8
13P2	14.409	758.109	0.0	4.1			
15P0	15.035	757.862	13.0	0.4	757.870	15.4	1.7
14P2	15.696	757.632	4.8	4.7	757.651	19.3	2.9
16P0	16.158	757.488	5.1	0.2			
17P0	16.926	757.274	10.0	1.5	757.283	5.5	
15P2	17.433	757.148	0.1	2.9			
18P0	18.061	757.007	7.0	0.1	757.009		
19P0	18.812	756.856	5.5	1.7	756.857		
16P2	19.276	756.772	0.7	1.2	756.789		
20P0	20.017	756.649	6.0	0.2	756.662		

[a] Intensities are calculated only for states which may autoionize with $\Delta v = -1$ and are normalized separately (very roughly) to the observed intensities for series converging to different vibrational levels of the ion.

[b] All observed intensities are normalized to 100.0 on the 8pσ v=1 state.

[c] Observed linewidths and intensities are given only for those states which may autoionize with $\Delta v = -1$.

References

1. U. Fano, J. Opt. Soc. Am. 65, 979 (1975).
2. G. Herzberg and Ch. Jungen, J. Mol. Spectrosc. 41, 425 (1972).
3. P. M. Dehmer and W. A. Chupka, J. Chem. Phys. 65, 2243 (1976).

DECAY OF RYDBERG STATES OF H_2 ABOVE THE IONIZATION THRESHOLD — COMPETITION AMONG AUTOIONIZATION, PREDISSOCIATION, AND FLUORESCENCE*

P. M. Dehmer and W. A. Chupka†

Unimolecular decay processes that can compete significantly with autoionization of Rydberg states of H_2 are predissociation and emission of light. These processes result in values of ionization efficiency (defined here as the ratio of ionization to absorption) less than unity. High resolution (0.016 Å, FWHM) photoabsorption and photoionization data on para-H_2 and on the ortho-para equilibrium mixture taken at 78 K have been analyzed in order to extract the ionization efficiencies of those states of low n which are expected to decay significantly via channels other than autoionization. A 2 Å region of the photoabsorption and photoionization spectra of ordinary H_2 is shown in Figure 1 as an example of the data. Data were taken in the wavelength region from 805 to 750 Å. The values of ionization efficiency are given in Table 1.

It is possible that fluorescence can account for a significant fraction of the decay of certain states for which both autoionization and predissociation are very slow. Autoionization is weakest for those states which have pure π character, and can autoionize only by a large change in vibrational quantum number of the ion core. Such states are the $^1\Pi_u^-$ states [the upper states of the Q(J) transitions] with minimum value of n, and hence maximum values of v for a given total energy. These states are only weakly predissociated as well, since the strong predissociation of $np\pi\ ^1\Pi_u$ states is due to interaction with $np\sigma\ ^1\Sigma_u^+$ states (with the same value of n), which can only predissociate the $^1\Pi_u^+$ components (P and R branches). The data on the Q(1) lines are particularly regular and amenable to straightforward interpretation for the most part. The

*A full report is given in J. Chem. Phys. 65, 2243 (1976).

†Physics Division, Argonne National Laboratory. Present address: Department of Chemistry, Yale University, New Haven, Connecticut 06520.

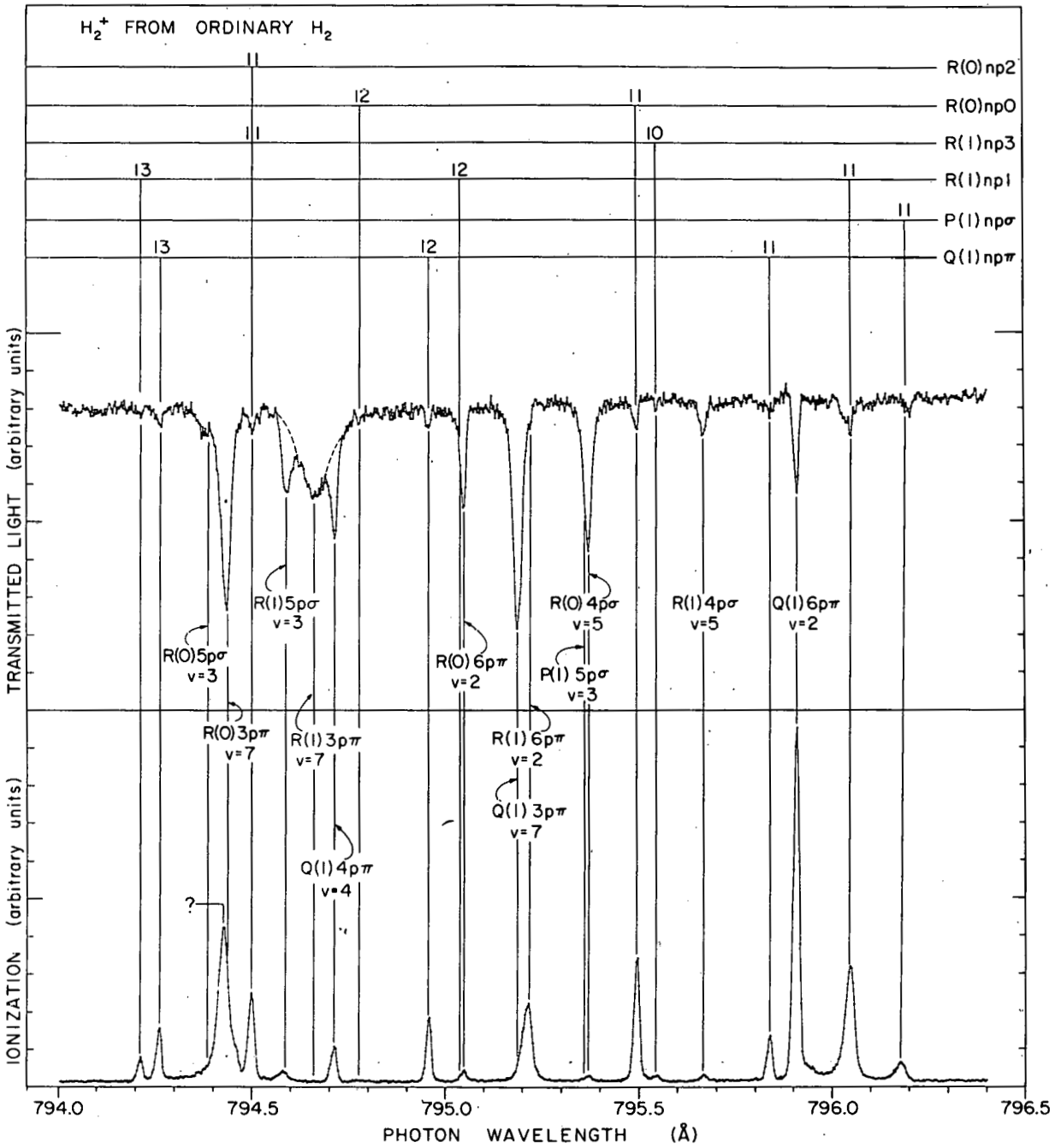

FIG. 1.--Spectra of transmitted light and ionization for ordinary H_2 (the ortho-para equilibrium mixture) at 78 K taken at a wavelength resolution of 0.016 Å in the region from 794 to 796.5 Å showing all of the assigned states in this region.

TABLE 1. Autoionization efficiency for Rydberg states of H_2.

	State		% Autoionization[a]		
		$-\Delta v$	R(0)	R(1)	Q(1)
$^1\Pi_u$ States	$3p\pi$, v= 7	7	0	0	0
	8	7	0	0	0
	9	8	0	0	0
	10	8	0	0	0
	11	8-9[b]	0	0	0
	12	9	0	0	0
	$4p\pi$, v= 4	4	12	(9)[c]	8
	5	4	85	18	(6)[c]
	6	4	3	8	80
	7	4	31	22	93
	8	5	c	c	80[d]
	$5p\pi$, v= 2	2	100	96	94
	3	3	67	(55)[c]	(40)[c]
	4	3	79	90	90
	5	3	84	67	109
	$6p\pi$, v= 2	2	2	(81)[c]	81
	3	2	>90	>90	100
	4	2	100	100	95
	5	2	86	c	91

	State	% Autoionization			
		Δv	R(0)	R(1)	P(1)
$^1\Sigma_u^+$ States	$4p\sigma$, v= 5	5	<2	5	c
	6	5	c	c	0
	7	6	0	(3)[c]	c
	$5p\sigma$, v= 3	3	c	4	c
	4	3	77	75	(100)[c]
	5	3	88	62	81
	$6p\sigma$, v= 2	2	100	98	c
	3	2	(35)[c]	c	c
	$7p\sigma$, v= 2	2	71	(49)[c]	(61)[c]
	3	2	c	c	c
	4	2	c	(77)[c]	c

[a] States which may autoionize with $\Delta v = 1$ were assumed to be 100% autoionized.

[b] Only the R(0) and R(1) branches of the $3p\pi$, $v=7$ $^1\Pi_u$ state may autoionize with $\Delta v = 8$. The Q(1) branch autoionizes with $\Delta v = -9$.

[c] The state is either not observed or is badly overlapped with another state. When the percept autoionization is given for such a state, it may have a substantial error of as much as 20%.

[d] The Q(1) $4p\pi$, $v=8$ state is calculated to appear at 757.64 Å using δ_π ($v=8$) = −0.1065 and $E_\infty = 138\,493.9$ cm^{-1}. An intense peak in both absorption and ionization is observed at this wavelength and is assumed to be Q(1) $4p\pi$, $v=8$.

general trend of increasing autoionization efficiency with decreasing Δv is strikingly obvious, and even the detailed behavior is in accord with expectations.

The analysis of the decay of the $^1\Sigma_u^+$ and $^1\Pi_u^+$ states (the upper levels of the P and R transitions) presents greater difficulties than that of the $^1\Pi_u^-$ states (upper levels of the Q transitions). The dominant competing decay modes are autoionization and predissociation. Both of these decay rates are much more sensitive to perturbations than are the fluorescence rates of the Π^- states, and observed erratic behavior of autoionization efficiency as seen in Table 1 is not surprising. However, the gross overall behavior of autoionizing efficiency is as expected, namely for low values of n and consequently large values of Δv for autoionization, predissociation predominates, while for larger n and hence decreasing Δv for autoionization, the autoionization predominates.

A full quantitative treatment of the data of Table 1 will require the extension of the present quantum defect theory methods to include the effects of predissociation. This is now being undertaken by Dill and Jungen.[1]

Reference

1. D. Dill (Boston University, Boston, Massachusetts) and Ch. Jungen (Universite de Paris-Sud, Orsay), private communication.

MECHANISM FOR VIBRATIONAL AUTOIONIZATION IN H_2*

P. M. Dehmer and W. A. Chupka†

Introduction

Rydberg states of H_2 that have energies within a few volts of the ionization threshold autoionize through vibration-electron interaction, that is, vibrational energy of the ion core is converted into kinetic energy of the outgoing electron. Berry[1] showed that the autoionization rate is largest for $\Delta v = 1$ transitions and decreases rapidly for $\Delta v = 2$ and $\Delta v = 3$ transitions, with the higher order processes accounting for only about 6 or 7 percent of the total autoionization rate. On the basis of more detailed calculations, Shaw and Berry[2] confirmed the general nature of this rule, but predicted that in a few cases for which autoionization via $\Delta v = 1$ is energetically allowed, autoionization actually proceeds substantially (or even predominantly) via $\Delta v = 2$.

The present experiment yields new information on the final vibrational state distributions for autoionizing Rydberg states in H_2 in the region between the ionization threshold and 735 Å. In this energy region ions are left in vibrational states from $v = 0$ to $v = 5$. Our work uses the fact that the reactions

$$H_2^+ + He \longrightarrow HeH^+ + H \qquad (1)$$

$$H_2^+ + Ne \longrightarrow NeH^+ + H \qquad (2)$$

have cross sections that are very sensitive to the vibrational state of H_2^*. Both reaction cross sections increase rapidly as a function of v for $v \leq 5$.[3] Consequently, if two Rydberg states autoionize leaving very different final vibrational state distributions of H_2^+, this will be reflected in the reaction rates with He or Ne. Thus, this experiment tests the predictions of Shaw and

---

*Summary of a paper presented at the VIII Meeting of the Division of Electron and Atomic Physics, Lincoln, Nebraska, December 6–8, 1976. To be published in J. Chem. Phys.

†Physics Division, Argonne National Laboratory. Present address: Department of Chemistry, Yale University, New Haven, Connecticut 06520.

Berry concerning preferential autoionization via v=2 in the presence of an available v=1 autoionization channel. It also determines if all the Rydberg states between the v and v+1 convergence limits in H_2^+ autoionize to give the same final vibrational state distribution, or if autoionization via v > 1 gives a broader distribution, as might be expected if the propensity rule breaks down for these larger changes in Δv.

Result and Discussion

The relative photoionization cross sections for para-H_2^+, HeH^+, and NeH^+ were determined at a wavelength resolution of 0.08 Å (FWHM) in the region from 805 to 725 Å, and the results are shown in Figure 1. The optically allowed Rydberg series converging to the various vibrational and rotational levels of H_2^+ are indicated on the figure. The high resolution photoionization mass spectrometer used to obtain the data has been described previously.[4]

The relative cross sections for reactions 1 and 2 were determined for the autoionizing levels shown in Figure 1 by measuring the relative heights above the background continua for the rare-gas hydride ion and the H_2^+ ion peaks. The ratio of the heights of corresponding peaks is then proportional to the cross section for the reaction of H_2^+ in the final vibrational state distribution produced by the autoionization process. The results are shown in Figure 2.

Two general results are apparent from the data shown in Figure 2. First, the final vibrational state distribution remains approximately the same for all the autoionizing Rydberg states between any two H_2^+ vibrational convergence limits v and v+1, as is evidenced by the near constancy of the H_2^+ reaction cross sections in these regions. Second, between any two vibrational convergence limits, autoionization via Δv=1 and Δv> 1 gives nearly the same final vibrational state distribution, with autoionization via Δv> 1 yielding a slightly larger fraction of lower vibrational levels.

Shaw and Berry predicted that the ratio of the autoionization rates k(Δv=2)/k(Δv=1) would be 2.8 for the 9pσ, v=5 state and is 2.1 for the 10pσ, v=5 state, as compared with the more typical value for this ratio of approximately 0.05. The data of Figure 2 show that this is certainly not the

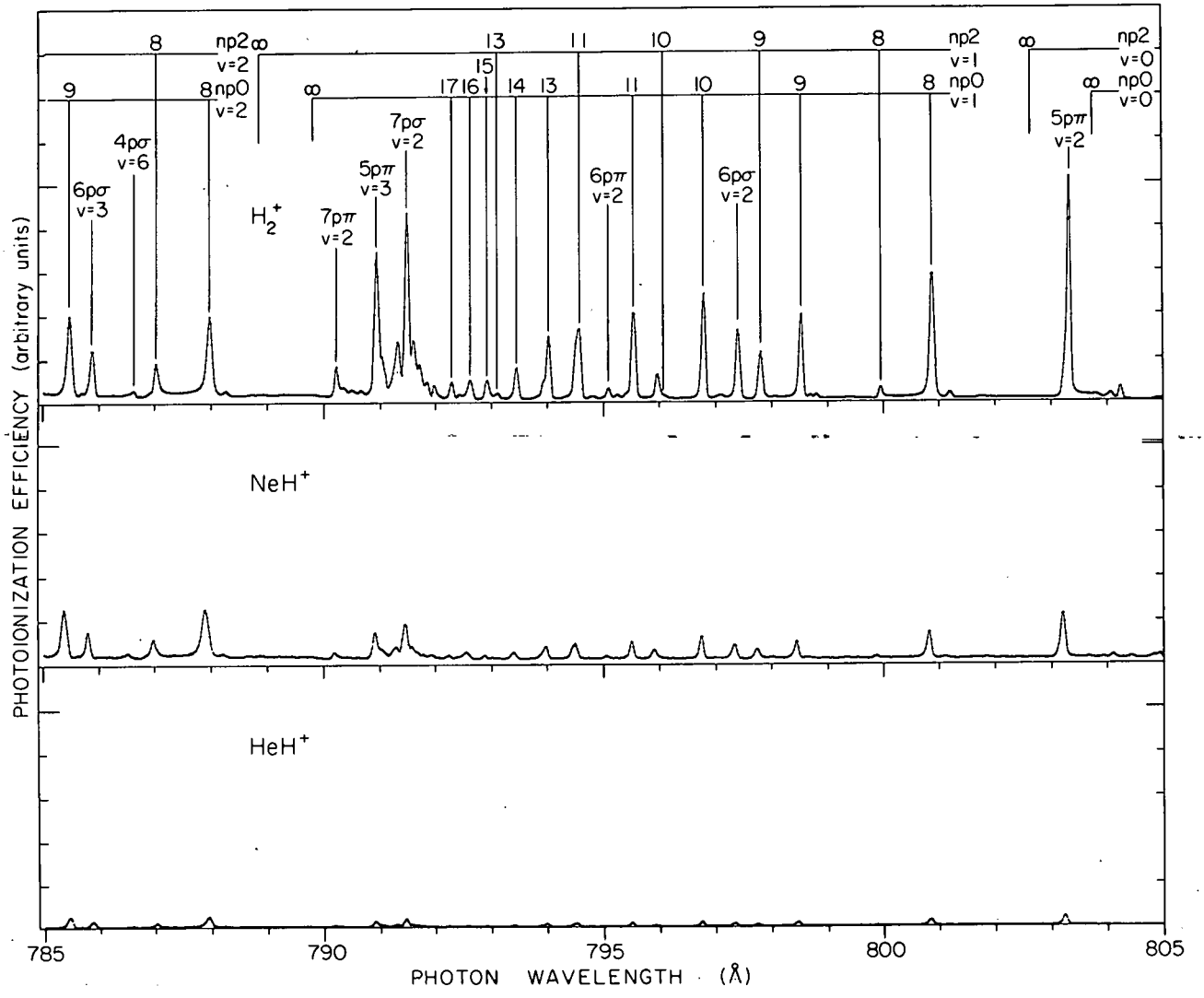

FIG. 1(a).--Relative photoionization cross section for para-H_2 (top) and relative reaction cross sections for formation of NeH^+ (middle) and HeH^+ (bottom) from the reaction of para-H_2^+ with Ne and He. All data were taken at 78 K and at a photon bandwidth of 0.08 Å.

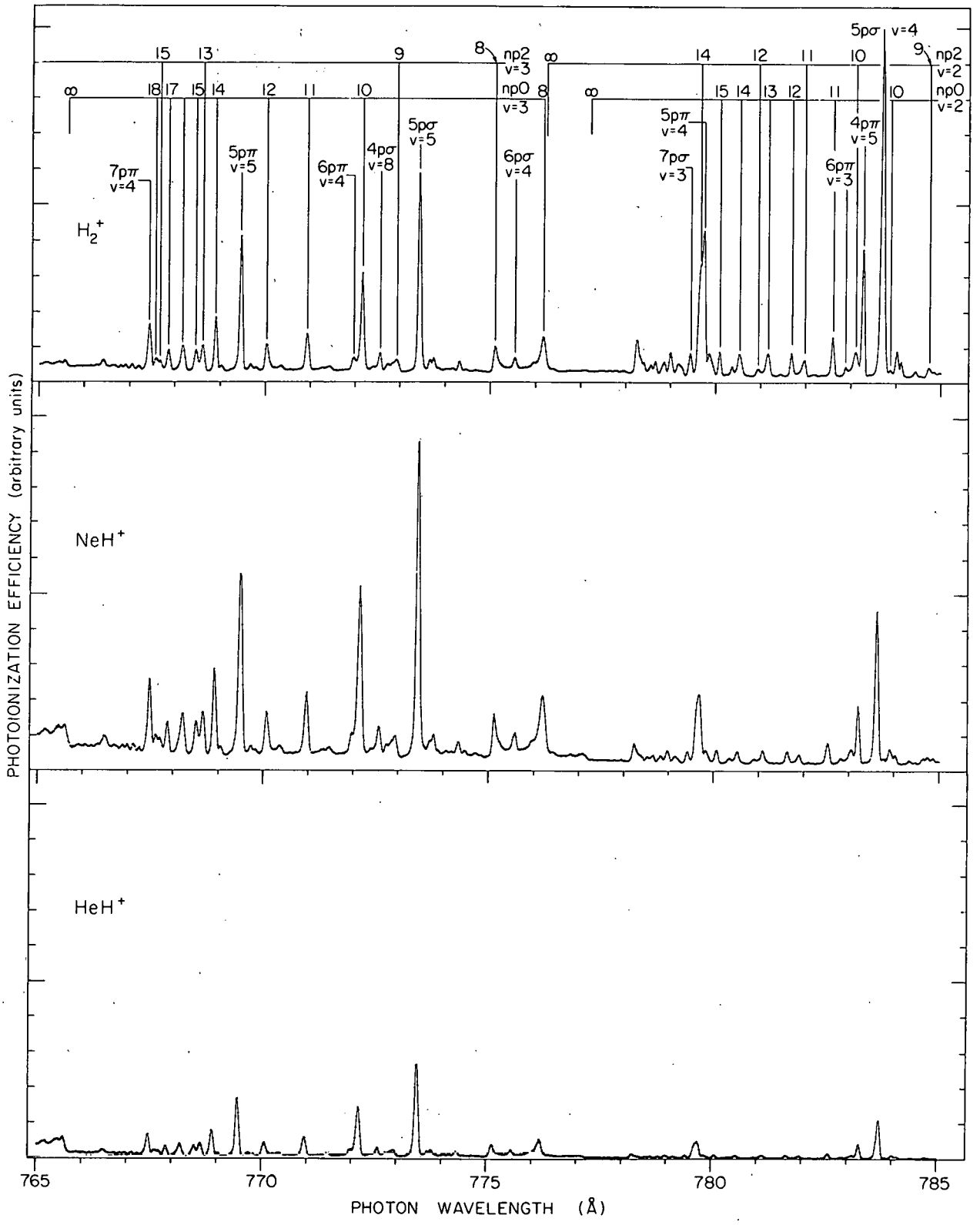
H2+
NeH+
HeH+
PHOTOIONIZATION EFFICIENCY (arbitrary units)
PHOTON WAVELENGTH (Å)
765
770
775
780
785
7pπ v=4
5pπ v=5
6pπ v=4
4pσ v=8
5pσ v=5
6pσ v=4
np2 v=3
npO v=3
5pπ v=4
7pσ v=3
6pπ v=3
4pπ v=5
5pσ v=4
np2 v=2
npO v=2

FIG. 1(b).

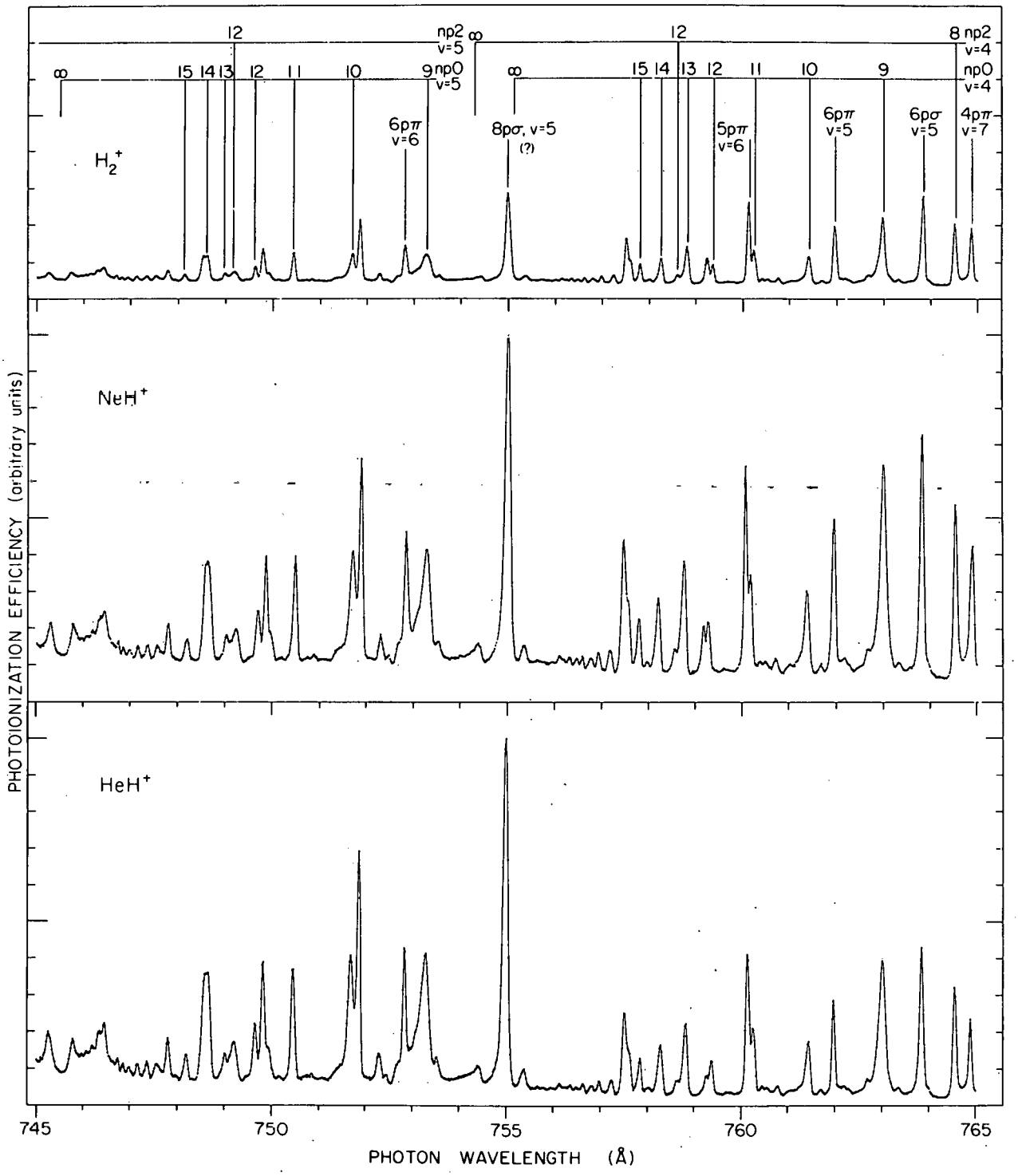
H2+
NeH+
HeH+
PHOTOIONIZATION EFFICIENCY (arbitrary units)
PHOTON WAVELENGTH (Å)
745
750
755
760
765
∞
15 14 13 12 11 10 9
12
np2 v=5
npO v=5
6pπ v=6
8pσ, v=5 (?)
5pπ v=6
6pπ v=5
6pσ v=5
8 np2 v=4
npO v=4
4pπ v=7

FIG. 1(c).

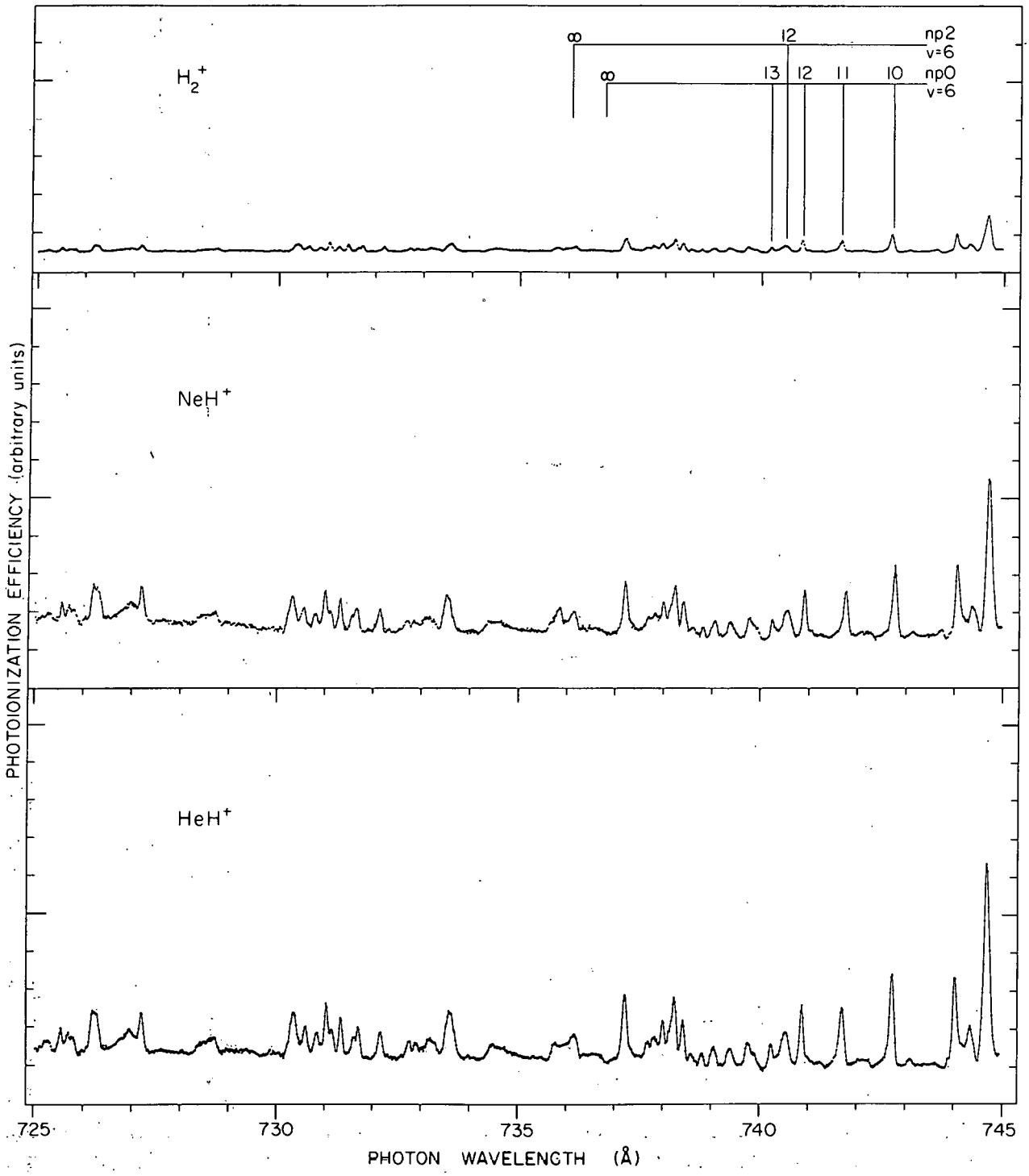
H_2^+
∞
12
np2
v=6
∞
13
12
11
10
np0
v=6
NeH^+
HeH^+
PHOTOIONIZATION EFFICIENCY (arbitrary units)
725
730
735
740
745
PHOTON WAVELENGTH (Å)

FIG. 1(d).

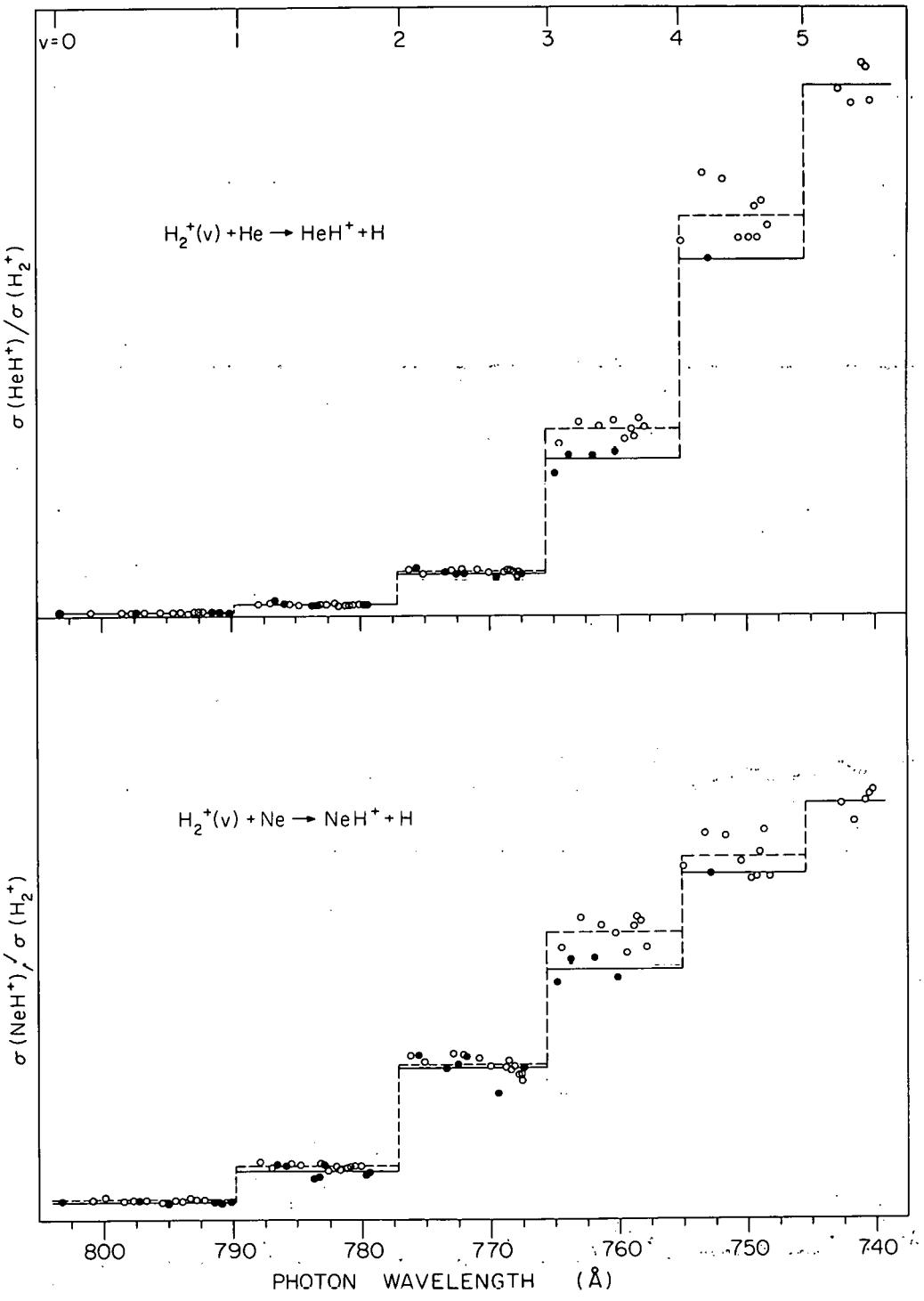

FIG. 2.--Relative cross section for the formation of HeH^+ and NeH^+ from the reaction of para-H_2^+ (formed by autoionization) with He and Ne. The points $\sigma_{hydride}/\sigma_{H_2^+}$ are plotted versus the wavelength of the H_2 autoionization level. The open circles denote Rydberg states which may autoionize with $\Delta v = 1$, and the closed circles denote Rydberg states which must autoionize with $\Delta v > 1$. The dashed vertical lines indicate $H_2^+ {}^2\Sigma_g^+$ vibrational convergence limits, and the dashed and solid horizontal lines are the averages of all the points between the v and v+1 convergence limits which autoionize with $\Delta v = 1$ and $\Delta v > 1$, respectively. (ANL Neg. 209-76-469)

case, since the 9pσ states in question have ratios $\sigma_{hydride}/\sigma_{H_2^+}$ in good agreement with the other values in their respective Rydberg series. Thus these data contradict the predictions of Shaw and Berry regarding significant competition from the $\Delta v = 2$ autoionization process in the presence of a $\Delta v = 1$ channel. From a consideration of the absolute decay rates for these 9pσ states determined from the observed half widths of the H_2^+ autoionizing lines, we concluded that Shaw and Berry's calculation severely underestimated the decay rate for the $\Delta v = 1$ autoionization process.

The data presented in Figure 2 also show that the reaction cross sections for states which autoionize with $\Delta v > 1$ appear systematically lower than the cross sections for states which autoionize with $\Delta v = 1$. This is especially true for the five states above the $v = 3$ convergence limit that autoionize with $\Delta v > 1$. A detailed analysis of the relative cross section data for these states showed that autoionization still proceeds predominantly ($\geq 75\%$) via the minimum change in Δv, but in these cases, there is a slightly broadened distribution of final vibrational states.

References

1. R. S. Berry, J. Chem. Phys. 45, 1228 (1966).
2. G. B. Shaw and R. S. Berry, J. Chem. Phys. 56, 5808 (1972).
3. W. A. Chupka and M. E. Russell, J. Chem. Phys. 49, 5426 (1968).
4. W. A. Chupka, P. M. Dehmer, and W. T. Jivery, J. Chem. Phys. 63, 3929 (1975).

COMPETITION BETWEEN AUTOIONIZATION AND RADIATIVE EMISSION IN THE DECAY OF EXCITED STATES OF THE OXYGEN ATOM*

P. M. Dehmer, W. L. Luken,† and W. A. Chupka‡

Introduction

According to the selection rules for LS coupling,[1] it is possible to make electric dipole transitions from the ^3P ground state of the oxygen atom to excited electronic states of $^3S^o$, $^3P^o$, and $^3D^o$ symmetries. All of these excited states may decay by re-emission of electromagnetic radiation, and, in addition, those states with energies above that of the ground state of the O^+ ion may also decay by autoionization. At energies between those of the ground state and first excited state of the O^+ ion, there are continua of $^3S^o$, $^3D^o$, and other symmetries, but there is no continuum of $^3P^o$ symmetry. Consequently, only the $^3S^o$ and $^3D^o$ states in this energy range decay rapidly by LS-allowed autoionization at rates of the order of 10^{12} sec^{-1}. Autoionization of the $^3P^o$ states is forbidden in LS coupling, and occurs primarily as a result of spin-orbit induced breakdown of LS coupling. Consequently, the autoionization rates of the $^3P^o$ states are smaller than those of the $^3S^o$ and $^3D^o$ states by factors of roughly 10^3. As a result, the (LS-forbidden) autoionization rates of these states, which are of the order of 10^9 sec^{-1}, are comparable to the (LS-allowed) radiative emission rates for these states, and it is possible to observe the decay of these states in photoionization[2] as well as photoemission.[3]

In addition, because the autoionization of these states depends on the spin-orbit interaction, the rates of autoionization depend on the total angular momentum J of each state. Consequently the lifetimes of these states, and

---

*Summary of a paper presented at the VII DEAP Meeting in Tucson, Arizona December 3–5, 1975. A full report will be published in the Journal of Chemical Physics.

†Department of Chemistry, Duke University, Durham, North Carolina 27706.

‡Physics Division, Argonne National Laboratory. Present address: Department of Chemistry, Yale University, New Haven, Connecticut 06520.

the branching ratios for autoionization vs. radiative emission, are different for each $^3P^o_J$ fine structure level. As a result, both the photoionization and photoemission spectra for these states exhibit unusual multiplet intensity distributions.[3] It should be noted that among the states in this category, the $3s''\,^3P^o$ and $2s2p^5\,^3P^o$ states are responsible for the two most prominent features in the photoionization spectrum of oxygen.[2] Evidence for similar competitive decay phenomena has also been found in the photoemission spectrum of the beryllium atom.[4]

Results and Discussion

The work described here reports new measurements of relative photoionization cross sections for a number of excited states of the oxygen atom. The data were taken with a high resolution apparatus at wavelength resolutions of 0.04 Å (FWHM). In previously reported photoionization measurements,[2] the wavelength resolution (0.16 Å, FWHM) was not sufficient to separate components of the $2p^4\,^3P_{J''} \rightarrow 3s''\,^3P^o_{J'}$ multiplet having the same value of J". In this work, all but two components of this multiplet are cleanly resolved. From these new data, along with previously reported photoemission data,[3] improved branching ratios for autoionization vs. radiative emission were determined. In addition, the lifetimes of the $2s2p^5\,^3P^o$ and $3s''\,^3P^o$ were determined using these (experimental) branching ratios and theoretical emission rates calculated using the non-closed shell many-electron theory (NCMET) of Sinanoglu.[5–7] The lifetimes determined in this manner are found to be in excellent agreement with values determined by means of beam-foil spectroscopy.*

The lifetimes of several rapidly (LS-allowed) autoionizing states were also determined in this work by observing the lifetime broadening in the measured linewidths of these states.

The relative photoionization cross sections for the 3s" and $2s2p^5\,^3P^o$ states are shown in Figures 1 and 2, respectively. The relative emission

---

*The details are discussed in a paper submitted for publication by the authors of this report.

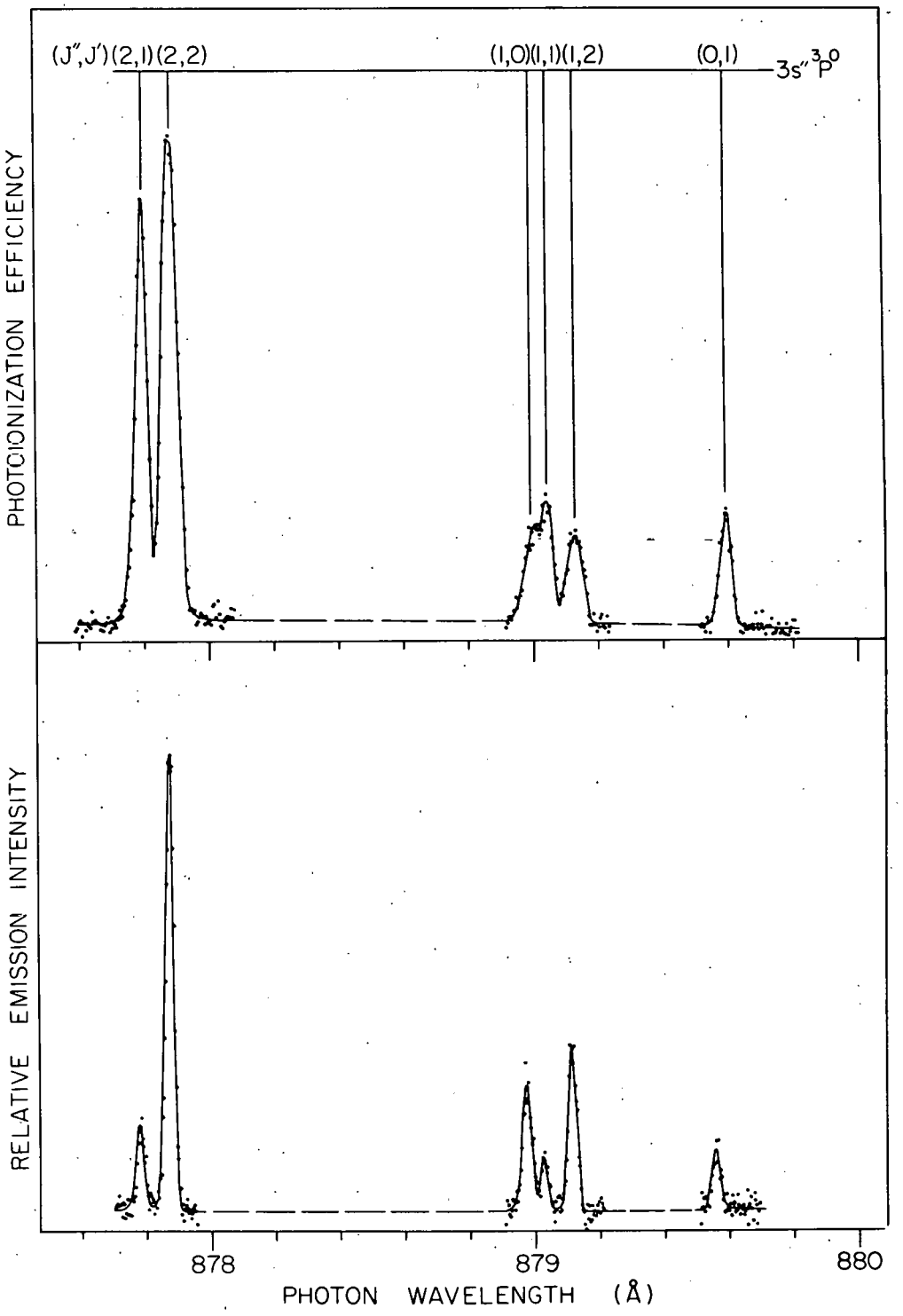

FIG. 1.--Relative photoionization cross section for O I 3s" $^3P^o$ taken at a wavelength resolution of 0.04 Å (upper trace). For comparison the emission spectra for this state taken at a wavelength resolution of 0.02_8 Å is also shown (lower trace) and is described in more detail in Ref. 3.
(ANL Neg. 209-75-383)

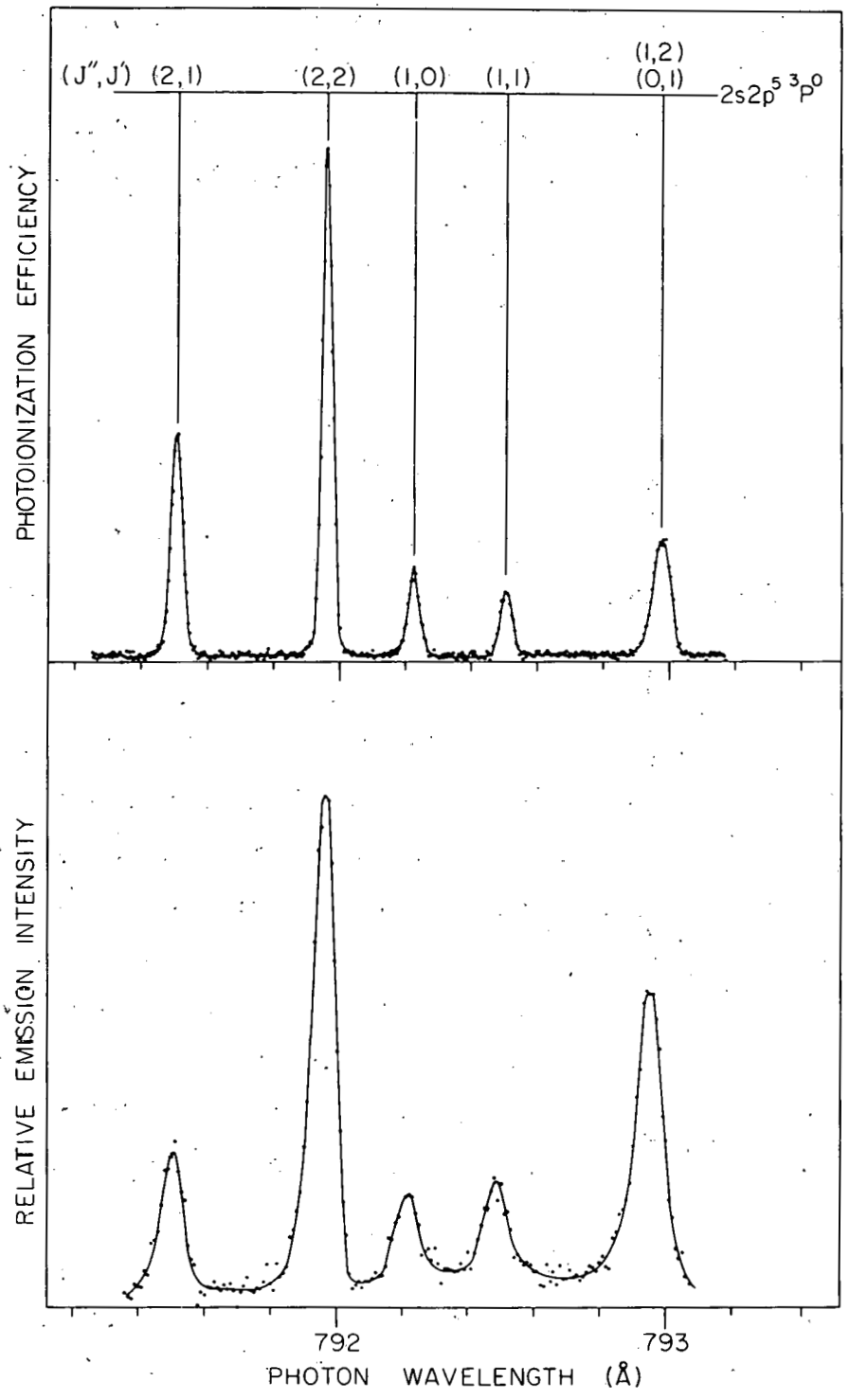

FIG. 2.--Relative photoionization cross section for O I $2s2p^5\ ^3P^o$ taken at a wavelength resolution of 0.04 Å (upper trace). For comparison the emission spectra for this state taken at a wavelength resolution of 0.08_5 Å is also shown (lower trace) and is described in more detail in Ref. 3.
(ANL Neg. 209-75-384)

cross sections reported previously[3] are also shown for comparison. Relative intensities of the fine structure components within each multiplet were determined from several scans and the results are summarized in Table 1.

The fraction of decay by emission B_e and by autoionization B_a are given by

$$B_e(J') = c_e I_e(J'', J')/g(J'', J') , \tag{1a}$$

$$B_a(J') = c_a I_a(J'', J')/g(J'', J') , \tag{1b}$$

where

$$B_e(J') + B_a(J') = 1 . \tag{1c}$$

Here g is the relative absorption probability for each line in LS coupling at the temperature appropriate to the experiment (T = 300 K for the autoionization Experiments and T = ∞ for the emission experiments), I_a and I_e are the relative autoionization and emission intensities, respectively, and c_a and c_e are constants to be determined from the I/g values. In the $3s''\,^3P^o$ multiplet the (1,1) and (1,0) lines were only partially resolved in the present ionization experiments. In order to obtain an I_a/g value for the J' = 0 state, a deconvolution was performed by assuming that the I_a/g value for the (1,1) transition is the average of the I_a/g values for the remaining two states with J' = 1 (i.e., the (0,1) and (2,1) transitions). The I_a/g values for these two states are in excellent agreement, differing by less than 0.5 percent. A least squares fit determined value of c_a and c_e to be 0.314 and 0.606 for the $3s''\,^3P^o$ state, and 0.451 and 0.504 for the $2s2p^5\,^3P^o$ state. The ratios B_a/B_e for each J' level are given in Table 1 for both states.

States of low principal quantum number which may autoionize in an LS-coupling scheme should have sufficiently short lifetimes for broadening to be observed in the measured linewidths. Such states are the $4s'\,^3D^o$, $3d'\,^3S^o$, and $^3D^o$, and possibly the $4d'\,^3S^o$ and $^3D^o$ levels. Broadening is clearly observed for the $4s'\,^3D^o$, and the $3d'\,^3S^o$ and $^3D^o$ states, while the $4d'\,^3S^o$ and $^3D^o$ states appear to be the resolution width (0.04 Å). The measured width of the broadened lines (at their half height) is $0.052_5 \pm 0.002_5$ Å. The natural linewidth is given by

TABLE 1. Determination of Branching Ratios for Autoionization versus Radiative Emission for the $3s''\ ^3P^o$ and $2s2p^5\ ^3P^o$ States of Atomic Oxygen.

State	(J'',J')[a]	λ(Å)	Relative Intensity Ratios[b] I_a[c]	I_a/g_{300}	I_e/g_∞[d]	Branching Ratio $R(J')=B_a/B_e$	$B_e + B_a$[e]
$3s''\ ^3P^o$	(0,1)	879.529	19.1	2.12	0.50	2.19	0.97
	(1,2)	879.088	18.3	1.17	1.05	0.58	1.00
	(1,1)	879.007	37.6	2.13[f]	0.57	1.93	1.01
	(1,0)	878.960		1.42[g]	1.05	0.70	1.08
	(2,2)	877.876	100.0	1.00	1.00	0.52	0.92
	(2.1)	877.799	71.1	2.13	0.55	2.01	1.00
$2s2p^5\ ^3P^o$	(0,1)	792.951	28.7	1.17[h]	0.97[h]	—	1.02
	(1,2)	792.951					
	(1,1)	792.501	12.0	1.28	0.95	1.21	1.06
	(1,0)	792.231	15.3	1.22	0.74	1.48	0.92
	(2,2)	791.966	100.0	1.00	1.00	0.89	0.95
	(2,1)	791.508	43.3	1.30	0.90	1.29	1.04

[a] Peak assignments and wavelengths are from R. E. Huffman, J. C. Larrabee, and Y. Tanaka.[13]

[b] g_{300} and g_∞ are the theoretical relative absorption probabilities at T = 300°K and T = ∞ respectively.

[c] The error in the absorption intensities I_a is approximately ± 7%.

[d] Emission data from P. M. Dehmer and W. A. Chupka.[3] The errors in the I_e/g values are approximately ± 5–7%.

[e] The sum of $B_e + B_a$ should equal 1.0 for all transitions. See Eq. 1a–1c of the text.

[f] The average of the I_a/g values for the (0,1) and (2,1) states.

[g] Obtained by deconvoluting the partially resolved (1,1) and (1,0) lines.

[h] "Effective" I/g values. A measure of the internal consistency for these values would be to calculate the theoretical I/g values for this unresolved pair using the average I/g values for J' = 1 and 2 obtained from resolved lines. This procedure gives effective I/g values of 1.11 for autoionization and 0.97 for emission, both in good agreement with the observed values.

$$\Delta\lambda_{natural} \cong [(\Delta\lambda_{meas})^2 - (\Delta\lambda_{res})^2]^{\frac{1}{2}} \quad , \tag{2}$$

yielding a natural linewidth of 0.034 ± 0.004 Å. The decay rate k is given by

$$k = 2\pi c\, \Delta\lambda/\lambda^2 \tag{3}$$

and is equal to $9.6 \pm 1.1 \times 10^{11}$ sec^{-1} for the $4s'\ ^3D^o$ state and $9.9 \pm 1.2 \times 10^{11}$ sec^{-1} for the $3d'\ ^3S^o$ and $^3D^o$ states. This corresponds to lifetimes of the order of 1×10^{-12} sec.

Based on the experimentally determined natural linewidth for states with $n^* \cong 3$, the natural linewidth for states with $n^* \cong 4$ should be approximately $(3/4)^3 \times 0.034$ Å or 0.014 Å. The predicted observed linewidth is then 0.042 Å, which is only slightly larger than the resolution width and probably could not be distinguished from a line having the resolution width. This is in agreement with the present observation that there is minimal lifetime broadening for the 4d' states. The statistics of the data for the 4d' states are poorer than those for the other states studied at high resolution; however, little or no broadening is observed for these lines as determined from two separate scans of these states.

The probability of autoionization from a discrete state d to a continuum state c is given by[8,9]

$$k = 2\pi \left| \langle \Psi_d \left| \sum_{i>j} 1/r_{ij} \right| \Psi_c \rangle \right|^2 \tag{4}$$

in atomic units. Preliminary calculations based on Eq. 4 have yielded the value of 2.4×10^{12} sec^{-1} for the autoionization rate of the $3d'\ ^3S^o$ state of the oxygen atom. This calculation made use of Hartree-Fock discrete (1s, 2s, 2p, and 3d) orbitals[10,11] and a hydrogenic (s-wave) continuum orbital.[9,12] Because of the approximate treatment of the continuum orbital accuracy of only an order of magnitude is expected in this calculation.[9] Consequently, this result is in satisfactory agreement with the experimental value of 1×10^{12} sec^{-1} obtained above.

Conclusions

The results of this work regarding the production and decay of the $3s''\ ^3P^o$ state of the oxygen atom are summarized as follows. This state can be treated initially by the absorption of a photon by a ground state oxygen atom. Subsequently, it can re-emit a photon and return to the ground state. In addition, it is energetically possible to emit an electron yielding a ground state O^+ ion. Within the restrictions of LS coupling, the $3s''\ ^3P^o$ state does not interact with any of the available continua. However, because of the spin-orbit interaction, the nominal $3s''\ ^3P$ state contains small amounts (of the order of one part in 10^3) of $^3S^o$, $^5S^o$, and $^3D^o$ character, allowing the J = 1 and J = 2 levels to interact electrostatically with the adjacent $^3S^o$, $^5S^o$, and $^3D^o$ continua. Likewise, the nominal $O^+\ ^4S^o$ ground state contains a small amount of $^2P^o$ character, giving a small amount of $^3P^o$ character to the corresponding s-wave and d-wave continua, which can then interact electrostatically with the dominant component of the $3s''\ ^3P^o$ state.

The situation for the $3d'\ ^3P^o$ states are similar, but more complex because of their strong mutual interactions. The $2s2p^5\ ^3P^o$ state is especially interesting because the $2s2p^5$ configuration gives rise to only two LS-coupled terms ($^3P^o$ and $^1P^o$), neither of which is found among the (LS-coupled) continua energetically available to the $2s2p^5\ ^3P^o$ state. Consequently, the spin-orbit interaction within this configuration makes no contribution to the observed autoionization rates. However, this state interacts so strongly with the $3d'\ ^3P^o$ state (electrostatically) that a relatively large portion of the $2s2p^5\ ^3P^o$ state autoionization rate may result from spin-orbit interaction of the $3d'\ ^3P^o$ state with other $2p^3 3d$ terms, which then interact electrostatically with available continua.

References

1. E. U. Condon and G. H. Shortley, The Theory of Atomic Spectra, Cambridge University Press, Cambridge, Ch. 6 (1951).
2. P. J. Dehmer, J. Berkowitz, and W. A. Chupka, J. Chem. Phys. 59, 5777 (1973).
3. P. M. Dehmer and W. A. Chupka, J. Chem. Phys. 62, 584 (1974).

4. L. Johansson, Phys. Scr. 10, 236 (1974).
5. W. L. Luken and O. Sinanoglu, Phys. Rev. A 13, 1293 (1976).
6. W. L. Luken and O. Sinanoglu, J. Chem. Phys. 64, 1495 (1976).
7. O. Sinanoglu, Atomic Physics, Vol. I, Plenum Publ. Co., New York (1969).
8. G. Wentzel, Z. Phys. 29, 321 (1928).
9. B. H. Bransden and A. Dalgarno, Proc. Phys. Soc. (London) A66, 904 (1953).
10. C. C. J. Roothaan and P. S. Kelly, Phys. Rev. 131, 1177 (1963).
11. P. S. Kelly, Astrophys. J. 140, 1247 (1964).
12. D. Herrick and O. Sinanoglu, Phys. Rev. A 11, 97 (1975).
13. R. E. Huffman, J. C. Larrabee, and Y. Tanaka, J. Chem. Phys. 46, 2213 (1967).

ELASTIC ELECTRON-MOLECULE SCATTERING. INTEGRATED CROSS SECTION FOR N_2 BETWEEN 0 and 1000 eV*

Dan Dill† and J. L. Dehmer

We present the integrated elastic cross section for electron-nitrogen scattering for incident energies 0 to 1000 eV. The calculations were based on the multiple-scattering model utilizing fixed-nuclei and Slater-exchange approximations, and represent the prototype for application of this method to larger molecular targets for which it is primarily intended. Within the limited flexibility of the model we are able to reproduce the position of the π_g shape resonance at 2.4 eV and achieve quantitative agreement with absolute measurements at high incident energies by respectively adopting two potentials whose difference is at least partially understood on physical grounds. Moreover, new insight into the dynamics of electron-molecule scattering is gained by inspecting the decomposition of the total cross section into component symmetries over the entire energy range covered.

*Abstract of a paper to be submitted for publication.

†Alfred P. Sloan Research Fellow; consultant to the Radiological and Environmental Research Division. Permament address; Department of Chemistry, Boston University, Boston, Massachusetts 02215.

FESHBACH RESONANCES IN CH_3X(X = Cl, Br, I). CLASSIFICATION OF RESONANCES AND PREDICTION OF RYDBERG STATES *

D. Spence

Using an electron transmission spectrometer we locate Feshbach resonances in the alkyl halides. Combination of data from the acid halides and alkyl halides indicate that for structurally related molecules the energies of Feshbach resonances $E_{n\ell\ell''}(m)$ are related to the appropriate ionization potentials I(m) by the relationship, $E_{n\ell\ell'}(m) = A_{n\ell\ell'}I(m)$ where $E_{n\ell\ell'}(m)$ is the nth resonance with excited electrons of angular momenta ℓ and ℓ' in species m, and $A_{n\ell\ell'}$ and $B_{n\ell\ell'}$ are constants independent of molecular species. This relationship permits easy identification or prediction of resonance energies in chemically related compounds. We show how low Rydberg state energies may be obtained from Feshbach resonance spectra.

---

* Abstract of a paper to be presented at the Annual Meeting of the American Physical Society, Chicago, 7–10 February 1977.

CLASSIFICATION OF FESHBACH RESONANCES IN Ne, Ar, Kr, AND Xe.*

D. Spence

We show that the energy location $E_{n\ell\ell'}(m)$ of the nth resonance with excited electron angular momenta $\ell\ell'$ in Ne, Kr, and Xe is related to the appropriate ionization potential I(m) by the equation

$$E_{n\ell\ell'}(m) = A_{n\ell\ell'} I(m) + B_{n\ell\ell'}$$

where $A_{n\ell\ell'}$ and $B_{n\ell\ell'}$ are constants independent of atomic species. We show how almost all resonances known in the rare gases ($\approx$50 with $^2P_{\frac{3}{2}}$ cores alone) can be classified according to this simple scheme. These results imply that for Feshbach resonances, electron-electron interactions dominate over electron-ion core interactions.

---

*Abstract of a paper presented at the 8th Annual Meeting of the Division of Electron and Atomic Physics, American Physical Society, Lincoln, Nebraska, 6–8 December 1976.

LONG-RANGE ELECTRON EFFECTS IN ELECTRON-IMPACT EXCITATION OF AUTOIONIZING STATES.*

D. Spence

Exchanges in energy between scattered and ejected electrons following near-threshold electron-impact excitation of short-lived autoionizing states have recently been discovered. In this Comment we focus on the techniques and observations which have served to expose this novel long-range interaction, with special emphasis on the $(2s^2)\,^1S$ state.

---

*Abstract of a paper published in Comments Atom. Mol. Phys. 5 (6), 159–172 (1976).

SPECTROSCOPIC AND BETHE CROSS-SECTION DATA FOR SODIUM-LIKE IONS

Y.-K. Kim and J.-P. Desclaux*

Wavelengths and dipole oscillator strengths for the 3s → 3p and 3s → 4p transitions of sodium-like ions are computed from the relativistic and nonrelativistic Hartree-Fock wavefunctions. The relativistic wavelength data for P v and heavier ions agree with available experimental data to 1% or better. As expected, the dependence of the oscillator strengths on the nuclear charge, Z, shows the same qualitative behavior observed in the resonance transitions of the Li sequence. For heavy ions (Z > 40), the sum of the relativistic oscillator strengths for the 3p and 4p transitions is 5 to 30% higher than the sum of nonrelativistic values. The Bethe cross sections, which contain the leading terms of the plane-wave Born approximation, indicate that the relativistic cross sections for heavy ions are 10 to 40% smaller than the nonrelativistic cross sections.

Introduction

Spectroscopic data, such as excitation energies and dipole oscillator strengths, (f values), for highly stripped ions are needed in the fusion reactor studies both for estimating the energy loss through impurity ions and for plasma diagnosis. In particular, the resonance transitions of alkali- and alkaline-earth-like ions are expected to stand out in the plasma because of their large oscillator strengths.[1]

With computer programs developed by one of us[2] we have calculated transition energies and f values for the 3s → 3p and 3s → 4p transitions, using both relativistic and nonrelativistic Hartree-Fock (HF) wavefunctions.

Spectroscopic Data

The excitation energies were computed by taking the differences in the total energies. All orbitals were made self-consistent for each state, and therefore, our results correspond to the "relaxed core" calculation. The relativistic energies include all one-electron terms from the Dirac Hamiltonian, and the Coulomb repulsion and the Breit operators for the two-electron terms.

*Centre d'Etudes Nucleaires de Grenoble, 38041 Grenoble, France.

Only the average configuration values for the Breit operator were computed, though the rest of the terms were calculated for a specific total angular momentum, J. The f values were computed in the length form, i.e., with $\vec{r}$ operator. The matrix elements were calculated only between valence electrons, retaining contributions from both large and small components. Contributions from the core-valence terms, as well as other relativistic operators (e.g., retardation effect when the transition energy is high), were ignored. The combined effects of the neglected terms are expected to be a few percent at the most.

The transition wavelengths and probabilities calculated from the relativistic HF wavefunctions are compared with available experimental data[3-6] in Table 1. The f values from Ref. 3 are based on both experimental and (nonrelativistic) theoretical results. As in the case of the Li sequence,[7] the relativistic HF results agree very well with available experimental data.

The nonrelativistic hydrogenic formulas show that the excitation energy, E, scales as Z^2, where Z is the nuclear charge, whereas the line strength,

$$S = \frac{2}{3} \left| \langle np|r|3s \rangle \right|^2 a_0^2 , \qquad a_0 = 0.529 \text{ Å} \tag{1}$$

scales as Z^{-2}. Hence, the oscillator strength

$$f = ES/6R, \qquad R = 13.6 \text{ eV} \tag{2}$$

is constant in Z.

Both relativistic HF (Table 2) and nonrelativistic HF (Table 3) data show very little of the hydrogenic behavior. Qualitative differences between the relativistic and nonrelativistic data for the Na sequence are similar to those observed in the Li sequence.[8-10]

In Figure 1, we present the sum of the f values as a function of Z. We note that (a) $s_{\frac{1}{2}} \rightarrow p_{\frac{1}{2}}$ transitions follow the nonrelativistic pattern, but (b) $s_{\frac{1}{2}} \rightarrow p_{\frac{3}{2}}$ transitions depart drastically from the nonrelativistic pattern. In the $3s \rightarrow 3p_{\frac{3}{2}}$ transition, the increase in the excitation energy is responsible for the increase in the f values for high Z. In contrast, in the $3s \rightarrow 4p_{\frac{3}{2}}$ transition, the decrease in the line strength is responsible for the decrease in the f values

TABLE 1. Comparison of the relativistic Hartree-Fock data with empirical and semi-empirical results for the Na sequence.

Ion	Transition[a]	Relativistic HF Wavelength (Å)	f	Other results Wavelength (Å)	f	Reference
Na I	3s → 3p*	6268,2	0.329	5897.6[b]	0.327	3
	→ 3p	6263.0	0.658	5891.6	0.655	
	→ 4p*	3456.0	0.004	3303.9	0.0048	
	→ 4p	3455.7	0.0089	3303.3	0.0094	
Mg II	3s → 3p*	2890.1	0.318	2803.5	0.313	3
	→ 3p	2882.8	0.637	2796.3	0.627	
	→ 4p*	1271.3	0.0001	1240.4	0.0001	
	→ 4p	1270.8	0.0002	1239.9	0.0002	
Al III	3s → 3p*	1894.3	0.293	1862.8	0.291	3
	→ 3p	1886.2	0.589	1854.7	0.585	
	→ 4p*	707.33	0.0039	696.21	0.0037	
	→ 4p	706.95	0.0074	695.82	0.0076	
P V	3s → 3p*	1133.7	0.247	1128.0	0.222	3
	→ 3p	1123.6	0.499	1118.0	0.448	
	→ 4p*	331.48	0.018	328.77	0.018	
	→ 4p	331.17	0.034	328.47	0.037	
Ar VIII	3s → 3p*	713.09	0.196	713.81	0.187	3
	→ 3p	699.70	0.401	700.24	0.380	
	→ 4p*	159.81	0.038	159.17	0.041	
	→ 4p	159.56	0.074	158.92	0.083	
V XIII	3s → 3p*	441.51	0.145	443.48		4
	→ 3p	421.18	0.306	422.81		
	→ 4p*	72.136	0.064	72.025		
	→ 4p	71.918	0.122	71.799		
Fe XVI	3s → 3p*	358.79	0.125	360.80		5
	→ 3p	333.85	0.272	335.41		
	→ 4p*	50.616	0.076			
	→ 4p	50.409	0.141			
Kr XXVI	3s → 3p*	218.05	0.086	220.6		6
	→ 3p	177.79	0.216	179.6		
	→ 4p*	21.374	0.0995			
	→ 4p	21.186	0.176			
Mo XXXII	3s → 3p*	174.55	0.0730	177		6
	→ 3p	126.87	0.206	129		
	→ 4p*	14.565	0.108			
	→ 4p	14.384	0.184			

a. $p^* = p_{\frac{1}{2}}$, $p = p_{\frac{3}{2}}$.

b. Vacuum wavelength.

for large Z. The sum of the f values tabulated in Tables 2 and 3, however, show ~ 30% difference at Z=90, as compared to less than 10% for the Li sequence.

Bethe Cross Sections

The Bethe parameters,[11] M^2 and ln c, for the resonance transitions were also calculated from the relativistic and nonrelativistic wavefunctions. The plane-wave Born cross section σ for the excitation of an ion to a discrete state by an electron or proton of velocity v is given by

$$\sigma = \frac{4\pi a_0^2}{T/R} M^2 \ln(4CT/R) , \tag{3}$$

where $T = \frac{1}{2} mv^2$ with electron mass m. For incident particles with relativistic velocities (T > 5 keV), a relativistic form of Eq. 3 should be used:

$$\sigma = \frac{4\pi a_0^2 \alpha^2}{\beta^2} \{ M^2 [\ln(\frac{\beta^2}{1-\beta^2}) - \beta^2] + C \} \tag{4}$$

where

$$C = M^2(\ln c + 11.23) . \tag{5}$$

In Eq. 4, α is the fine structure constant. Although Eqs. 3 and 4 are based on the plane-wave Born approximation (PWBA), it is easy to show that the leading term containing M^2 [M^2 ln 4T in Eq. 3] does not change in the Coulomb-Born approximation.[12] A comparison of some numerical data on dipole-allowed transitions indicates that the Coulomb-Born cross sections converge toward the PWBA results rather quickly for fast incident particles. Therefore, the Bethe parameters in Tables 2 and 3 would provide a dependable check for the asymptotic behavior on the Coulomb-Born cross sections.

Comparison of the Bethe cross sections for the 3s → 3p excitation of Mo^{31+} by electron impact (Figure 2) show that the relativistic cross sections are smaller than corresponding nonrelativistic values. The cross sections are smaller because of (a) the relativistic contraction of orbitals, i.e., reduced geometrical cross sections, and (b) the reduced range of momentum transfer

TABLE 2. Relativistic Hartree-Fock Data for the Na Sequence

ATOM	Z	|0⟩[a]	⟨N|[b]	E/Z**2[c]	S*Z**2[d]	F	M**2[d]	LN C
NA	11	3S	3P*	0.1201D-02	0.1643D 04	0.3290D 00	0.2263D 01	0.1303D 01
NA	11	3S	3P	0.1202D-02	0.3285D 04	0.6583D 00	0.4525D 01	0.1301D 01
NA	11	3S	4P*	0.2179D-02	0.1201D 02	0.4362D-02	0.1654D-01	0.1108D 02
NA	11	3S	4P	0.2179D-02	0.2441D 02	0.8868D-02	0.3363D-01	0.1092D 02
MG	12	3S	3P*	0.2190D-02	0.8703D 03	0.3176D 00	0.1007D 01	0.6917D 00
MG	12	3S	3P	0.2195D-02	0.1741D 04	0.6369D 00	0.2015D 01	0.6854D 00
MG	12	3S	4P*	0.4978D-02	0.1222D 00	0.1014D-03	0.1415D-03	0.3344D 03
MG	12	3S	4P	0.4980D-02	0.1927D 00	0.1599D-03	0.2230D-03	0.4291D 03
AL	13	3S	3P*	0.2847D-02	0.6179D 03	0.2931D 00	0.6094D 00	0.3952D 00
AL	13	3S	3P	0.2859D-02	0.1236D 04	0.5891D 00	0.1219D 01	0.3851D 00
AL	13	3S	4P*	0.7623D-02	0.3068D 01	0.3898D-02	0.3026D-02	0.2719D 01
AL	13	3S	4P	0.7627D-02	0.5821D 01	0.7399D-02	0.5740D-02	0.3134D 01
P	15	3S	3P*	0.3573D-02	0.4146D 03	0.2468D 00	0.3071D 00	0.8427D-01
P	15	3S	3P	0.3604D-02	0.8302D 03	0.4987D 00	0.6149D 00	0.6456D-01
P	15	3S	4P*	0.1222D-01	0.8669D 01	0.1765D-01	0.6421D-02	-0.3150D 01
P	15	3S	4P	0.1223D-01	0.1667D 02	0.3398D-01	0.1235D-01	-0.3107D 01
AR	18	3S	3P*	0.3944D-02	0.2986D 03	0.1963D 00	0.1536D 00	-0.1429D 00
AR	18	3S	3P	0.4020D-02	0.5987D 03	0.4011D 00	0.3080D 00	-0.1835D 00
AR	18	3S	4P*	0.1760D-01	0.1312D 02	0.3849D-01	0.6750D-02	-0.4336D 01
AR	18	3S	4P	0.1763D-01	0.2514D 02	0.7387D-01	0.1293D-01	-0.4330D 01
V	23	3S	3P*	0.3902D-02	0.2233D 03	0.1452D 00	0.7034D-01	-0.3266D 00
V	23	3S	3P	0.4090D-02	0.4489D 03	0.3060D 00	0.1414D 00	-0.4251D 00
V	23	3S	4P*	0.2388D-01	0.1618D 02	0.6441D-01	0.5099D-02	-0.5175D 01
V	23	3S	4P	0.2395D-01	0.3051D 02	0.1218D 00	0.9614D-02	-0.5185D 01
FE	26	3S	3P*	0.3757D-02	0.2003D 03	0.1254D 00	0.4939D-01	-0.3930D 00
FE	26	3S	3P	0.4038D-02	0.4037D 03	0.2717D 00	0.9953D-01	-0.5424D 00
FE	26	3S	4P*	0.2663D-01	0.1703D 02	0.7560D-01	0.4199D-02	-0.5520D 01
FE	26	3S	4P	0.2674D-01	0.3170D 02	0.1413D 00	0.7817D-02	-0.5536D 01
KR	36	3S	3P*	0.3225D-02	0.1609D 03	0.8646D-01	0.2069D-01	-0.5329D 00
KR	36	3S	3P	0.3955D-02	0.3271D 03	0.2156D 00	0.4207D-01	-0.9514D 00
KR	36	3S	4P*	0.3290D-01	0.1815D 02	0.9952D-01	0.2334D-02	-0.6343D 01
KR	36	3S	4P	0.3319D-01	0.3190D 02	0.1765D 00	0.4103D-02	-0.6786D 01
MO	42	3S	3P*	0.2960D-02	0.1480D 03	0.7302D-01	0.1399D-01	-0.5934D 00
MO	42	3S	3P	0.4072D-02	0.3032D 03	0.2058D 00	0.2865D-01	-0.1246D 01
MO	42	3S	4P*	0.3547D-01	0.1832D 02	0.1083D 00	0.1731D-02	-0.6709D 01
MO	42	3S	4P	0.3592D-01	0.3076D 02	0.1841D 00	0.2907D-02	-0.6770D 01
XE	54	3S	3P*	0.2570D-02	0.1308D 03	0.5601D-01	0.7473D-02	-0.7014D 00
XE	54	3S	3P	0.4735D-02	0.2727D 03	0.2152D 00	0.1558D-01	-0.1947D 01
XE	54	3S	4P*	0.3939D-01	0.1822D 02	0.1196D 00	0.1042D-02	-0.7287D 01
XE	54	3S	4P	0.4027D-01	0.2714D 02	0.1822D 00	0.1551D-02	-0.7396D 01
W	74	3S	3P*	0.2220D-02	0.1105D 03	0.4086D-01	0.3362D-02	-0.8875D 00
W	74	3S	3P	0.7231D-02	0.2399D 03	0.2892D 00	0.7303D-02	-0.3299D 01
W	74	3S	4P*	0.4461D-01	0.1744D 02	0.1296D 00	0.5307D-03	-0.7999D 01
W	74	3S	4P	0.4666D-01	0.1887D 02	0.1467D 00	0.5743D-03	-0.8210D 01
AU	79	3S	3P*	0.2172D-02	0.1059D 03	0.3833D-01	0.2828D-02	-0.9373D 00
AU	79	3S	3P	0.8178D-02	0.2328D 03	0.3174D 00	0.6218D-02	-0.3647D 01
AU	79	3S	4P*	0.4589D-01	0.1716D 02	0.1312D 00	0.4582D-03	-0.8146D 01
AU	79	3S	4P	0.4835D-01	0.1657D 02	0.1335D 00	0.4424D-03	-0.8386D 01
TH	90	3S	3P*	0.2102D-02	0.9580D 02	0.3357D-01	0.1971D-02	-0.1045D 01
TH	90	3S	3P	0.1086D-01	0.2170D 03	0.3927D 00	0.4465D-02	-0.4409D 01
TH	90	3S	4P*	0.4890D-01	0.1644D 02	0.1340D 00	0.3382D-03	-0.8443D 01
TH	90	3S	4P	0.5249D-01	0.1144D 02	0.1001D 00	0.2355D-03	-0.8729D 01

a. Initial state.
b. Final state, $p^* = p_{\frac{1}{2}}$, $p = p_{\frac{3}{2}}$.
c. In rydberg.
d. In atomic units.

TABLE 3. Nonrelativistic Hartree-Fock Data for the Na Sequence

ATOM	Z	|0⟩[a]	|N|[b]	E/Z**2 [c]	S*Z**2 [d]	F	M**2 [d]	LN C
NA	11	3S	3P	0.1198D-02	0.4941D 04	0.9868D 00	0.6806D 01	0.1307D 01
NA	11	3S	4P	0.2176D-02	0.3578D 02	0.1298D-01	0.4929D-01	0.1117D 02
MG	12	3S	3P	0.2183D-02	0.2619D 04	0.9526D 00	0.3031D 01	0.6955D 00
MG	12	3S	4P	0.4968D-02	0.3919D 00	0.3245D-03	0.4535D-03	0.3127D 03
AL	13	3S	3P	0.2836D-02	0.1860D 04	0.8791D 00	0.1834D 01	0.3998D 00
AL	13	3S	4P	0.7606D-02	0.9337D 01	0.1184D-01	0.9208D-02	0.2638D 01
P	15	3S	3P	0.3552D-02	0.1250D 04	0.7396D 00	0.9256D 00	0.9179D-01
P	15	3S	4P	0.1218D-01	0.2627D 02	0.5334D-01	0.1946D-01	-0.3154D 01
AR	18	3S	3P	0.3907D-02	0.9022D 03	0.5875D 00	0.4641D 00	-0.1306D 00
AR	18	3S	4P	0.1752D-01	0.3979D 02	0.1162D 00	0.2047D-01	-0.4334D 01
V	23	3S	3P	0.3836D-02	0.6782D 03	0.4336D 00	0.2137D 00	-0.3041D 00
V	23	3S	4P	0.2369D-01	0.4925D 02	0.1945D 00	0.1552D-01	-0.5170D 01
FE	26	3S	3P	0.3673D-02	0.6110D 03	0.3741D 00	0.1507D 00	-0.3627D 00
FE	26	3S	4P	0.2636D-01	0.5198D 02	0.2284D 00	0.1281D-01	-0.5512D 01
KR	36	3S	3P	0.3076D-02	0.4995D 03	0.2561D 00	0.6424D-01	-0.4693D 00
KR	36	3S	4P	0.3223D-01	0.5607D 02	0.3012D 00	0.7211D-02	-0.6331D 01
MO	42	3S	3P	0.2769D-02	0.4662D 03	0.2152D 00	0.4405D-01	-0.5038D 00
MO	42	3S	4P	0.3448D-01	0.5712D 02	0.3282D 00	0.5397D-02	-0.6692D 01
XE	54	3S	3P	0.2290D-02	0.4271D 03	0.1630D 00	0.2441D-01	-0.5463D 00
XE	54	3S	4P	0.3752D-01	0.5819D 02	0.3639D 00	0.3326D-02	-0.7260D 01
W	74	3S	3P	0.1764D-02	0.3946D 03	0.1160D 00	0.1201D-01	-0.5833D 00
W	74	3S	4P	0.4045D-01	0.5893D 02	0.3973D 00	0.1793D-02	-0.7947D 01
AU	79	3S	3P	0.1668D-02	0.3895D 03	0.1082D 00	0.1040D-01	-0.5893D 00
AU	79	3S	4P	0.4096D-01	0.5903D 02	0.4029D 00	0.1576D-02	-0.8087D 01
TH	90	3S	3P	0.1507D-02	0.3804D 03	0.9557D-01	0.7827D-02	-0.6267D 00
TH	90	3S	4P	0.4189D-01	0.5919D 02	0.4133D 00	0.1218D-02	-0.8366D 01

a. Initial state.
b. Final state, $p^* = p_{\frac{1}{2}}$, $p = p_{\frac{3}{2}}$.
c. In rydberg.
d. In atomic units.

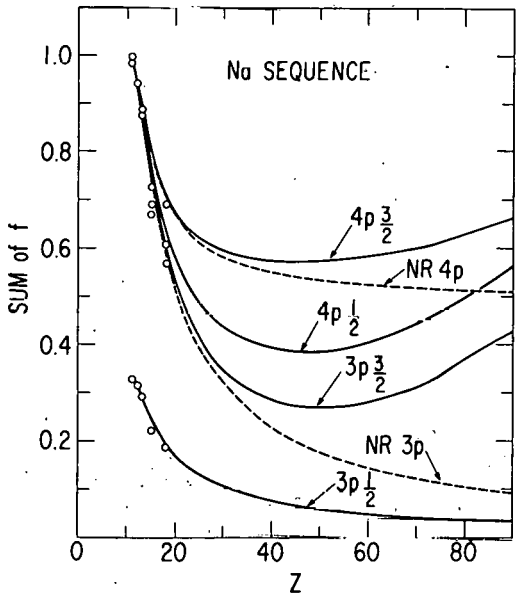

FIG. 1.--Sum of f values versus nuclear charge Z. All transitions are from the 3s state. Dashed curves marked NR represent nonrelativistic results. Open circles are the f values recommended in Ref. 3.

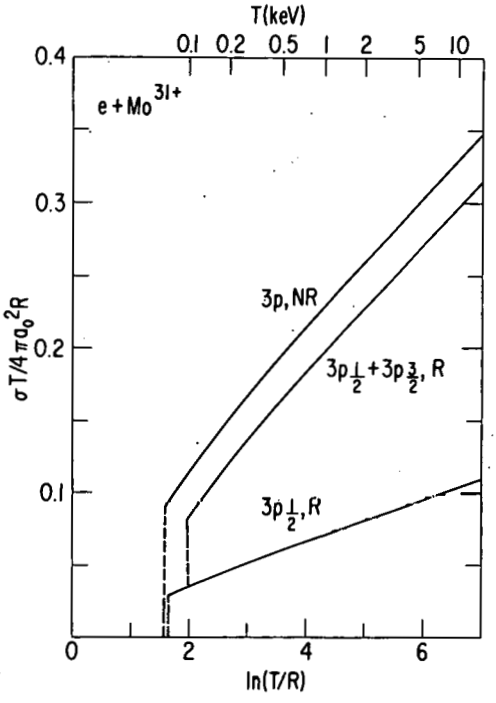

FIG. 2.--The Fano plot (equivalent to collision strength vs. logarithm of incident energy) for the electron-impact excitation of Mo^{31+} ion. The curves marked R and NR represent relativistic and nonrelativistic results, respectively. All transitions are from the 3s state. The excitation thresholds are shown as dashed lines. T is incident electron energy. See Eq. 3 of the text for other notations.

to be integrated over (mainly increase in the minimum momentum transfer) owing to a relativistic increase in the excitation energy. Cross sections for the $3s \rightarrow 3p_{\frac{3}{2}}$ transitions are affected most by (b) above, resulting in the ratio

$$\sigma(\text{relativistic})/\sigma(\text{nonrelativistic}) \approx 0.6 - 0.8 \text{ for } Z > 40.$$

The relativistic change of the momentum-transfer range is reflected mostly in the values of ln c. A comparison of ln c values in Tables 2 and 3 indicates that the relativistic effects are discernible (>20%) even for the phosphorus ion (Z=15). It is obvious, therefore, that appropriate relativistic data should be used to estimate dependable cross sections for stripped ions. All qualitative conclusions on the Bethe cross sections for the Na sequence presented in this report are also true for the Li sequence, according to our (unpublished) Bethe cross sections for the Li sequence.

References

1. U.S. ERDA Report, ERDA-76/106 (1975).
2. J.-P. Desclaux, Comput. Phys. Commun. 9, 31 (1975).
3. W. L. Wiese, M. W. Smith, and B. M. Miles, NRDA-NBS Report 22 (1969)
4. L. Cohen and W. E. Behring, J. Opt. Soc. Am. 66, 899 (1976).

5. U. Feldman, L. Katz, W. Behring, and L. Cohen, J. Opt. Soc. Am. 61, 9 (1971).
6. E. Hinnov, Phys. Rev. A 14, 1533 (1976).
7. G. A. Martin and W. L. Wiese, Phys. Rev. A 13, 699 (1976).
8. Y.-K. Kim and J.-P. Desclaux, Phys. Rev. Lett. 36, 139 (1976).
9. A. W. Weiss, to be published.
10. L. Armstrong, Jr., W. R. Fielder, and D. L. Lin, Phys. Rev. A 14, 1114 (1976).
11. W. F. Miller and R. L. Platzman, Proc. Phys. Soc. (London) A70, 299 (1957).
12. C. J. Mullin and E. Guth, Phys. Rev. 82, 141 (1951).

ATOMIC FORM FACTORS AND INCOHERENT-SCATTERING FUNCTIONS OF Cs^+ AND Au^+

Sara Dawson,* and Yong-Ki Kim

Atomic form factors and incoherent-scattering functions of Cs^+, Cs, Au^+, and Au were calculated. These data are necessary for estimating total inelastic cross sections for total cross sections for inelastic scattering of heavy ions by background gases.

Introduction

Recently, R. Martin and R. Arnold of Argonne National Laboratory have proposed the release of thermonuclear energy from a small pellet containing a D-T gas mixture that is ignited by fast heavy ions (at approximately 0.5 GeV/nucleon).[1] Incoherent-scattering functions, $S_{inc}(K)$, for heavy ions (e.g., Cs^+) are needed to estimate the total cross section for inelastic scattering by background gases (N_2, O_2, etc.) in a heavy-ion accelerator. Once $S_{inc}(K)$ is determined, the Born approximation may be used to calculate upper limits to the desired cross sections.[2,3] Ionization of the projectile ions will put them out of phase with the accelerating field and eventually the ions will be lost from the beam. Thus, the pressure of the background gas must be reduced to prevent an excessive attenuation of the beam. An accurate determination of the vacuum requirement is necessary to estimate the cost of such an accelerator.

Since both Cs^+ and Au^+ have closed valence shells, they are not easily ionized and so are good candidates for use in an accelerator. The calculations given here are based on Schroedinger wavefunctions; however, for an ion as heavy as gold, more accurate description requires the Dirac relativistic wavefunctions.

---

*Participant in the Undergraduate Research Participation Program, ANL Center for Educational Affairs, June 14–August 20, 1976. Present address: Department of Physics, Duke University, Durham, North Carolina 27706.

Data are available in the literature[4] for the atomic form factors of a limited class of heavy ions, but not for the incoherent-scattering functions of heavy ions. Thus, we carried out the present calculations, and the incoherent-scattering functions for Cs^+ and Au^+ are the first of their kind.

Background

The atomic form factor, F(K), and the incoherent-scattering function, $S_{inc}(K)$, for an atom or ion are defined as follows:[5]

$$F(K) = \sum_{j=1}^{N} \langle \exp(i\vec{K} \cdot \vec{r}_j) \rangle , \tag{1}$$

$$S_{inc}(K) = N^{-1} \left[\sum_{j,k=1}^{N} \langle \exp[i\vec{K} \cdot (\vec{r}_j - \vec{r}_k)] \rangle - |F(K)|^2 \right] . \tag{2}$$

where $\langle\ \rangle$ is the expectation value in the ground state, N is the number of atomic electrons, and $\vec{r}_j$ is the position vector from the nucleus to the jth electron. The momentum transfer K is defined in terms of the initial and final momenta, $\vec{k}_0$ and $\vec{k}_n$, as

$$\vec{K} = \vec{k}_0 - \vec{k}_n . \tag{3}$$

In x-ray scattering, the following variable is frequently used: $\frac{\sin(\theta/2)}{\lambda} = \frac{K}{4\pi}$. Here λ is the photon wavelength and θ is the angle at which the photon scatters.

Applications of F(K) and $S_{inc}(K)$ to various problems in atomic scattering are discussed elsewhere.[5]

Results and Discussion

A Hartree-Fock wavefunction program developed by Desclaux[6] was used to calculate wavefunctions for Cs, Cs^+, Au, and Au^+. Atomic data from these computer calculations are shown in Tables 1–3. For small K, $S_{inc}(K)$ has the form

$$S_{inc}(K) = M_{tot}^2 (Ka_0)^2 + \ldots , \tag{4}$$

TABLE 1. Orbital Energies in Rydbergs

Orbital	Cs^+	Cs	Au^+	Au
1s	2545.8938	2545.5377	5414.2216	5413.6667
2s	396.6432	396.2876	914.9184	914.3655
2p	372.9879	372.6321	878.3655	877.8120
3s	85.7413	85.3861	219.0755	218.5221
3p	75.5473	75.1917	201.7993	201.2452
3d	56.8078	56.4522	169.9916	169.4373
4s	17.7452	17.3911	49.2608	48.7079
4p	13.8920	13.5370	41.6959	41.1414
4d	7.1137	6.7590	27.8662	27.3109
4f	—	—	9.2116	8.6566
5s	2.8129	2.4632	8.1720	7.6178
5p	1.7175	1.3669	5.6300	5.0687
5d	—	—	1.6013	1.0420
6s	—	0.2473	—	0.4416

Rydberg = 13.6 eV

TABLE 2. Total Energies in Hartrees

Cs^+	-7553.8141
Cs	-7553.9356
Au^+	-17865.1909
Au	-17865.4099

Hartree = 27.2 eV

TABLE 3. $\langle r^2 \rangle$ for Valence Orbitals and M_{tot}^2 in a_0^2

	Orbital	$\langle r^2 \rangle$	M_{tot}^2
Cs^+	5p	5.099637	9.4865
Cs	6s	44.988506	24.2628
Au^+	5d	2.746265	8.5142
Au	6s	15.888460	14.0554

a_0 = 0.529 Å

and M_{tot}^2 is defined as

$$M_{tot}^2 = \sum_{j,k} \langle x_i x_j \rangle / a_0^2 \quad , \tag{5}$$

where x is a Cartesian component of $\vec{r}$.

Atomic form factors and incoherent-scattering functions for Cs and Cs^+ are given in Table 4 and those for Au and Au^+ in Table 5. These data are plotted in Figures 1 and 2. The maximum point in each of these graphs is the number of electrons in the atom or ion as opposed to the nuclear charge. For example, F(K) of Au has a peak value of 79 at K=0, while that of Au^+ has a maximum value of 78.

The value of F(K) and $S_{inc}(K)$ are in a sense complementary. Coherent scattering, represented by F(K), is the major process at low K; as the momentum transfer increases, incoherent scattering becomes dominant and the atomic form factor diminishes to zero. Some incoherent scattering, however, is present, even at very low values of K, and it is necessary to go to extremely large values of the momentum transfer (K ≅ 100 atomic units) before F(K) decreases almost to zero.

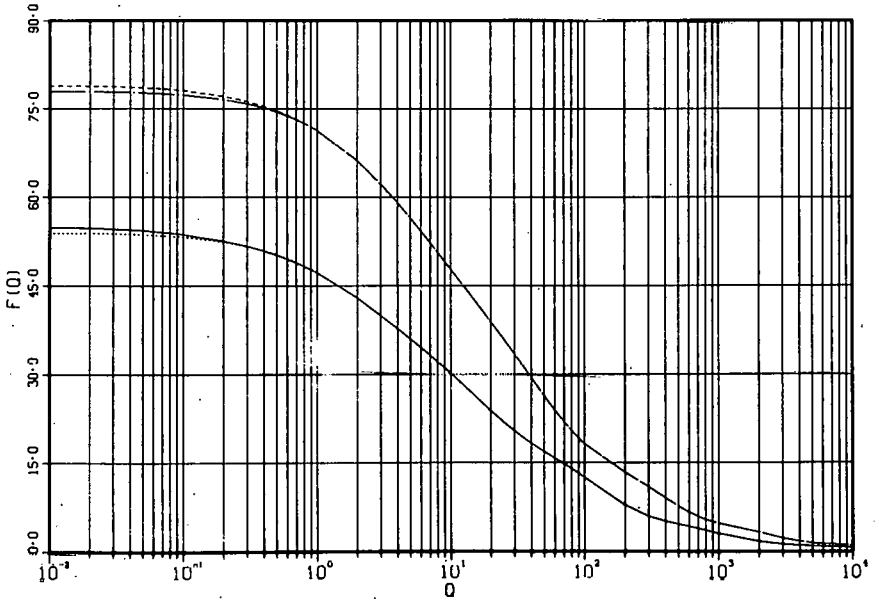

FIG. 1.--Atomic form factors F(Q) as functions of $Q = (Ka_0)^2$, where K is the momentum transfer and a_0 is the Bohr radius (a_0 = 0.529 Å). ---, Au; —·—, Au^+; ——, Cs; ...., Cs^+.

TABLE 4

COHERENT AND INCOHERENT ATOMIC FORM FACTORS FROM THE HARTREE-FOCK WAVEFUNCTIONS

	Cs		Cs+	
$Q=(Ka_0)^2$	F(Q)	S(Q)	F(Q)	S(Q)
0.0	0.55000000D 02	0.0	0.54000000D 02	0.0
0.01	0.54839689D 02	0.66201876D 00	0.53912672D 02	0.94317779D-01
0.02	0.54684773D 02	0.81369205D 00	0.53825830D 02	0.18749793D 00
0.03	0.54534903D 02	0.95630046D 00	0.53739470D 02	0.27957913D 00
0.04	0.54389755D 02	0.10909434D 01	0.53653587D 02	0.37058110D 00
0.05	0.54249033D 02	0.12185730D 01	0.53568180D 02	0.46052317D 00
0.06	0.54112459D 02	0.13400143D 01	0.53483244D 02	0.54942428D 00
0.07	0.53979777D 02	0.14559830D 01	0.53398775D 02	0.63730302D 00
0.08	0.53850750D 02	0.15671001D 01	0.53314770D 02	0.72417759D 00
0.09	0.53725159D 02	0.16739052D 01	0.53231226D 02	0.81006587D 00
0.10	0.53602798D 02	0.17768671D 01	0.53148139D 02	0.89498535D 00
0.20	0.52521059D 02	0.26635232D 01	0.52341683D 02	0.16945126D 01
0.30	0.51618142D 02	0.34031694D 01	0.51577386D 02	0.24140799D 01
0.40	0.50825449D 02	0.40615400D 01	0.50852270D 02	0.30664068D 01
0.50	0.50106689D 02	0.46604485D 01	0.50163604D 02	0.36619560D 01
0.60	0.49441670D 02	0.52103310D 01	0.49508875D 02	0.42093424D 01
0.70	0.48818565D 02	0.57183113D 01	0.48885775D 02	0.47156681D 01
0.80	0.48230054D 02	0.61901699D 01	0.48292176D 02	0.51867954D 01
0.90	0.47671330D 02	0.66308183D 01	0.47726118D 02	0.56275703D 01
1.00	0.47139037D 02	0.70444374D 01	0.47185790D 02	0.60420051D 01
2.00	0.42887635D 02	0.10246297D 02	0.42885070D 02	0.92571619D 01
3.00	0.39922458D 02	0.12515287D 02	0.39911880D 02	0.11524984D 02
4.00	0.37700027D 02	0.14248877D 02	0.37691450D 02	0.13253699D 02
5.00	0.35931449D 02	0.15618489D 02	0.35926308D 02	0.14620378D 02
6.00	0.34456313D 02	0.16738301D 02	0.34454081D 02	0.15739062D 02
7.00	0.33182165D 02	0.17686988D 02	0.33182013D 02	0.16687458D 02
8.00	0.32053735D 02	0.18516933D 02	0.32054889D 02	0.17517347D 02
9.00	0.31036555D 02	0.19262172D 02	0.31038505D 02	0.18262529D 02
10.00	0.30108562D 02	0.19944650D 02	0.30110801D 02	0.18944906D 02
12.00	0.28464140D 02	0.21173523D 02	0.28466474D 02	0.20173554D 02
14.00	0.27045136D 02	0.22269989D 02	0.27046787D 02	0.21269953D 02
16.00	0.25806828D 02	0.23266781D 02	0.25808151D 02	0.22266889D 02
18.00	0.24720592D 02	0.24182746D 02	0.24720892D 02	0.23183141D 02
20.00	0.23761686D 02	0.25030316D 02	0.23762410D 02	0.24031039D 02
25.00	0.21815722D 02	0.26903836D 02	0.21815965D 02	0.25905148D 02
30.00	0.20349746D 02	0.28494638D 02	0.20347983D 02	0.27496015D 02
35.00	0.19208998D 02	0.29859776D 02	0.19208782D 02	0.28860867D 02
40.00	0.18296028D 02	0.31039520D 02	0.18295465D 02	0.30040218D 02
45.00	0.17537369D 02	0.32065494D 02	0.17537744D 02	0.31065843D 02
50.00	0.16889659D 02	0.32963824D 02	0.16887864D 02	0.31963912D 02
60.00	0.15794867D 02	0.34461238D 02	0.15793339D 02	0.33461087D 02
70.00	0.14858923D 02	0.35665345D 02	0.14861310D 02	0.34665186D 02
80.00	0.14028114D 02	0.36665633D 02	0.14025183D 02	0.35665557D 02
90.00	0.13254052D 02	0.37520579D 02	0.13255888D 02	0.36520599D 02

TABLE 4 (CONTINUED)

	Cs		Cs+	
$Q=(Ka_0)^2$	F(Q)	S(Q)	F(Q)	S(Q)
100.00	0.12544779D 02	0.38268194D 02	0.12542535D 02	0.37268300D 02
200.00	0.78347145D 01	0.42920763D 02	0.78368817D 01	0.41921006D 02
300.00	0.59352663D 01	0.45394096D 02	0.59374132D 01	0.44394143D 02
400.00	0.50853506D 01	0.47008877D 02	0.50830750D 01	0.46008851D 02
500.00	0.45856299D 01	0.48177517D 02	0.45862304D 01	0.47177499D 02
600.00	0.42317122D 01	0.49071341D 02	0.42305723D 01	0.48071355D 02
700.00	0.38549666D 01	0.49777172D 02	0.38556178D 01	0.48777212D 02
800.00	0.35608485D 01	0.50345294D 02	0.35614782D 01	0.49345344D 02
900.00	0.32657298D 01	0.50809593D 02	0.32659960D 01	0.49809651D 02
1000.00	0.30440035D 01	0.51193424D 02	0.30449735D 01	0.50193476D 02
2000.00	0.16941190D 01	0.52985988D 02	0.16945507D 01	0.51985990D 02
3000.00	0.12356145D 01	0.53613362D 02	0.12355456D 01	0.52613365D 02
4000.00	0.10372699D 01	0.53968596D 02	0.10379708D 01	0.52968609D 02
5000.00	0.93715315D 00	0.54207934D 02	0.93691987D 00	0.53207949D 02
6000.00	0.86404533D 00	0.54379973D 02	0.86385421D 00	0.53379991D 02
7000.00	0.84676246D 00	0.54506822D 02	0.84619116D 00	0.53506839D 02
8000.00	0.73796975D 00	0.54603575D 02	0.73737438D 00	0.53603593D 02
9000.00	0.72143686D 00	0.54676646D 02	0.94317779D-01	0.53676661D 02
10000.00	0.59530196D 00	0.54734433D 02	0.18749793D 00	0.53734448D 02

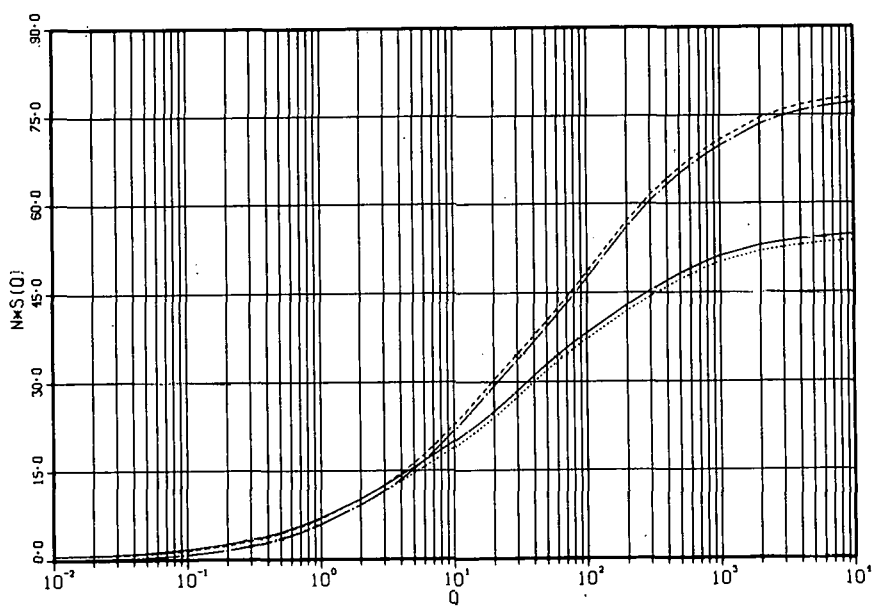

FIG. 2.--Incoherent-scattering functions $S_{inc}(Q)$ as functions of $Q=(Ka_0)^2$, where K is the momentum transfer, a_0 is the Bohr radius, and N is the number of electrons. ---, Au; —·—, Au^+; ——, Cs; and ..., Cs^+.

TABLE 5

COHERENT AND INCOHERENT ATOMIC FORM FACTORS FROM THE HARTREE-FOCK WAVEFUNCTIONS

	AU		AU+	
$Q=(Ka_0^2)$	F(Q)	S(Q)	F(Q)	S(Q)
0.0	0.79000000D 02	0.0	0.78000000D 02	0.0
0.01	0.78893321D 02	0.61291718D 00	0.77920904D 02	0.84773490D-01
0.02	0.78787647D 02	0.72357102D 00	0.77842086D 02	0.16880736D 00
0.03	0.78682956D 02	0.83205612D 00	0.77763544D 02	0.25211311D 00
0.04	0.78579224D 02	0.93845800D 00	0.77685276D 02	0.33469978D 00
0.05	0.78476430D 02	0.10428579D 01	0.77607281D 02	0.41657627D 00
0.06	0.78374553D 02	0.11453328D 01	0.77529557D 02	0.49775137D 00
0.07	0.78273572D 02	0.12459559D 01	0.77452103D 02	0.57823373D 00
0.08	0.78173467D 02	0.13447968D 01	0.77374918D 02	0.65803190D 00
0.09	0.78074220D 02	0.14419216D 01	0.77297999D 02	0.73715431D 00
0.10	0.77975811D 02	0.15373931D 01	0.77221345D 02	0.81560927D 00
0.20	0.77034167D 02	0.24130223D 01	0.76469080D 02	0.15651981D 01
0.30	0.76159708D 02	0.31741775D 01	0.75741790D 02	0.22563887D 01
0.40	0.75341028D 02	0.38506744D 01	0.75038161D 02	0.28958315D 01
0.50	0.74569491D 02	0.44620629D 01	0.74356974D 02	0.34893402D 01
0.60	0.73838436D 02	0.50216640D 01	0.73697091D 02	0.40420051D 01
0.70	0.73142644D 02	0.55388988D 01	0.73057454D 02	0.45582894D 01
0.80	0.72477956D 02	0.60206690D 01	0.72437074D 02	0.50421127D 01
0.90	0.71841007D 02	0.64721977D 01	0.71835029D 02	0.54969220D 01
1.00	0.71229038D 02	0.68975541D 01	0.71250455D 02	0.59257525D 01
2.00	0.66112255D 02	0.10218018D 02	0.66209882D 02	0.92458038D 01
3.00	0.62199192D 02	0.12620959D 02	0.62269976D 02	0.11618732D 02
4.00	0.59046263D 02	0.14586641D 02	0.59084759D 02	0.13564262D 02
5.00	0.56427039D 02	0.16295329D 02	0.56441465D 02	0.15265787D 02
6.00	0.54202629D 02	0.17826152D 02	0.54201234D 02	0.16797258D 02
7.00	0.52280161D 02	0.19218832D 02	0.52269161D 02	0.18193921D 02
8.00	0.50594260D 02	0.20496309D 02	0.50577972D 02	0.19476112D 02
9.00	0.49097260D 02	0.21673778D 02	0.49078575D 02	0.20657813D 02
10.00	0.47753477D 02	0.22762538D 02	0.47734278D 02	0.21749906D 02
12.00	0.45422564D 02	0.24709157D 02	0.45405435D 02	0.23700575D 02
14.00	0.43447262D 02	0.26395483D 02	0.43433910D 02	0.25388589D 02
16.00	0.41730030D 02	0.27868551D 02	0.41720676D 02	0.26862246D 02
18.00	0.40206609D 02	0.29166835D 02	0.40200883D 02	0.28160777D 02
20.00	0.38833386D 02	0.30321867D 02	0.38830664D 02	0.29316057D 02
25.00	0.35878175D 02	0.32739477D 02	0.35880366D 02	0.31734721D 02
30.00	0.33406172D 02	0.34692832D 02	0.33410364D 02	0.33689354D 02
35.00	0.31278557D 02	0.36345541D 02	0.31282918D 02	0.35343103D 02
40.00	0.29418735D 02	0.37791697D 02	0.29422927D 02	0.36789979D 02
45.00	0.27780855D 02	0.39086722D 02	0.27783745D 02	0.38085509D 02
50.00	0.26330432D 02	0.40264775D 02	0.26332756D 02	0.39263963D 02
60.00	0.23899889D 02	0.42352486D 02	0.23899857D 02	0.41352412D 02
70.00	0.21970132D 02	0.44166965D 02	0.21970571D 02	0.43167597D 02
80.00	0.20432309D 02	0.45772979D 02	0.20430703D 02	0.44774192D 02
90.00	0.19191640D 02	0.47213008D 02	0.19191856D 02	0.46214581D 02

TABLE 5 (CONTINUED)

$Q=(Ka_0^2)$	AU F(Q)	AU S(Q)	AU+ F(Q)	AU+ S(Q)
100.00	0.18187540D 02	0.48516672D 02	0.18184940D 02	0.47518394D 02
200.00	0.13412636D 02	0.57067172D 02	0.13412933D 02	0.56066917D 02
300.00	0.10937600D 02	0.61489518D 02	0.10938944D 02	0.60489400D 02
400.00	0.90307288D 01	0.64193646D 02	0.90315915D 01	0.63193968D 02
500.00	0.76131437D 01	0.66055307D 02	0.76125443D 01	0.65055705D 02
600.00	0.66212419D 01	0.67443057D 02	0.66227077D 01	0.66443333D 02
700.00	0.59108572D 01	0.68536858D 02	0.59130073D 01	0.67536989D 02
800.00	0.53820807D 01	0.69432988D 02	0.53835837D 01	0.68432978D 02
900.00	0.50310941D 01	0.70189567D 02	0.50332142D 01	0.69189471D 02
1000.00	0.47372286D 01	0.70841485D 02	0.47401511D 01	0.69841345D 02
2000.00	0.32705309D 01	0.74506675D 02	0.32680700D 01	0.73506683D 02
3000.00	0.22679061D 01	0.75992322D 02	0.22687074D 01	0.74992361D 02
4000.00	0.17555901D 01	0.76731647D 02	0.17539363D 01	0.75731662D 02
5000.00	0.14342256D 01	0.77170248D 02	0.14353446D 01	0.76170263D 02
6000.00	0.12695583D 01	0.77467971D 02	0.12696576D 01	0.76467982D 02
7000.00	0.13039267D 01	0.77688751D 02	0.13036720D 01	0.76688760D 02
8000.00	0.10757659D 01	0.77864249D 02	0.10753539D 01	0.76864264D 02
9000.00	0.11770845D 01	0.78006543D 02	0.11767693D 01	0.77006557D 02
10000.00	0.95550223D 00	0.78126160D 02	0.95511124D 00	0.77126180D 02

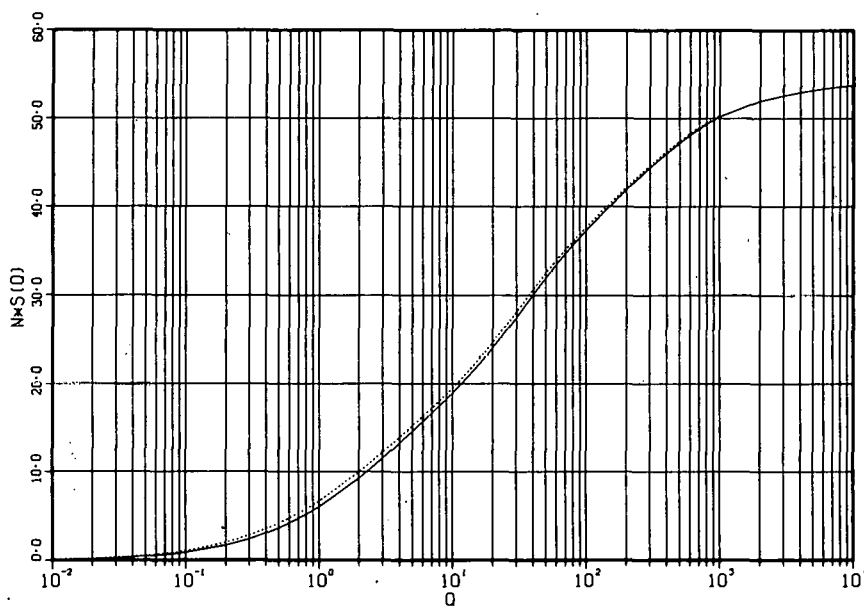

FIG. 3.--Incoherent-scattering functions $S_{inc}(Q)$ as functions of $Q=(Ka_0)^2$. ..., Xe; ——, Cs^+; N is the number of electrons.

The data obtained here were compared with those published earlier for neutral atoms and almost identical results were obtained. In Figure 3, our results for Cs^+ were also compared with the data for xenon.[4] The calculations are seen to be similar, demonstrating that the number of electrons in the atom or ion is the dominant feature in determining the shape of these curves.

References

1. R. L. Martin and R. C. Arnold, ANL/HEP-76-13 (1976).
2. H. Levy, II, Phys. Rev. 185, 7 (1969).
3. G. H. Gillespie, Phys. Rev. A, to be published.
4. J. H. Hubbell, W. J. Veigele, E. A. Briggs, R. T. Brown, D. T. Cromer, and R. J. Howerton, J. Phys. Chem. Ref. Data 4, 471 (1975).
5. Y.-K. Kim and M. Inokuti, Phys. Rev. 165, 39 (1968).
6. J.-P. Desclaux, private communication.

COMPARISON OF THE BORN AND GLAUBER CROSS SECTIONS FOR THE 2s → 3p TRANSITION OF H

F. T. Chan,*† C. H. Chang,† M. Lieber,† and Y.-K. Kim

Minima in the generalized oscillator strength for the 2s → 3p transition of H deduced from the Glauber approximation are found to shift from the Born approximation results in qualitative agreement with known experimental data on the resonance transitions of rare gases and Hg.

Introduction

The Born cross sections for discrete excitations often show undulations in angular distributions arising from the zero minima in the corresponding generalized oscillator strength (GOS). The structure in the GOS comes from a combination of the nodes in the initial- and final-state wavefunctions of the target atom and the nodes in the transition operator.[1,2] Predictions from the Born cross sections have been verified qualitatively in many experiments.‡

In the Born approximation, the GOS as a function of the momentum transfer, $\vec{K}\hbar$, is independent of the incident energy, and hence the positions of the minima and maxima in the GOS remain fixed as incident energy is varied. The minima in the Born GOS occur when the transition matrix element changes sign, and therefore, the GOS vanishes at the minima.

Experimental data, however, differ from the Born results in three aspects: (a) the "experimental" GOS does not vanish at the minimum, (b) the magnitude of the GOS at the minimum increases as the incident energy is reduced (down to ~ 15 times the excitation energy), and (c) the position of the first minimum (expressed in $\vec{K}$) is shifted toward smaller $\vec{K}$ at intermediate to low incident electron energies (< 500 eV). Owing to the low intensity for large angle scattering, subsequent minima at higher $\vec{K}$ have not been observed in any experiment so far.

---

*Participant, Center for Educational Affairs Faculty Research Participation Program, June 1—August 23, 1976.

†Department of Physics, University of Arkansas, Fayetteville, Arkansas 92701.

‡See Ref. 3 and references therein.

Recently, the Glauber approximation was shown to produce cross sections in excellent agreement with various electron-impact data on small atoms at lower incident energies where the Born cross sections compare poorly with the experiment.* One drawback of the Glauber approximation is that various integrals needed for the transition matrix element are so complicated that in practice only analytic (Roothaan-type) wavefunctions can be used. Unfortunately, high-quality, analytic wavefunctions for excited states are scarce, and production of such wavefunctions are costly compared to numerical wavefunctions.

To provide for a sensitive test of the Glauber approximation at lower incident energies, we studied the dependence of the minima and maxima of the "Glauber" GOS on incident energies. The "Glauber" GOS, $f^G(K)$, is deduced from the Glauber cross section, using the same relation as that between the Born cross section and the Born GOS:

$$f^G(K) = \frac{d\sigma^G}{d\Omega} \frac{E}{R} \frac{k}{k'} \frac{(Ka_0)^2}{4a_0^2} , \qquad (1)$$

where $d\sigma^G/d\Omega$ is the differential cross section in the Glauber approximation, E/R is the excitation energy in rydbergs, a_0 is the Bohr radius. The momentum transfer, $\vec{K}\hbar$, is defined in terms of the incident-electron momentum before and after the collision, $\vec{k}\hbar$ and $\vec{k'}\hbar$, respectively:

$$\vec{K} = \vec{k} - \vec{k'} . \qquad (2)$$

Contrary to the Born GOS, the Glauber GOS is dependent on the incident energy.

To avoid uncertainties from approximate wavefunctions, we chose the $2s \rightarrow 3p$ transition of H, which is the simplest case for which the GOS has minima both in the Born and Glauber approximations.

The Born GOS

The GOS in the Born approximation is defined as

---

*See, for instance, Ref. 4 and references therein.

$$f^B(K) = \frac{E}{R} \sum_m \frac{|\langle 3pm|e^{i\vec{K}\cdot\vec{r}}|2s\rangle|^2}{(Ka_0)^2} , \quad (3)$$

where $\vec{r}$ is the position vector of the bound electrons, and m is the magnetic quantum number. When appropriate expressions for the wavefunctions[5] are substituted in Eq. 3, we get

$$f^B(K) = \frac{E}{R} \frac{2^8}{3^4} (Q^2 - \frac{28}{15}\lambda^2 Q + \frac{1}{3}\lambda^4)^2 (Q + \lambda^2)^{-10} , \quad (4)$$

where $E/R = 5/36$ for the $2s \rightarrow 3p$ transition, $Q = (Ka_0)^2$, and $\lambda = 5/6$. Note that only the m = 0 substate of 3p contributes to $f^B(K)$ when $\vec{K}$ is taken as the axis of quantization. The Born GOS has two minima at the roots of

$$Q^2 - \frac{28}{15}\lambda^2 Q + \frac{1}{3}\lambda^4 = 0 ,$$

i.e., at Q = 0.139 and 1.16.

The Glauber GOS

The Glauber cross section, $d\sigma^G/d\Omega$ is given in terms of the scattering amplitude F^G:

$$\frac{d\sigma^G}{d\Omega} = \frac{k'}{k} \sum_m |F^G(2s \rightarrow 3pm; K)|^2 , \quad (5)$$

where the amplitude is defined, in turn, as

$$F^G = \frac{ik}{2\pi} \int \psi_{3pm}^*(\vec{r}) \left[1 - \left(\frac{|\vec{b} - \vec{s}|}{b}\right)^{2i\eta}\right] \psi_{2s}(\vec{r}) e^{i\vec{K}\cdot\vec{b}} d^2b d\vec{r} , \quad (6)$$

where $\eta = (ka_0)^{-1}$. Customary assumptions and definitions of variables of the Glauber approximation are adopted in Eq. 6 also.[6] For instance, $\vec{b}$ and $\vec{K}$ are perpendicular to $\vec{k}$, and $\vec{s}$ is the projection of $\vec{r}$ (of the bound electron) on the plane perpendicular to $\vec{k}$. With the axis of quantization along $\vec{k}$, the amplitude F^G for m = 0 vanishes, and F^G for m = +1 and -1 are the same.[6] Hence, Eq. 5 becomes

$$\frac{d\sigma^G}{d\Omega} = 2(k'/k)\left|F^G(2s \rightarrow 3p,\ m=1;\ K)\right|^2 . \qquad (5a)$$

The scattering amplitude, F^G, can be expressed in a closed form, though complicated, in terms of a generating function:[7]

$$F^G(2s \rightarrow 3p,\ m=1;\ K) = ie^{-i\phi}\frac{\sqrt{2}}{27}\left[\frac{\partial I}{\partial\lambda} + \frac{2}{3}\frac{\partial^2 I}{\partial\lambda^2} + \frac{1}{12}\frac{\partial^3 I}{\partial\lambda^3}\right]_{\lambda=5/6} \qquad (7)$$

where ϕ is the azimuth of $\vec{K}$ in the plane containing $\vec{b}$ and $\vec{K}$, and the generating function I is given by

$$I(\lambda,K) = \frac{16\pi\eta^2}{e^{\pi\eta} - e^{-\pi\eta}}\ \frac{1}{\lambda^2(Ka_0)^3}\left(\frac{Ka_0}{\lambda}\right)^{2i\eta}$$

$$\times\left\{(1-i\eta)\,{}_2F_1(2-i\eta,\ 1-i\eta;\ 1;\ -\lambda^2/K^2a_0^2)\right.$$

$$\left. -(1+\eta^2)\,{}_2F_1(2-i\eta,\ 1-i\eta;\ 2;\ -\lambda^2/K^2a_0^2)\right\}, \qquad (8)$$

with the hypergeometric functions, ${}_2F_1$. After some manipulation, one can reduce $I(\lambda,K)$ to a form suitable for the high incident energy limit, $(\eta \rightarrow 0)$:

$$I(\lambda,K) = I_0(\lambda,K) + i\eta I_1(\lambda,K) + O(\eta^2) \qquad (9)$$

where $\chi \equiv \lambda^2/(Ka_0)^2$ and

$$I_0(\lambda,K) = 8(Ka_0)^{-5}(1+\chi)^{-2}, \qquad (10)$$

and

$$I_1(\lambda,K) = \lambda^{-2}(Ka_0)^{-3}(1+\chi)^{-2}$$

$$\times\{-2 + \chi(1+\ln\chi) + (2+\chi^{-1}-\chi)\ln(1+\chi)\}\ . \qquad (11)$$

In the limit $\eta \rightarrow 0$, the substitution of Eq. 10 into Eq. 7 produces $[f^G(K)]_{\eta=0} = f^B(K)$, as expected. For lower incident energies, one can calculate the minima and maxima of the Glauber GOS by taking the roots of $\partial f^G/\partial(K^2) = 0$ after substituting Eqs. 5a, 7, and 8 into 1. The resulting expressions are too cumbersome to reproduce here, but the trajectories of the

minima and maxima of the Glauber GOS as functions of $\eta = (ka_0)^{-1}$ are presented in Figure 1. The values of the Glauber GOS at the first minumum and the following maximum is listed in Table 1.

Conclusion

First of all, since the Glauber amplitude is complex (Eqs. 8 and 9), the minima in the Glauber GOS do not vanish, and this is in accord with experimental observations.* Secondly, not only do the positions of the minima change as the incident energy is reduced, but also the number of minima apparently depends on the incident energy. At very high incident energy, the Glauber GOS reduces to the Born GOS, with corresponding maxima and minima. As is shown in Table 1, heights of the GOS at the extrema increase as the incident energy is reduced to ~ 15 times the threshold energy (1.89 eV) and the heights reduce as the incident energy is lowered further. The increasing heights are in qualitative agreement with the experimental data[8] on the resonance transition of Hg. There are, however, no experimetal data to check the decreasing heights.

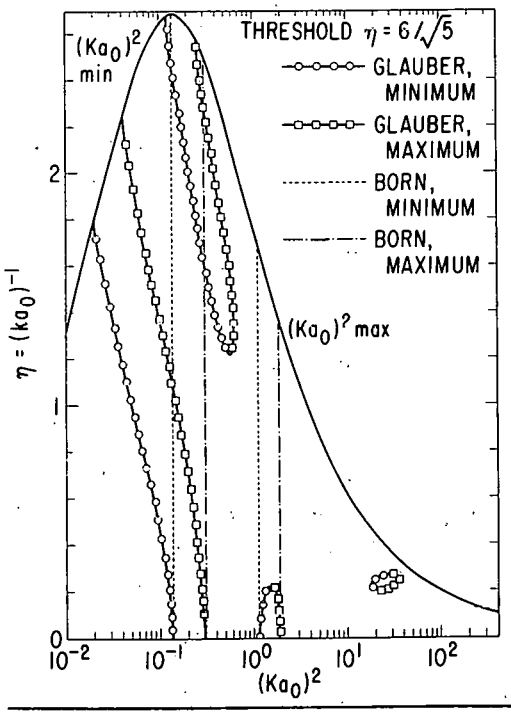

FIG. 1.--Trajectories of the minima and maxima in the generalized oscillator strengths as a function of the momentum transfer (in a.u.) Ka_0 and $\eta = (ka_0)^{-1}$, where ka_0 is the incident electron momentum in a.u. The outermost curve marked $(Ka_0)^2_{min}$ and $(Ka_0)^2_{max}$ are the lower and upper limits of the momentum transfer.

*For the best illustrations of the energy dependence of the experimental GOS, see Ref. 8.

TABLE 1. Values of the Glauber GOS at the First Minimum and Maximum

η	T/E^a	Q_{min}	f^G_{min} ($\times 10^{-3}$)	Q_{max}	f^G_{max} ($\times 10^{-2}$)
0.10	720	0.137	0.635	0.295	0.962
0.15	320	0.134	1.367	0.289	1.054
0.20	180	0.130	2.287	0.282	1.176
0.25	115.2	0.125	3.307	0.274	1.322
0.30	80	0.120	4.334	0.266	1.483
0.35	58.8	0.114	5.287	0.257	1.651
0.40	45	0.108	6.099	0.249	1.818
0.45	35.6	0.102	6.726	0.241	1.975
0.50	28.8	0.0962	7.152	0.233	2.116
0.75	12.8	0.0698	6.770	0.193	2.488
1.0	7.2	0.0501	4.841	0.152	2.412
1.1	5.95	0.0440	4.163	0.135	2.339
1.2	5	0.0392	3.598	0.121	2.270
1.3	4.26	0.0343	3.126	0.107	2.213
1.4	3.67	0.0305	2.742	0.0956	2.171
1.5	3.2	0.0271	2.427	0.0852	2.142

[a] T/E = incident energy in units of the excitation energy (1.89 eV)

With the remarkable progress in measuring the electron-impact cross sections of the metastable hydrogen atom,[9] we may not have to wait long for an experimental verification of the Glauber theory in greater detail, although the second and third minima and maxima are too small in magnitude for experimental detection.

References

1. Y.-K. Kim, M. Inokuti, G. E. Chamberlain, and S. R. Mielczarek, Phys. Rev. Lett. 21, 1146 (1968).
2. M. Matsuzawa, K. Omidvar, and M. Inokuti, J. Phys. B 9, 2173 (1976).
3. T. C. Wong, J. S. Lee, and R. A. Bonham, Phys. Rev. A 11, 1963 (1975).
4. F. T. Chan and C. H. Chang, Phys. Rev. A 11, 1097 (1975).
5. H. A. Bethe and E. E. Salpeter, Quantum Mechanics of One- and Two-Electron Atoms, Springer Verlag, Berlin, p. 15 (1957).
6. H. Tai, R. H. Bassel, E. Gerjuoy, and V. Franco, Phys. Rev. A 1, 1819 (1970).
7. B. K. Thomas and E. Gerjuoy, J. Math. Phys. 12, 1567 (1971).
8. F. Hanne and J. Kessler, Phys. Rev. A 5, 2457 (1972).
9. A. J. Dixon, A. von Engel, and M. F. A. Harrison, Proc. R. Soc. (London) A 343, 333 (1975).

SYSTEMATICS OF ZERO-ENERGY PHASE SHIFTS FOR ATOMIC IONS

C. E. Theodosiou,* J. L. Dehmer, U. Fano,* and M. Inokuti

In an ongoing study to map out the gross systematics of properties of atomic ions, we have employed the Hartree-Slater model to calculate the zero-energy phase shifts for atoms between He and Rb at all stages of ionization. The results, presented here as phase-shift surfaces, indicate several pronounced trends in the electronic structure of atomic ions.

At an ionization threshold there is a union between discrete states, usually characterized by their quantum defects and treated by spectroscopic methods, and continuum states, usually characterized by their scattering phase shifts and treated by collision theory. Quantum defect theory,[1] among other things, shows that the apparent discontinuity between these two manifolds of states can easily be removed by suitable renormalization. This reveals the Rydberg series to be an appendage to the continuum so that the most basic wavefunction parameters, phase and amplitude, vary smoothly through threshold. In particular, the quantum defect at the limit of the Rydberg series and the zero-energy scattering phase shift are related simply by

$$\pi\mu_\ell(n \to \infty) = \delta_\ell(E = 0) \ .$$

In approaching the problem of mapping out the behavior of phase shifts as a function of both atomic number and ionic charge, we decided to begin by limiting the scope of the study to a single standard energy. We have chosen as our standard energy the ionization limit where the asymptotic local kinetic energy of the one-electron states equals zero. Consequently, our discussion pertains directly to properties of nearby states both below and above the threshold for ionization. These data are presented as absolute quantum defects, $\mu_\ell(Z,z)$, in Figures 1–3 for $0 \le \ell \le 2$, $1 \le Z \le 37$, and $0 \le z \le Z-1$.

The gross behavior of the three surfaces in Figures 1–3 is understandable once one identifies $\pi\mu_\ell$ as the phase shift relative to the regular solution

*Department of Physics, University of Chicago, Chicago, Illinois 60637

of a hydrogenic field of charge $z+1$. Consequently, μ_ℓ is zero along the isoelectronic cut $z=Z-1$, corresponding to a single electron moving in a pure Coulomb field of charge Z. Elsewhere on the $\mu_\ell(Z,z)$ surfaces one must consider the strength of the attractive core potential $V_{CORE}(r)$, where

$$|V_{CORE}(r)| = |V_{TOTAL}(r)| - |2(z+1)/r| ,$$

since it is the additional attraction of the partially screened nuclear field in the ionic core which induces the phase difference between the ionic wavefunction and the hydrogen-like function characteristic of a pure Coulomb field with the net charge of the ion. Generally speaking, isonuclear cuts exhibit decreasing μ_ℓ with increasing ionic charge brought on by an increasing reference phase. For an isoionic cut, the reference phase is fixed and μ_ℓ increases with increasing Z as the core potential becomes more attractive with increasing nuclear charge.

Comparing the three surfaces in Figures 1–3, it is clear that for a given (Z,z), $\mu_\ell > \mu_{\ell+1}$. This is a consequence of the repulsive centrifugal potential, $\ell(\ell+1)/r^2$, implicit in $V_{TOTAL}(r)$ above, which causes the net $V_{CORE}(r)$ to decrease with increasing angular momentum. Put another way, lower angular momentum electrons approach the nucleus more closely during their penetration into the core and, therefore, accumulate more phase shift. For instance, s electrons can penetrate with finite probability all the way to the K shell, whereas p, d, etc. electrons can penetrate only into the L, M, etc. shells.

The most outstanding substructures on the surfaces in Figures 1–3 are the creases along the isoelectronic paths $Z-z=10$ or 28. These electron numbers correspond to the closing of the L and M shell, respectively, according to hydrogenic ordering of subshells, and do not correspond to the most stable neutral electron numbers of 10 and 18. As discussed in more detail below, the delicate balance between Coulomb interactions and centrifugal forces in neutral atoms that results in the filling of levels according to the Aufbau principle shifts very rapidly toward hydrogenic ordering with the re-

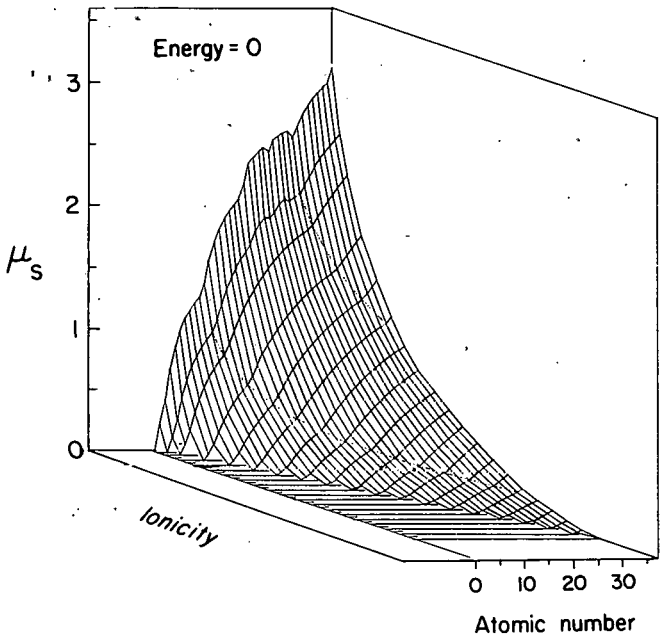

FIG. 1.--s-wave, zero-energy quantum defects for all atomic ions with $1 \leq Z \leq 37$.

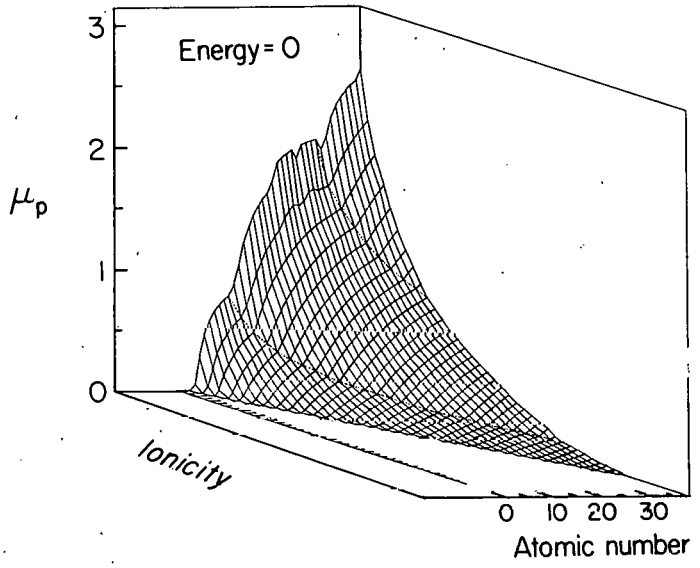

FIG. 2.--p-wave, zero-energy quantum defects for all atomic ions with $1 \leq Z \leq 37$.

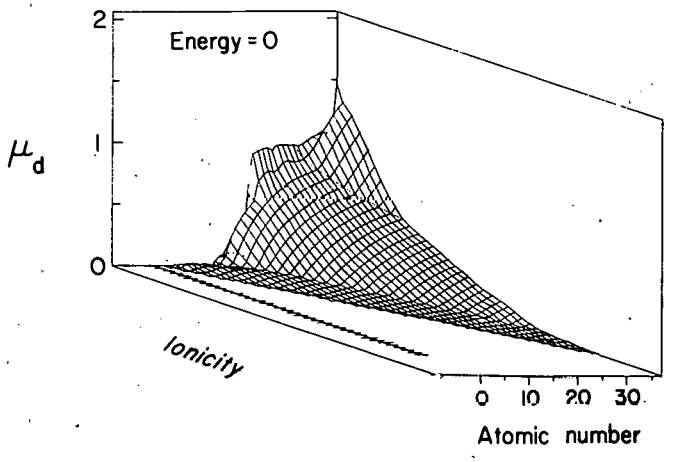

FIG. 3.--d-wave, zero-energy quantum defects for all atomic ions with $1 \leq Z \leq 37$.

moval of one or two electrons (for the ranges of Z treated here). Consequently, nearly all atomic ions will exhibit their greatest local stability at the magic numbers 10, 28, 60. This closed-shell stability will be reflected in many other atomic parameters which will be discussed elsewhere. In the case of zero-energy phase shifts, ions in these isoelectronic sequences represent the starting points for upturns in the function $\mu_\ell(Z,z)$ with increasing Z. This is most clearly observed in the $\ell=1,2$ surfaces and is due to the starting of a new shell in the core which adds to the phase shift producing capacity of V_{CORE}. Due to the generally larger penetration of lower ℓ wavefunctions, reflected in their larger phase shifts, the magic-number crease is less pronounced for low ℓ than for high ℓ. The crease is most dramatic at the $N=10$ isoelectronic cut for $\ell=2$, where μ_2 remains vanishingly small until the $n=3$ shell begins to fill. Owing to the large centrifugal repulsion for $\ell=2$, d waves have finite penetration only as far as the M shell. Consequently, the core must contain an M electron before the $\ell=2$ phase shift departs appreciably from the hydrogenic limit. For the case of f waves, departure from $\mu_3 \sim 0$ is delayed until $Z-z>60$, which accounts for the absence of an $\ell=3$ surface in this report.

The third level of substructure is the jagged and, for $\ell=2$, step-like variations in the isoionic curves $z=0,1$. The $z=0$ curve has been discussed extensively by Manson[2] and Fano et al.,[3] and the jagged structures have been accounted for. Generally they derive from the delicate balance between Coulomb interactions and centrifugal forces in neutral atoms, which causes the subshells to fill in an irregular fashion as the periodic table is traversed. The order of filling obeys the Aufbau principle fairly well although there are several exceptions. Thus, the 4s subshell fills before the 3d except for $Z=24,29$, where a 4s is transferred to the 3d shell to achieve the enhanced stability of a d^5 or d^{10} configuration. These discontinuities in the order of filling result in discontinuities in all atomic properties, even those involving deep inner shells, and are clearly reflected in the zero-energy phase shifts.

For $\ell=2$, the balance among the forces acting on the electrons is known[4] to produce a potential barrier on the fringes of the electron distribution ($r \sim 1-2$ a.u.). This potential barrier separates the inner atomic well from the

weaker Coulomb attraction outside the atoms so that a bimodel potential is formed. This causes the stair-like variation in $\mu_2(Z,0)$ as the d wave cannot smoothly penetrate the core with increasing Z. Rather, it is held outside the core in the outer well until the inner well can support an entire loop of a d-type wavefunction. This occurs one atomic number before a d subshell becomes occupied in the ground state and is accompanied by a sudden increase in phase by $\sim \pi$ as a loop of the wavefunction rapidly penetrates the classically forbidden region at the position of the barrier.

Note that for $z=1$, the jagged structure persists, although it is diminished, and by $z=2$ it is gone. The stair-like structure for $\ell=2$, however, has completely vanished for $z=1$ since the additional charge is enough to shift the balance between Coulomb and centrifugal forces resulting in a monotonic potential at $r \sim 1-2$ a.u.

We express our gratitude to Dr. J.-P. Desclaux for providing his Hartree-Slater program, which we used to generate atomic-ion potentials.

References

1. M. J. Seaton, Mon. Not. R. Astron. Soc. 118, 504 (1958).
2. B. T. Manoon, Phys. Rev. 182, 97 (1969).
3. U. Fano, C. E. Theodosiou, and J. L. Dehmer, Rev. Mod. Phys. 48, 49 (1976).
4. A. R. P. Rau and U. Fano, Phys. Rev. 167, 7 (1968).

ON THE THEORY OF IONIZATION BY ELECTRON COLLISIONS*

U. Fano† and Mitio Inokuti

Cross sections for inelastic collisions of fast electrons have long been accessible to rather dependable calculation by the (first) Born approximation. This approximation fails at lower energies, notably in the range of the cross-section maxima and nearer the threshold. Alternative methods of calculation have been applied in this range, but with only limited success, owing, we think, to our poor understanding of the basic features of the low-energy collisions. [For example, it is often difficult to disentangle effects of two kinds of approximations; schematization of the Hamiltonian (such as the use of a phenomenological potential) on the one hand, and an analytical or numerical approximation of its solution on the other.] However, our qualitative understanding has recently progressed considerably to a point where we may attempt at least a sketchy survey of the whole problem. Our immediate objective is to point out the areas in which one can proceed confidently by current techniques and those where further development work seems in order.

In low-energy collisions, the incident and target electrons intermingle to such an extent that we feel it necessary to treat them as a single many-electron complex, except for the cases of high incident angular momenta in which the incident electron fails to penetrate the target. An ionizing collision is then represented by a state of the continuous spectrum of this complex, which evolves from an initial channel with a single electron outside the target to a final channel with two detached electrons.

Detachment of two electrons from a complex has been poorly studied thus far. Accordingly, current computing methods are inherently incapable of

---

*Summary of an Argonne topical report, ANL-76-80 (June 1976).

†Department of Physics, The University of Chicago, Chicago, Illinois 60637. Also Appointee, Faculty Research Participation Program, Center for Educational Affairs, ANL. Work performed in part through Contract No. COO-1674-119.

calculating the probability of this transition from the initial channel to the final channel under general conditions. However, a new R-matrix approach proposed here should permit one to characterize the critical central state of the transition by an effort comparable to a few-configuration SCF calculation of discrete spectral levels. It is suggested that such calculations alone might be adequate to estimate total ionization cross sections to about 10 to 20%, and that they could be programmed (at this level of accuracy) with a rather modest effort. When the initial target itself an ion of sufficiently high charge, the transition probability should be amenable to evaluation by a first-order perturbation theory.

We treat collisions of electrons with both neutral atoms and ionized atoms with considerable emphasis on the latter. However, most of our considerations will apply to molecules and to molecular ions as well.

A comprehensive framework for our discussion is provided by cross-section formulas employed extensively by Seaton,[1,2] and also from a complementary point of view, by Platzman's school (as described in Ref. 3). These formulas represent cross sections as sums of numerous terms, and we shall map out which of the terms can be calculated appropriately by various methods for various ranges of incident energy, types of transitions, or properties of target species. The formulation also lends itself to applications of sum rules ranging from familiar ones to others whose existence is merely suspected at this time.

References

1. M. J. Seaton, Phil. Trans. R. Soc. A245, 469 (1953).
2. M. J. Seaton, Advances in Atomic and Molecular Physics, Vol. 11, D. R. Bates and B. Bederson, Eds., Academic Press, New York, p. 83 (1975).
3. U. Fano, Radiat. Res., 64, 217 (1975).

BORN-APPROXIMATION CALCULATIONS OF THE ENERGY AND ANGULAR DISTRIBUTION OF ELECTRONS EJECTED BY PROTON-IMPACT IONIZATION OF HELIUM

D. H. Madison,* R. Calhoun,† S. T. Manson,‡ and A. Msezane§

Cross sections for the energy and angular distributions of electrons ejected by proton-impact ionization of helium have been calculated in the Born approximation. Results are presented for incident energies from 1 keV to 200 MeV.

Electron spectroscopy is a powerful tool which can be used to obtain information on the details of ion-atom collisions. In addition, the energy and angular distribution of ejected electrons is of importance in numerous areas including plasma physcis, atmospheric and space physics, and radiation physics. Recent work[1-3] has shown Born-approximation calculations of proton-impact ionization using fairly good non-hydrogenic atomic wavefunctions for initial discrete and final continuum states to be rather good for ionization of helium in most ranges. The major exception is for small angles in the proton energy range from ~ 50 keV to several MeV where another process, i.e., charge transfer to the continuum[4,5] is of great importance.

In this paper extensive results are presented for the energy and angular distribution of electrons ejected from helium by proton-impact ionization over a range of incident energies from 1 keV to 200 MeV. The calculations were performed using nonrelativistic Hartree-Slater wavefunctions[6] with no core relaxation via a formulation described in Refs. 1 and 2.

*Department of Physics, Drake University, Des Moines, Iowa 50311

†Department of Physics, Drake University, Des Moines, Iowa 50311. Work supported by the Research Corporation.

‡Consultant, Radiological and Environmental Research Division, Argonne National Laboratory. Department of Physics, Georgia State University, Atlanta, Georgia 30303.

§Department of Physics, Georgia State University, Atlanta, Georgia 30303. Work supported by NSF and U.S. ARO.

TABLE 1. Doubly differential cross section $d^2\sigma/d\epsilon d\Omega$ measured in units of $m^2\ eV^{-1}$ steradian^{-1} for proton-impact ionizatio of helium. In the heading E(RYD) denotes the kinetic energy of ejected electrons and THETA (DEG) is the angle of electron ejection measured in degrees from the incident proton direction. Each page shows a different proton kinetic energy, T, which is indicated in the heading. The FORTRAN notation is used: e.g., 2.46 E-26 means 2.46×10^{-26}.

PROTON ENERGY = .001 MEV

E(RYD)	1	2	4	6	8	12	16	24
E(EV)	13.6	27.2	54.4	81.6	108.8	163.3	217.7	326.5
THETA(DEG)								
0	2.46E-26	1.86E-27	3.42E-29	1.71E-30	1.62E-31	4.24E-33	2.53E-34	3.93E-36
5	2.46E-26	1.86E-27	3.41E-29	1.71E-30	1.62E-31	4.23E-33	2.52E-34	3.92E-36
10	2.45E-26	1.84E-27	3.39E-29	1.70E-30	1.61E-31	4.21E-33	2.51E-34	3.91E-36
15	2.43E-26	1.82E-27	3.35E-29	1.68E-30	1.59E-31	4.17E-33	2.49E-34	3.88E-36
20	2.40E-26	1.79E-27	3.29E-29	1.65E-30	1.57E-31	4.12E-33	2.46E-34	3.84E-36
25	2.36E-26	1.76E-27	3.22E-29	1.62E-30	1.54E-31	4.05E-33	2.43E-34	3.80E-36
30	2.32E-26	1.72E-27	3.14E-29	1.58E-30	1.50E-31	3.97E-33	2.39E-34	3.75E-36
35	2.28E-26	1.68E-27	3.06E-29	1.54E-30	1.47E-31	3.88E-33	2.34E-34	3.69E-36
40	2.23E-26	1.63E-27	2.96E-29	1.50E-30	1.43E-31	3.78E-33	2.29E-34	3.63E-36
45	2.19E-26	1.58E-27	2.86E-29	1.45E-30	1.38E-31	3.67E-33	2.24E-34	3.56E-36
50	2.14E-26	1.53E-27	2.76E-29	1.40E-30	1.34E-31	3.56E-33	2.18E-34	3.48E-36
55	2.09E-26	1.48E-27	2.65E-29	1.35E-30	1.29E-31	3.45E-33	2.13E-34	3.40E-36
60	2.04E-26	1.43E-27	2.55E-29	1.30E-30	1.25E-31	3.33E-33	2.07E-34	3.32E-36
65	2.00E-26	1.38E-27	2.45E-29	1.25E-30	1.20E-31	3.21E-33	2.01E-34	3.24E-36
70	1.96E-26	1.34E-27	2.35E-29	1.20E-30	1.15E-31	3.09E-33	1.95E-34	3.16E-36
75	1.92E-26	1.29E-27	2.26E-29	1.15E-30	1.11E-31	2.98E-33	1.90E-34	3.08E-36
80	1.88E-26	1.25E-27	2.17E-29	1.10E-30	1.06E-31	2.87E-33	1.84E-34	3.00E-36
85	1.85E-26	1.21E-27	2.08E-29	1.06E-30	1.02E-31	2.76E-33	1.79E-34	2.92E-36
90	1.82E-26	1.18E-27	2.00E-29	1.02E-30	9.81E-32	2.66E-33	1.74E-34	2.85E-36
95	1.79E-26	1.15E-27	1.93E-29	9.80E-31	9.43E-32	2.56E-33	1.69E-34	2.77E-36
100	1.77E-26	1.12E-27	1.86E-29	9.44E-31	9.07E-32	2.47E-33	1.64E-34	2.70E-36
105	1.74E-26	1.09E-27	1.80E-29	9.10E-31	8.74E-32	2.38E-33	1.60E-34	2.64E-36
110	1.73E-26	1.07E-27	1.74E-29	8.80E-31	8.43E-32	2.30E-33	1.56E-34	2.57E-36
115	1.71E-26	1.04E-27	1.69E-29	8.52E-31	8.14E-32	2.23E-33	1.52E-34	2.52E-36
120	1.70E-26	1.02E-27	1.64E-29	8.26E-31	7.88E-32	2.16E-33	1.49E-34	2.46E-36
125	1.68E-26	1.01E-27	1.60E-29	8.03E-31	7.64E-32	2.10E-33	1.46E-34	2.41E-36
130	1.67E-26	9.91E-28	1.57E-29	7.82E-31	7.43E-32	2.05E-33	1.43E-34	2.36E-36
135	1.66E-26	9.77E-28	1.53E-29	7.64E-31	7.23E-32	2.00E-33	1.40E-34	2.32E-36
140	1.65E-26	9.65E-28	1.50E-29	7.47E-31	7.06E-32	1.95E-33	1.38E-34	2.29E-36
145	1.65E-26	9.55E-28	1.48E-29	7.33E-31	6.92E-32	1.91E-33	1.36E-34	2.25E-36
150	1.64E-26	9.47E-28	1.46E-29	7.21E-31	6.79E-32	1.88E-33	1.34E-34	2.22E-36
155	1.64E-26	9.40E-28	1.44E-29	7.11E-31	6.68E-32	1.85E-33	1.33E-34	2.20E-36
160	1.64E-26	9.34E-28	1.42E-29	7.03E-31	6.60E-32	1.83E-33	1.32E-34	2.18E-36
165	1.63E-26	9.30E-28	1.41E-29	6.96E-31	6.53E-32	1.81E-33	1.31E-34	2.16E-36
170	1.63E-26	9.26E-28	1.41E-29	6.92E-31	6.48E-32	1.80E-33	1.30E-34	2.15E-36
175	1.63E-26	9.25E-28	1.40E-29	6.89E-31	6.45E-32	1.79E-33	1.30E-34	2.15E-36
180	1.63E-26	9.24E-28	1.40E-29	6.88E-31	6.44E-32	1.79E-33	1.30E-34	2.14E-36

PROTON ENERGY = .005 MEV

E(RYD)	1	2	4	6	8	12	16	24
E(EV)	13.6	27.2	54.4	81.6	108.8	163.3	217.7	326.5
THETA(DEG)								
0	3.45E-24	5.91E-25	2.66E-26	2.06E-27	2.37E-28	8.03E-30	5.88E-31	1.25E-32
5	3.43E-24	5.87E-25	2.64E-26	2.05E-27	2.36E-28	7.98E-30	5.85E-31	1.24E-32
10	3.37E-24	5.75E-25	2.59E-26	2.01E-27	2.31E-28	7.86E-30	5.77E-31	1.23E-32
15	3.27E-24	5.56E-25	2.50E-26	1.94E-27	2.24E-28	7.65E-30	5.64E-31	1.21E-32
20	3.14E-24	5.31E-25	2.39E-26	1.85E-27	2.15E-28	7.38E-30	5.46E-31	1.18E-32
25	2.99E-24	5.02E-25	2.25E-26	1.75E-27	2.04E-28	7.05E-30	5.24E-31	1.14E-32
30	2.82E-24	4.69E-25	2.10E-26	1.64E-27	1.92E-28	6.68E-30	5.00E-31	1.09E-32
35	2.65E-24	4.36E-25	1.95E-26	1.52E-27	1.79E-28	6.28E-30	4.73E-31	1.04E-32
40	2.48E-24	4.02E-25	1.79E-26	1.40E-27	1.65E-28	5.86E-30	4.45E-31	9.93E-33
45	2.31E-24	3.70E-25	1.63E-26	1.28E-27	1.52E-28	5.44E-30	4.16E-31	9.39E-33
50	2.15E-24	3.39E-25	1.49E-26	1.16E-27	1.39E-28	5.03E-30	3.88E-31	8.85E-33
55	2.01E-24	3.11E-25	1.35E-26	1.06E-27	1.27E-28	4.62E-30	3.60E-31	8.31E-33
60	1.88E-24	2.85E-25	1.22E-26	9.57E-28	1.16E-28	4.24E-30	3.34E-31	7.78E-33
65	1.77E-24	2.62E-25	1.11E-26	8.67E-28	1.05E-28	3.89E-30	3.08E-31	7.27E-33
70	1.67E-24	2.42E-25	1.01E-26	7.87E-28	9.59E-29	3.56E-30	2.85E-31	6.79E-33
75	1.58E-24	2.25E-25	9.21E-27	7.15E-28	8.74E-29	3.26E-30	2.63E-31	6.33E-33
80	1.51E-24	2.10E-25	8.43E-27	6.52E-28	7.98E-29	2.98E-30	2.43E-31	5.90E-33
85	1.45E-24	1.97E-25	7.75E-27	5.96E-28	7.30E-29	2.74E-30	2.24E-31	5.51E-33
90	1.40E-24	1.86E-25	7.17E-27	5.48E-28	6.70E-29	2.52E-30	2.08E-31	5.14E-33
95	1.36E-24	1.76E-25	6.66E-27	5.05E-28	6.17E-29	2.32E-30	1.93E-31	4.81E-33
100	1.33E-24	1.68E-25	6.23E-27	4.69E-28	5.70E-29	2.15E-30	1.79E-31	4.51E-33
105	1.30E-24	1.62E-25	5.86E-27	4.37E-28	5.29E-29	1.99E-30	1.67E-31	4.23E-33
110	1.28E-24	1.56E-25	5.54E-27	4.09E-28	4.94E-29	1.86E-30	1.56E-31	3.99E-33
115	1.26E-24	1.51E-25	5.27E-27	3.85E-28	4.63E-29	1.74E-30	1.47E-31	3.77E-33
120	1.25E-24	1.47E-25	5.03E-27	3.65E-28	4.35E-29	1.64E-30	1.38E-31	3.57E-33
125	1.24E-24	1.44E-25	4.84E-27	3.47E-28	4.12E-29	1.54E-30	1.31E-31	3.40E-33
130	1.23E-24	1.41E-25	4.67E-27	3.32E-28	3.92E-29	1.46E-30	1.25E-31	3.24E-33
135	1.22E-24	1.39E-25	4.52E-27	3.19E-28	3.74E-29	1.40E-30	1.19E-31	3.11E-33
140	1.21E-24	1.37E-25	4.40E-27	3.07E-28	3.59E-29	1.34E-30	1.14E-31	2.99E-33
145	1.21E-24	1.35E-25	4.30E-27	2.98E-28	3.47E-29	1.29E-30	1.10E-31	2.89E-33
150	1.21E-24	1.34E-25	4.21E-27	2.90E-28	3.36E-29	1.24E-30	1.06E-31	2.81E-33
155	1.20E-24	1.33E-25	4.15E-27	2.84E-28	3.27E-29	1.21E-30	1.03E-31	2.74E-33
160	1.20E-24	1.32E-25	4.09E-27	2.79E-28	3.21E-29	1.18E-30	1.01E-31	2.68E-33
165	1.20E-24	1.31E-25	4.05E-27	2.75E-28	3.15E-29	1.16E-30	9.94E-32	2.64E-33
170	1.20E-24	1.31E-25	4.02E-27	2.72E-28	3.12E-29	1.15E-30	9.81E-32	2.60E-33
175	1.20E-24	1.31E-25	4.00E-27	2.71E-28	3.09E-29	1.14E-30	9.74E-32	2.59E-33
180	1.20E-24	1.31E-25	4.00E-27	2.70E-28	3.09E-29	1.13E-30	9.71E-32	2.58E-33

PROTON ENERGY = .010 MEV

E(RYD)	1	2	4	6	8	12	16	24
E(EV)	13.6	27.2	54.4	81.6	108.8	163.3	217.7	326.5
THETA(DEG)								
0	1.88E-23	5.01E-24	3.51E-25	3.59E-26	5.11E-27	2.00E-28	1.54E-29	3.32E-31
5	1.86E-23	4.96E-24	3.47E-25	3.56E-26	5.06E-27	1.98E-28	1.53E-29	3.30E-31
10	1.82E-23	4.80E-24	3.36E-25	3.45E-26	4.92E-27	1.93E-28	1.50E-29	3.24E-31
15	1.74E-23	4.55E-24	3.18E-25	3.28E-26	4.69E-27	1.85E-28	1.44E-29	3.14E-31
20	1.64E-23	4.24E-24	2.95E-25	3.06E-26	4.39E-27	1.74E-28	1.37E-29	3.01E-31
25	1.53E-23	3.87E-24	2.69E-25	2.80E-26	4.04E-27	1.62E-28	1.29E-29	2.86E-31
30	1.40E-23	3.49E-24	2.42E-25	2.54E-26	3.67E-27	1.49E-28	1.19E-29	2.68E-31
35	1.27E-23	3.10E-24	2.15E-25	2.26E-26	3.30E-27	1.35E-28	1.10E-29	2.50E-31
40	1.14E-23	2.73E-24	1.89E-25	2.00E-26	2.93E-27	1.21E-28	9.98E-30	2.31E-31
45	1.03E-23	2.39E-24	1.65E-25	1.76E-26	2.58E-27	1.08E-28	9.02E-30	2.12E-31
50	9.16E-24	2.09E-24	1.43E-25	1.53E-26	2.26E-27	9.60E-29	8.10E-30	1.94E-31
55	8.19E-24	1.82E-24	1.24E-25	1.33E-26	1.97E-27	8.48E-29	7.25E-30	1.76E-31
60	7.35E-24	1.60E-24	1.08E-25	1.16E-26	1.72E-27	7.48E-29	6.46E-30	1.60E-31
65	6.64E-24	1.41E-24	9.43E-26	1.01E-26	1.50E-27	6.59E-29	5.75E-30	1.45E-31
70	6.05E-24	1.25E-24	8.28E-26	8.82E-27	1.31E-27	5.81E-29	5.11E-30	1.31E-31
75	5.58E-24	1.13E-24	7.31E-26	7.74E-27	1.14E-27	5.14E-29	4.55E-30	1.18E-31
80	5.20E-24	1.02E-24	6.51E-26	6.83E-27	1.01E-27	4.55E-29	4.06E-30	1.07E-31
85	4.90E-24	9.38E-25	5.85E-26	6.07E-27	8.93E-28	4.05E-29	3.62E-30	9.73E-32
90	4.67E-24	8.70E-25	5.30E-26	5.44E-27	7.95E-28	3.62E-29	3.25E-30	8.85E-32
95	4.49E-24	8.15E-25	4.85E-26	4.91E-27	7.14E-28	3.25E-29	2.93E-30	8.07E-32
100	4.35E-24	7.71E-25	4.47E-26	4.46E-27	6.45E-28	2.93E-29	2.65E-30	7.39E-32
105	4.24E-24	7.35E-25	4.16E-26	4.09E-27	5.87E-28	2.66E-29	2.40E-30	6.79E-32
110	4.17E-24	7.06E-25	3.91E-26	3.78E-27	5.38E-28	2.42E-29	2.20E-30	6.27E-32
115	4.11E-24	6.82E-25	3.69E-26	3.52E-27	4.97E-28	2.22E-29	2.02E-30	5.81E-32
120	4.06E-24	6.63E-25	3.51E-26	3.30E-27	4.62E-28	2.05E-29	1.87E-30	5.41E-32
125	4.03E-24	6.47E-25	3.37E-26	3.12E-27	4.33E-28	1.91E-29	1.73E-30	5.07E-32
130	4.01E-24	6.34E-25	3.24E-26	2.97E-27	4.08E-28	1.78E-29	1.62E-30	4.77E-32
135	3.99E-24	6.24E-25	3.14E-26	2.84E-27	3.87E-28	1.68E-29	1.53E-30	4.51E-32
140	3.98E-24	6.15E-25	3.05E-26	2.73E-27	3.69E-28	1.59E-29	1.45E-30	4.29E-32
145	3.97E-24	6.09E-25	2.98E-26	2.64E-27	3.54E-28	1.51E-29	1.38E-30	4.11E-32
150	3.97E-24	6.03E-25	2.93E-26	2.57E-27	3.42E-28	1.45E-29	1.32E-30	3.95E-32
155	3.96E-24	5.99E-25	2.88E-26	2.51E-27	3.32E-28	1.40E-29	1.28E-30	3.82E-32
160	3.96E-24	5.95E-25	2.85E-26	2.46E-27	3.24E-28	1.36E-29	1.24E-30	3.72E-32
165	3.96E-24	5.93E-25	2.82E-26	2.42E-27	3.18E-28	1.33E-29	1.21E-30	3.64E-32
170	3.96E-24	5.91E-25	2.80E-26	2.40E-27	3.14E-28	1.31E-29	1.19E-30	3.59E-32
175	3.96E-24	5.90E-25	2.79E-26	2.38E-27	3.12E-28	1.30E-29	1.18E-30	3.55E-32
180	3.96E-24	5.90E-25	2.78E-26	2.38E-27	3.11E-28	1.30E-29	1.18E-30	3.54E-32

PROTON ENERGY = .020 MEV

E(RYD)	1	2	4	6	8	12	16	24
E(EV)	13.6	27.2	54.4	81.6	108.8	163.3	217.7	326.5
THETA(DEG)								
0	5.18E-23	2.43E-23	3.88E-24	5.70E-25	9.82E-26	5.13E-27	4.54E-28	1.00E-29
5	5.14E-23	2.40E-23	3.82E-24	5.61E-25	9.67E-26	5.06E-27	4.49E-28	9.90E-30
10	5.02E-23	2.32E-23	3.64E-24	5.33E-25	9.21E-26	4.86E-27	4.32E-28	9.60E-30
15	4.82E-23	2.19E-23	3.36E-24	4.90E-25	8.52E-26	4.54E-27	4.06E-28	9.14E-30
20	4.56E-23	2.03E-23	3.01E-24	4.38E-25	7.67E-26	4.14E-27	3.73E-28	8.54E-30
25	4.25E-23	1.83E-23	2.63E-24	3.81E-25	6.74E-26	3.70E-27	3.36E-28	7.84E-30
30	3.89E-23	1.62E-23	2.24E-24	3.25E-25	5.80E-26	3.23E-27	2.97E-28	7.10E-30
35	3.51E-23	1.41E-23	1.87E-24	2.72E-25	4.91E-26	2.70E-27	2.59E-28	6.35E-30
40	3.13E-23	1.20E-23	1.53E-24	2.24E-25	4.10E-26	2.37E-27	2.23E-28	5.61E-30
45	2.76E-23	1.01E-23	1.25E-24	1.83E-25	3.40E-26	1.99E-27	1.90E-28	4.92E-30
50	2.40E-23	8.40E-24	1.01E-24	1.49E-25	2.80E-26	1.66E-27	1.61E-28	4.28E-30
55	2.09E-23	6.97E-24	8.18E-25	1.22E-25	2.30E-26	1.39E-27	1.35E-28	3.71E-30
60	1.81E-23	5.79E-24	6.66E-25	9.97E-26	1.90E-26	1.15E-27	1.14E-28	3.20E-30
65	1.57E-23	4.84E-24	5.47E-25	8.22E-26	1.57E-26	9.60E-28	9.61E-29	2.76E-30
70	1.38E-23	4.09E-24	4.55E-25	6.84E-26	1.31E-26	8.03E-28	8.12E-29	2.38E-30
75	1.22E-23	3.51E-24	3.84E-25	5.76E-26	1.10E-26	6.75E-28	6.90E-29	2.06E-30
80	1.10E-23	3.07E-24	3.29E-25	4.90E-26	9.32E-27	5.71E-28	5.89E-29	1.78E-30
85	1.01E-23	2.73E-24	2.87E-25	4.23E-26	7.99E-27	4.88E-28	5.06E-29	1.55E-30
90	9.43E-24	2.48E-24	2.55E-25	3.70E-26	6.92E-27	4.20E-28	4.38E-29	1.36E-30
95	8.95E-24	2.28E-24	2.29E-25	3.28E-26	6.06E-27	3.65E-28	3.82E-29	1.19E-30
100	8.61E-24	2.14E-24	2.09E-25	2.94E-26	5.37E-27	3.20E-28	3.35E-29	1.06E-30
105	8.39E-24	2.03E-24	1.93E-25	2.67E-26	4.80E-27	2.83E-28	2.97E-29	9.42E-31
110	8.24E-24	1.95E-24	1.80E-25	2.44E-26	4.35E-27	2.53E-28	2.65E-29	8.45E-31
115	8.16E-24	1.88E-24	1.70E-25	2.26E-26	3.97E-27	2.28E-28	2.38E-29	7.65E-31
120	8.11E-24	1.83E-24	1.62E-25	2.12E-26	3.66E-27	2.07E-28	2.15E-29	6.97E-31
125	8.09E-24	1.79E-24	1.55E-25	2.00E-26	3.40E-27	1.90E-28	1.97E-29	6.40E-31
130	8.09E-24	1.76E-24	1.49E-25	1.90E-26	3.19E-27	1.75E-28	1.81E-29	5.92E-31
135	8.11E-24	1.74E-24	1.45E-25	1.81E-26	3.02E-27	1.63E-28	1.68E-29	5.52E-31
140	8.12E-24	1.72E-24	1.41E-25	1.75E-26	2.87E-27	1.53E-28	1.57E-29	5.19E-31
145	8.14E-24	1.71E-24	1.38E-25	1.69E-26	2.75E-27	1.45E-28	1.48E-29	4.91E-31
150	8.17E-24	1.70E-24	1.36E-25	1.64E-26	2.65E-27	1.38E-28	1.41E-29	4.68E-31
155	8.19E-24	1.69E-24	1.34E-25	1.61E-26	2.58E-27	1.33E-28	1.35E-29	4.50E-31
160	8.20E-24	1.68E-24	1.33E-25	1.58E-26	2.51E-27	1.29E-28	1.30E-29	4.35E-31
165	8.22E-24	1.67E-24	1.31E-25	1.56E-26	2.47E-27	1.25E-28	1.27E-29	4.24E-31
170	8.23E-24	1.67E-24	1.31E-25	1.54E-26	2.44E-27	1.23E-28	1.24E-29	4.16E-31
175	8.23E-24	1.67E-24	1.30E-25	1.54E-26	2.42E-27	1.22E-28	1.23E-29	4.12E-31
180	8.23E-24	1.67E-24	1.30E-25	1.53E-26	2.41E-27	1.21E-28	1.22E-29	4.10E-31

PROTON ENERGY = .050 MEV

E(RYD)	1	2	4	6	8	12	16	24
E(EV)	13.6	27.2	54.4	81.6	108.8	163.3	217.7	326.5
THETA(DEG)								
0	5.41E-23	3.36E-23	1.59E-23	7.89E-24	3.36E-24	3.91E-25	4.46E-26	1.27E-27
5	5.40E-23	3.35E-23	1.58E-23	7.75E-24	3.25E-24	3.76E-25	4.32E-26	1.24E-27
10	5.35E-23	3.33E-23	1.56E-23	7.40E-24	3.00E-24	3.38E-25	3.95E-26	1.16E-27
15	5.28E-23	3.28E-23	1.51E-23	6.92E-24	2.69E-24	2.94E-25	3.47E-26	1.05E-27
20	5.18E-23	3.21E-23	1.44E-23	6.30E-24	2.35E-24	2.47E-25	2.95E-26	9.17E-28
25	5.03E-23	3.10E-23	1.34E-23	5.52E-24	1.95E-24	2.00E-25	2.42E-26	7.77E-28
30	4.84E-23	2.95E-23	1.21E-23	4.64E-24	1.55E-24	1.55E-25	1.93E-26	6.41E-28
35	4.59E-23	2.76E-23	1.06E-23	3.74E-24	1.19E-24	1.17E-25	1.50E-26	5.18E-28
40	4.30E-23	2.52E-23	8.93E-24	2.91E-24	8.81E-25	8.72E-26	1.15E-26	4.11E-28
45	3.97E-23	2.25E-23	7.27E-24	2.19E-24	6.41E-25	6.41E-26	8.67E-27	3.22E-28
50	3.61E-23	1.96E-23	5.72E-24	1.61E-24	4.62E-25	4.71E-26	6.55E-27	2.51E-28
55	3.22E-23	1.66E-23	4.39E-24	1.17E-24	3.33E-25	3.48E-26	4.95E-27	1.94E-28
60	2.84E-23	1.38E-23	3.31E-24	8.52E-25	2.42E-25	2.60E-26	3.76E-27	1.51E-28
65	2.47E-23	1.12E-23	2.49E-24	6.26E-25	1.79E-25	1.97E-26	2.88E-27	1.18E-28
70	2.14E-23	9.11E-24	1.88E-24	4.70E-25	1.36E-25	1.51E-26	2.24E-27	9.29E-29
75	1.84E-23	7.39E-24	1.45E-24	3.62E-25	1.06E-25	1.19E-26	1.76E-27	7.38E-29
80	1.60E-23	6.07E-24	1.15E-24	2.88E-25	8.42E-26	9.46E-27	1.40E-27	5.94E-29
85	1.41E-23	5.08E-24	9.43E-25	2.36E-25	6.89E-26	7.68E-27	1.13E-27	4.83E-29
90	1.26E-23	4.38E-24	7.98E-25	1.99E-25	5.77E-26	6.35E-27	9.26E-28	3.99E-29
95	1.16E-23	3.88E-24	6.96E-25	1.72E-25	4.94E-26	5.34E-27	7.70E-28	3.33E-29
100	1.09E-23	3.55E-24	6.24E-25	1.52E-25	4.32E-26	4.56E-27	6.50E-28	2.82E-29
105	1.04E-23	3.32E-24	5.72E-25	1.37E-25	3.83E-26	3.95E-27	5.56E-28	2.41E-29
110	1.02E-23	3.17E-24	5.33E-25	1.26E-25	3.46E-26	3.46E-27	4.81E-28	2.09E-29
115	1.01E-23	3.08E-24	5.05E-25	1.17E-25	3.16E-26	3.08E-27	4.22E-28	1.83E-29
120	1.01E-23	3.02E-24	4.83E-25	1.10E-25	2.92E-26	2.77E-27	3.74E-28	1.62E-29
125	1.02E-23	2.99E-24	4.67E-25	1.04E-25	2.72E-26	2.52E-27	3.36E-28	1.45E-29
130	1.03E-23	2.97E-24	4.54E-25	9.94E-26	2.56E-26	2.31E-27	3.04E-28	1.32E-29
135	1.05E-23	2.96E-24	4.43E-25	9.57E-26	2.43E-26	2.15E-27	2.79E-28	1.20E-29
140	1.06E-23	2.96E-24	4.35E-25	9.27E-26	2.33E-26	2.01E-27	2.58E-28	1.11E-29
145	1.08E-23	2.96E-24	4.29E-25	9.02E-26	2.24E-26	1.90E-27	2.40E-28	1.04E-29
150	1.09E-23	2.96E-24	4.23E-25	8.82E-26	2.17E-26	1.81E-27	2.27E-28	9.79E-30
155	1.10E-23	2.96E-24	4.19E-25	8.67E-26	2.12E-26	1.73E-27	2.15E-28	9.32E-30
160	1.11E-23	2.96E-24	4.16E-25	8.54E-26	2.07E-26	1.68E-27	2.07E-28	8.95E-30
165	1.12E-23	2.97E-24	4.14E-25	8.45E-26	2.04E-26	1.63E-27	2.00E-28	8.67E-30
170	1.12E-23	2.97E-24	4.12E-25	8.39E-26	2.02E-26	1.60E-27	1.96E-28	8.49E-30
175	1.13E-23	2.97E-24	4.11E-25	8.35E-26	2.00E-26	1.58E-27	1.93E-28	8.37E-30
180	1.13E-23	2.97E-24	4.11E-25	8.34E-26	2.00E-26	1.58E-27	1.92E-28	8.34E-30

PROTON ENERGY = .070 MEV

E(RYD)	1	2	4	6	8	12	16	24
E(EV)	13.6	27.2	54.4	81.6	108.8	163.3	217.7	326.5
THETA(DEG)								
0	4.32E-23	2.57E-23	1.27E-23	7.86E-24	5.03E-24	1.44E-24	2.52E-25	8.18E-27
5	4.31E-23	2.57E-23	1.27E-23	7.84E-24	4.96E-24	1.38E-24	2.41E-25	7.93E-27
10	4.30E-23	2.58E-23	1.27E-23	7.78E-24	4.81E-24	1.26E-24	2.15E-25	7.27E-27
15	4.29E-23	2.58E-23	1.27E-23	7.66E-24	4.59E-24	1.12E-24	1.84E-25	6.35E-27
20	4.26E-23	2.58E-23	1.27E-23	7.43E-24	4.25E-24	9.43E-25	1.51E-25	5.33E-27
25	4.20E-23	2.57E-23	1.25E-23	7.04E-24	3.78E-24	7.49E-25	1.17E-25	4.31E-27
30	4.12E-23	2.53E-23	1.21E-23	6.44E-24	3.20E-24	5.65E-25	8.74E-26	3.37E-27
35	4.00E-23	2.46E-23	1.14E-23	5.64E-24	2.57E-24	4.10E-25	6.32E-26	2.56E-27
40	3.84E-23	2.34E-23	1.03E-23	4.71E-24	1.97E-24	2.88E-25	4.49E-26	1.92E-27
45	3.64E-23	2.18E-23	9.01E-24	3.72E-24	1.43E-24	1.98E-25	3.16E-26	1.42E-27
50	3.39E-23	1.98E-23	7.50E-24	2.81E-24	1.01E-24	1.36E-25	2.23E-26	1.05E-27
55	3.11E-23	1.75E-23	5.99E-24	2.04E-24	6.98E-25	9.39E-26	1.58E-26	7.75E-28
60	2.80E-23	1.50E-23	4.61E-24	1.45E-24	4.82E-25	6.58E-26	1.14E-26	5.75E-28
65	2.48E-23	1.25E-23	3.45E-24	1.03E-24	3.37E-25	4.72E-26	8.36E-27	4.30E-28
70	2.17E-23	1.03E-23	2.57E-24	7.36E-25	2.42E-25	3.48E-26	6.25E-27	3.26E-28
75	1.88E-23	8.31E-24	1.92E-24	5.40E-25	1.79E-25	2.63E-26	4.76E-27	2.50E-28
80	1.63E-23	6.74E-24	1.46E-24	4.10E-25	1.38E-25	2.05E-26	3.71E-27	1.95E-28
85	1.43E-23	5.53E-24	1.15E-24	3.24E-25	1.10E-25	1.63E-26	2.94E-27	1.54E-28
90	1.26E-23	4.65E-24	9.41E-25	2.66E-25	9.02E-26	1.33E-26	2.38E-27	1.24E-28
95	1.14E-23	4.03E-24	8.01E-25	2.26E-25	7.64E-26	1.11E-26	1.96E-27	1.01E-28
100	1.05E-23	3.61E-24	7.06E-25	1.98E-25	6.64E-26	9.48E-27	1.64E-27	8.43E-29
105	9.97E-24	3.33E-24	6.42E-25	1.78E-25	5.89E-26	8.20E-27	1.39E-27	7.11E-29
110	9.67E-24	3.16E-24	5.97E-25	1.63E-25	5.32E-26	7.20E-27	1.20E-27	6.09E-29
115	9.55E-24	3.06E-24	5.66E-25	1.52E-25	4.87E-26	6.41E-27	1.05E-27	5.28E-29
120	9.56E-24	3.00E-24	5.43E-25	1.43E-25	4.52E-26	5.78E-27	9.27E-28	4.64E-29
125	9.65E-24	2.98E-24	5.27E-25	1.36E-25	4.23E-26	5.27E-27	8.30E-28	4.13E-29
130	9.80E-24	2.97E-24	5.14E-25	1.31E-25	4.00E-26	4.85E-27	7.51E-28	3.72E-29
135	9.98E-24	2.98E-24	5.04E-25	1.27E-25	3.81E-26	4.51E-27	6.87E-28	3.39E-29
140	1.02E-23	2.99E-24	4.97E-25	1.23E-25	3.66E-26	4.23E-27	6.35E-28	3.12E-29
145	1.04E-23	3.00E-24	4.91E-25	1.20E-25	3.53E-26	4.01E-27	5.92E-28	2.90E-29
150	1.05E-23	3.02E-24	4.87E-25	1.18E-25	3.43E-26	3.82E-27	5.57E-28	2.73E-29
155	1.07E-23	3.03E-24	4.83E-25	1.16E-25	3.35E-26	3.67E-27	5.30E-28	2.59E-29
160	1.08E-23	3.04E-24	4.80E-25	1.14E-25	3.29E-26	3.56E-27	5.09E-28	2.48E-29
165	1.09E-23	3.05E-24	4.79E-25	1.13E-25	3.24E-26	3.47E-27	4.92E-28	2.40E-29
170	1.10E-23	3.06E-24	4.77E-25	1.13E-25	3.21E-26	3.41E-27	4.82E-28	2.35E-29
175	1.10E-23	3.06E-24	4.76E-25	1.12E-25	3.19E-26	3.37E-27	4.75E-28	2.32E-29
180	1.10E-23	3.06E-24	4.76E-25	1.12E-25	3.18E-26	3.36E-27	4.72E-28	2.31E-29

PROTON ENERGY = .100 MEV

E(RYD)	1	2	4	6	8	12	16	24
E(EV)	13.6	27.2	54.4	81.6	108.8	163.3	217.7	326.5
THETA(DEG)								
0	3.17E-23	1.76E-23	8.02E-24	5.02E-24	3.70E-24	2.29E-24	1.06E-24	6.95E-26
5	3.18E-23	1.77E-23	8.06E-24	5.05E-24	3.72E-24	2.24E-24	9.90E-25	6.49E-26
10	3.19E-23	1.78E-23	8.19E-24	5.14E-24	3.77E-24	2.16E-24	8.75E-25	5.57E-26
15	3.20E-23	1.81E-23	8.39E-24	5.28E-24	3.84E-24	2.10E-24	7.88E-25	4.65E-26
20	3.21E-23	1.84E-23	8.65E-24	5.44E-24	3.90E-24	1.96E-24	6.68E-25	3.72E-26
25	3.22E-23	1.87E-23	8.92E-24	5.59E-24	3.89E-24	1.73E-24	5.19E-25	2.79E-26
30	3.22E-23	1.89E-23	9.14E-24	5.65E-24	3.77E-24	1.44E-24	3.78E-25	2.00E-26
35	3.19E-23	1.90E-23	9.23E-24	5.55E-24	3.48E-24	1.12E-24	2.62E-25	1.39E-26
40	3.13E-23	1.89E-23	9.09E-24	5.21E-24	3.02E-24	8.07E-25	1.74E-25	9.53E-27
45	3.04E-23	1.84E-23	8.64E-24	4.62E-24	2.43E-24	5.49E-25	1.13E-25	6.49E-27
50	2.91E-23	1.75E-23	7.84E-24	3.84E-24	1.82E-24	3.59E-25	7.29E-26	4.43E-27
55	2.74E-23	1.62E-23	6.75E-24	2.98E-24	1.28E-24	2.31E-25	4.75E-26	3.05E-27
60	2.54E-23	1.45E-23	5.51E-24	2.19E-24	8.69E-25	1.50E-25	3.16E-26	2.13E-27
65	2.30E-23	1.26E-23	4.29E-24	1.55E-24	5.80E-25	9.96E-26	2.17E-26	1.52E-27
70	2.06E-23	1.06E-23	3.22E-24	1.07E-24	3.91E-25	6.85E-26	1.54E-26	1.10E-27
75	1.81E-23	8.72E-24	2.38E-24	7.51E-25	2.71E-25	4.90E-26	1.13E-26	8.17E-28
80	1.58E-23	7.09E-24	1.76E-24	5.39E-25	1.96E-25	3.66E-26	8.53E-27	6.18E-28
85	1.38E-23	5.76E-24	1.33E-24	4.04E-25	1.49E-25	2.84E-26	6.64E-27	4.78E-28
90	1.21E-23	4.74E-24	1.04E-24	3.17E-25	1.18E-25	2.28E-26	5.30E-27	3.76E-28
95	1.08E-23	4.00E-24	8.53E-25	2.61E-25	9.79E-26	1.88E-26	4.33E-27	3.03E-28
100	9.82E-24	3.49E-24	7.31E-25	2.24E-25	8.40E-26	1.60E-26	3.62E-27	2.48E-28
105	9.16E-24	3.16E-24	6.52E-25	1.99E-25	7.41E-26	1.38E-26	3.06E-27	2.07E-28
110	8.77E-24	2.96E-24	6.02E-25	1.81E-25	6.68E-26	1.22E-26	2.64E-27	1.75E-28
115	8.59E-24	2.84E-24	5.68E-25	1.69E-25	6.14E-26	1.09E-26	2.31E-27	1.51E-28
120	8.56E-24	2.78E-24	5.46E-25	1.60E-25	5.71E-26	9.82E-27	2.05E-27	1.31E-28
125	8.64E-24	2.76E-24	5.32E-25	1.53E-25	5.38E-26	9.00E-27	1.84E-27	1.16E-28
130	8.78E-24	2.77E-24	5.22E-25	1.47E-25	5.11E-26	8.32E-27	1.67E-27	1.04E-28
135	8.97E-24	2.79E-24	5.15E-25	1.43E-25	4.89E-26	7.77E-27	1.52E-27	9.45E-29
140	9.18E-24	2.81E-24	5.09E-25	1.40E-25	4.71E-26	7.32E-27	1.41E-27	8.68E-29
145	9.39E-24	2.84E-24	5.06E-25	1.37E-25	4.57E-26	6.95E-27	1.32E-27	8.05E-29
150	9.58E-24	2.87E-24	5.03E-25	1.35E-25	4.45E-26	6.64E-27	1.24E-27	7.55E-29
155	9.76E-24	2.89E-24	5.01E-25	1.33E-25	4.36E-26	6.41E-27	1.19E-27	7.16E-29
160	9.91E-24	2.91E-24	5.00E-25	1.32E-25	4.28E-26	6.22E-27	1.14E-27	6.85E-29
165	1.00E-23	2.93E-24	4.99E-25	1.31E-25	4.23E-26	6.07E-27	1.10E-27	6.62E-29
170	1.01E-23	2.94E-24	4.98E-25	1.30E-25	4.19E-26	5.98E-27	1.08E-27	6.48E-29
175	1.02E-23	2.95E-24	4.97E-25	1.29E-25	4.16E-26	5.92E-27	1.06E-27	6.38E-29
180	1.02E-23	2.95E-24	4.97E-25	1.29E-25	4.16E-26	5.89E-27	1.05E-27	6.33E-29

PROTON ENERGY = .300 MEV

E(RYD)	1	2	4	6	8	12	16	24
E(EV)	13.6	27.2	54.4	81.6	108.8	163.3	217.7	326.5
THETA(DEG)								
0	1.05E-23	4.75E-24	1.57E-24	7.42E-25	4.32E-25	2.12E-25	1.41E-25	1.06E-25
5	1.05E-23	4.78E-24	1.58E-24	7.50E-25	4.37E-25	2.15E-25	1.43E-25	1.08E-25
10	1.06E-23	4.87E-24	1.62E-24	7.74E-25	4.54E-25	2.26E-25	1.52E-25	1.16E-25
15	1.08E-23	5.01E-24	1.69E-24	8.15E-25	4.83E-25	2.45E-25	1.68E-25	1.32E-25
20	1.11E-23	5.21E-24	1.79E-24	8.78E-25	5.28E-25	2.75E-25	1.93E-25	1.57E-25
25	1.15E-23	5.47E-24	1.93E-24	9.65E-25	5.91E-25	3.19E-25	2.31E-25	1.93E-25
30	1.18E-23	5.78E-24	2.11E-24	1.08E-24	6.79E-25	3.81E-25	2.85E-25	2.39E-25
35	1.23E-23	6.13E-24	2.33E-24	1.23E-24	7.95E-25	4.67E-25	3.58E-25	2.82E-25
40	1.27E-23	6.52E-24	2.59E-24	1.42E-24	9.43E-25	5.76E-25	4.43E-25	2.92E-25
45	1.30E-23	6.90E-24	2.87E-24	1.64E-24	1.12E-24	6.94E-25	5.14E-25	2.48E-25
50	1.32E-23	7.23E-24	3.15E-24	1.85E-24	1.28E-24	7.83E-25	5.20E-25	1.67E-25
55	1.33E-23	7.46E-24	3.38E-24	2.02E-24	1.39E-24	7.80E-25	4.35E-25	9.36E-26
60	1.32E-23	7.53E-24	3.47E-24	2.06E-24	1.37E-24	6.60E-25	2.98E-25	4.80E-26
65	1.29E-23	7.37E-24	3.38E-24	1.93E-24	1.19E-24	4.73E-25	1.76E-25	2.45E-26
70	1.23E-23	6.98E-24	3.07E-24	1.63E-24	9.19E-25	2.98E-25	9.70E-26	1.31E-26
75	1.16E-23	6.36E-24	2.60E-24	1.25E-24	6.37E-25	1.75E-25	5.35E-26	7.58E-27
80	1.06E-23	5.59E-24	2.07E-24	8.95E-25	4.15E-25	1.03E-25	3.10E-26	4.77E-27
85	9.61E-24	4.76E-24	1.57E-24	6.14E-25	2.65E-25	6.25E-26	1.94E-26	3.24E-27
90	8.58E-24	3.96E-24	1.16E-24	4.18E-25	1.73E-25	4.08E-26	1.32E-26	2.34E-27
95	7.63E-24	3.27E-24	8.59E-25	2.94E-25	1.20E-25	2.89E-26	9.70E-27	1.79E-27
100	6.80E-24	2.71E-24	6.55E-25	2.17E-25	8.89E-26	2.22E-26	7.61E-27	1.42E-27
105	6.13E-24	2.30E-24	5.24E-25	1.72E-25	7.11E-26	1.81E-26	6.27E-27	1.16E-27
110	5.63E-24	2.01E-24	4.43E-25	1.46E-25	6.07E-26	1.56E-26	5.36E-27	9.76E-28
115	5.30E-24	1.83E-24	3.97E-25	1.31E-25	5.45E-26	1.39E-26	4.71E-27	8.36E-28
120	5.11E-24	1.73E-24	3.72E-25	1.22E-25	5.07E-26	1.27E-26	4.22E-27	7.28E-28
125	5.04E-24	1.69E-24	3.60E-25	1.18E-25	4.82E-26	1.18E-26	3.83E-27	6.44E-28
130	5.06E-24	1.68E-24	3.55E-25	1.15E-25	4.66E-26	1.11E-26	3.53E-27	5.77E-28
135	5.14E-24	1.70E-24	3.55E-25	1.14E-25	4.54E-26	1.05E-26	3.28E-27	5.23E-28
140	5.27E-24	1.73E-24	3.58E-25	1.13E-25	4.46E-26	1.01E-26	3.08E-27	4.81E-28
145	5.42E-24	1.77E-24	3.61E-25	1.13E-25	4.39E-26	9.74E-27	2.91E-27	4.46E-28
150	5.57E-24	1.81E-24	3.65E-25	1.12E-25	4.34E-26	9.44E-27	2.78E-27	4.18E-28
155	5.71E-24	1.85E-24	3.68E-25	1.12E-25	4.30E-26	9.20E-27	2.67E-27	3.97E-28
160	5.84E-24	1.88E-24	3.72E-25	1.13E-25	4.27E-26	9.01E-27	2.59E-27	3.80E-28
165	5.95E-24	1.91E-24	3.74E-25	1.13E-25	4.25E-26	8.87E-27	2.52E-27	3.67E-28
170	6.03E-24	1.93E-24	3.76E-25	1.13E-25	4.24E-26	8.77E-27	2.48E-27	3.59E-28
175	6.08E-24	1.94E-24	3.77E-25	1.13E-25	4.23E-26	8.71E-27	2.45E-27	3.53E-28
180	6.10E-24	1.94E-24	3.77E-25	1.13E-25	4.22E-26	8.69E-27	2.44E-27	3.50E-28

PROTON ENERGY = .500 MEV

E(RYD)	1	2	4	6	8	12	16	24
E(EV)	13.6	27.2	54.4	81.6	108.8	163.3	217.7	326.5
THETA(DEG)								
0	6.14E-24	2.63E-24	7.89E-25	3.42E-25	1.83E-25	7.52E-26	4.13E-26	2.03E-26
5	6.17E-24	2.65E-24	7.95E-25	3.46E-25	1.85E-25	7.62E-26	4.20E-26	2.07E-26
10	6.26E-24	2.70E-24	8.15E-25	3.56E-25	1.91E-25	7.94E-26	4.41E-26	2.21E-26
15	6.40E-24	2.78E-24	8.49E-25	3.74E-25	2.02E-25	8.51E-26	4.79E-26	2.48E-26
20	6.61E-24	2.90E-24	8.99E-25	4.00E-25	2.19E-25	9.41E-26	5.40E-26	2.91E-26
25	6.86E-24	3.06E-24	9.68E-25	4.38E-25	2.43E-25	1.08E-25	6.35E-26	3.62E-26
30	7.16E-24	3.26E-24	1.06E-24	4.90E-25	2.78E-25	1.27E-25	7.79E-26	4.75E-26
35	7.49E-24	3.49E-24	1.18E-24	5.60E-25	3.25E-25	1.56E-25	9.99E-26	6.59E-26
40	7.84E-24	3.76E-24	1.32E-24	6.52E-25	3.91E-25	1.99E-25	1.33E-25	9.48E-26
45	8.18E-24	4.05E-24	1.50E-24	7.71E-25	4.79E-25	2.59E-25	1.83E-25	1.35E-25
50	8.49E-24	4.34E-24	1.70E-24	9.15E-25	5.91E-25	3.39E-25	2.47E-25	1.72E-25
55	8.72E-24	4.60E-24	1.91E-24	1.07E-24	7.17E-25	4.26E-25	3.07E-25	1.73E-25
60	8.85E-24	4.80E-24	2.09E-24	1.21E-24	8.27E-25	4.86E-25	3.21E-25	1.26E-25
65	8.85E-24	4.89E-24	2.19E-24	1.29E-24	8.70E-25	4.70E-25	2.64E-25	7.01E-26
70	8.68E-24	4.83E-24	2.17E-24	1.25E-24	8.06E-25	3.73E-25	1.73E-25	3.40E-26
75	8.35E-24	4.60E-24	2.01E-24	1.09E-24	6.50E-25	2.49E-25	9.69E-26	1.63E-26
80	7.87E-24	4.22E-24	1.72E-24	8.59E-25	4.64E-25	1.49E-25	5.16E-26	8.35E-27
85	7.28E-24	3.73E-24	1.38E-24	6.23E-25	3.06E-25	8.55E-26	2.81E-26	4.71E-27
90	6.62E-24	3.20E-24	1.06E-24	4.31E-25	1.96E-25	5.03E-26	1.64E-26	2.96E-27
95	5.96E-24	2.69E-24	7.89E-25	2.95E-25	1.27E-25	3.16E-26	1.06E-26	2.04E-27
100	5.34E-24	2.24E-24	5.90E-25	2.07E-25	8.65E-26	2.17E-26	7.49E-27	1.52E-27
105	4.80E-24	1.88E-24	4.55E-25	1.53E-25	6.37E-26	1.63E-26	5.78E-27	1.21E-27
110	4.37E-24	1.61E-24	3.68E-25	1.22E-25	5.09E-26	1.33E-26	4.78E-27	9.98E-28
115	4.05E-24	1.43E-24	3.15E-25	1.04E-25	4.38E-26	1.15E-26	4.14E-27	8.49E-28
120	3.84E-24	1.32E-24	2.86E-25	9.48E-26	3.98E-26	1.04E-26	3.70E-27	7.41E-28
125	3.72E-24	1.26E-24	2.71E-25	8.99E-26	3.77E-26	9.74E-27	3.39E-27	6.58E-28
130	3.69E-24	1.24E-24	2.66E-25	8.77E-26	3.65E-26	9.24E-27	3.15E-27	5.92E-28
135	3.71E-24	1.24E-24	2.65E-25	8.71E-26	3.58E-26	8.89E-27	2.96E-27	5.41E-28
140	3.77E-24	1.26E-24	2.68E-25	8.72E-26	3.55E-26	8.61E-27	2.81E-27	4.99E-28
145	3.86E-24	1.29E-24	2.72E-25	8.77E-26	3.54E-26	8.39E-27	2.69E-27	4.64E-28
150	3.97E-24	1.32E-24	2.77E-25	8.84E-26	3.53E-26	8.22E-27	2.59E-27	4.38E-28
155	4.07E-24	1.36E-24	2.81E-25	8.90E-26	3.53E-26	8.08E-27	2.51E-27	4.16E-28
160	4.17E-24	1.38E-24	2.85E-25	8.96E-26	3.53E-26	7.97E-27	2.44E-27	3.99E-28
165	4.25E-24	1.41E-24	2.89E-25	9.01E-26	3.53E-26	7.89E-27	2.39E-27	3.87E-28
170	4.31E-24	1.43E-24	2.91E-25	9.05E-26	3.53E-26	7.83E-27	2.36E-27	3.78E-28
175	4.35E-24	1.44E-24	2.92E-25	9.07E-26	3.53E-26	7.79E-27	2.34E-27	3.73E-28
180	4.36E-24	1.44E-24	2.93E-25	9.08E-26	3.53E-26	7.78E-27	2.33E-27	3.73E-28

PROTON ENERGY = 1.000 MEV

E(RYD)	1	2	4	6	8	12	16	24
E(EV)	13.6	27.2	54.4	81.6	108.8	163.3	217.7	326.5
THETA(DEG)								
0	3.01E-24	1.21E-24	3.38E-25	1.47E-25	6.94E-26	2.83E-26	1.46E-26	1.89E-27
5	3.03E-24	1.22E-24	3.40E-25	1.47E-25	6.89E-26	2.65E-26	1.31E-26	2.86E-27
10	3.08E-24	1.24E-24	3.46E-25	1.49E-25	6.87E-26	2.38E-26	1.10E-26	4.77E-27
15	3.17E-24	1.28E-24	3.58E-25	1.53E-25	7.17E-26	2.49E-26	1.18E-26	5.58E-27
20	3.30E-24	1.34E-24	3.77E-25	1.60E-25	7.79E-26	2.91E-26	1.46E-26	6.13E-27
25	3.45E-24	1.42E-24	4.05E-25	1.72E-25	8.57E-26	3.27E-26	1.64E-26	6.86E-27
30	3.63E-24	1.52E-24	4.42E-25	1.88E-25	9.53E-26	3.59E-26	1.78E-26	7.53E-27
35	3.84E-24	1.64E-24	4.91E-25	2.11E-25	1.10E-25	4.26E-26	2.21E-26	1.09E-26
40	4.07E-24	1.79E-24	5.53E-25	2.44E-25	1.32E-25	5.52E-26	3.01E-26	1.39E-26
45	4.31E-24	1.95E-24	6.32E-25	2.89E-25	1.62E-25	7.20E-26	4.02E-26	1.90E-26
50	4.55E-24	2.13E-24	7.30E-25	3.48E-25	2.03E-25	9.41E-26	5.55E-26	3.22E-26
55	4.77E-24	2.32E-24	8.45E-25	4.23E-25	2.57E-25	1.29E-25	8.34E-26	5.53E-26
60	4.95E-24	2.49E-24	9.69E-25	5.12E-25	3.26E-25	1.78E-25	1.23E-25	7.86E-26
65	5.07E-24	2.63E-24	1.08E-24	6.01E-25	3.97E-25	2.27E-25	1.56E-25	8.61E-26
70	5.11E-24	2.71E-24	1.15E-24	6.64E-25	4.44E-25	2.50E-25	1.60E-25	7.11E-26
75	5.06E-24	2.71E-24	1.16E-24	6.70E-25	4.39E-25	2.28E-25	1.29E-25	4.29E-26
80	4.92E-24	2.61E-24	1.10E-24	6.10E-25	3.79E-25	1.73E-25	8.23E-26	1.87E-26
85	4.68E-24	2.42E-24	9.68E-25	4.98E-25	2.86E-25	1.10E-25	4.32E-26	7.32E-27
90	4.38E-24	2.17E-24	8.00E-25	3.72E-25	1.95E-25	6.30E-26	2.20E-26	4.80E-27
95	4.03E-24	1.89E-24	6.27E-25	2.63E-25	1.26E-25	3.68E-26	1.31E-26	3.48E-27
100	3.66E-24	1.61E-24	4.76E-25	1.84E-25	8.33E-26	2.33E-26	8.09E-27	1.19E-27
105	3.32E-24	1.36E-24	3.60E-25	1.31E-25	5.69E-26	1.51E-26	4.61E-27	7.14E-28
110	3.01E-24	1.16E-24	2.80E-25	9.67E-26	4.03E-26	1.00E-26	3.41E-27	6.07E-28
115	2.76E-24	1.01E-24	2.29E-25	7.64E-26	3.11E-26	7.94E-27	3.47E-27	5.48E-28
120	2.57E-24	9.03E-25	1.98E-25	6.57E-26	2.72E-26	7.42E-27	2.95E-27	4.58E-28
125	2.43E-24	8.36E-25	1.81E-25	6.05E-26	2.53E-26	6.79E-27	2.75E-27	2.35E-28
130	2.36E-24	8.00E-25	1.72E-25	5.76E-26	2.37E-26	6.02E-27	2.64E-27	2.21E-28
135	2.32E-24	7.86E-25	1.70E-25	5.65E-26	2.29E-26	5.87E-27	2.57E-27	2.21E-28
140	2.32E-24	7.89E-25	1.71E-25	5.72E-26	2.35E-26	5.89E-27	2.39E-27	2.13E-28
145	2.35E-24	8.01E-25	1.74E-25	5.86E-26	2.38E-26	5.93E-27	1.74E-27	2.03E-28
150	2.39E-24	8.19E-25	1.79E-25	5.94E-26	2.42E-26	5.95E-27	1.70E-27	1.91E-28
155	2.43E-24	8.38E-25	1.82E-25	5.98E-26	2.43E-26	5.96E-27	1.42E-27	1.86E-28
160	2.48E-24	8.56E-25	1.86E-25	6.10E-26	2.44E-26	5.98E-27	1.31E-27	1.79E-28
165	2.52E-24	8.71E-25	1.88E-25	6.26E-26	2.56E-26	6.30E-27	1.31E-27	1.75E-28
170	2.55E-24	8.83E-25	1.90E-25	6.31E-26	2.54E-26	5.97E-27	1.33E-27	1.75E-28
175	2.57E-24	8.90E-25	1.91E-25	6.22E-26	2.39E-26	5.44E-27	1.33E-27	1.75E-28
180	2.58E-24	8.92E-25	1.91E-25	6.14E-26	2.29E-26	5.11E-27	1.34E-27	1.74E-28

PROTON ENERGY = 2.000 MEV

E(RYD)	1	2	4	6	8	12	16	24
E(EV)	13.6	27.2	54.4	81.6	108.8	163.3	217.7	326.5
THETA(DEG)								
0	1.52E-24	5.96E-25	1.58E-25	5.91E-26	2.80E-26	9.61E-27	5.52E-27	3.67E-27
5	1.53E-24	6.00E-25	1.59E-25	5.99E-26	2.85E-26	9.68E-27	4.97E-27	2.54E-27
10	1.56E-24	6.11E-25	1.62E-25	6.18E-26	2.97E-26	9.76E-27	4.01E-27	6.67E-28
15	1.61E-24	6.31E-25	1.67E-25	6.41E-26	3.07E-26	9.98E-27	3.97E-27	5.43E-28
20	1.68E-24	6.59E-25	1.74E-25	6.72E-26	3.21E-26	1.06E-26	4.92E-27	1.87E-27
25	1.76E-24	6.97E-25	1.86E-25	7.22E-26	3.47E-26	1.18E-26	5.80E-27	2.42E-27
30	1.86E-24	7.46E-25	2.02E-25	7.95E-26	3.87E-26	1.33E-26	6.06E-27	1.72E-27
35	1.98E-24	8.06E-25	2.23E-25	8.91E-26	4.38E-26	1.51E-26	6.62E-27	1.71E-27
40	2.11E-24	8.80E-25	2.50E-25	1.02E-25	5.10E-26	1.83E-26	8.72E-27	3.42E-27
45	2.26E-24	9.65E-25	2.84E-25	1.20E-25	6.18E-26	2.37E-26	1.21E-26	5.26E-27
50	2.41E-24	1.06E-24	3.29E-25	1.44E-25	7.73E-26	3.12E-26	1.59E-26	6.34E-27
55	2.55E-24	1.17E-24	3.84E-25	1.77E-25	9.83E-26	4.19E-26	2.21E-26	9.65E-27
60	2.69E-24	1.27E-24	4.48E-25	2.17E-25	1.27E-25	5.90E-26	3.47E-26	1.91E-26
65	2.80E-24	1.37E-24	5.17E-25	2.66E-25	1.64E-25	8.43E-26	5.47E-26	3.28E-26
70	2.87E-24	1.45E-24	5.78E-25	3.15E-25	2.03E-25	1.12E-25	7.46E-26	4.27E-26
75	2.90E-24	1.49E-24	6.15E-25	3.48E-25	2.29E-25	1.27E-25	8.23E-26	4.11E-26
80	2.87E-24	1.49E-24	6.18E-25	3.51E-25	2.28E-25	1.20E-25	7.16E-26	2.90E-26
85	2.79E-24	1.43E-24	5.80E-25	3.17E-25	1.97E-25	9.30E-26	4.85E-26	1.47E-26
90	2.66E-24	1.33E-24	5.09E-25	2.59E-25	1.49E-25	6.00E-26	2.61E-26	5.62E-27
95	2.49E-24	1.19E-24	4.20E-25	1.94E-25	1.03E-25	3.49E-26	1.29E-26	2.60E-27
100	2.30E-24	1.04E-24	3.32E-25	1.39E-25	6.80E-26	2.10E-26	7.76E-27	2.07E-27
105	2.10E-24	8.96E-25	2.56E-25	9.92E-26	4.57E-26	1.36E-26	5.25E-27	1.27E-27
110	1.92E-24	7.69E-25	1.99E-25	7.21E-26	3.17E-26	8.61E-27	2.87E-27	8.53E-28
115	1.75E-24	6.66E-25	1.59E-25	5.48E-26	2.30E-26	5.58E-27	2.20E-27	7.41E-28
120	1.62E-24	5.89E-25	1.33E-25	4.45E-26	1.84E-26	4.78E-27	1.87E-27	6.19E-28
125	1.51E-24	5.35E-25	1.17E-25	3.89E-26	1.64E-26	4.73E-27	1.66E-27	6.04E-28
130	1.44E-24	5.00E-25	1.08E-25	3.60E-26	1.51E-26	4.04E-27	1.48E-27	4.93E-28
135	1.40E-24	4.82E-25	1.04E-25	3.47E-26	1.43E-26	3.37E-27	8.85E-28	9.59E-29
140	1.37E-24	4.75E-25	1.04E-25	3.46E-26	1.44E-26	3.27E-27	1.33E-27	6.72E-29
145	1.37E-24	4.76E-25	1.05E-25	3.52E-26	1.50E-26	3.18E-27	1.43E-27	5.38E-29
150	1.38E-24	4.83E-25	1.07E-25	3.59E-26	1.51E-26	3.15E-27	1.55E-27	4.66E-29
155	1.39E-24	4.92E-25	1.10E-25	3.64E-26	1.52E-26	3.47E-27	8.24E-28	5.07E-29
160	1.41E-24	5.01E-25	1.12E-25	3.71E-26	1.54E-26	3.72E-27	6.11E-28	5.52E-29
165	1.42E-24	5.10E-25	1.13E-25	3.79E-26	1.61E-26	4.69E-27	4.09E-28	5.88E-29
170	1.44E-24	5.17E-25	1.14E-25	3.83E-26	1.62E-26	4.57E-27	3.89E-28	5.87E-29
175	1.45E-24	5.21E-25	1.15E-25	3.83E-26	1.56E-26	3.16E-27	3.89E-28	5.86E-29
180	1.45E-24	5.22E-25	1.15E-25	3.82E-26	1.51E-26	2.24E-27	3.89E-28	5.85E-29

PROTON ENERGY = 5.000 MEV

E(RYD)	1	2	4	6	8	12	16	24
E(EV)	13.6	27.2	54.4	81.6	108.8	163.3	217.7	326.5
THETA(DEG)								
0	5.85E-25	2.34E-25	6.06E-26	2.11E-26	9.67E-27	2.29E-27	4.65E-28	2.40E-28
5	5.90E-25	2.36E-25	6.09E-26	2.15E-26	1.01E-26	2.78E-27	9.36E-28	2.44E-28
10	6.04E-25	2.41E-25	6.20E-26	2.23E-26	1.08E-26	3.58E-27	1.69E-27	2.50E-28
15	6.29E-25	2.49E-25	6.39E-26	2.32E-26	1.12E-26	3.74E-27	1.77E-27	2.55E-28
20	6.63E-25	2.62E-25	6.69E-26	2.42E-26	1.14E-26	3.43E-27	1.83E-27	2.92E-28
25	7.06E-25	2.78E-25	7.10E-26	2.59E-26	1.21E-26	3.57E-27	1.91E-27	3.39E-28
30	7.57E-25	2.99E-25	7.67E-26	2.84E-26	1.34E-26	4.33E-27	1.97E-27	6.48E-28
35	8.17E-25	3.24E-25	8.42E-26	3.17E-26	1.51E-26	5.01E-27	2.30E-27	7.08E-28
40	8.84E-25	3.55E-25	9.40E-26	3.58E-26	1.70E-26	5.46E-27	2.89E-27	7.80E-28
45	9.57E-25	3.92E-25	1.07E-25	4.16E-26	2.01E-26	6.55E-27	3.77E-27	8.47E-28
50	1.03E-24	4.34E-25	1.23E-25	4.98E-26	2.48E-26	8.81E-27	4.10E-27	1.51E-27
55	1.11E-24	4.81E-25	1.43E-25	6.07E-26	3.14E-26	1.19E-26	5.73E-27	2.05E-27
60	1.19E-24	5.31E-25	1.68E-25	7.49E-26	4.03E-26	1.60E-26	7.87E-27	2.90E-27
65	1.26E-24	5.81E-25	1.98E-25	9.31E-26	5.27E-26	2.29E-26	1.24E-26	5.68E-27
70	1.31E-24	6.26E-25	2.28E-25	1.15E-25	6.90E-26	3.37E-26	2.05E-26	1.10E-26
75	1.35E-24	6.60E-25	2.53E-25	1.35E-25	8.56E-26	4.55E-26	2.94E-26	1.62E-26
80	1.36E-24	6.76E-25	2.67E-25	1.48E-25	9.59E-26	5.22E-26	3.36E-26	1.75E-26
85	1.35E-24	6.70E-25	2.65E-25	1.47E-25	9.42E-26	4.94E-26	3.00E-26	1.36E-26
90	1.31E-24	6.42E-25	2.47E-25	1.31E-25	8.06E-26	3.83E-26	2.08E-26	7.51E-27
95	1.25E-24	5.95E-25	2.16E-25	1.06E-25	6.10E-26	2.51E-26	1.17E-26	3.04E-27
100	1.17E-24	5.36E-25	1.79E-25	8.06E-26	4.25E-26	1.50E-26	6.01E-27	1.38E-27
105	1.09E-24	4.73E-25	1.43E-25	5.91E-26	2.89E-26	9.21E-27	3.57E-27	1.04E-27
110	9.96E-25	4.12E-25	1.13E-25	4.35E-26	2.01E-26	6.09E-27	2.35E-27	6.03E-28
115	9.11E-25	3.59E-25	9.04E-26	3.28E-26	1.45E-26	4.08E-27	1.43E-27	5.52E-28
120	8.35E-25	3.16E-25	7.45E-26	2.57E-26	1.09E-26	2.83E-27	9.54E-28	4.62E-28
125	7.70E-25	2.83E-25	6.39E-26	2.14E-26	8.94E-27	2.33E-27	9.21E-28	3.58E-28
130	7.19E-25	2.59E-25	5.72E-26	1.91E-26	8.03E-27	2.19E-27	8.90E-28	2.51E-28
135	6.80E-25	2.44E-25	5.34E-26	1.79E-26	7.59E-27	2.04E-27	8.18E-28	1.73E-28
140	6.52E-25	2.34E-25	5.16E-26	1.73E-26	7.32E-27	1.90E-27	7.49E-28	1.63E-28
145	6.33E-25	2.29E-25	5.11E-26	1.72E-26	7.28E-27	1.92E-27	7.32E-28	1.55E-28
150	6.22E-25	2.28E-25	5.16E-26	1.75E-26	7.50E-27	2.05E-27	7.11E-28	1.50E-28
155	6.16E-25	2.29E-25	5.24E-26	1.79E-26	7.75E-27	2.08E-27	7.06E-28	1.48E-28
160	6.14E-25	2.31E-25	5.32E-26	1.82E-26	7.85E-27	2.10E-27	6.86E-28	1.47E-28
165	6.14E-25	2.33E-25	5.39E-26	1.83E-26	7.87E-27	2.12E-27	6.74E-28	1.46E-28
170	6.15E-25	2.35E-25	5.43E-26	1.86E-26	8.04E-27	2.14E-27	6.70E-28	1.45E-28
175	6.16E-25	2.36E-25	5.45E-26	1.90E-26	8.31E-27	2.19E-27	6.63E-28	1.44E-28
180	6.16E-25	2.37E-25	5.46E-26	1.92E-26	8.46E-27	2.24E-27	6.60E-28	1.44E-28

PROTON ENERGY = 10.000 MEV

E(RYD)	1	2	4	6	8	12	16	24
E(EV)	13.6	27.2	54.4	81.6	108.8	163.3	217.7	326.5
THETA(DEG)								
0	2.94E-25	1.17E-25	2.96E-26	1.05E-26	4.54E-27	1.06E-27	2.49E-28	1.42E-28
5	2.97E-25	1.18E-25	2.98E-26	1.06E-26	4.70E-27	1.27E-27	2.52E-28	1.45E-28
10	3.05E-25	1.21E-25	3.04E-26	1.10E-26	5.01E-27	1.64E-27	2.62E-28	1.45E-28
15	3.19E-25	1.25E-25	3.15E-26	1.14E-26	5.23E-27	1.73E-27	2.73E-28	1.47E-28
20	3.38E-25	1.32E-25	3.30E-26	1.19E-26	5.37E-27	1.70E-27	3.15E-28	1.54E-28
25	3.62E-25	1.41E-25	3.52E-26	1.26E-26	5.70E-27	1.84E-27	5.83E-28	1.63E-28
30	3.91E-25	1.52E-25	3.81E-26	1.38E-26	6.31E-27	1.96E-27	8.51E-28	1.75E-28
35	4.24E-25	1.66E-25	4.18E-26	1.53E-26	7.09E-27	2.28E-27	1.02E-27	1.92E-28
40	4.62E-25	1.82E-25	4.66E-26	1.73E-26	7.98E-27	2.47E-27	1.06E-27	2.46E-28
45	5.03E-25	2.02E-25	5.27E-26	1.99E-26	9.27E-27	2.85E-27	1.11E-27	2.93E-28
50	5.47E-25	2.24E-25	6.06E-26	2.36E-26	1.13E-26	3.74E-27	1.63E-27	5.26E-28
55	5.93E-25	2.49E-25	7.05E-26	2.86E-26	1.42E-26	5.06E-27	2.36E-27	8.68E-28
60	6.37E-25	2.76E-25	8.30E-26	3.52E-26	1.81E-26	6.73E-27	3.12E-27	1.02E-27
65	6.79E-25	3.04E-25	9.78E-26	4.38E-26	2.37E-26	9.41E-27	4.58E-27	1.63E-27
70	7.14E-25	3.31E-25	1.14E-25	5.44E-26	3.13E-26	1.40E-26	7.78E-27	3.58E-27
75	7.40E-25	3.52E-25	1.29E-25	6.57E-26	4.02E-26	2.01E-26	1.24E-26	6.52E-27
80	7.54E-25	3.66E-25	1.39E-25	7.46E-26	4.74E-26	2.52E-26	1.62E-26	8.65E-27
85	7.54E-25	3.68E-25	1.42E-25	7.74E-26	4.96E-26	2.64E-26	1.66E-26	8.33E-27
90	7.40E-25	3.58E-25	1.36E-25	7.26E-26	4.53E-26	2.28E-26	1.34E-26	5.82E-27
95	7.13E-25	3.38E-25	1.23E-25	6.16E-26	3.64E-26	1.63E-26	8.46E-27	2.92E-27
100	6.76E-25	3.10E-25	1.05E-25	4.84E-26	2.64E-26	1.02E-26	4.49E-27	1.15E-27
105	6.32E-25	2.78E-25	8.59E-26	3.65E-26	1.84E-26	6.19E-27	2.44E-27	5.99E-28
110	5.83E-25	2.45E-25	6.91E-26	2.73E-26	1.30E-26	4.10E-27	1.63E-27	4.75E-28
115	5.35E-25	2.15E-25	5.58E-26	2.08E-26	9.44E-27	2.84E-27	1.12E-27	2.78E-28
120	4.90E-25	1.90E-25	4.59E-26	1.63E-26	7.05E-27	1.92E-27	6.61E-28	9.69E-29
125	4.50E-25	1.70E-25	3.91E-26	1.33E-26	5.59E-27	1.42E-27	4.72E-28	9.15E-29
130	4.16E-25	1.54E-25	3.45E-26	1.16E-26	4.88E-27	1.32E-27	5.20E-28	8.56E-29
135	3.89E-25	1.42E-25	3.16E-26	1.07E-26	4.53E-27	1.29E-27	5.32E-28	8.36E-29
140	3.67E-25	1.35E-25	2.99E-26	1.01E-26	4.26E-27	1.14E-27	4.12E-28	6.39E-29
145	3.51E-25	1.29E-25	2.91E-26	9.85E-27	4.11E-27	1.04E-27	3.39E-28	5.89E-29
150	3.39E-25	1.27E-25	2.89E-26	9.88E-27	4.19E-27	1.09E-27	3.24E-28	5.53E-29
155	3.31E-25	1.25E-25	2.90E-26	1.01E-26	4.30E-27	1.14E-27	3.12E-28	5.26E-29
160	3.25E-25	1.25E-25	2.92E-26	1.02E-26	4.35E-27	1.16E-27	3.26E-28	5.22E-29
165	3.22E-25	1.25E-25	2.94E-26	1.02E-26	4.36E-27	1.24E-27	3.34E-28	6.39E-29
170	3.20E-25	1.25E-25	2.96E-26	1.04E-26	4.39E-27	1.29E-27	3.83E-28	9.56E-29
175	3.19E-25	1.25E-25	2.96E-26	1.06E-26	4.64E-27	1.41E-27	3.92E-28	1.54E-28
180	3.18E-25	1.25E-25	2.97E-26	1.07E-26	4.79E-27	1.57E-27	3.94E-28	1.85E-28

PROTON ENERGY = 25.000 MEV

E(RYD)	1	2	4	6	8	12	16	24
E(EV)	13.6	27.2	54.4	81.6	108.8	163.3	217.7	326.5
THETA(DEG)								
0	1.23E-25	4.67E-26	1.18E-26	4.35E-27	1.84E-27	4.79E-28	1.00E-28	2.42E-29
5	1.25E-25	4.71E-26	1.19E-26	4.38E-27	1.87E-27	5.18E-28	1.53E-28	2.97E-29
10	1.28E-25	4.85E-26	1.22E-26	4.49E-27	1.95E-27	5.97E-28	2.51E-28	3.42E-29
15	1.34E-25	5.07E-26	1.27E-26	4.65E-27	2.03E-27	6.34E-28	2.81E-28	4.17E-29
20	1.43E-25	5.38E-26	1.34E-26	4.87E-27	2.12E-27	6.26E-28	2.85E-28	5.30E-29
25	1.54E-25	5.79E-26	1.43E-26	5.18E-27	2.25E-27	6.43E-28	2.88E-28	6.54E-29
30	1.67E-25	6.30E-26	1.55E-26	5.61E-27	2.46E-27	7.27E-28	2.95E-28	8.14E-29
35	1.82E-25	6.92E-26	1.71E-26	6.18E-27	2.75E-27	8.41E-28	3.70E-28	1.33E-28
40	1.98E-25	7.65E-26	1.90E-26	6.93E-27	3.10E-27	9.36E-28	3.86E-28	1.03E-28
45	2.17E-25	8.50E-26	2.15E-26	7.92E-27	3.57E-27	1.06E-27	4.06E-28	7.05E-29
50	2.37E-25	9.48E-26	2.47E-26	9.29E-27	4.28E-27	1.33E-27	5.42E-28	1.42E-28
55	2.58E-25	1.06E-25	2.86E-26	1.11E-26	5.31E-27	1.77E-27	7.84E-28	2.71E-28
60	2.79E-25	1.18E-25	3.36E-26	1.36E-26	6.73E-27	2.36E-27	1.05E-27	3.38E-28
65	2.99E-25	1.30E-25	3.96E-26	1.69E-26	8.73E-27	3.23E-27	1.46E-27	4.38E-28
70	3.16E-25	1.43E-25	4.63E-26	2.10E-26	1.15E-26	4.74E-27	2.39E-27	9.07E-28
75	3.30E-25	1.53E-25	5.29E-26	2.58E-26	1.51E-26	7.02E-27	4.04E-27	1.91E-27
80	3.39E-25	1.61E-25	5.82E-26	3.00E-26	1.85E-26	9.45E-27	5.88E-27	3.04E-27
85	3.42E-25	1.64E-25	6.07E-26	3.23E-26	2.04E-26	1.08E-26	6.85E-27	3.55E-27
90	3.39E-25	1.62E-25	5.98E-26	3.16E-26	1.98E-26	1.02E-26	6.26E-27	3.02E-27
95	3.30E-25	1.55E-25	5.54E-26	2.80E-26	1.68E-26	7.95E-27	4.47E-27	1.85E-27
100	3.16E-25	1.45E-25	4.87E-26	2.29E-26	1.28E-26	5.28E-27	2.57E-27	8.11E-28
105	2.97E-25	1.32E-25	4.10E-26	1.78E-26	9.19E-27	3.29E-27	1.38E-27	3.32E-28
110	2.77E-25	1.18E-25	3.38E-26	1.36E-26	6.60E-27	2.18E-27	8.83E-28	2.49E-28
115	2.55E-25	1.05E-25	2.77E-26	1.05E-26	4.86E-27	1.54E-27	6.34E-28	1.99E-28
120	2.34E-25	9.29E-26	2.31E-26	8.34E-27	3.66E-27	1.06E-27	3.91E-28	7.84E-29
125	2.15E-25	8.28E-26	1.96E-26	6.83E-27	2.87E-27	7.55E-28	2.41E-28	7.23E-29
130	1.97E-25	7.46E-26	1.72E-26	5.87E-27	2.44E-27	6.66E-28	2.30E-28	6.34E-29
135	1.82E-25	6.81E-26	1.55E-26	5.28E-27	2.20E-27	6.48E-28	2.19E-28	5.86E-29
140	1.70E-25	6.32E-26	1.43E-26	4.90E-27	2.02E-27	5.69E-28	2.17E-28	5.83E-29
145	1.60E-25	5.95E-26	1.37E-26	4.66E-27	1.90E-27	4.93E-28	2.15E-28	5.81E-39
150	1.52E-25	5.69E-26	1.33E-26	4.57E-27	1.88E-27	4.85E-28	2.15E-28	6.06E-29
155	1.45E-25	5.51E-26	1.31E-26	4.56E-27	1.82E-27	4.70E-28	2.28E-28	6.26E-29
160	1.41E-25	5.39E-26	1.30E-26	4.55E-27	1.81E-27	4.83E-28	2.32E-28	6.49E-29
165	1.37E-25	5.31E-26	1.29E-26	4.53E-27	1.85E-27	4.97E-28	2.38E-28	8.37E-29
170	1.35E-25	5.26E-26	1.29E-26	4.55E-27	1.88E-27	5.22E-28	2.62E-28	8.83E-29
175	1.34E-25	5.24E-26	1.29E-26	4.64E-27	1.98E-27	6.66E-28	3.11E-28	1.30E-28
180	1.33E-25	5.23E-26	1.28E-26	4.68E-27	2.05E-27	7.58E-28	4.06E-28	1.57E-28

PROTON ENERGY = 50.000 MEV

E(RYD)	1	2	4	6	8	12	16	24
E(EV)	13.6	27.2	54.4	81.6	108.8	163.3	217.7	326.5
THETA(DEG)								
0	7.72E-26	2.47E-26	5.90E-27	2.20E-27	9.56E-28	2.79E-28	8.50E-29	4.35E-29
5	7.77E-26	2.49E-26	5.96E-27	2.22E-27	9.62E-28	2.83E-28	9.37E-29	4.51E-29
10	7.93E-26	2.56E-26	6.13E-27	2.27E-27	9.87E-28	3.00E-28	1.05E-28	4.67E-29
15	8.19E-26	2.68E-26	6.41E-27	2.36E-27	1.03E-27	3.16E-28	1.17E-28	4.79E-29
20	8.56E-26	2.84E-26	6.80E-27	2.48E-27	1.08E-27	3.25E-28	1.25E-28	4.87E-29
25	9.03E-26	3.06E-26	7.31E-27	2.65E-27	1.15E-27	3.36E-28	1.33E-28	5.05E-29
30	9.61E-26	3.33E-26	7.96E-27	2.87E-27	1.24E-27	3.64E-28	1.40E-28	5.12E-29
35	1.03E-25	3.65E-26	8.78E-27	3.16E-27	1.38E-27	4.15E-28	1.72E-28	5.23E-29
40	1.11E-25	4.04E-26	9.81E-27	3.55E-27	1.56E-27	4.69E-28	1.92E-28	5.36E-29
45	1.19E-25	4.48E-26	1.11E-26	4.04E-27	1.79E-27	5.31E-28	2.05E-28	5.59E-29
50	1.29E-25	5.00E-26	1.27E-26	4.71E-27	2.13E-27	6.45E-28	2.54E-28	5.90E-29
55	1.39E-25	5.57E-26	1.47E-26	5.62E-27	2.61E-27	8.43E-28	3.57E-28	1.13E-28
60	1.49E-25	6.20E-26	1.72E-26	6.84E-27	3.30E-27	1.12E-27	4.88E-28	1.56E-28
65	1.59E-25	6.86E-26	2.02E-26	8.44E-27	4.24E-27	1.52E-27	6.68E-28	1.94E-28
70	1.68E-25	7.52E-26	2.37E-26	1.05E-26	5.58E-27	2.19E-27	1.05E-27	3.59E-28
75	1.75E-25	8.10E-26	2.72E-26	1.29E-26	7.33E-27	3.27E-27	1.80E-27	7.85E-28
80	1.80E-25	8.53E-26	3.01E-26	1.52E-26	9.14E-27	4.53E-27	2.74E-27	1.37E-27
85	1.82E-25	8.76E-26	3.17E-26	1.66E-26	1.03E-26	5.40E-27	3.40E-27	1.76E-27
90	1.81E-25	8.73E-26	3.16E-26	1.66E-26	1.03E-26	5.33E-27	3.31E-27	1.65E-27
95	1.77E-25	8.44E-26	2.98E-26	1.50E-26	9.00E-27	4.35E-27	2.52E-27	1.12E-27
100	1.71E-25	7.94E-26	2.66E-26	1.25E-26	7.04E-27	3.00E-27	1.53E-27	5.35E-28
105	1.62E-25	7.30E-26	2.28E-26	9.93E-27	5.17E-27	1.91E-27	8.33E-28	2.16E-28
110	1.52E-25	6.60E-26	1.91E-26	7.73E-27	3.76E-27	1.27E-27	5.22E-28	1.43E-28
115	1.42E-25	5.91E-26	1.58E-26	6.06E-27	2.80E-27	9.04E-28	3.77E-28	1.21E-28
120	1.32E-25	5.27E-26	1.33E-26	4.84E-27	2.12E-27	6.37E-28	2.44E-28	5.69E-29
125	1.22E-25	4.72E-26	1.13E-26	3.97E-27	1.67E-27	4.58E-28	1.52E-28	1.26E-29
130	1.13E-25	4.25E-26	9.90E-27	3.40E-27	1.40E-27	3.92E-28	1.44E-28	2.21E-29
135	1.05E-25	3.87E-26	8.87E-27	3.02E-27	1.24E-27	3.74E-28	1.39E-28	2.65E-29
140	9.88E-26	3.57E-26	8.14E-27	2.76E-27	1.12E-27	3.29E-28	1.28E-28	3.18E-29
145	9.36E-26	3.34E-26	7.64E-27	2.58E-27	1.03E-27	2.83E-28	8.77E-29	3.28E-29
150	8.94E-26	3.17E-26	7.31E-27	2.48E-27	1.02E-27	2.72E-28	8.52E-29	3.35E-29
155	8.61E-26	3.03E-26	7.10E-27	2.44E-27	1.01E-27	2.57E-28	8.42E-29	3.50E-29
160	8.37E-26	2.94E-26	6.97E-27	2.40E-27	9.90E-28	2.68E-28	8.30E-29	3.58E-29
165	8.19E-26	2.87E-26	6.87E-27	2.36E-27	9.52E-28	2.72E-28	8.59E-29	3.67E-29
170	8.07E-26	2.83E-26	6.80E-27	2.35E-27	9.54E-28	2.81E-28	8.89E-29	2.71E-29
175	8.00E-26	2.80E-26	6.76E-27	2.38E-27	1.00E-27	3.03E-28	9.08E-29	3.73E-29
180	7.98E-26	2.79E-26	6.75E-27	2.40E-27	1.03E-27	3.20E-28	9.19E-29	3.75E-29

PROTON ENERGY = 100.000 MEV

E(RYD)	1	2	4	6	8	12	16	24
E(EV)	13.6	27.2	54.4	81.6	108.8	163.3	217.7	326.5
THETA(DEG)								
0	3.17E-26	1.18E-26	2.95E-27	1.14E-27	4.76E-28	1.57E-28	5.79E-29	8.65E-30
5	3.20E-26	1.19E-26	2.98E-27	1.15E-27	4.77E-28	1.54E-28	5.57E-29	8.71E-30
10	3.32E-26	1.23E-26	3.07E-27	1.17E-27	4.85E-28	1.54E-28	5.58E-29	1.17E-29
15	3.51E-26	1.30E-26	3.23E-27	1.22E-27	5.06E-28	1.61E-28	6.09E-29	1.59E-29
20	3.77E-26	1.40E-26	3.45E-27	1.29E-27	5.38E-28	1.72E-28	6.62E-29	1.67E-29
25	4.11E-26	1.53E-26	3.73E-27	1.38E-27	5.76E-28	1.78E-28	6.68E-29	1.77E-29
30	4.51E-26	1.68E-26	4.09E-27	1.49E-27	6.25E-28	1.88E-28	6.96E-29	1.92E-29
35	4.97E-26	1.87E-26	4.53E-27	1.65E-27	6.97E-28	2.11E-28	8.30E-29	2.23E-29
40	5.50E-26	2.09E-26	5.08E-27	1.84E-27	7.92E-28	2.41E-28	9.76E-29	2.43E-29
45	6.07E-26	2.34E-26	5.75E-27	2.10E-27	9.11E-28	2.72E-28	1.06E-28	2.56E-29
50	6.69E-26	2.62E-26	6.58E-27	2.43E-27	1.08E-27	3.23E-28	1.24E-28	2.67E-29
55	7.33E-26	2.94E-26	7.61E-27	2.88E-27	1.31E-27	4.14E-28	1.70E-28	4.82E-29
60	7.97E-26	3.28E-26	8.89E-27	3.49E-27	1.65E-27	5.48E-28	2.35E-28	7.33E-29
65	8.59E-26	3.64E-26	1.04E-26	4.28E-27	2.11E-27	7.37E-28	3.19E-28	9.19E-29
70	9.15E-26	4.00E-26	1.22E-26	5.29E-27	2.76E-27	1.05E-27	4.87E-28	1.54E-28
75	9.61E-26	4.32E-26	1.40E-26	6.50E-27	3.62E-27	1.56E-27	8.26E-28	3.37E-28
80	9.94E-26	4.56E-26	1.56E-26	7.69E-27	4.56E-27	2.20E-27	1.30E-27	6.26E-28
85	1.01E-25	4.71E-26	1.66E-26	8.51E-27	5.23E-27	2.69E-27	1.68E-27	8.61E-28
90	1.01E-25	4.71E-26	1.67E-26	8.61E-27	5.31E-27	2.74E-27	1.71E-27	8.63E-28
95	9.92E-26	4.59E-26	1.58E-26	7.93E-27	4.74E-27	2.31E-27	1.36E-27	6.25E-28
100	9.58E-26	4.35E-26	1.43E-26	6.73E-27	3.79E-27	1.64E-27	8.60E-28	3.22E-28
105	9.10E-26	4.02E-26	1.24E-26	5.42E-27	2.83E-27	1.07E-27	4.80E-28	1.33E-28
110	8.53E-26	3.66E-26	1.05E-26	4.28E-27	2.08E-27	7.14E-28	2.97E-28	8.01E-29
115	7.90E-26	3.29E-26	8.84E-27	3.39E-27	1.57E-27	5.12E-28	2.15E-28	6.76E-29
120	7.26E-26	2.94E-26	7.48E-27	2.73E-27	1.20E-27	3.68E-28	1.45E-28	3.64E-29
125	6.63E-26	2.63E-26	6.41E-27	2.26E-27	9.41E-28	2.69E-28	9.27E-29	3.04E-29
130	6.04E-26	2.36E-26	5.61E-27	1.93E-27	7.81E-28	2.26E-28	8.31E-29	2.69E-29
135	5.51E-26	2.13E-26	5.01E-27	1.71E-27	6.82E-28	2.11E-28	8.38E-29	2.29E-29
140	5.03E-26	1.94E-26	4.56E-27	1.54E-27	6.05E-28	1.86E-28	7.36E-29	1.88E-29
145	4.62E-26	1.79E-26	4.24E-27	1.43E-27	5.45E-28	1.59E-28	5.20E-29	1.26E-29
150	4.27E-26	1.67E-26	4.01E-27	1.35E-27	5.16E-28	1.59E-28	5.66E-29	1.26E-29
155	3.98E-26	1.57E-26	3.84E-27	1.31E-27	5.06E-28	1.63E-28	7.51E-29	1.34E-29
160	3.75E-26	1.50E-26	3.72E-27	1.27E-27	4.90E-28	1.68E-28	6.97E-29	1.17E-29
165	3.58E-26	1.44E-26	3.64E-27	1.24E-27	4.65E-28	1.74E-28	6.44E-29	1.35E-29
170	3.46E-26	1.41E-26	3.57E-27	1.22E-27	4.61E-28	1.77E-28	6.78E-29	1.86E-29
175	3.38E-26	1.38E-26	3.54E-27	1.23E-27	4.80E-28	1.80E-28	6.85E-29	1.93E-29
180	3.36E-26	1.38E-26	3.52E-27	1.24E-27	4.94E-28	2.02E-28	6.90E-28	1.97E-29

PROTON ENERGY = 200.000 MEV

E(RYD)	1	2	4	6	8	12	16	24
E(EV)	13.6	27.2	54.4	81.6	108.8	163.3	217.7	326.5
THETA(DEG)								
0	1.57E-26	6.10E-27	1.72E-27	5.86E-28	2.50E-28	8.24E-29	3.49E-29	8.04E-30
5	1.59E-26	6.17E-27	1.73E-27	5.89E-28	2.49E-28	7.93E-29	3.16E-29	8.05E-30
10	1.65E-26	6.40E-27	1.78E-27	6.03E-28	2.52E-28	7.64E-29	2.80E-29	8.06E-30
15	1.76E-26	6.78E-27	1.85E-27	6.29E-28	2.63E-28	8.00E-29	3.02E-29	8.07E-30
20	1.91E-26	7.31E-27	1.95E-27	6.68E-28	2.81E-28	8.75E-29	3.52E-29	8.09E-30
25	2.10E-26	8.00E-27	2.09E-27	7.17E-28	3.01E-28	9.20E-29	3.62E-29	8.11E-30
30	2.32E-26	8.84E-27	2.26E-27	7.79E-28	3.26E-28	9.59E-29	3.78E-29	8.32E-30
35	2.59E-26	9.83E-27	2.47E-27	8.60E-28	3.63E-28	1.07E-28	4.15E-29	9.37E-30
40	2.88E-26	1.10E-26	2.73E-27	9.65E-28	4.12E-28	1.24E-28	5.04E-29	1.17E-29
45	3.20E-26	1.23E-26	3.05E-27	1.10E-27	4.73E-28	1.41E-28	5.56E-29	1.22E-29
50	3.54E-26	1.38E-26	3.46E-27	1.27E-27	5.54E-28	1.64E-28	6.27E-29	1.28E-29
55	3.90E-26	1.55E-26	3.97E-27	1.49E-27	6.72E-28	2.08E-28	8.32E-29	2.15E-29
60	4.25E-26	1.73E-26	4.60E-27	1.80E-27	8.38E-28	2.74E-28	1.16E-28	3.51E-29
65	4.60E-26	1.92E-26	5.37E-27	2.19E-27	1.06E-27	3.66E-28	1.57E-28	4.51E-29
70	4.91E-26	2.11E-26	6.26E-27	2.70E-27	1.38E-27	5.14E-28	2.32E-28	6.98E-29
75	5.17E-26	2.28E-26	7.18E-27	3.30E-27	1.81E-27	7.58E-28	3.91E-28	1.50E-28
80	5.36E-26	2.42E-26	8.00E-27	3.92E-27	2.28E-27	1.08E-27	6.25E-28	2.91E-28
85	5.46E-26	2.50E-26	8.54E-27	4.36E-27	2.65E-27	1.34E-27	8.30E-28	4.21E-28
90	5.47E-26	2.51E-26	8.65E-27	4.46E-27	2.72E-27	1.40E-27	8.72E-28	4.42E-28
95	5.39E-26	2.46E-26	8.30E-27	4.15E-27	2.47E-27	1.21E-27	7.16E-28	3.36E-28
100	5.21E-26	2.34E-26	7.58E-27	3.57E-27	2.00E-27	8.80E-28	4.67E-28	1.82E-28
105	4.97E-26	2.18E-26	6.66E-27	2.91E-27	1.52E-27	5.82E-28	2.67E-28	7.79E-29
110	4.66E-26	2.00E-26	5.71E-27	2.33E-27	1.13E-27	3.92E-28	1.65E-28	4.40E-29
115	4.32E-26	1.81E-26	4.87E-27	1.86E-27	8.55E-28	2.83E-28	1.19E-28	3.65E-29
120	3.97E-26	1.62E-26	4.17E-27	1.52E-27	6.59E-28	2.07E-28	8.26E-29	2.15E-29
125	3.62E-26	1.46E-26	3.64E-27	1.26E-27	5.20E-28	1.53E-28	5.46E-29	1.40E-29
130	3.28E-26	1.31E-26	3.23E-27	1.08E-27	4.29E-28	1.27E-28	4.82E-29	9.01E-30
135	2.97E-26	1.18E-26	2.92E-27	9.47E-28	3.70E-28	1.16E-28	4.67E-29	9.53E-30
140	2.69E-26	1.08E-26	2.69E-27	8.50E-28	3.25E-28	1.01E-28	4.12E-29	1.04E-29
145	2.44E-26	9.89E-27	2.52E-27	7.77E-28	2.88E-28	8.59E-29	3.99E-29	1.34E-30
150	2.23E-26	9.16E-27	2.40E-27	7.27E-28	2.67E-28	8.30E-29	8.08E-29	1.71E-29
155	2.05E-26	8.57E-27	2.31E-27	6.93E-28	2.57E-28	7.80E-29	3.90E-29	1.88E-29
160	1.90E-26	8.11E-27	2.25E-27	6.65E-28	2.45E-28	7.42E-29	3.94E-29	2.03E-29
165	1.79E-26	7.76E-27	2.20E-27	6.41E-28	2.30E-28	7.19E-29	4.00E-29	2.39E-29
170	1.71E-26	7.52E-27	2.17E-27	6.28E-28	2.25E-28	7.18E-29	4.09E-29	2.42E-29
175	1.66E-26	7.37E-27	2.14E-27	6.27E-28	2.33E-28	7.28E-29	4.23E-29	2.49E-29
180	1.64E-26	7.32E-27	2.14E-27	6.29E-28	2.39E-28	7.50E-29	4.39E-29	2.51E-29

Table 1 presents the doubly differential cross section (DDCS) for proton-impact ionization of helium. The cross section is differential in the energy and solid angle of the ejected electrons, i.e., we present $d^2\sigma/d\epsilon d\Omega$, where ϵ is the ejected electron energy. The DDCS is given in units of $m^2\ eV^{-1}\ steradian^{-1}$. The results given span the space of electron ejection angle, $\theta = 0°$ to $180°$, ejected electron energy, ϵ = 1 Ry (13.6 eV) to 24 Ry (326.4 eV) and proton energy, T = 0.001 MeV to 200 MeV. To obtain cross sections for values of θ, ϵ, T not presented, we expect that graphical interpolation would provide reasonable (10–20%) approximations.

References

1. D. H. Madison, Phys. Rev. A 8, 2449 (1973).
2. S. T. Manson, L. H. Toburen, D. H. Madison, and N. Stolterfoht, Phys. Rev. A 12, 60 (1975).
3. M. E. Rudd and D. H. Madison, Phys. Rev. A 14, 128 (1976).
4. J. Macek, Phys. Rev. A 1, 235 (1970).
5. M. E. Rudd and J. Macek, Case Studies Atomic. Collision Phys. 3, 47 (1972).
6. F. Herman and S. Skillman, Atomic Structure Calculations, Prentice-Hall Englewood Cliffs, N.J. (1963).

CALCULATION OF THE ENERGY TO FORM AN ION PAIR FOR PROTONS*

Hans Bichsel† and Mitio Inokuti

The specific ionization j (the number of ion pairs per unit pathlength) for high-energy protons in a pure gas can be calculated from the following data: 1. the total ionization cross section, $\sigma_i(E_p)$, for a proton of energy, E_p; 2. the distribution $\sigma(\epsilon, E_p)d\epsilon$ of kinetic energy ϵ of secondary electrons in an ionizing collision; 3. the mean energy $W(\epsilon)$ for an ion pair for an electron of energy ϵ. For a gas of unit molecular density, the number j_1 of ion pairs directly produced by protons is $\sigma_j(E_p)$, the number j_2 of ion pairs due to secondary electrons is given by

$$j_2 = \int [\epsilon/W(\epsilon)]\, \sigma(\epsilon, E_p)d\epsilon \ , \tag{1}$$

and

$$j = j_1 + j_2 \ . \tag{2}$$

If the stopping cross section $S(E_p)$ of the gas for protons is known, then one obtains the "differential W value" as

$$\omega(E_p) = S(E_p)/j \ . \tag{3}$$

If $\omega(E_p)$ is established for the entire range of E_p, one may calculate the (integral) W value as

$$E_p/W(E_p) = \int_I^{E_p} [S(E)/\omega(E)]\, dE \ ,$$

where I is the (first) ionization energy of the gas. However, our calculation

---

*Summary of a paper presented at the 24th Annual Meeting of the Radiation Research Society, San Francisco, 27 June–2 July 1976. See abstract in Radiat. Res. 67, 613 (1976).

†Department of Radiology, University of Washington, Seattle, Washington 98195. Work supported in part by National Cancer Institute Grant No. CA-124411.

is restricted to $\omega(E_p)$ at high E_p.

Equations 1–3 have been used to evaluate $\omega(E_p)$ for Ar, CH_4, and N_2. It may be noted that Jacobi and Stolterfoht[1] used the same set of equations differently; they estimated j_2 from the knowledge of j_1 and $W(E_p)$. Our results are summarized below.

Ar

For E_p = 1 MeV, we obtain $j_1 = 1.25$ by the use of $\sigma_i(E_p)$ evaluated through integration of Toburen's[2-4] $\sigma(\epsilon, E_p)$. We obtain $j_2 = 2.05$ by using the Toburen data[2-4] and a semiempirical expression[5]

$$W(\epsilon) \cong W_a \epsilon/(\epsilon - U) , \tag{4}$$

which reproduce several theoretical calculations for ϵ much greater than the ionization energy, W_a and U being constants with the energy dimension. (For Ar, we take[5] U = 11 eV.) As a consequence, we arrive at $\omega = 30.2$ eV.

The total ionization cross section $\sigma_i(E_p)$ has been measured directly, too.[6-8] The results in Refs. 6–8 are larger than the integrals of the Toburen data by about 25%, and lead to $j_i = 1.57$. If we renormalize the Toburen data and use them in Eq. 2, we obtain $j_2 = 2.57$. Thence, we have $\omega = 24.1$ eV. This value is somewhat closer to the experimental result,[9] $\omega = 26.6 \pm 0.5$ eV for 3.6-MeV protons.

CH_4

For E_p = 1 MeV, the Toburen data lead to $j_1 = 1.66$. We have calculated j_2 by use of the Toburen data and two sets of $W(\epsilon)$ values. First, the experimental data by Waker and Booz[10] give $j_2 = 1.55$, and thence $\omega = 28.5$ eV. Second, $W(\epsilon)$ of Eq. 4 with U = 9 eV gives $j_2 = 1.99$ and thence $\omega = 25.1$ eV. The first result is closer to experimental W values ranging from 29 eV to 31 eV, although the distinction between ω and W should be borne in mind. No experimental ω values seems to be available. Calculations for E_p = 0.3 MeV give $\omega = 27.7$ eV by use of the data of Waker and Booz,[10] and $\omega = 24.1$ eV by use of Eq. 4.

N_2

Again for E_p = 1 MeV, we obtain j_1 = 1.33 from $\sigma_i(E_p)$ derived from the Toburen data.[2-4] The combination of the Toburen data and the Cole measurement[11] of W(ϵ) leads to j_2 = 1.43, and thence ω = 32.4 eV. This is somewhat lower than the known W value of about 36 eV. (No experimental ω value is available.) The use of Eq. 4 with U = 9 eV leads to j_2 = 1.83 and ω = 30.3 eV.

Finally, we discuss estimates of uncertainties in the data. The uncertainty of the stopping cross section may be 2 to 4%, and that of the directly measured $\sigma_i(E_p)$ may be about 10%. The absolute uncertainty for $\sigma(\epsilon, E_p)$ is stated[2-4] as 25%. The uncertainty in measured W(ϵ) is difficult to assess.

If we assume that the calculated $\omega(E_p)$ is uncertain by 20% or so, we must conclude that W(ϵ), given by Eq. 4, is consistent with experiment for Ar (but not for CH_4 and N_2). The experimental W(ϵ) for CH_4 and N_2 give better $\omega(E_p)$ results.

References

1. W. Jacobi and N. Stolterfoht, Proc. Third Symposium on Microdosimetry, Stresa, Italy, October 1971, H. G. Ebert et al., Eds., Commission of the European Communities, Luxembourg, EUR-4810 d-f-e, p. 109 (1972).
2. L. H. Toburen, Phys. Rev. A 3, 216 (1971).
3. W. E. Wilson and L. H. Toburen, Phys. Rev. A 11, 1303 (1975).
4. Personal communication from Dr. L. H. Toburen, Battelle Pacific Northwest Laboratory.
5. M. Inokuti, Radiat. Res. 64, 5 (1975).
6. J. W. Hooper, D. S. Harmer, D. W. Martin, and E. W. McDaniel, Phys. Rev. 125, 2000 (1962).
7. S. Wexler, J. Chem. Phys. 41, 1714 (1964); 44, 2221 (1966).
8. L. I. Pivovar and Yu. Z. Levchenko, Zh. Eksperim. i. Toer. Fiz. 52, 42 [English transl.: Soviet Phys. — JETP 25, 27 (1967)].
9. J. E. Parks, G. S. Hurst, T. E. Stewart, and H. L. Weidner, J. Chem. Phys. 57, 5467 (1972).
10. A. J. Waker and J. Booz, 2nd Symposium on Nentron Dosimetry in Biology and Medicine, Neuherberg/Munich, October 1973, G. Burger and H. G. Ebert, Eds., Commission of the European Communities, Luxembourg, EUR-5452, d-e-f, p. 455 (1975).
11. A. Cole, Radiat. Res. 38, 7 (1969).

ELECTRON ENERGY DEGRADATION IN MOLECULAR HYDROGEN

D. A. Douthat*

We have calculated the degradation and the subexcitation spectra in dilute molecular hydrogen produced by monoenergetic source electrons with energies of 2 and 10 keV. The cross-section data of Gerhart were re-examined and refined. A new code for computation of degradation spectra is discussed, and sensitivity of the results to variation in the input data is examined. A previously discovered scaling of the yield of ions is also examined for this case.

In our earlier work on helium,[1,2] the primary purpose was to demonstrate the possibility of accurate calculations of complete electron degradation spectra (DGS) in the media for which reasonably complete inelastic-collision cross-section data are known. We were also concerned with some systematics, e.g., the slow variation of the mean energy per ion pair with the source energy, T_0. In view of recent progress — in both experiment and theory — much accurate data are now being acquired and analyzed for a variety of gases.[3–5] There have also been several recent studies of electron energy degradation and energy deposition, including applications to mixtures[6] and to partially ionized H_2.[7] Very extensive studies by Sato and co-workers (see Ref. 6 and Ref. 8 and references therein) based on schematic cross sections (obtained from a binary-collision model) exist for more complex gases and mixtures. Although it is difficult to assess the accuracy of these results, they are nonetheless very interesting as a first step.

The present calculation is based on Gerhart's data[3] which were compiled from a variety of experimental and theoretical sources. Gerhart's data analysis included extensive consistency checks as a means of assessing the trustworthiness of the experiments. The final data were required to meet a number

*Consultant, Radiological and Environmental Research Division. Present address: The Centre for Interdisciplinary Studies in Chemical Physics, The University of Western Ontario, London, Ontario, Canada.

of constraints, including several sum rules. Furthermore, all cross sections possess the correct high-energy (Bethe) form. This approach to the degradation problem was suggested by Platzman and has been recently reviewed by Fano[9] and Inokuti et al.[10]

There were several aims of this calculation. They included the provision of data on molecular hydrogen (for complete degradation and subexcitation spectra and primary yields), systematic exploration of the sensitivity of these spectra and yields with respect to variation of the input cross sections, and further testing of scaling properties[1,11] associated with the DGS. We intend also to utilize the data in this report in studying the systematics of irradiated systems and in computation of electron thermalization times.

Since our calculations extended to higher energies than did Gerhart's, we found some inconsistency in his data. However, other studies of H_2[7,12-15] employed cross-section data that were subjected to fewer internal and external checks than those used by Gerhart.

Method of Calculation

Our code for the computation of electron degradation spectra represents a modification of the earlier version[1] and is much faster. In fact, we are able to compute complete degradation and subexcitation spectra and all primary yields in 1.3 minutes for T_0 = 10 keV on the CDC Cyber 73 system (1.2 million operations/sec). The required computation time depends on T_0 as ln T_0 (vs. T_0 in the earlier code).

We feel that the Spencer-Fano approach to the study of primary yields now recommends itself for two reasons: (1) The DGS, as we demonstrated earlier, provides a more informative viewpoint than any other method in current use. In addition, A.R.P. Rau has recently found[16] that knowledge of the DGS provides, in principle, a complete description of the irradiated system, including fluctuations in the yields; (2) Our code compares well in speed with the fastest method for determining primary yields now in use, i.e., the continuous slowing down approximation, and is considerably faster than any other method of comparable accuracy.

While the more expensive stochastic methods (such as the Monte-Carlo method) may provide the only tractable solution if additional variables such as angle or depth of penetration are under consideration,[17-21] the use of stochastic methods in determining primary yields seems less desirable than direct numerical solution of either the Fowler equation or the Spencer-Fano equation. In any case, the yields should be equivalent since the early work of Knipp, Equchi, Ohta and Nagata[22] effectively demonstrates the equivalence of Fowler-equation results and stochastically computed yields. (The equivalence of yields computed from the DGS and the Fowler equation was recently provided.[10]) In view of these connections, the recent numerical comparisons of Garvey and Green[14] reflect the expected equivalence of yields based on the various exact methods.

The accuracy of our method was checked by comparison of the mean energy per ion pair computed in 3 ways: (1) from the DGS, (2) from solution of the Fowler equation, and (3) from the subexcitation spectrum. Methods (1) and (2) agree within about 1% and are lower than method (3) by about 4%. As an additional accuracy check, the energy balance equation (Platzman[23]) is satisfied to within 0.6% with a source energy T_0 = 2 keV and 3.7% for T_0 = 10 keV.

There remain two obvious sources of error in the calculation: (1) error in the use of the Spencer-Fano approximation (which is used for T > 600 eV) and (2) error due to remaining inconsistencies in the cross-section data, e.g., the 5 to 10% difference between values of the stopping power computed from the cross sections for energies between 2 and 10 keV and the Bethe result for the stopping power (which is used implicitly in the Spencer-Fano approximation).

Modification of Gerhart's Data

Since this calculation extended beyond the energy range of Gerhart's data, we found that his value of M_i^2 and c_i are inconsistent with his choice of the Rapp-Golden[24] total ionization data below 1 keV. We chose to modify the data in two ways, referred to as I and II and representing "extremes" with regard to the total ionization cross section, $\sigma_i(T)$. For case I, we chose

$M_i^2 = 0.721$ and $c_i = 3.825$, which give a smooth junction of the Bethe result for $_i(T)$ and the Rapp-Golden data at 1 keV. A reduction by about 28% in each of the excitation cross sections was required in order to satisfy both the IKP sum rule[25] for the total inelastic collision cross section and the oscillator-strength moment S(-1). We also chose the differential ionization cross section $d\sigma(T,E)/dE = C(T)\,E^{-3.1}$ for $T \leq 300$ eV, where E is the energy transfer. Choice of the exponent as -3.1 gives a continuous curve for the stopping power through 300 eV. For case II, we used the Gerhart values of $M_i^2 = 0.623$ and $c_i = 1.63$. This choice suggests a reduction of the Rapp-Golden data by a factor of 0.7665 if the Bethe form is assumed to be valid for T around 1 or 2 keV. For $T < 300$ eV $d\sigma(T,E)/dE = C(T)\,E^{-3.1}$ was again used. Different values from those of Gerhart were required for the functions $\phi(E)$ and C(T) in the form for $(d\sigma T,E)/dE$ with $T > 300$ eV. (The product of these functions partitions the differential ionization cross section into the hard and soft components.)

Neither the case I nor the case II modifications produced perfect agreement between the high-energy stopping power computed directly from the cross sections and the Bethe result. The differences were smaller for the case I data — about 5 to 10% for the region $1 - 10$ keV.

Results

Figure 1 displays the DGS for source energies T_0 of 2 and 10 keV. The rise at low energies and the smoothness are familiar features. (Structure near the source energy is not shown.) The two curves for $T_0 = 2$ keV represent the results from case I and case II data. The differences are substantial, ranging from 20% at 100 eV to 50% at 16 eV. More detailed data, e.g., the value of α in the low-T form $d\sigma(T,E)/dE = C(T)\,e^{-\alpha}$ are less important. We found earlier[26] that changing α from 2 to 3 produced a change of only 10% in the DGS of helium near the ionization threshold and smaller changes at higher energies. In other words, the current 10 to 20% spread of values in measured total ionization cross sections[24,27–29] leads to far greater uncertainty in computed spectra and yields than does a 10–20% uncertainty in the shape of the secondary electron ejection cross sections.[30,31] Furthermore, the sensitivity of the

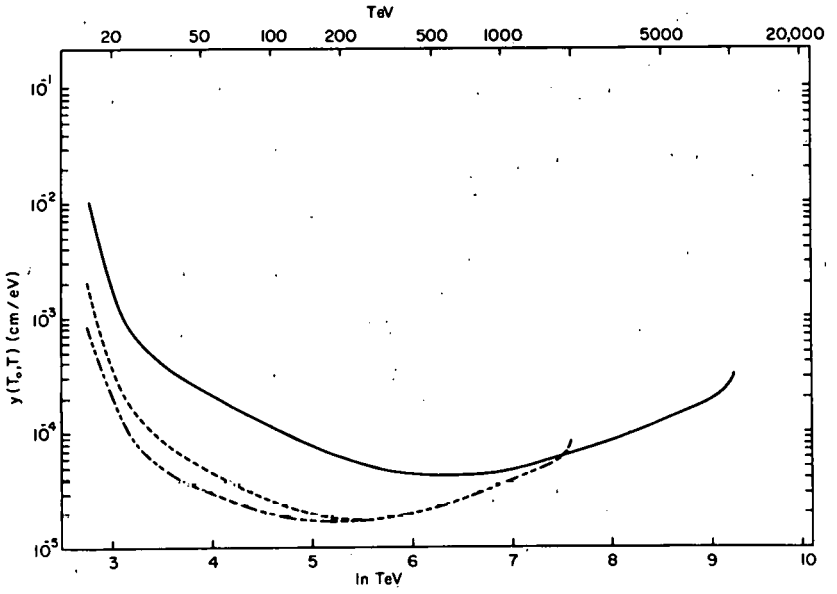

FIG. 1.--Degradation spectra for H_2 gas at 0 C and 1 atmosphere. T_0 = 10 keV, Case I data, ————————; T_0 = 2 keV, Case I data, ----------; T_0 = 2 keV, Case II data, — — — — —;

yield results is also higher than expected. The case I data give a mean energy per ion pair of 35 eV, while case II data give 49 eV at T_0 = 2 keV. The possible importance of collateral ionization[3] remains unsettled by these calculations.

Figure 2 displays the "quasi-invariance" of the ionization yield with respect to the initial energy T_0. This behavior was demonstrated empirically for helium[1] and a theoretical explanation was provided by Fano and Spencer.[11] As we would expect from the absence of inner-shell electrons, quasi-invariance is also exhibited for H_2.

Table 1 gives the yield N_s per source electron for each state s, the total energy $N_s E_s$ initially utilized in exciting N_s states with excitation energy E_s, and the corresponding percentage of the source energy T_0 that $N_s E_s$ represents.

Acknowledgements

I would like to thank Dr. Mitio Inokuti for suggesting this problem and for many helpful discussions. I am also grateful to Dr. D. Gerhart for discussion of his data, to Dr. Y.-K. Kim for comments on total ionization cross sections, to Prof. A. R. P. Rau for communicating the results of his work, and to Dr. R. H. Garvey for providing information on computation times.

The hospitality of the Centre for Interdisciplinary Studies in Chemical Physics at the University of Western Ontario and their provision of a Visiting Fellowship are also gratefully acknowledged.

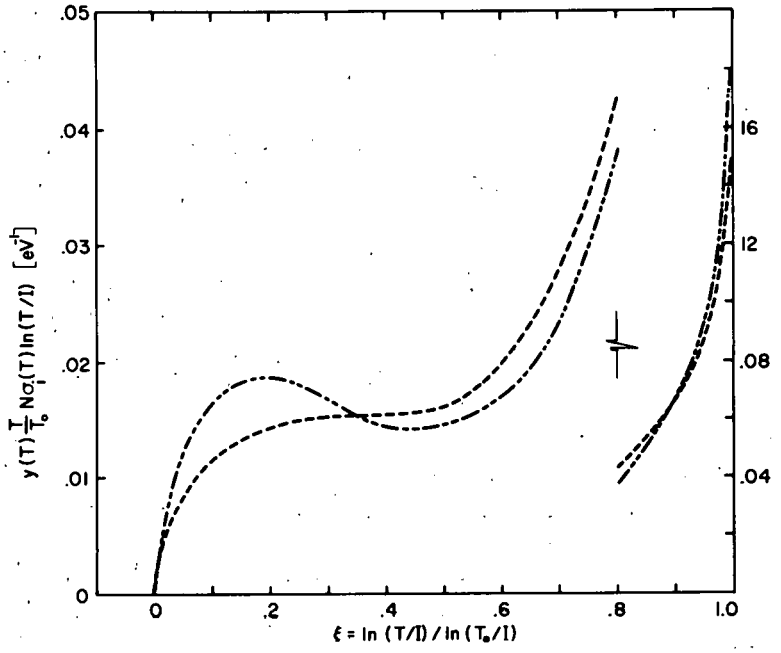

FIG. 2.--Differential distribution in energy of the ionization yield as explained in Refs. 11 and 1. The area under each curve is the reciprocal of the mean energy per ion pair. Curve (---) corresponds to T_0 = 2 keV, and curve (———) to T_0 = 10 keV.

TABLE 1. Various Yields for T_0 = 10 keV Calculated from Case-I Cross Sections

Transition	N_s (per primary)	$E_s N_s$, eV	Energy absorbed, % of total
Lyman	96.8	1210	11.7
Werner	112.1	1457	14.0
H (2P)	5.6	84	.8
Slow H (2s)	29.6	453	4.4
Fast H (2s)	5.3	175	1.7
H (n=3)	3.2	47	0.5
Remaining	12.2	177	1.7
Ions	295.6	4759	45.9
Triplets	102.6	1036	10.0
Subexcitation electrons	295.6	975	9.4
	Total	10370 eV	

References

1. D. A. Douthat, Radiat. Res. 61, 1 (1975).
2. D. A. Douthat, Radiat. Res. 64, 141 (1975).
3. D. E. Gerhart, J. Chem. Phys. 62, 821 (1975).
4. E. Eggarter, J. Chem. Phys. 62, 833 (1975).
5. S. C. Soong, Radiat. Res. 67, 187 (1976).
6. K. Okazaki, S. Sato, and S. Ohno, Bull. Chem. Soc. Jap. 49, 174 (1976).
7. T. E. Cravens, G. A. Victor, and A. Dalgarno, Planet. Space Sci. 23, 1059 (1975).
8. K. Okazaki, E. Oku, and S. Sato, Bull. Chem. Soc. Jap. 49, 1230 (1976).
9. U. Fano, Radiat. Res. 64, 217 (1975).
10. M. Inokuti, D. A. Douthat, and A. R. P. Rau, Proc. Fifth Symposium on Microdosimetry, Verbania-Pallanza, Italy, September 1975, p. 977 (1976).
11. U. Fano and L. V. Spencer, Int. J. Radiat. Phys. Chem. 7, 63 (1975).
12. W. T. Miles, R. Thompson, and A. E. S. Green, J. Appl. Phys. 43, 678 (1972).
13. J. J. Olivero, J. N. Bass, and A. E. S. Green, J. Geophys. Res. 78, 2812 (1973).
14. R. H. Garvey and A. E. S. Green, Phys. Rev. A 14, 946 (1976).
15. W. M. Jones, J. Chem. Phys. 59, 5688 (1973).
16. A. R. P. Rau, Louisiana State University, Baton Rouge, personal communication (1976).
17. M. G. Heaps and A. E. S. Green, J. Appl. Phys. 45, 3183 (1974).
18. M. J. Berger, Methods in Computational Physics, Academic Press, New York, Vol. I, (1963).
19. U. Fano, L. V. Spencer, and M. J. Berger, Encyclopedia of Physics, S. Flügge, Ed., Springer, Berlin, Vol. 38/2, p. 660 (1959).
20. R. N. Hamm, H. A. Wright, R. H. Ritchie, J. E. Turner, and T. P. Turner, Proc. Fifth Symp. on Microdosimetry, Verbania-Pallanza, Italy, September 1975, Commission of the European Communities, Luxembourg, EUR 5452 d-e-f, p. 1037 (1976).
21. H. G. Paretzke, Proc. Fifth Symp. on Microdosimetry, Verbania-Pallanza, Italy, September 1975, Commission of the European Communities, Luxembourg, EUR 5452 d-e-f, p. 41 (1976).
22. J. K. Knipp, T. Eguchi, M. Ohta, and S. Nagata, Prog. Theor. Phys. 10, 24 (1953).
23. R. L. Platzman, Int. J. Appl. Radiat. Isotopes 10, 116 (1961).
24. D. Rapp and P. Englander-Golden, J. Chem. Phys. 43, 1465 (1965).
25. M. Inokuti, Y.-K. Kim, and R. L. Platzman, Phys. Rev. 164, 55 (1967).
26. D. A. Douthat, Radiological and Environmental Research Division Annual Report, July 1974–June 1975, ANL 75-60, Part I, p. 92
27. J. T. Tate and P. T. Smith, Phys. Rev. 39, 270 (1932).
28. B. L. Schram, F. J. de Heer, M. J. van der Wiel, and J. Kistemaker, Physica 31, 94 (1964).
29. F. F. Rieke and W. Prepejchal, Phys. Rev. A 6, 1507 (1972).
30. C. B. Opal, E. C. Beaty, and W. K. Peterson, Atom. Data 4, 209 (1972).
31. N. Oda, Radiat. Res. 64, 80 (1975).

TOTAL CROSS SECTIONS FOR COLLISIONS BETWEEN ATOMIC PARTICLES AT HIGH VELOCITIES

Mitio Inokuti

General principles governing elastic and inelastic collisions between particles with electronic structure are presented. The treatment presumes relative translational velocities far exceeding the mean orbital velocity of electrons in either of the colliding particles, and closely follows the Bethe theory for the collisions of a structureless particle with an atom or molecule. For illustration, numerical results are given for collisions between two hydrogen-like ions.

Introduction

The well-known Bethe theory[1-3] treats collisions of a structureless charged particle with an atom or molecule at high relative velocities. Considerations of the impact of more general atomic particles, i.e., particles having internal electronic structure, do not seem to have been put forth systematically, although Bohr[4] explained qualitatively that electrons orbiting around the particle at speed less than the particle speed will be efficiently stripped off upon collisions with an atom or molecule.

Following is an initial report of new work aimed at extending the Bethe theory to collisions between particles with electrons for application to radiological physics, heavy-ion physics, and plasma physics.

Basics

Consider the collision

$$A + B \rightarrow A_m + B_n ,$$

where A and B represent atomic particles (atoms, molecules, or ions) in their electronic ground state. The suffix m or n denotes an electronic state, either discrete or continuum. Throughout the discussion, the relative velocity v of colliding partners is taken as much greater than the mean orbital velocity of electrons in either A or B.

For definiteness, let us take as A and B atomic ions that have nuclei with charges $Z_a e$ and $Z_b e$, as well as N_a and N_b electrons, respectively. The total Coulomb energy of the interactions between A and B is given as

$$V = Z_a Z_b e^2 R^{-1} - Z_a e^2 \sum_{k=1}^{N_b} |\vec{R} + \vec{r}_k|^{-1}$$

$$- Z_b e^2 \sum_{j=1}^{N_a} |\vec{R} - \vec{r}_j|^{-1} + e^2 \sum_{j=1}^{N_a} \sum_{k=1}^{N_b} |\vec{r}_j - \vec{r}_k + \vec{R}|^{-1} , \qquad (1)$$

where $\vec{R}$ is the vector distance from nucleus A to nucleus B, $\vec{r}_j$ is the position of the jth electron in A measured from nucleus A, and $\vec{r}_k$ is the position of the kth electron in B measured from nucleus B. An alternative expression is

$$V = (2\pi^2)^{-1} e^2 \int d\vec{q}\, q^{-2} \{ Z_a Z_b \exp(-i\vec{q} \cdot \vec{R})$$

$$- Z_a \sum_{k=1}^{N_b} \exp[-i\vec{q} \cdot (\vec{R} + \vec{r}_k)] - Z_b \sum_{j=1}^{N_a} \exp[-i\vec{q} \cdot (\vec{R} - \vec{r}_j)]$$

$$+ \sum_{j=1}^{N_a} \sum_{k=1}^{N_b} \exp[-i\vec{q} \cdot (\vec{r}_k - \vec{r}_j + \vec{R})] \} , \qquad (2)$$

where $\vec{q}$ is a variable of the Fourier integral. When one applies the first-order perturbation theory (i.e., the first Born approximation), the cross section for the process is given as[5]

$$d\sigma_{mn} = 4\pi a_0^2 (v_0/v)^2 |\phi_m(K)|^2 |\phi_n(K)|^2 d(Ka_0)^2/(Ka_0)^4 , \qquad (3)$$

where $a_0 = \hbar^2/m_e e^2 = 0.529 \times 10^{-8}$ cm, and $v_0 = \hbar/e^2 = c/137 = 2.188 \times 10^8$ cm/sec. The factor $(v_0/v)^2$ may be expressed as

$$(v_0/v)^2 = R/T \qquad (4)$$

in terms of the Rydberg energy $R = m_e e^4/2\hbar^2 = 13.6$ eV and of the symbol $T = \frac{1}{2} m_e v^2$, m_e being the electron (rest) mass, used in Ref. 3. Further, $\hbar\vec{K}$ is the momentum transfer in the collision, and its magnitude is given by

$$(Ka_0)^2 = 2(M/m_e)^2 (T/R) \{ 1 - m_e E/2MT - (1 - m_e E/MT)^{\frac{1}{2}} \cos\theta \} , \qquad (5)$$

where M is the reduced mass of the colliding particles, θ is the scattering angle, and E is the sum of electronic excitation energies E_m and E_n in A and B, respectively. Finally, $\phi_m(K)$ is a matrix element between eigenstates of particle A

$$\phi_m(K) = (m|Z_a - \sum_{j=1}^{N_a} \exp(i\vec{K}\cdot\vec{r}_j)|0) \ . \tag{6}$$

Similarly,

$$\phi_n(K) = (n|Z_b - \sum_{k=1}^{N_b} \exp(i\vec{K}\cdot\vec{r}_k)|0) \tag{7}$$

for particle B. Notice that $\phi_m(K)$ is a property of particle A only and $\phi_n(K)$ is a property of particle B; in other words, $\phi_m(K)$ and $\phi_n(K)$ refer to different particles and are independent of each other. To remind us of this distinction, I adhere to the stipulation that suffixes m and j always refer to particle A and the suffixes n and k to particle B throughout the present article.

For brevity of presentation, the present discussion will be restricted to nonrelativistic velocities v. Extension to relativistic velocities is straightforward insofar as one excludes extremely relativistic velocities for which radiative effects such as coupling with Bremsstrahlung become appreciable. This qualification is the same as in the Bethe theory for structureless charged particles (cf. Sec. 2.3 of Ref. 3).

The goal of the present analysis is to integrate Eq. 3 over all possible momentum transfers (or alternatively, over all scattering angles θ) and thereby to derive compact cross-section formulas for high (but nonrelativistic) v.

The first step deals with the behavior of $\phi_m(K)$ and $\phi_n(K)$ at small K. The familiar Taylor expansion of the exponentials, together with the orthogonality of eigenstates, leads to

$$\phi_0(K) = Z_a - N_a + (Ka_0)^2 (X^2)_0/2 - (Ka_0)^4 (X^4)_0/24 + \ldots \ , \tag{8}$$

and

$$\phi_{m\neq 0}(K) = -i(Ka_0)(X)_m + (Ka_0)^2 (X^2)_m/2 + i(Ka_0)^3 (X^3)_m/6 - (Ka_0)^4 (X^4)_m/24 + \ldots \ , \tag{9}$$

where

$$X = \sum_{j=1}^{N_a} (\vec{K} \cdot \vec{r}_j)/Ka_0 \tag{10}$$

and

$$(X^\kappa)_m = (m|X^\kappa|0) \qquad (\kappa = 1,2,3,4,\ldots) . \tag{11}$$

Therefore, one obtains

$$|\phi_{0a}(K)|^2 = (Z_a - N_a)^2 + (Z_a - N_a)(Ka_0)^2 (X^2)_0 + \ldots \tag{12}$$

and

$$|\phi_{m\neq 0}(K)|^2 = (Ka_0)^2 |(X)_m|^2 + [\tfrac{1}{4}|(X^2)_m|^2 - \tfrac{1}{3}(X)_m^* (X^3)_m - \tfrac{1}{3}(X^3)_m^* (X)_m](Ka_0)^4 + \ldots , \tag{13}$$

in accordance with Ref. 3 (p. 313).

Equations 8–13 refer to particle A. Similar equations hold for particle B; one obtains them by replacement: $Z_a \rightarrow Z_b$, $N_a \rightarrow N_b$, $m \rightarrow n$, and $j \rightarrow k$.

The different behavior of $|\phi_m(K)|^2$ or $|\phi_n(K)|^2$ at small K makes it necessary to treat three classes of collisions differently: (1) elastic collisions, i.e., $m = 0$ and $n = 0$; (2) singly inelastic collisions, i.e., either $m \neq 0$ and $n = 0$ or $m = 0$ and $n \neq 0$; (3) doubly inelastic collisions, i.e., $m \neq 0$ and $n \neq 0$.

The meaning of the labels m and n for the electronic states of atomic particles must be made more precise. In what follows, it is assumed that the atomic particles are either spherical or randomly oriented in the initial state. Furthermore, one always implies by labels m and n that the customary summation over magnetic quantum numbers of the final state of the atomic particle is to be carried out. (In other words, the rotational symmetry is assumed for each atomic particle.) Under this stipulation, $|\phi_m(K)|^2$ or $|\phi_n(K)|^2$ is an even function of K. Thus, it is justified to use the variable

$$Q = (Ka_0)^2 \tag{14}$$

for concise expression and regard the $|\phi|^2$ as a function of Q. In what follows, the notations $|\phi_m(Q)|^2$ and $|\phi_n(Q)|^2$ will be used. Thus, one may rewrite Eq. 3 as

$$d\sigma_{mn} = 4\pi a_0^2 (R/T) |\phi_m(Q)|^2 |\phi_n(Q)|^2 Q^{-2} dQ , \tag{15}$$

with the use of Eq. 4.

Elastic Collision

The total collision cross section for elastic collision is given as

$$\sigma_{00} = 4\pi a_0^2 (R/T) \int_0^{Q_{max}} |\phi_{a0}(Q)|^2 |\phi_{b0}(Q)|^2 Q^{-2} dQ , \tag{16}$$

according to Eq. 15, where $\phi_{a0}(Q)$ and $\phi_{b0}(Q)$ are ground-state expectation values [Eqs. 6 and 7] for A and B, respectively. The lower limit of the Q-integration is zero because the minimum value of the momentum transfer for elastic collision is zero. The upper limit is given by

$$Q_{max} = 4(M/m_e)^2 (T/R) . \tag{17}$$

From the low-Q behavior of $|\phi_{a0}(Q)|^2$ (Eq. 12), one immediately sees that σ_{00} is divergent unless $Z_a = N_a$ or $Z_b = N_b$, i.e., unless one of the colliding particles is neutral. This observation is not at all surprising; indeed, the Rutherford scattering has a divergent total cross section owing to the long-range Coulomb force. Therefore, we shall assume that B is neutral, i.e., $Z_b = N_b$; however, A may be either neutral or charged. Then, $|\phi_{ob}(Q)|^2 = O(Q^2)$ for small Q, and thus the integrand of Eq. 15 is analytic for $Q \geq 0$.

Because Q_{max} as given by Eq. 17 is large, it is appropriate to write the integral of Eq. 16 in two terms

$$\int_0^\infty - \int_{Q_{max}}^\infty .$$

The first term is independent of T. the second term may be evaluated approximately as

$$\int_{Q_{max}}^{\infty} |\phi_{0a}(Q)|^2 |\phi_{0b}(Q)|^2 Q^{-2} dQ$$

$$= Z_a^2 Z_b^2 \int_{Q_{max}}^{\infty} Q^{-2} dQ + O(Q_{max}^{-2})$$

$$= \tfrac{1}{4} Z_a^2 Z_b^2 (m_e/M)^2 (R/T) + O((m_e/M)^4 (R/T)^2) .$$

Consequently, one obtains

$$(T/R)(\sigma_{00}/4\pi a_0^2) = \int_0^{\infty} |\phi_{0a}(Q)|^2 |\phi_{0b}(Q)|^2 Q^{-2} dQ$$

$$- \tfrac{1}{4} Z_a^2 Z_b^2 (m_e/M)^2 (R/T) + O((m_e/M)^4 (R/T)^2) . \qquad (18)$$

Note that the right-hand side is very nearly independent of T, the second term being extremely small because m_e/M is 10^{-3} or smaller.

Singly Inelastic Collisions (for Individual Excitation)

To be specific, let us consider the case in which A becomes excited but B remains unexcited (i.e., $m \neq 0$ and $n = 0$). The total cross section is given as

$$\sigma_{m0} = 4\pi a_0^2 (R/T) \int_{Q_{min}}^{Q_{max}} |\phi_{ma}(Q)|^2 |\phi_{0b}(Q)|^2 Q^{-2} dQ . \qquad (19)$$

Here, the lower limit of the Q integration is nonvanishing; it has the value

$$Q_{min} = (E_m^2/4RT)[1 + \tfrac{1}{2}(m_e E_m/MT) + O((m_e E_m/MT)^2)] , \qquad (20)$$

exactly the same as the value for inelastic collisions of A with a structureless particle [cf. Eq. 2.17 of Ref. 3]. Similarly, the upper limit is given by

$$Q_{max} = 4(T/R)(M/m_e)^2 [1 - \tfrac{1}{2}(m_e E_m/MT) + O((m_e E_m/MT))] . \qquad (21)$$

To analyze the T dependence of the integral, it is convenient to write

$$|\phi_{0b}(Q)|^2 = [(Z_b - N_b) + \varphi(Q)]^2$$

$$= (Z_b - N_b)^2 + 2(Z_b - N_b)\varphi(Q) + \varphi^2(Q) \ . \qquad (22)$$

According to Eq. 8, the function $\varphi(Q)$ behaves like Q at small Q. Accordingly, the integral in Eq. 19 may be separated into three terms as

$$\int_{Q_{min}}^{Q_{max}} |\phi_{ma}(Q)|^2 |\phi_{0b}(Q)|^2 Q^{-2} dQ$$

$$= (Z_b - N_b)^2 \int_{Q_{min}}^{Q_{max}} |\phi_{ma}(Q)|^2 Q^{-2} dQ$$

$$+ 2(Z_b - N_b) \int_{Q_{min}}^{Q_{max}} |\phi_{ma}(Q)|^2 \varphi(Q) Q^{-2} dQ$$

$$+ \int_{Q_{min}}^{Q_{max}} |\phi_m(Q)|^2 \varphi^2(Q) Q^{-2} dQ \ . \qquad (23)$$

The first term has precisely the same form as in the standard Bethe theory for a structureless particle with net charge $Z_b - N_b$. Therefore, the value of the first term of Eq. 23 can be expressed as

$$(Z_b - N_b)^2 \int_{Q_{min}}^{Q_{max}} |\phi_m(Q)|^2 Q^{-2} dQ$$

$$= (Z_b - N_b)^2 [M_m^2 \ln(4c_m T/R) + \gamma_m R/T] + O(E_m^2/T^2) \ , \qquad (24)$$

according to Eq. 4.18 of Ref. 3, where M_m^2 is the squared dipole moment (measured in atomic units)

$$M_m^2 = |(m|X|0)|^2 \ , \qquad (25)$$

and c_m and γ_m are parameters defined by Eqs. 4.14 and 4.19 of Ref. 3.

The second integral of Eq. 23 is now being considered. The integral is analytic for $Q \geq 0$, and therefore may be separated into three parts as

$$\int_0^{\infty} - \int_0^{Q_{min}} - \int_{Q_{max}}^{\infty} .$$

The first part is obviously independent of T. The second part may be evaluated by the use of Eqs. 12 and 13 as

$$\begin{aligned} &\int_0^{Q_{min}} |\phi_m(Q)|^2 \varphi(Q)\, Q^{-2}\, dQ \\ &\quad = \tfrac{1}{2} |(X_m)|^2 (X^2)_{0b}\, Q_{min} + O(Q_{min}^2) \\ &\quad = (X^2)_{0b}\, M_m^2 E_m^2/(8RT) + O(E_m^4/R^2T^2) . \end{aligned} \tag{26}$$

To evaluate the third part, one must only recall the high-Q asymptotic behavior $|\phi_m(Q)|^2 = O(Q^{-4})$ or smaller and $\varphi(Q) = N_b + O(Q^{-2})$, as given by Rau and Fano.[6] Therefore,

$$\int_{Q_{max}}^{\infty} |\phi_m(Q)|^2 \varphi(Q)\, Q^{-2}\, dQ = O(Q_{max}^{-5}) , \tag{27}$$

an extremely small contribution. Combining Eqs. 26 and 27, one arrives at

$$\begin{aligned} &2(Z_b - N_b) \int_{Q_{min}}^{Q_{max}} |\phi_m(Q)|^2 \varphi(Q)\, Q^{-2}\, dQ \\ &\quad = 2(Z_b - N_b) \int_0^{\infty} |\phi_m(Q)|^2 \varphi(Q)\, Q^{-2}\, dQ \\ &\quad - (Z_b - N_b)(X^2)_{0b}\, M_m^2 E_m^2/(4RT) + O(E_m^4/R^2T^2) . \end{aligned} \tag{28}$$

Similarly, the last integral of Eq. 23 is given as

$$\int_{Q_{min}}^{Q_{max}} |\phi_m(Q)|^2 \varphi^2(Q) Q^{-2} dQ$$

$$= \int_0^{\infty} |\phi_m(Q)|^2 \varphi^2(Q) Q^{-2} dQ + O(E_m^2/R^2T^2) . \quad (29)$$

Consequently, the cross section for the singly inelastic collision takes the form

$$(T/R)(\sigma_{m0}/4\pi a_0^2) = (Z_b - N_b)^2 [M_m^2 \ln(4c_m/TR) + \gamma_m R/T]$$

$$+ 2(Z_b - N_b)[\int_0^{\infty} |\phi_m(Q)|^2 \varphi(Q) Q^{-2} dQ - (X)_{0b}^2 E_m^2 M_m^2/8RT]$$

$$+ \int_0^{\infty} |\phi_m(Q)|^2 \varphi^2(Q) Q^{-2} dQ + O(E_m^4/R^2T^2) . \quad (30)$$

Total Cross Section for Singly Inelastic Collisions

The sum of σ_{m0} of Eq. 30 over all $m \neq 0$ may be called the total cross section σ_{*0} for singly inelastic collisions. The method of Inokuti, Kim, and Platzman[7,8] may be readily extended to the evaluation of σ_{*0}. The basis of the method is a sum rule (Eq. 3.17 of Ref. 3)

$$\sum_{m\neq 0} |\phi_m(Q)|^2 = N_a S_{inc,a}(Q) , \quad (31)$$

where $S_{inc,a}(Q)$ is the incoherent-scattering function of A and is defined in terms of the ground-state expectation values (denoted by $\langle \ldots \rangle$) as

$$N_a S_{inc,a}(Q) = \langle | \sum_{j=1}^{N_a} \exp(i\vec{K} \cdot \vec{r}_j) |^2 \rangle - \langle \sum_{j=1}^{N_a} \exp(i\vec{K} \cdot \vec{r}_j) \rangle^2 . \quad (32)$$

Considering the limit $Q \rightarrow 0$ of Eq. 31, one obtains

$$\sum_{m\neq 0} M_m^2 = \sum_{m\neq 0} \lim |\phi_m(Q)|^2/Q^2 = \langle (\sum_{j=1}^{N_a} x_j/a_0)^2 \rangle . \quad (33)$$

The sum $\sum_{m\neq 0} M_m^2$ is called[7] the total squared dipole matrix element and is denoted by $M_{tot,a}^2$. (See Eq. 3.18 of Ref. 3.)

Let us consider the summation of Eq. 30 over $m \neq 0$. The first line of the right-hand side is precisely the same as the Bethe cross section treated in Refs. 7 and 8. Therefore, one may immediately write

$$\sum_{m\neq 0} (Z_b - N_b)^2 \left[M_n^2 \ln(4c_m T/R) + \gamma_m R/T \right]$$

$$= (Z_b - N_b)^2 \left[M_{tot,a}^2 \ln(4c_{tot,a} T/R) - \tfrac{1}{4} S_a^{(1)}(1) R/T - \tfrac{1}{4} N_a R/T \right] , \tag{34}$$

where $M_{tot,a}^2$ has been defined already, and $c_{tot,a}$ is given by[7]

$$M_{tot,a}^2 \ln c_{tot} = \left[I_1 - I_2 - 2L(-1) \right]_a . \tag{35}$$

The quantities I_1 and I_2, as well as $L(-1)$, are properties of A discussed in Ref. 7 (and also in Section 4.3 of Ref. 3). The summation $\sum_{m\neq 0} \gamma_m$ has been expressed as $-\frac{1}{4} S_a^{(1)}(1)$ by use of the notation in Ref. 3. In other words,

$$S_a^{(1)}(1) = \sum_{m\neq 0} (E_m/R) \left[d f_m(Q)/dQ \right]_{Q=0}$$

$$= \sum_{m\neq 0} (E_m/R)^2 \left[dQ^{-1} \left| \phi_m(Q) \right|^2 / dQ \right]_{Q=0} , \tag{36}$$

where $f_m(Q)$ is the generalized oscillator strength for the transition $0 \rightarrow m$ in A. According to Ref. 8, $S_a^{(1)}(1)$ may be replaced by N_a to a good approximation, as will be done hereafter in the present treatment. [The above evaluation of $\sum_{m\neq 0} \gamma_m$ has also neglected a contribution of the small magnitude $-\frac{1}{2} (m_e/M) N_a$, which arises from the second term of Eq. 4.19 of Ref. 3.]

The summation of the second line of Eq. 30 is simpler, and proceeds as follows:

$$\sum_{m\neq 0} 2(Z_b - N_b) \left[\int_0^\infty \left| \phi_m(Q) \right|^2 \varphi(Q)\, Q^{-2}\, dQ - (X^2)_{0b} E_m^2 M_m^2 / 3RT \right]$$

$$= 2(Z_b - N_b)\left[\int_0^\infty N_a S_{inc,a}(Q)\,\varphi(Q)\,Q^{-2}\,dQ - \frac{1}{8}(X^2)_{0b} S_a(1) R/T\right] , \tag{37}$$

where use has been made of Eq. 13 and $S_a(1)$ is defined by

$$S_a(1) = \sum_{m\neq 0} (E_m/R)\, f_m = \sum_{m\neq 0} (E_m/R)^2 M_m^2 , \tag{38}$$

f_m being the dipole oscillator strength for the transition $0 \rightarrow m$ in A. According to the well-known sum rule (Eq. 3.29 of Ref. 3), $S_a(1)$ may be evaluated as

$$S_a(1) = (4/3R)\,\langle (\sum_{j=1}^{N_a} \vec{p}_j)^2/2m_e \rangle_a , \tag{39}$$

where $\vec{p}_j$ is the momentum of the jth electron in A.

The summation of the third line of Eq. 30 gives

$$\sum_{m\neq 0} \int_0^\infty |\phi_m(Q)|^2 \varphi^2(Q)\, Q^2\, dQ = \int_0^\infty N_a S_{inc,a}(Q)\,\varphi^2(Q)\,Q^{-2}\,dQ , \tag{40}$$

again by the use of Eq. 31.

Finally, one may combine Eqs. 34, 37, and 40 to arrive at

$$(T/R)(\sigma_{*0}/4\pi a_0^2) = (Z_b - N_b)^2 [M^2_{tot,a} \ln(4c_{tot,a} T/R) - \tfrac{1}{2} N_a R/T]$$

$$+ 2(Z_b - N_b)\left[\int_0^\infty N_a S_{inc,a}(Q)\,\varphi(Q)\,Q^{-2}\,dQ - \frac{1}{8}(X^2)_{0b} S_a(1) R/T\right]$$

$$+ \int_0^\infty N_a S_{inc,a}(Q)\,\varphi^2(Q)\,Q^{-2}\,dQ + O(R^2/T^2) . \tag{41}$$

Doubly Inelastic Collision

When both atomic particles A and B become excited (or ionized) after a single collision, I call that collision doubly inelastic. The cross section for exciting A to state m and B to state n is written as

$$\sigma_{mn} = 4\pi a_0^2 (R/T) \int_{Q_{min}}^{Q_{max}} |\phi_m(Q)|^2\, |\phi_n(Q)|^2\, Q^{-2}\, dQ , \tag{42}$$

according to Eq. 15. The lower limit of the integration is given by

$$Q_{min} = [(E_m + E_n)^2/4RT]\{1 + \tfrac{1}{2} m_e(E_m + E_n)/MT + O((m_e(E_m + E_n)/MT)^2)\}, \quad (43)$$

and the upper limit by

$$Q_{max} = 4(T/R)(M/m_e)\{1 + O(m_e(E_m + E_n)/MT)\} . \quad (44)$$

Because $|\phi_m(Q)|^2$ and $|\phi_n(Q)|^2$ both behave like Q for small Q (as seen in Eq. 13), the integrand of Eq. 42 is well-behaved near Q = 0. The same integrand decreases at least like Q^{-8} for large Q, according to the result of Rau and Fano,[6] so that the upper limit of the integration may be extended to infinity without introducing an appreciable error. Thus, one may write the integral as

$$\int_{Q_{min}}^{Q_{max}} = \int_0^{\infty} - \int_0^{Q_{min}} ,$$

to obtain

$$\sigma_{mn} = 4\pi a_0^2 (R/T) \left[\int_0^{\infty} |\phi_m(Q)|^2 |\phi_n(Q)|^2 Q^{-2} dQ - \int_0^{Q_{min}} |\phi_m(Q)|^2 |\phi_n(Q)|^2 Q^{-2} dQ \right] . \quad (45)$$

The first term in the square bracket is independent of T, and the second term may be evaluated by the use of the low-Q behavior of $|\phi|$'s (Eq. 13) as

$$\int_0^{Q_{min}} |\phi_m(Q)|^2 |\phi_n(Q)|^2 Q^{-2} dQ = M_m^2 M_n^2 Q_{min} + O(Q_{min}^2)$$

$$= M_m^2 M_n^2 (E_m + E_n)^2/4RT + O[(E_m + E_n)^2/T^2]$$

$$= -(R/4T) f_m f_n (E_m/E_n + 2 + E_n/E_m) + O((E_m + E_n)^2/T^2) , \quad (46)$$

where use has been made of Eq. 43, and f_m and f_n are dipole oscillator strengths of A and B, respectively, for transitions $0 \rightarrow m$ and $0 \rightarrow n$.

For large T/R, σ_{mn} is almost proportional to R/T, with a small correction given by the second term of Eq. 45 or by Eq. 46.

Let us now consider the sum of σ_{mn} over all $m \neq 0$ and $n \neq 0$. Using Eqs. 31, 45, and 46, one may write the total cross section, σ_{**}, for doubly inelastic collisions as

$$\sigma_{**} = \sum_{m\neq 0} \sum_{n\neq 0} \sigma_{mn}$$

$$= 4\pi a_0^2 (R/T) \left\{ \int_0^\infty N_a S_{inc,a}(Q)\, N_b S_{inc,b}(Q)\, Q^{-2}\, dQ \right.$$

$$\left. - \tfrac{1}{4} (R/T) \left[S_a(1)\, S_b(-1) + 2 S_a(0)\, S_b(0) + S_a(-1)\, S_b(1) \right] \right\} , \qquad (47)$$

where $S_a(\mu)$ and $S_b(\mu)$ are the moments of the dipole oscillator strength defined (Section 3.3 of Ref. 3) by

$$S_a(\mu) = \sum_{m\neq 0} (E_m/R)^\mu f_m \qquad (48)$$

and

$$S_b(\mu) = \sum_{n\neq 0} (E_n/R)^\mu f_n . \qquad (49)$$

The second term in the square bracket of Eq. 47 is always negative.

Collisions Between Two Hydrogen-Like Atomic Ions as an Example

When the colliding atomic particles A and B have one electron each, all the quantities appearing in the present treatment may be readily evaluated. For this purpose, one should note the following analytic results:

$$|\phi_{0a}(Q)|^2 = [Z_a - (1+aQ)^{-2}]^2 , \qquad (50)$$

$$|\phi_{0b}(Q)|^2 = [Z_b - (1+bQ)^{-2}]^2 , \qquad (51)$$

$$\sum_{m\neq 0} |\phi_m(Q)|^2 = S_{inc,a}(Q) = 1 - (1+aQ)^{-4} \tag{52}$$

$$\sum_{n\neq 0} |\phi_n(Q)|^2 = S_{inc,b}(Q) = 1 - (1+bQ)^{-4} , \tag{53}$$

where

$$a = 1/(4Z_a^2) , \tag{54}$$

and

$$b = 1/(4Z_b^2) . \tag{55}$$

As a corollary of Eqs. 52 and 53, one may also note that

$$M^2_{tot,a} = 1/Z_a^2 \tag{56}$$

and

$$M^2_{tot,b} = 1/Z_b^2 . \tag{57}$$

For simple presentation, I give below only the leading terms of the cross sections σ_{00}, σ_{0*}, and σ_{**}. In the following equations, I imply by the notation .... terms of the order of magnitude R/T or smaller.

For consideration of <u>elastic collisions</u>, it is presumed that B is neutral, i.e., $Z_b = 1$ and therefore $b = 1/4$. (Otherwise the total elastic-collision cross section diverges.) Substituting Eqs. 50 and 51 into Eq. 18 and carrying out elementary integrals, one obtains

$$(T/R)\sigma_{00}/4\pi a_0^2 = \int_0^\infty [Z_a - (1+aQ)^{-2}]^2 [1 - (1+bQ)^{-2}] Q^{-2} dQ + ...$$

$$= Z_a^2 C_0 - 2Z_a C_1 + C_2 + ... , \tag{58}$$

where

$$C_0 = 7b/3 , \tag{59}$$

$$C_1 = (12a^3 + 19a^2 b - 26ab^2 + 7b^3) b^2 (b-a)^{-4}/3 - 2(6a^2 - 5ab + b^2) ab^3 (b-a)^{-5} \ln(b/a) , \tag{60}$$

and

$$C_2 = (4a^5 - 30a^4b + 121a^3b^2 - 11a^2b^3 - 31ab^4 + 7b^5)\, b^2\, (b-a)^{-6}/3$$

$$- 4(11a^2 - 7ab + b^2)\, ab^5\, (b-a)^{-7} \ln(b/a) \ . \qquad (61)$$

Despite their appearance, Eqs. 60 and 61 are nonsingular at $a = b$, as they ought to be. Indeed, one can readily verify that $C_1 \to 31b/30$ and $C_2 \to 71b/105$ as $a \to b$. In other words, for $a = b = 1/4$ (i.e., for collisions between two hydrogen atoms), Eq. 58 reduces to

$$(T/R)\sigma_{00}/4\pi a_0^2 = 33/140 + \ldots . \qquad (62)$$

In another limit $a \to 0$ (i.e., $Z_a \gg 1$), both C_1 and C_2 tend to $7b/3$. In other words, Eq. 58 reduces to

$$(T/R)\sigma_{00}/4\pi a_0^2 = 7(Z_a - 1)^2/12 + \ldots , \qquad (63)$$

a result readily obtained from the Bethe theory for collision of a structureless particle having net charge $Z_a - 1$ with a hydrogen atom.

For <u>singly inelastic collisions</u> leading to excitation of A only, substitution of Eqs. 51 and 52 into Eq. 41 gives

$$(T/R)\sigma_{*0}/4\pi a_0^2 = (Z_b - 1)^2 D_0 + 2(Z_b - 1) D_1 + D_2 + \ldots , \qquad (64)$$

where

$$D_0 = Z_a^{-2} [\ln(T/R) + 0.449469 - 2 \ln Z_a] , \qquad (65)$$

according to Ref. 7,

$$D_1 = ab[(8a^3 - 29a^2b + 34ab^2 - b^3)(b-a)^{-4}/3$$

$$+ 2(a^4 - 5a^3b + 10a^2b^2 - 10ab^3 + 2b^4)(b-a)^{-5} \ln(b/a)] , \qquad (66)$$

and

$$D_2 = ab[(7a^5 - 46a^4b + 135a^3b^2 - 261a^2b^3 + 116ab^4 - 11b^5)(b-a)^{-6}/3$$

$$+ 4(11a^2 - 7ab + b^2)\, b^4\, (b-a)^{-7} \ln(b/a)] \ . \qquad (67)$$

Here again, D_1 and D_2 are nonsingular at $a = b$. In fact, $D_1 \to 101b/30$ and $D_2 \to 58b/35$ as $a \to b$. When $b \to 0$ (i.e., when Z_b is so large that B may

be regarded as virtually structureless), $D_1 \to 0$ and $D_2 \to 0$; in other words, Eq. 64 reduces to the result of the standard Bethe theory.

The total cross section for doubly inelastic collisions is obtained by use of Eqs. 47, 52, and 53. The result is

$$(T/R)\sigma_{**}/4\pi a_0^2 = ab[(a+b)(9a^4 - 53a^3b + 118a^2b^2 - 53ab^3 + 9b^4)(b-a)^{-6}/3 + 4(a^6 - 7a^5b + 21a^4b^2 - 35a^3b^3 + 21a^2b^4 - 7ab^5 + b^6) \times (b-a)^{-7} \ln(b/a)] + \ldots . \quad (68)$$

This expression tends to $533b/105$ as $a \to b$.

Commentary on Collisions Between Hydrogen Atoms

Let us review the results of the previous section in the special case of two hydrogen atoms, i.e., $Z_a = Z_b = 1$. First of all, for each class of collision, the cross section is proportional to T^{-1} for large T. The quantity $(T/R)\sigma/4\pi a_0^2$, which may be called the collision strength,[9] is shown in Table 1.

Second, the doubly inelastic collisions are the most probable (with over 50% relative probability), singly inelastic collisions next most probable, and elastic collisions the least probable, as noted by Bates and Griffing.[10,11] To understand why this order of different cross sections arises, let us start with Eqs. 50–53, which give probabilities for each of the hydrogen atoms to stay either excited or unexcited after a collision with a given Q. To put the

TABLE 1. Collision Strengths $(T/R)\sigma/4\pi a_0^2$ for Two Hydrogen Atoms at Large T

Class of collision	Collision strength	Percentage
Elastic collisions	33/140 = 0.2357	10.10
Singly inelastic collisions resulting in excitation of either one of the two atoms	29/35 = 0.8286	35.51
Doubly inelastic collisions	533/420 = 1.2690	54.39
Total	7/3 = 2.333	100.00

content of those equations simply, the probability $w_0 Q^{-2} dQ$ for one hydrogen atom to stay unexcited is given by

$$w_0 = (1 - f)^2 , \tag{69}$$

where

$$f = (1 + Q/4)^{-2} . \tag{70}$$

Likewise, the probability $w_* Q^{-2} dQ$ for one hydrogen atom to become excited is given by

$$w_* = 1 - f^2 . \tag{71}$$

By subtraction of Eq. 69 from Eq. 71, one obtains

$$w_* - w_0 = 2f(1 - f) . \tag{72}$$

The right-hand side of Eq. 72 is non-negative because $0 \leq f \leq 1$ according to Eq. 70. Therefore, $w_* \leq w_0$. Moreover, the equality holds only when $f = 0$ or $f = 1$ (i.e., when $Q = 0$ or ∞).

Now, each cross section for collisions between two hydrogen atoms is, in essence, an integral of the product of w's. Because $w_* \leq w_0$ at all $Q \leq 0$, it is obvious that $w_*^2 \leq w_* w_0 \leq w_0^2$ at all $Q \leq 0$. Consequently, the doubly inelastic collisions are the most probable, the singly inelastic collisions the next, and the elastic collisions the least — the conclusion we wanted to understand.

Commentary on Collisions Between an Ion and a Neutral Atom

Let us start with a simple example, namely collisions between H and He^+ (i.e., $Z_a = 1$, $Z_b = 2$). Table 2 shows the collision strength $(T/R)\sigma/\pi a_0^2$ for different classes of possible collisions. Every class of collisions, except those leading to $H^* + He^+$, has a collision strength tending to a constant at large T. The collisions resulting in $H^* + He^+$ have a collision strength

TABLE 2. Collision strengths for collisions of H and He^+ at large T. The asterisk signifies any of the possible excited states, either discrete or ionized.

Final states of the colliding particles	Collision strength	Percentage at T/R=10
$H + He^+$ (elastic collisions)	1.045	19.09
$H + (He^+)^*$	0.2619	4.78
$H^* + He^+$	$\ln(T/R) + 1.2867$	65.57
$H^* + (He^+)^*$	0.5777	10.55
Total	$\ln(T/R) + 3.1713$	100.00

increasing with the logarithmic T dependence and, therefore, dominate at large T. The reason for the logarithmic T dependence is familiar in the Bethe theory;[1-3] it arises from the dipole interactions with long range, i.e., at small momentum transfer.

The dominance of the inelastic collisions due to any charged particle is universally true for any pair of colliding partners at high relative speed, as pointed out by Bohr.[4]

Commentary on the Dependence of Cross Sections for Collisions between Hydrogenic Ions upon Nuclear Charges Z_a and Z_b

I have generated a considerable number of numerical data for collision strengths in a variety of cases by use of Eqs. 58-68. It is not easy to sum up all of the data in a few words. In an attempt to give an idea of systematics of the data, I present Figures 1-3. All inelastic cross sections behave like Z_a^{-2} for large Z_a. Every curve in Figures 1-3 shows the behavior monotonic in both Z_a and Z_b.

Concluding Remarks

The foregoing treatment rests on the validity of the first Born approximation. It is generally believed that the first Born approximation will be valid for collisions at sufficiently high velocities, i.e., velocities far exceeding the mean orbital velocity of electrons within colliding particles. For collisions between ions (i.e., when $Z_a \neq N_a$ and $Z_b \neq N_b$) in particular, the net Coulomb force between the colliding partners may distort the trajectory appreciably

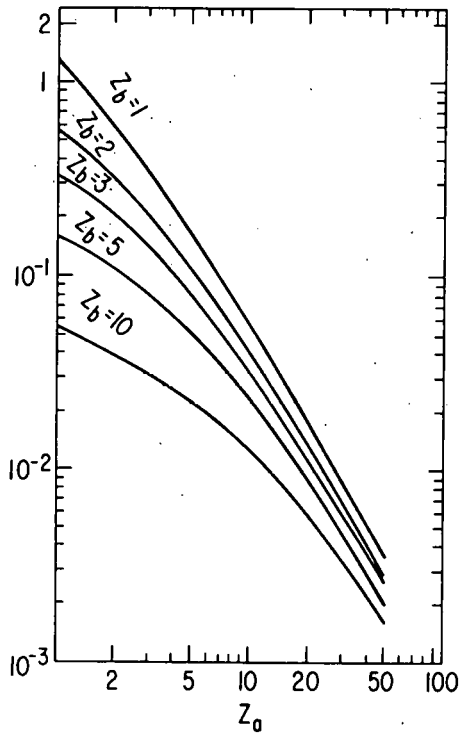

FIG. 1.--The collision strength $(T/R)\sigma_{**}/4\pi a_0^2$ for doubly inelastic collisions between hydrogenic ions with nuclear charges Z_a and Z_b. Each curve shows the collision strength for fixed Z_b (as indicated) as a function of Z_a. All curves are independent of the relative speed so long as it is sufficiently high, and approach a Z_a^{-2} behavior for large Z_a.

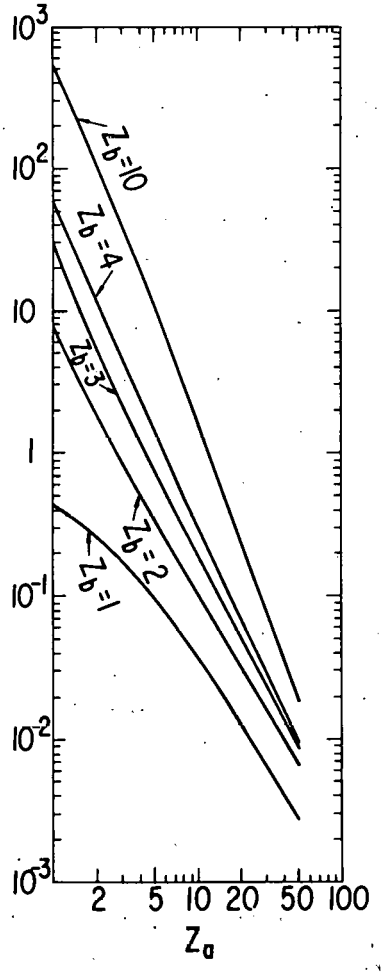

FIG. 2.--The collision strength $(T/R)\sigma_{*0}/4\pi a_0^2$ for singly elastic collisions between hydrogenic ions with nuclear charges Z_a and Z_b. Ion A becomes excited or ionized, and ion B remains unexcited after the collisions. The collision strength contains a logarithmic dependence of speed v, and the plotted values are for $v/v_0 = 10$, where $v_0 = e^2/\hbar$ is the Bohr speed. Each curve shows the collision strength for fixed Z_b (as indicated) as a function of Z_a. All curves approach a Z_a^{-2} dependence for large Z_a.

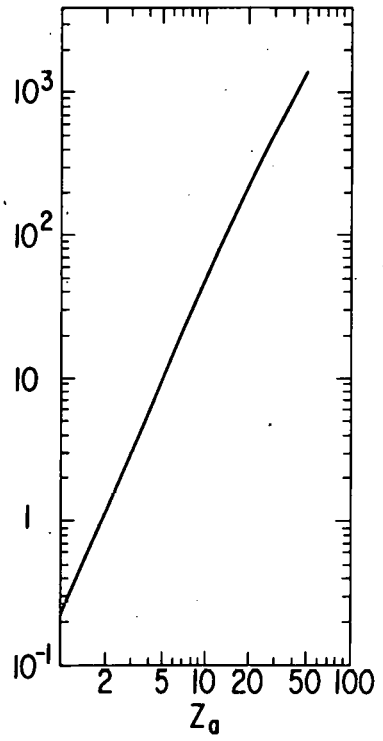

FIG. 3.--The collision strength $(T/R)\sigma_{00}/4\pi a_0^2$ for elastic collisions between a hydrogenic ion with nuclear charge Z_a with a hydrogen atom ($Z_b = 1$). The curve shows the collision strength as a function of Z_a and is independent of the relative speed so long as it is sufficiently high.

even at high velocities; then, a Coulomb-Born approximation for the relative motion will be required. Furthermore, the validity of the first Born approximation is likely to depend also upon the magnitude of momentum transfer, as that is the case for electron collision with atoms and molecules.[3] For collisions between heavy particles, the role of the momentum transfer as a criterion for the first Born approximation does not seem to have been studied in detail. In this respect, I suggest the following approach, which follows a highly successful development in electron-collision studies (cf. Sec. 3.1 of Ref. 3). Suppose one measures the differential cross section $d\sigma_{mn}/d\omega$ per unit solid-angle element $d\omega$ for the collision

$$A + B \rightarrow A_m + B_n$$

at various scattering angles and at various T. From the resulting data one evaluates

$$\Phi_{mn} = (T/R)(4\pi a_0^2)^{-1} Q^2 \, d\sigma_{mn}/dQ \, ,$$

and checks whether Φ_{mn} is a function of Q only. If the first Born approximation

holds, Φ_{mn} is not only a function of Q, but also must factorize into $|\phi_m(Q)|^2$ and $|\phi_n(Q)|^2$ according to Eq. 15. This factorization can be probed either by taking data for alternative sets of m and n of the same colliding partners A and B, or by studying alternative combinations of A and B. Actually, the determination of $d\sigma_{mn}/d\omega$ for a completely specified set of m and n takes multiple coincidence measurements which would be prohibitive in time and effort. But the suggested idea also applies to more modest experiments in which one determines the final state m of particle A only, for example. Then, one may obtain the sum $\sum_n \Phi_{mn}$, although Q no longer will be uniquely determined owing to its dependence on E_n (Eq. 5). Nevertheless, the resulting uncertainty in Q may be insignificant sometimes, for example, when B is an electronically loose system such as a negative ion.

The following remarks pertain to earlier studies relevant to the present treatment. Perhaps the earliest work on atom-atom collisions at high relative velocities was carried out by Bates and co-workers.[5,10–13] (See Chapter 23 of the treatise[14] by Massey, Burhop, and Gilbody for fuller documentation.) Attention of that series of work was focussed chiefly on cross sections for individual classes of collisions (i.e., for selected sets of m and n), in contrast to a comprehensive survey of all collision consequences and their relative probabilities — the goal of the present treatment. Later detailed studies on individual collisions of simpler particles such as H, He^+, and He, are abundantly found in the literature.[14]

The sum-rule method for collisions between atomic particles was mentioned by Bates and Griffing,[10] as well as by McDowell and Peach,[15] and was later developed by Victor[16] and by Levy.[17] Recently Gillespie[18] has applied the same method very successfully to collisions of H^- with H and He. All of the findings in these earlier studies[10–18] of the asymptotic behavior of cross sections are consistent with the general conclusion of the present treatment.

Finally, the present article has been intended to illustrate a close connection between electron collisions with atoms and molecules, on the one hand, and interatomic or intermolecular collisions, on the other hand. The basis of this connection lies in Eq. 2, which factorizes interactions between A and B

into functions of electron coordinates $\vec{r}_j$ of A and $\vec{r}_k$ of B. At least in the domain of validity of the first Born approximation, the cross sections for collisions between A and B factorized into individual properties of A and B (Eq. 3), and each of those properties may be studied by electron collisions with A or B. This point of view warrants extensive studies in the future. Indeed, this general idea has been successfully explored in several examples by Green and co-workers[19–21] and by Huo.[22]

References

1. H. Bethe, Ann. Physik 5, 325 (1930).
2. H. Bethe, Handbuch der Physik, H. Geiger and K. Scheel, Eds., Springer, Berlin, Vol. 24/1, p. 273 (1933).
3. M. Inokuti, Rev. Mod. Phys. 43, 297 (1971).
4. N. Bohr, Kgl. Danske Videnskab. Selskab, Mat-Fys. Medd. 18 (No. 8) (1948).
5. D. R. Bates and G. W. Griffing, Proc. Phys. Soc. (London) A 66, 961 (1953).
6. A. R. P. Rau and U. Fano, Phys. Rev. 162, 68 (1967).
7. M. Inokuti, Y.-K. Kim, and R. L. Platzman, Phys. Rev. 164, 55 (1967).
8. Y.-K. Kim and M. Inokuti, Phys. Rev. A 3, 665 (1971).
9. M. J. Seaton, Phil. Trans. R. Soc. A245, 469 (1953).
10. D. R. Bates and G. W. Griffing, Proc. Phys. Soc. (London) A 67, 663 (1954).
11. D. R. Bates and G. W. Griffing, Proc. Phys. Soc. (London) A 68, 90 (1955).
12. B. L. Moiseiwitsch and A. L. Stewart, Proc. Phys. Soc. (London) A 67, 1069 (1954).
13. T. J. M. Boyd, B. L. Moiseiwitsch, and A. L. Stewart, Proc. Phys. Soc. (London) A 70, 110 (1957).
14. H. S. W. Massey, E. H. S. Burhop, and H. B. Gilbody, Electronic and Ionic Impact Phenomena, 2nd Ed., Vol. IV, (Clarendon Press, Oxford (1974)).
15. M. R. C. McDowell and G. Peach, Proc. Phys. Soc. (London) 74, 463 (1959).
16. G. A. Victor, Phys. Rev. 184, 43 (1969).
17. H. Levy II, Phys. Rev. 185, 7 (1969).
18. G. H. Gillespie, Double closure calculation of the electron-loss cross sections for H^- in high-energy collision with H and He, Phys. Rev. A in press.
19. T. A. Green, Phys. Rev. 157, 103 (1967).
20. J. M. Peek, T. A. Green, and W. H. Weihofen, Phys. Rev. 160, 117 (1969).
21. T. A. Green and J. M. Peek, Phys. Rev. 169, 37 (1968).
22. W. M. Huo, Resonant energy transfer cross sections formulated in terms of form factors; an appraisal of the first Born approximation, J. Chem. Phys. in press.

CHEMI-IONIZATION REACTIONS IN ACCELERATED URANIUM-O_2 CROSSED MOLECULAR BEAMS *

C. E. Young, † P. M. Dehmer, R. B. Cohen, ‡ L. G. Pobo, † and S. Wexler †

Chemi-ionization and electron transfer reactions in accelerated uranium-atom-oxygen-molecule collisions have been studied by cross molecular beam techniques:

$U + O_2 \rightarrow UO_2^+ + e$, associative ionization (1);

$U + O_2 \rightarrow UO^+ + (O + e)$, rearrangement (reactive) ionization (2);

$U + O_2 \rightarrow U^+ + (O_2 + e)$, electron transfer (3).

Cross sections for the three ionization channels were measured as a function of relative collision energy from 0.2 to 60 eV. The thresholds observed for channels (2) and (3), which are closed at thermal energies, are in good agreement with values calculated from thermochemical data. The cross section for associative ionization varied inversely with v_r, the relative collision velocity, as predicted for weak autoionizing transitions. With the use of a rough absolute calibration and a $1/v_r$ extrapolation to lower energies, the UO_2^+ cross section was found to be in agreement with the previously reported value measured with thermal beams. In the case of rearrangement ionization, the cross section rose rapidly at threshold, peaked near the threshold for the electron transfer process, and then declined with increasing collision energy. The electron transfer cross section increased with a power-law dependence of the excess energy above threshold throughout the range investigated. The maximum absolute cross section measured was 1.4×10^{-17} cm^2. The dynamics of ionization processes (2) and (3) were elucidated from the energy dependence

---

*A full report is given in J. Chem. Phys. 64, 306 (1976).

†Chemistry Division. A major part of the work was done in the Chemistry Division.

‡Visiting Scientist from the Chemistry Department, Illinois Institute of Technology, Chicago, Illinois 60616. Present address: The Aerospace Corporation, El Segundo, California 90009.

of the cross sections and from measurements of the angular and kinetic energy distributions of the product ions. The results support the conclusion that rearrangement ionization proceeds by a "spectator-stripping" mechanism. Both the UO^+ from this reaction and the U^+ from electron transfer are scattered predominantly in the forward direction.

SURVEY OF CHEMI-IONIZATION REACTIONS IN ACCELERATED ATOM-O_2 CROSSED MOLECULAR BEAMS *

C. E. Young,† R. B. Cohen,‡ P. M. Dehmer, L. G. Pobo,† and S. Wexler†

The chemi-ionization reactions, associative ionization, and rearrangement (reactive) ionization, and the electron transfer reaction have been investigated in the crossed-molecular beam collisions of more than 20 accelerated (by sputtering) metal and nonmetal atoms with O_2 molecules. The observations support a generalization on the scope of these chemi-ionization reactions and their relation to electronic structure, namely that associative and rearrangement ionization reactions do not occur for collision partners for which the thermodynamic threshold energy for electron transfer is lower than the thresholds for the chemi-ionization. On the other hand, rearrangement and associative ionization may be prominent reaction channels when their thermodynamic thresholds are less than that for electron transfer.

---

*A full report is given in J. Chem. Phys. 65, 2562 (1976).

†Chemistry Division. A major part of the work was done in the Chemistry Division.

‡Visiting Scientist from the Chemistry Department, Illinois Institute of Technology, Chicago, Illinois 60616. Present address: The Aerospace Corporation, El Segundo, California 90009.

EXACT NUMERICAL SOLUTION OF THE SCHROEDINGER EQUATION WITH THE LENNARD-JONES POTENTIAL

S. Tani*† and Y. M. Jan*

The series solution of a differential equation in an immediate neighborhood of an irregular singularity has a finite convergence radius. For the Lennard-Jones potential, devised as a model for Li^+-He scattering, the convergence radius is so small that the repulsive potential is still extremely strong at a point near the convergence limit. Consequently, any standard numerical method cannot start from such a point. In the domain intermediate between the convergence limit of the series and the starting point of a standard numerical integration, the solution involves a part that varies rapidly. A special numerical method has been developed to deal with the solution in this domain.

Tani and Inokuti[1] examined the low-energy Li^+-He scattering, using the Sutherland potential. It is believed that the results obtained there are good qualitative representations of the general features of the system, in spite of the fact that the Sutherland potential has a sharp spike right outside its hard core. The spike is narrow but unrealistic in shape. In order to check this point, we have recently investigated the same problem using the more realistic Lennard-Jones (8.4) potential. In the course of this investigation, we developed a method of precision integration for the Schroedinger equation with a singular potential, and encountered a problem that does not appear to have been fully discussed before.

Using the same notations as employed in Ref. 1, the partial-wave Schroedinger equation may be written as

$$\psi'' + [k^2 - \zeta^2 \xi^4 \rho^{-8} + \zeta^2 \rho^{-4} - \ell(\ell+1)\rho^{-2}]\psi = 0. \qquad (1)$$

The strength of the short-range repulsive singular potential is determined by an additional parameter ξ, whose numerical value is

$$\xi = 1.035958\ . \qquad (2)$$

*Physics Department, Marquette University, Milwaukee, Wisconsin 53233.

†Consultant, Radiological and Environmental Research Division, Argonne National Laboratory.

This value is so chosen as to satisfy the condition that the system at zero energy and zero angular momentum is precisely at the midpoint between the seventh and eighth zero-energy bound states. The value of the parameter ζ is

$$\zeta = 27.000 \ , \tag{3}$$

as it is in Ref. 1.

Since the singularity at $r=0$ is irregular, we have to develop the Laurent series for the wavefunction ψ of Eq. 1. The standard method of dealing with the Laurent series is to set the wavefunction in the exponential form

$$\psi = \exp \sigma \ , \tag{4}$$

and solve the Riccati equation[2]

$$\sigma'' + \sigma'^2 + k^2 - \zeta^2 \xi^4 \rho^{-8} + \zeta^2 \rho^{-4} - \ell(\ell+1)\rho^{-2} \equiv 0 \ . \tag{5}$$

Quantum mechanics of a system with a singular potential was discussed by Case[3] in his classical paper, and some other aspects, for example the non-analytic property in potential strength, were further studied by Tiktopoulos and Treiman[4] and others. Mathematical study of a differential equation in an immediate neighborhood of an irregular singularity is presented in Ince's book.[2]

The series solution of σ' may be assumed to take the form

$$\sigma' = \zeta \xi^2 \rho^{-4} + 2\rho^{-1} + \sum_{n=0}^{\infty} a_n \rho^n \ . \tag{6}$$

The four coefficients a_n $(n=0, 1, 2, 3)$ are

$$\begin{aligned} a_0 &= -\zeta (2\xi^2)^{-1} \ , \\ a_1 &= 0 \ , \\ a_2 &= [\ell(\ell+1) - 2] (2\zeta\xi^2)^{-1} \\ a_3 &= \xi^{-4} \ . \end{aligned} \tag{7}$$

The general term for n which is larger than three satisfies the equation

$$a_{n+3} = -(2\zeta\xi^2)^{-1} [(n+4) a_n + \sum_{j=1}^{n} a_{n-j} a_{j-1}], \quad (n=1,2,3,\ldots); \tag{8}$$

it may be determined through an arbitrary n with a straightforward calculation

with a computer by substituting previously-determined coefficients on the right-hand side.

The computer result shows that, for n larger than 50 or so, the a_n alternates in sign and its magnitude starts to increase steadily. That the magnitude of a_n does not increase until n becomes at least as large as 50 is a consequence of a large parameter $(2\zeta\xi^2) \sim 54$ in the denominator of Eq. 8. For most parameters of the Schroedinger equation1, the ratio of two adjacent terms is of the order of -1.6 for n around 100:

$$a_{n+1}/a_n \sim -1.6, \qquad n \sim 100 . \tag{9}$$

On that score, we guess that the convergence radius ρ_0 of series 6 is of the order of 0.6, i.e.,

$$\rho_0 \sim 0.6 . \tag{10}$$

Assume that the asymptotic form of a_n for very large n takes the form

$$a_n = (-1)^n \lambda^n C(n) + \Delta_n , \tag{11}$$

where λ is a constant and Δ_n is a small fluctuating term that tends to zero as n tends to infinity,

$$\lim_{n \to \infty} \Delta_n = 0 , \tag{12}$$

and the quantity C(n) is slowly varying but tends to unity as n tends to infinity:

$$\lim_{n \to \infty} C(n) = 1 . \tag{13}$$

Then it may be shown that Eq. 11 is consistent with Eq. 8. However, we will have to undertake further work before we can derive a formula of the type of Eq. 11 forcefully as a consequence of Eq. 8.

The wavefunction ψ of Eq. 4 starts to oscillate in the outer region where the attractive potential dominates and will have a node at some finite distance from the origin. At a node of the real function ψ, the logarithm σ' must diverge. This proves that the series for σ' cannot represent an entire function, but its convergence radius must be finite.

Suppose we choose a point $\rho = \rho_a$ within the convergence radius of the

series for σ',

$$\rho_a < \rho_0 \ , \tag{14}$$

and determine the value of σ' at that point by using Eq. 6:

$$\sigma'(\rho_a) = \chi_a \ . \tag{15}$$

Clearly the repulsive potential is still very strong at that point so that a standard method of numerical integration, such as the Runge-Kutta method, is not applicable. Therefore, we must develop a special numerical method that deals with the solution in the intervening region.

In the intervening region, we assume that the function σ' is of the form

$$\sigma' = \zeta\xi^2\rho^{-4} = 2\rho^{-1} - \zeta(2\xi^2)^{-1} + \Phi(\rho) \ , \tag{16}$$

where the value of the function Φ at $\rho = \rho_a$ is determined by the series solution

$$\Phi(\rho_a) = \omega_a = \chi_a - [\zeta\xi^2\rho_a^{-4} + 2\rho_a^{-1} - \zeta(2\xi^2)^{-1}] \ . \tag{17}$$

The function Φ is a rapidly growing function. The value of ω_a is small when ρ_a is sufficiently small, but its value at the starting point of the standard numerical method is substantial. The differential equation satisfied by Φ is

$$\begin{aligned} &\Phi' + 2[\zeta\xi^2\rho^{-4} + 2\rho^{-1} - \zeta(2\xi^2)^{-1}]\Phi + \Phi^2 \\ &\quad + [2 - \ell(\ell+1)]\rho^{-2} - (2\zeta)\xi^{-2}\rho^{-1} \\ &\quad + [k^2 + \zeta^2(4\xi^4)^{-1}] = 0 \ . \end{aligned} \tag{18}$$

As compared with the original Riccati equation (Eq. 5), the singular term of the highest order $\zeta^2\xi^4\rho^{-8}$ has been eliminated from Eq. 18, but there is still a singular term $\zeta\xi^2\rho^{-4}$, akin to the original irregular singularity, left. To eliminate any term which is more strongly singular than ρ^{-2}, we factor an exponential function out of Φ

$$\Phi = \exp[2A] \cdot \Omega \ , \tag{19}$$

with the exponent A

$$A = \zeta\xi^2 (3\rho^3)^{-1} - 2 \ln\rho + \zeta (2\xi^2)^{-1} \rho \ . \tag{20}$$

The function A satisfies the equation

$$A' = - [\zeta\xi^2\rho^{-4} + 2\rho^{-1} - \zeta (2\xi^2)^{-1}] \ . \tag{21}$$

The differential equation to be satisfied by Ω is

$$\Omega' + \exp(2A)\,\Omega^2$$
$$+ \exp(-2A)\{ [2 - \ell(\ell+1)]\,\rho^{-2} - (2\zeta)\,\xi^{-2}\rho^{-1} + [k^2 + \zeta^2(4\xi^4)^{-1}] \} = 0. \tag{22}$$

In Eq. 22 any term which is more strongly singular than ρ^{-2} has been eliminated. The only problem that remains with Eq. 22 is that the exponential factor, $\exp(2A)$, varies over a wide range as ρ varies from the starting value, ρ_a, through the end of the intervening region. To tackle this problem, we integrate the differential Eq. 22 step by step over a relatively small range of ρ in which the relative change of the exponential factor $\exp(2A)$ remains within a certain bound.

Suppose the value of Φ of Eq. 16 is known at $\rho = \rho_i$,

$$\Phi(\rho_i) = \omega_i \ . \tag{23}$$

Then we try to integrate Eq. 22, by way of its modified version, in the interval

$$\rho_i \le \rho \le \rho_i + \gamma_i = \rho_{i+1} \ . \tag{24}$$

Let us assume that Φ takes the form

$$\Phi(\rho) = \exp[2B_i]\,\Omega_i(\rho) \ , \tag{25}$$

where

$$B_i(\rho) = A(\rho) - A(\rho_i) \ . \tag{26}$$

The differential equation to be satisfied by Ω_i is closely similar to Eq. 22, but the exponential function will be replaced by $\exp[2B_i]$;

$$\Omega_i' + \exp(2B_i)\,\Omega_i^2$$
$$+ \exp(-2B_i)\{ [2 - \ell(\ell+1)]\,\rho^{-2} - (2\zeta)\xi^{-2}\rho^{-1} + [k^2 + \zeta^2(4\xi^4)^{-1}] \} = 0. \tag{27}$$

Since we have

$$B_i(\rho_i) = 0 \ , \tag{28}$$

the initial value of Ω_i is

$$\Omega_i(\rho_i) = \omega_i \ . \tag{29}$$

Since there is no term whose behavior is problematic in Eq. 27, it may be integrated numerically using the Runge-Kutta method in the interval defined by Eq. 24. We monitor the value of B_i as the deviation of ρ from ρ_i grows. If the condition

$$|B_i(\rho_i + \gamma_i)| > \Gamma \tag{30}$$

is satisfied for the first time at $\rho = \rho_i + \gamma_i$ while repeating the Runge-Kutta cycles, then we evaluate the value of Φ at $\rho = \rho_i$ from

$$\Phi(\rho_{i+1}) = \omega_{i+1} = \exp[2B_i(\rho_{i+1})]\ \Omega_i(\rho_{i+1}) \ . \tag{25a}$$

The ω_{i+1} thus determined will be used as the initial value for the next interval

$$\rho_{i+1} \leq \rho \leq \rho_{i+1} + \gamma_{i+1} = \rho_{i+2} \ . \tag{24a}$$

The parameter Γ in the inequality (30) may be chosen as 4.60, say; then the variation of the exponential factor in Eq. 27 will be limited by

$$\exp(-9.20) = 10^{-4} < |\exp(\pm 2B_i)| < \exp(9.20) = 10^{4} \ . \tag{31}$$

The standard numerical integration of the original Schroedinger equation (1) may start from $\rho = \rho_b$, say. The logarithmic derivative of the wavefunction at $\rho = \rho_b$

$$\psi'(\rho_b)/\psi(\rho_b) = \sigma'(\rho_b) \tag{32}$$

may be determined by the method shown above with a high precision.

References

1. S. Tani and M. Inokuti, J. Chem. Phys. 61, 4422 (1974).
2. E. L. Ince, Ordinary Differential Equations, Ch. XVII, Dover Publ. New York, N.Y. (1944).
3. K. M. Case, Phys. Rev. 80, 797 (1950).
4. G. Tiktopoulos and S. B. Treiman, Phys. Rev. 134, B844 (1964).

PUBLICATIONS BY THE STAFF OF THE FUNDAMENTAL MOLECULAR PHYSICS AND CHEMISTRY SECTION FOR THE PERIOD JULY 1975—SEPTEMBER 1976.

MAJOR PAPERS

K. D. Chao, J. L. Dehmer, U. Fano, M. Inokuti, S. T. Manson, A. Msezane, R. F. Reilman, and C. E. Theodosiou, Spectral and Electron Collision Properties of Atomic Ions, Beam-Foil Spectroscopy, Vol. 2, Ivan A. Sellin and David J. Pegg, Eds., pp. 637—641 (1976).

W. A. Chupka, P. M. Dehmer, and W. T. Jivery, High Resolution Photoionization Study of Ion-Pair Formation in H_2, HD, and D_2, J. Chem. Phys. 63, 3929—3944 (November 1975).

J. L. Dehmer and D. Dill, Shape Resonances in K-Shell Photoionization of Diatomic Molecules, Phys. Rev. Lett. 35 (4), 213—215 (July 1075).

J. L. Dehmer, W. A. Chupka, J. Berkowitz, and W. T. Jivery, Wavelength Dependence of the Photoelectron Angular Distributions of the Rare Gases, Phys. Rev. A 12 (5), 1966—1973 (November 1975).

J. L. Dehmer, Mitio Inokuti, and R. P. Saxon, Systematics of Moments of Dipole Oscillator-Strength Distributions for Atoms of the First and Second Row, Phys. Rev. A 12, 102—121 (July 1975).

J. L. Dehmer and Dan Dill, Molecular Effects in Inner-Shell Photoabsorption, Shape Resonances and EXAFS, Proc. 2nd Int. Conf. on Inner-Shell Ionization Phenomena, March 29—April 2, 1976, Freiburg, West Germany, Fakultät für Physik, Universität Freiburg, Germany, pp. 221—238 (1976).

P. M. Dehmer and W. A. Chupka, Very High Resolution Study of Photoabsorption, Photoionization, and Predissociation in H_2, J. Chem. Phys. 65, 2243—2273 (September 1976).

U. Fano and M. Inokuti, On the Theory of Ionization by Electron Collisions, Argonne National Laboratory Topical Report, ANL-76-80 (June 1976).

U. Fano, C. E. Theodosiou, and J. L. Dehmer, Electron-Optical Properties of Atomic Fields, Rev. Mod. Phys. 48, 49—68 (January 1976).

R. H. Huebner, R. J. Celotta, S. R. Mielczarek, and C. E. Kuyatt, Apparent Oscillator Strengths for Molecular Oxygen Derived from Electron Energy-Loss Measurements, J. Chem. Phys. 63, 241—248 (July 1976).

R. H. Huebner, D. L. Bushnell, Jr., R. J. Celotta, S. R. Mielczarek, and C. E. Kuyatt, Ultraviolet Photoabsorption of Halocarbons 11 and 12 from Electron-Impact Measurements, Nature 257, 376—378 (October 1975).

R. H. Huebner, R. J. Celotta, S. R. Mielczarek, and C. E. Kuyatt, Energy Absorption by N_2O in the 4- to 14-eV Region, J. Chem. Phys. 63, 4490–4494 (November 1975).

M. Inokuti, Ionization Yields in Gases under Electron Radiation, Radiat. Res. 64, 6–22 (October 1975).

M. Inokuti, Introduction to the Symposium on the Basic Physics of the Interactions of Radiation with Matter, Radiation Research, Biomedical, Chemical, and Physical Perspectives, Proc. Vth Int. Cong. of Radiation Research, Seattle, July 1974, O. F. Nygaard, H. I. Adler, and W. K. Sinclair, Eds., Academic Press, New York, pp. 184–187 (1975).

M. Inokuti, Theoretical Aspects of Electron Correlations in Electron Collisions, Proc. NATO Advanced Study Institute on Photoionization and Other Probes of Many-Electron Interactions, 31 August–13 September 1975, Carry-le-Rouet, France, Plenum Press, New York, pp. 165–186 (1976).

M. Inokuti, Concluding Remarks, Proc. NATO Advanced Study Institute on Photoionization and Other Probes of Many-Electron Interactions, 31 August–13 September 1975, Carry-le-Rouet, France, Plenum Press, New York, pp. 431–440 (1976).

M. Inokuti, D. A. Douthat, A. R. P. Rau, Degradation Spectra and Ionization Yields of Electrons in Gases, Proc. Vth Symp. on Microdosimetry, Verbania-Pallanza, Italy, 22–25 September 1975, Commission of the European Committes, Luxembourg, EUR-5452-d-e-f, Vol. II, pp. 977–1006 (May 1976).

M. Inokuti, Vistas to the Future of Radiation Chemistry and Physics (in Japanese), Hoshasen Kagkau (Radiation Chemistry) 11 (22), 16–18, 24 (Sept. 1976).

Yong-Ki Kim, Energy Distribution of Secondary Electrons, Radiat. Res. 64, 96–105 (October 1975).

Yong-Ki Kim, Energy Distribution of Secondary Electrons. II. Normalization and Extrapolation of Experimental Data, Radiat. Res. 64, 205–216 (November 1975).

Yong-Ki Kim, Secondary Electron Spectra, Radiation Research, Biomedical, Chemical, and Physical Perspectives, Proc. Vth Int. Cong. of Radiation Research, Seattle, July 1974, O. F. Nygaard, H. I. Adler, and W. K. Sinclair, Eds., Academic Press, New York, pp. 219–226 (1975).

Yong-Ki Kim and J.-P. Desclaux, Relativistic f Values for the Resonance Transitions of Li- and Be-Like Ions, Phys. Rev. Lett 36 (3), 139–141 (January 1976).

Yong-Ki Kim, Basic Aspects of Secondary-Electron Distributions, Invited Papers, Proc. IXth Int. Conf. on the Physics of Electronic and Atomic Collisions, Seattle, 24–30 July 1975, John S. Risley and R. Geballe, Eds., U. Washington Press, Seattle, pp. 741–755 (1975).

M. Matsuzawa and M. Inokuti, Total Cross Section for Elastic Scattering of Fast Charged Particles by a Neutral Atom, Proc. Int. Symp. on Electron and Photon Interactions with Atoms, in Honor of Ugo Fano, July 16–19, 1974, Stirling, Scotland, Plenum Publishing Corp., New York, pp. 595–600 (1976).

J. C. Person, R. L. Watkins, and D. L. Howard, Collisional Ionization of Highly Excited Rydberg States of Polyatomic Molecules, J. Phys. B: Atom. Molec. Phys. 9 (10), 1811–1822 (July 1976).

J. Siegel, D. Dill, and J. L. Dehmer, Continuum and Bound Molecular Electronic Wavefunctions for Generalized Multiple-Scattering Potentials, J. Chem. Phys. 64 (8), 3204–3206 (April 1976).

S. C. Soong and Yong-Ki Kim, Inelastic-Collision Cross Sections for Ne, Argonne National Laboratory Topical Report, ANL-76-66 (1976).

David Spence, Classification of Feshbach Resonances in Electron-Molecule Scattering, Invited Papers, Proc. IXth Int. Conf. on the Physics of Electronic and Atomic Collisions, Seattle, 24–30 July 1975, John S. Risley and R. Geballe, Eds., U. Washington Press, Seattle, pp. 241–255.

David Spence, Additional Resonances in Electron Scattering by Atomic Oxygen, Phys. Rev. A 12 (2), 721–724 (August 1975).

David Spence, Cross Sections and Threshold Effects for Electron-Impact Excitation of the $(2s^2)^1S$ and $(2s2p)^3P$ States of Helium, Phys. Rev. A 12 (6), 2353–2360 (December 1975).

David Spence, Long-Range Electron-Correlation Effects in Electron-Impact Excitation of Autoionizing States, Comments in Atom. Mol. Phys. 5 (6), 159–172 (1976).

H. C. Tuckwell and Yong-Ki Kim, Effects of Partial Cross Sections on the Energy Distribution of Slow Secondary Electrons, J. Chem. Phys. 64 (1), 333–336 (January 1976).

C. E. Young, P. M. Dehmer, R. B. Cohen, L. G. Pobo, and S. Wexler, Chemi-Ionization Reactions in Accelerated Uranium-O_2 Crossed Molecular Beams, J. Chem. Phys. 64, 306–319 (January 1976).

CONFERENCE PAPERS AND ABSTRACTS

Hans Bichsel and Mitio Inokuti, Calculation of the Energy to Form an Ion Pair for Protons, Abstracts of Papers, 24th Annual Meeting of the Radiation Research Society, San Francisco, California, 27 June–2 July 1976, Radiat. Res. 67 (3), 613 (September 1976).

J. L. Dehmer and Dan Dill, Shape Resonance Effects in X-Ray Absorption Spectra of Molecules, Program and Extended Abstracts, Int. Conf. on the Physics of X-Ray Spectra, August 30–September 2, 1976, NBS, Gaithersburg, Maryland, p. 75 (1976).

S. Wexler, C. E. Young, P. M. Dehmer, and R. B. Cohen, Chemi-Ionization Reactions in Accelerated Crossed Molecular Beams, 2nd IUPAC Plasma Chemistry Symp., Rome, 18–23 September 1975.

Presented at the VII Meeting of the Division of Electron and Atomic Physics, Tucson, Arizona, 3–5 December 1975 and published in Bull. Am. Phys. Soc. 20 (1975).

D. L. Bushnell, Jr., R. H. Huebner, R. J. Celotta, and S. R. Mielczarek, Electron Energy-Loss Analysis of the Chlorofluoromethanes, p. 1455.

W. A. Chupka and P. M. Dehmer, Formation and Reaction of Metastable H and D Atoms in H_2, HD, and D_2, p. 1454.

J. L. Dehmer and Dan Dill, Molecular Effects in the K-Shell Photoionization of N_2, p. 1461.

P. M. Dehmer, W. A. Chupka, and W. Luken, High-Resolution Photoionization Study of Autoionizing States of Atomic Oxygen, p. 1460.

P. M. Dehmer and W. A. Chupka, Decay of Rydberg States of H_2, p. 1457.

Presented at IXth Int. Conf. on the Physics of Electronic and Atomic Collisions, Seattle, Washington, 24–30 July 1975, and published in the Proceedings, John S. Risley and R. Geballe, Eds., U. Washington Press, Seattle, 1975.

W. A. Chupka, P. M. Dehmer, and W. T. Jivery, High-Resolution Study of Photoionization Processes in H_2, HD, and D_2, p. 1130.

J. L. Dehmer, W. A. Chupka, and J. Berkowitz, Wavelength Dependence of Photo-electron Angular Distributions: Kr, Xe, and N_2, p. 565.

R. H. Huebner, R. J. Celotta, S. R. Mielczarek, and C. E. Kuyatt, Apparent Oscillator Strengths for Nitrous Oxide, p. 1043.

M. Inokuti, Remarks on the Significance of Electron Correlations in Two Oscillator-Strength Sum Rules, p. 1035.

Yong-Ki Kim and J.-P. Desclaux, Relativistic Effects in the Resonance Transitions of Li-Like Ions, p. 1047.

S. T. Manson, J. L. Dehmer, U. Fano, M. Inokuti, and C. E. Theodosiou, Dependence of Electron-Scattering Phase Shifts and of Photoabsorption Cross Sections in Both Atomic Number and Ionic Charge for Atomic Ions, p. 693.

J. C. Person, R. L. Watkins, and D. L. Howard, Collisional Ionization of Highly-Excited Polyatomic Molecules, p. 723.

David Spence, Threshold Effects in Electron-Impact Excitation of the $(2s^2)^1S$ and $(2s2p)^3P$ Autoionizing States of Helium, p. 195.

David Spence, New Resonances in the Scattering of Electrons by Atomic Oxygen, p. 633.

S. Tani, A. C. Chen, and M. Inokuti, Numerical Tests of the Weinberg Separable-Potential, the Orthogonality-Constraint, and Other Related Methods, p. 81.

DISTRIBUTION

Internal Distribution

ANL Contract Copy
TIS copies (5)
Library (4)
A. B. Krisciunas (15)
President AUA
E. N. Pettitt
R. G. Sachs
M. V. Nevitt
R. V. Laney
S. A. Miller
M. Fieldhouse
W. K. Sinclair
R. J. Royston
D. C. Price
P. R. Fields
P. M. Failla
P. F. Gustafson
S. Wexler
M. S. Matheson
S. Gordon
J. Berkowitz
T. Gilbert
M. C. Sauer
A. C. Wahl
G. T. Garvey
F. Clark
J. Dehmer
P. M. Dehmer
P. Frenzen
P. Groer
R. H. Huebner
Y.-K. Kim
P. Nicole
R. C. Person
R. E. Rowland
F. E. Throw
R. Schlenker
D. Spence
A. F. Stehney
O. J. Steingraber
C. Yack
Y. Band
G. Berry
J. Eland
M. Peshkin
RER Division (100)

External Distribution

ERDA-TIC for distribution per UC-48 (198)
Chicago Patent Group
Manager, ERDA-CH
Radiological and Environmental Research Division Review Committee:
F. I. Badgley, University of Washington, Seattle, Washington
R. S. Berry, University of Chicago, Chicago, Illinois
E. D. Goldberg, Scripps Institution of Oceanography, La Jolla, California
G. H. Lauff, W. K. Kellogg Biological Station, Hickory Corners, Michigan
W. F. Neuman, University of Rochester, Rochester, New York
E. L. Saenger, Cincinnati General Hospital, Cincinnati, Ohio
F. T. Smith, Stanford Research Institute, Menlo Park, California
W. H. Smith, Yale University, New Haven, Connecticut
AUA Biology Representatives:
S. Abrahamson, University of Wisconsin, Madison, Wisconsin
W. C. Ashby, Southern Illinois University, Carbondale, Illinois
R. S. Caldecott, University of Minnesota, St. Paul, Minnesota
W. Chavin, Wayne State University, Detroit, Michigan
J. Courtright, Marquette University, Milwaukee, Wisconsin
W. F. Danforth, Illinois Institute of Technology, Chicago, Illinois
H. S. Ducoff, University of Illinois, Urbana, Illinois
A. Eisenstark, University of Missouri, Columbia, Missouri
D. Feir, St. Louis University, St. Louis, Missouri
D. L. Hartl, Purdue University, Lafayette, Indiana
B. H. Judd, University of Texas at Austin, Austin, Texas
A. L. Koch, Indiana University, Bloomington, Indiana
J. C. Loper, University of Cincinnati, Cincinnati, Ohio
W. R. Martin, University of Chicago, Chicago, Illinois
H. J. McDonald, Loyola University Medical Center, Maywood, Illinois
R. P. McIntosh, University of Notre Dame, Notre Dame, Indiana
W. C. Myser, Ohio State University, Columbus, Ohio
R. R. Novales, Northwestern University, Evanston, Illinois
J. W. Osborne, University of Iowa, Iowa City, Iowa
R. J. Perkins, University of Kansas, Lawrence, Kansas
R. J. Robel, Kansas State University, Manhattan, Kansas
R. C. Rustad, Case Western Reserve University, Cleveland, Ohio
S. Silver, Washington University, St. Louis, Missouri
E. A. Stull, University of Arizona, Tucson, Arizona
A. S. Sussman, University of Michigan, Ann Arbor, Michigan
P. W. Todd, Pennsylvania State University, University Park, Pennsylvania
M. J. Ulmer, Iowa State University, Ames, Iowa
I. Ungar, Ohio University, Athens, Ohio
J. J. Wolken, Mellon Institute, Pittsburgh, Pennsylvania
L. Wolterink, Michigan State University, East Lansing, Michigan

Adams, William, U.S. ERDA, Washington, D.C.
Argersinger, W. J., Jr., Univ. of Kansas
Arkansas, Univ. of, Medical Center Library, Little Rock
Ausloos, P., National Bureau of Standards, Washington, D.C.
Auxier, J. A., Oak Ridge National Laboratory, Oak Ridge, Tennessee
Barr, N. F., U.S. ERDA, Washington, D.C.
Beaty, E. C., JILA, Univ. of Colorado, Boulder
Becker, Klaus, Oak Ridge National Laboratory, Oak Ridge, Tennessee
Bederson, Benjamin, New York U., New York, New York
Berger, Martin, National Bureau of Standards, Washington, D.C.
Bhalla, Chander C., Kansas State Univ., Manhattan, Kansas
Bichsel, Hans, Univ. of Washington, Seattle, Washington
Birkhoff, Robert D., Oak Ridge National Laboratory, Oak Ridge, Tennessee
Blahd, Wm. H., Vet. Admin. Ctr., Los Angeles, California
Blaunstein, R. P., U.S. ERDA, Washington, D.C.
Boness, M. J. W., Avco Everett Research Corp., Everett, Massachusetts
Bonham, Russell A., Indiana University, Bloomington, Indiana
Boring, J. W., Univ. of Virginia, Charlottesville, Virginia
Brandt, Werner, New York University, New York, New York
Brill, A. B., Vanderbilt University, Nashville, Tennessee
Bruckner, Benjamin H., Nat. Ctr. for Radiol. Health, U.S. HEW, Rockville, Maryland
Bull, Stanley R., University of Missouri, Columbia, Missouri
Burnstein, R. A., Illinois Institute of Technology, Chicago, Illinois
Burr, W. W., Jr., U.S. ERDA, Washington, D.C.
Burrow, P. D., University of Nebraska, Lincoln, Nebraska
Bustad, Leo K., Washington State University, Pullman, Washington
Carlson, T. A., Oak Ridge National Laboratory, Oak Ridge, Tennessee
Castleman, A. W., Jr., University of Colorado, Boulder, Colorado
Caswell, R. S., National Bureau of Standards, Washington, D.C.
Celotta, R. J., National Bureau of Standards, Washington, D.C.
Chen, Joseph, C. Y., University of California, San Diego
Christian, John E., Purdue University, Lafayette, Indiana
Christophorou, L. G., Oak Ridge National Laboratory, Oak Ridge, Tennessee
Chupka, W. A., Yale University, New Haven, Connecticut
Cochran, R. G., Texas A&M, College Station, Texas
Cohn, Stanton H., Brookhaven National Lab., Upton, Long Island, New York
Cole, Alan L., Bowman Gray School of Medicine, Winston-Salem, N.C.
Colorado University, Joint Inst. for Laboratory Astrophysics (JILA), Boulder
Compton, Robert N., Oak Ridge National Laboratory, Oak Ridge, Tennessee
Congel, Frank J., Macalester College, St. Paul, Minnesota
Cooper, J. W., National Bureau of Standards, Washington, D.C.
Cornell University Library, Geneva, New York
Cummings, John A., Wisconsin State University,
Dalgarno, A., Harvard College Observatory and Smithsonian Astrophysical Observ.
Dill, Dan, Boston University, Boston, Massachusetts
Dohm, George G. A., Radiation Processing, Inc., Westbury, New York.

Doniach, S., Stanford University, Stanford, California
Durso, M. P., HASL, New York, New York
Ederer, David L, National Bureau of Standards, Washington, D.C.
Edmund, Carl E., Milwaukee, Wisconsin
Evans, Robley D., Scottsdale, Arizona
Fano, Ugo, University of Chicago, Chicago, Illinois
Flannery, M. R., Georgia Institute of Technology, Atlanta, Georgia
Fredregill, C., University of Houston Libraries, Houston, Texas
Garrett, W. R., Oak Ridge National Laboratory, Oak Ridge, Tennessee
Geballe, R., University of Washington, Seattle, Washington
Geltman, Sydney, JILA, University of Colorado, Boulder, Colorado
Glass, William A., Battelle Northwest Laboratory, Richland, Washington
Goldman, Marvin, University of California, Davis, California
Green, Alex E. S., University of Florida, Gainesville, Florida
Green, Thomas A., Sandia Laboratory, Albuquerque, New Mexico
Grunewald, Ralph, University of Wisconsin, Milwaukee, Wisconsin
Haverfield, A. Judd, Battelle Northwest Laboratory, Richland, Washington
Holeman, George R., Yale University, New Haven, Connecticut
Hudson, Frank P., U.S. ERDA, Washington, D.C.
Hurst, G. Samuel, Oak Ridge National Laboratory, Oak Ridge, Tennessee
Illinois, University of, Library, Chicago, Illinois
Johnson, K. H., Massachusetts Institute of Technology, Cambridge, Mass.
Kessler, Wayne V., Purdue University, Lafayette, Indiana
Klappenbach, Edward W., U.S. EPA, Chicago, Illinois
Krause, M. O., Oak Ridge National Laboratory, Oak Ridge, Tennessee
Kupperman, Aron, California Institute of Technology, Pasadena, California
Kuyatt, C. E., National Bureau of Standards, Washington, D.C.
Lambropoulos, Peter, University of Southern California
Lassettre, E. N., Carnegie-Mellon University, Pittsburgh, Pennsylvania
Levine, S. H., Pennsylvania State University, University Park, Pennsylvania
Lineberger, W. C., University of Colorado, Boulder, Colorado
Lipsky, Sanford, University of Minnesota, Minneapolis, Minnesota
Lohr, Lawrence L., Jr., University of Michigan, Ann Arbor, Michigan
Lorents, C. D., Stanford Research Institute, Stanford, California
Lowden, Arlene, Nuclear-Chicago Corp., Chicago, Illinois
Maccabee, Howard, Lawrence Berkeley Laboratory, Berkeley, California
Macek, Joseph H., University of Nebraska, Lincoln, Nebraska
Madden, Robert P., National Bureau of Standards, Washington, D.C.
Magee, John L., University of Notre Dame, Notre Dame, Indiana
Maletskos, C. J., Bay View, Gloucester, Massachusetts
Manson, S. T., Georgia State University, Atlanta, Georgia
Martell, E. A., NCAR, Boulder, Colorado
Martinez, J. V., U.S. ERDA, Washington, D.C.
Mayo Clinic Library, Rochester, Minnesota
McGlynn, S. P., Louisiana State University, Baton Rouge, Louisiana
McKelvie, Douglas H., Colorado State University, Fort Collins, Colorado
McKoy, Vincent, California Institute of Technology, Pasadena, California
McLaughlin, James E., U.S. ERDA, New York City

Meer, Robert, Massachusetts General Hospital
Meisels, G. G, University of Nebraska, Lincoln, Nebraska
Mentall, James, NASA Goddard Space Flight Center
Michigan Technological University Library, Houghton, Michigan
Moeller, Dade W., Kresge Center for Environmental Health, Boston, Mass.
Moseley, Robert D., Jr., University of New Mexico Medical School, Albuquerque
Murphy, Glenn, Iowa State University, Ames, Iowa
Myers, William G., Ohio State University Hospital, Columbus, Ohio
Naismith, D. P., University of North Dakota, Grand Forks, North Dakota
National Center for Atmospheric Research, Boulder, Colorado
Ney, W. R., NCRP, Washington, D.C.
Nichols, G., Jr., Boston, Massachusetts
Ohanian, M. J., University of Florida, Gainesville, Florida
Orvis, Alan L., Mayo Clinic, Rochester, Minnesota
Ovadia, Jacques, Michael Reese Hospital, Chicago, Illinois
Pan, Jaming, Purdue University, Calumet Campus, Indiana
Phelps, A. V., University of Colorado, Boulder, Colorado
Pool, M. L., Ohio State University, Columbus, Ohio
Pope, Martin, New York University
Powell, Cedric, National Bureau of Standards, Washington, D.C.
Rau, A. R. P., Louisiana State University, Baton Rouge, Louisiana
Reinhardt, W. P., University of Colorado, Boulder, Colorado
Robertson, J. S., Mayo Clinic, Rochester, Minnesota
Roesch, W. C., Battelle Northwest Laboratory, Richland, Washington
Rossi, Harald H., Columbia University, New York, New York
Rudd, M. E., University of Nebraska, Lincoln, Nebraska
Rust, J. H., University of Chicago, Chicago, Illinois
Saenger, E. L., Cincinnati General Hospital, Cincinnati, Ohio
Samson, J. A. R., University of Nebraska, Lincoln, Nebraska
Saxon, Roberta P., Stanford Research Institute, Stanford, California
Schuler, R. H., University of Notre Dame, Notre Dame, Indiana
Shalmon, E., Silver Springs, Maryland
Shirley, David A., University of California, Berkeley, California
Shyn, T. W., University of Michigan, Ann Arbor, Michigan
Smathers, James B., Texas A&M, College Station, Texas
Smith, Felix T., Stanford Research Institute, Stanford, California
Spencer, Lewis V., National Bureau of Standards, Washington, D.C.
Starace, A. F., University of Nebraska, Lincoln, Nebraska
Stone, Philip M., U.S. ERDA, Washington, D.C.
Tani, Smio, Marquette University, Milwaukee, Wisconsin
Taylor, Howard S., University of Southern California
Taylor, L. S., NBS, Bethesda, Maryland
Thiess, P. E., Catholic University of America, Washington, D.C.
Thomas, J. K., University of Notre Dame, Notre Dame, Indiana
Thomas, James, Kings County Hospital Center, New York
Tobias, C. A., Donner Laboratory, University of California, Berkeley, Cal.
Toburen, L. H., Battelle Northwest Laboratory, Richland, Washington
Trajmer, S., Jet Propulsion Laboratory, Pasadena, California

Truppa, Michael, Waldie & Briggs, Chicago, Illinois
Upton, A. C., SUNY at Stony Brook, New York
Varney, Dan, Eastern Kentucky University, Richmond, Kentucky
Vroom, D. A., Gulf Energy & Environmental Systems, San Diego, California
Williams, R. H., University of Michigan, Ann Arbor, Michigan
Wilson, W. E., Battelle Northwest Laboratory, Richland, Washington
Witzig, W. F., Pennsylvania State University, University Park, Pennsylvania
Wood, R. E., U.S. ERDA, Washington, D.C.
Wylie, K. F., University of Missippi, University, Mississippi
Zare, R. N., Stanford University, Stanford, California
Comision Nacional de Energia Atomica, Library, Argentina
Cancer Institute Library, Melbourne, Australia
Dudley, R. A., IAEA, Vienna, Austria
Debois, J. M., St. Norbertus Hospital, Duffel, Belgium
Heyndrickx, A., University of Ghent, Belgium
Barker, G. O., National Research Council, Ottawa, Canada
Booth, A. H., National Health & Welfare, Ottawa, Canada
Brearley, N., University of British Columbia, Vancouver, Canada
Brion, C. E., University of British Columbia, Vancouver, Canada
Canadian Forces Base, Halifax, Canada
Carette, J. D., Universite Laval, Quebec, Canada
Cowper, G., Atomic Energy of Canada Ltd., Chalk River, Canada
McGowan, J. W., University of Western Ontario, London, Ontario, Canada
Ross, D. A., DSIS, Ottawa, Canada
Toronto, University of, Library, Canada
Cheng, C. H., Tsing Hua University, China
Cermak, V., Czechoslovak Academy of Sciences, Prague
Czechoslovak Atomic Energy Commission
Faber, M., Finsen Institute, Copenhagen, Denmark
Boag, J. W., Institute for Cancer Research, Belmont, England
Briggs, J. S., AERE, Harwell, England
Burch, P. R. J., University of Leeds, England
Codling, K., University of Reading, Reading, England
Dolder, K. T., The University, Newcastle-upon-Tyne, England
Edgington, J. A., Queen Mary College, London, England
Fowler, J. F., Mt. Vernon Hospital, Northwood, England
Harris, S. J., University of Surrey, England
Hill, C. R., Institute of Cancer Research, Belmont, England
Loutit, J. F., MRC Radiobiology Unit, Harwell, England
Mayneord, W. V., Tadworth, Surrey, England
McDowell, M. R. C. Royal Holoway College, Surrey, England
National Radiological Protection Board, Library, Harwell, England
Peirson, D. H., AERE, Harwell, England
Pochin, E. E., National Radiological Protection Board, Harwell, England
Read, F. H., University of Manchester, England
Swallow, A. J., Christie Hospital & Holt Radium Inst., Manchester, England
West, J. B., Daresbury Laboratory, Daresbury, England
Åberg, R., Helsinki University of Technology, Otaniemi, Finland

Institute of Radiation Physics, Helsinki, Finland
Coursaget, J., CEA, Saclay, France
Desclaux, J.-P., CEN/G DRF-CPN, Grenoble, France
Durup, J., Laboratoire de Physico-chemie des Collisions Ioniques, Orsay, France
Fiquet-Fayare, F., Lab. de Collisions Electroniques, Orsay, France
Guyon, P. M., University of Paris, Orsay, France
Wuilleumier, F., University of Paris, Orsay, France
Buenker, R. J., Universitat Bonn, Bonn, Germany
Drexler, G., Institut für Strahlenschutz, Munich
Ehrhardt, H., Trier-Kaiserslautern University, Germany
Geiger, J., Trier-Kaiserslautern University, Germany
Gesellschaft für Strahlenforschung m.b.H., Frankfurt, Germany
Haensel, R., U. of Kiel, Kiel, West Germany
Hotop, H., Universitat Freiburg, Freiburg, Germany
Kaul, A., Klinikum Steglitz der F.U. Berlin, Germany
Mehlhorn, W., University of Freiburg, Freiburg, Germany
Muth, H., O. Saarlandes, Homburg, Germany
Niehaus, A., Universitat Freiburg, Freiburg, Germany
Oberhausen, E., Universitat Saarlandes, Homburg, Germany
Paretzke, H. G., Gesellschaft für Strahlen und Umweltforschung, MBH,
Institut für Strahlenschutz, Munich, Germany
Peyerimhoff, S. D., Universitat Bonn, Bonn, Germany
Sonntag, B., Deutsches Elektronen Synchrotron, Hamburg, Germany
Vogt, K. J., Kernforschungslange, Julich, Germany
Hukkoo, R. K., Bhabha Atomic Research Centre, Bombay, India
Berlman, I. B., Hebrew University, Jerusalem, Israel
Feige, Y., Israle AEC, Yavne, Israel
Benco, A., CCR EURATOM, Ispra, Italy
Casnati, E., CNEN, Rome, Italy
Cigna, A., CNEN, Rome, Italy
Clemente, G. F., CNEN, Rome, Italy
Gianturco, F. A., Istituto di Chimica Fisica, Universita degli Studi, Pisa, Italy
Prodi, V., CNEN Centro di Calcolo, Bologna, Italy
Rimondi, O., CNEN Centro di Calcolo, Bologna, Italy
Hatano, Y., Tokyo Inst. Tech., Tokyo, Japan
Higashimura, T., Kyoto University, Kyoto, Japan
Itikawa, Y., University of Tokyo, Tokyo, Japan
Kaneko, S., University of Tokyo, Tokyo, Japan
Matsuzawa, M., U. of Electro-Communications, Tokyo, Japan
Oda, N., Tokyo Inst. of Technology, Tokyo, Japan
Sasaki, T., University of Tokyo, Tokyo, Japan
Suzuki, H., Sophia University, Japan
Takahashi, T., Inst. of Physical and Chemical Res., Japan
Takayanagi, K., University of Tokyo, Japan
Watanabe, T., University of Tokyo, Japan
Lee, Sang-Soo, The Korea Advanced Inst. of Science, Seoul, Korea
Korean Atomic Energy Research Institute, Seoul, Korea
Brongersma, H.H., Philips Research Laboratories, Eindhoven, The Netherlands

de Heer, F. J., FOM Institute for Atomic and Molecular Physics, Amsterdam, The Netherlands
Kistemaker, J., FOM Institute for Atomic and Molecular Physics, Amsterdam, The Netherlands
van der Wiel, M., FOM Institute for Atomic and Molecular Physics, Amsterdam, The Netherlands
Burke, P. G., The Queen's University of Belfast, Northern Ireland
Shaikh, M. U., Pakistan Atomic Energy Commission, Rawalpindi, Pakistan
Cherry, R. D., University of Cape Town, South Africa
Liden, K., Radiation Phys. Dept., Lasarettet, Lund, Sweden
National Institute of Radiation Protection, FACK, Stockholm, Sweden
Gunther, A., CERN, Geneva, Switzerland
Cosandey, M., Service Cantonal de Controle des Irradiations, Geneva, Switzerland
Willax, H., Schweizerisches Inst. fur Nuklearforschung, Zurich, Switzerland
Komarov, E., Central Res. Inst. of Roentgenology and Radiology, Leningrad, U.S.S.R.
Tal'roze, V., Academy of Sciences of the USSR, Moscos, U.S.S.R.
Srdoc, D., Judjer Boskovic Inst., Zagreb, Yugoslavia
Wedin, G., Inst. of Theoretical Physics, FACK, Goteborg, Sweden
Seaton, M. J., U. College London, England